MECHANICAL BEHAVIOUR OF UFG ZIRCALOY-2 PROCESSED BY CRYOROLLING: EXPERIMENTS & SIMULATION

Ph.D. THESIS

by

SUNKULP GOEL

DEPARTMENT OF METALLURGICAL & MATERIAL ENGINEERING
INDIAN INSTITUTE OF TECHNOLOGY ROORKEE
ROORKEE-247667 (INDIA)

MACRH, 2015

MECHANICAL BEHAVIOUR OF UFG ZIRCALOY-2 PROCESSED BY CRYOROLLING: EXPERIMENTS & SIMULATION

A THESIS

Submitted in partial fulfilment of the
requirements for the award of the degree

of

DOCTOR OF PHILOSOPHY

in

METALLURGICAL & MATERIAL ENGINEERING

by

SUNKULP GOEL

DEPARTMENT OF METALLURGICAL & MATERIAL ENGINEERING
INDIAN INSTITUTE OF TECHNOLOGY ROORKEE
ROORKEE-247667 (INDIA)

MACRH, 2015

©INDIAN INSTITUTE OF TECHNOLOGY ROORKEE, ROORKEE-2015
ALL RIGHTS RESERVED

INDIAN INSTITUTE OF TECHNOLOGY ROORKEE
ROORKEE

CANDIDATE'S DECLARATION

I hereby certify that the work, which is being presented in the thesis entitled **"MECHANICAL BEHAVIOUR OF UFG ZIRCALOY-2 PROCESSED BY CRYOROLLING: EXPERIMENTS & SIMULATION"** in partial fulfilment of the requirements for the award of the degree of Doctor of Philosophy and submitted in the Department of Metallurgical & Material Engineering, Indian Institute of Technology Roorkee, Roorkee, is an authentic record of my own work carried out during a period from July, 2010 to March, 2015 under the supervision of Dr. R. Jayaganthan, Professor, Department of Metallurgical and Material Engineering, and Dr. I.V. Singh, Associate Professor, Department of Mechanical and Industrial Engineering, Indian Institute of Technology Roorkee, Roorkee.

The matter presented in this thesis has not been submitted by me for the award of any other degree of this or any other institute.

(SUNKULP GOEL)

This is to certify that the above statement made by the candidate is correct to the best of our knowledge.

(R. Jayaganthan)	(I. V. Singh)
Supervisor	Supervisor

Date: March , 2015

ABSTRACT

Zircaloy-2 is used for fabricating core components in nuclear power reactors. The alloy in the form of tubes i) 60 mm diameter with a wall thickness of 1 to 2 mm is used as Calandria tubes in Pressurised Heavy Water Reactor (PWR). ii) Less than 30 mm diameter is used as a fuel cladding in Boiling Water Reactor (BWR). These components are exposed to temperature of $400^{o}C$ to the inner surface and outer surface temperature of 280 to $350^{o}C$.

Almost 90% of the zirconium produced is used in nuclear plants and it cannot be recycled due to high cost factor. It is very essential to improve the mechanical and corrosion resistance properties of the Zr alloys, for enhancing service life of the structural components, through new thermo mechanical processing routes without altering its chemical composition. Ultrafine and nanostructured bulk materials produced by SPD techniques exhibit enhanced mechanical and functional properties as compared to bulk alloys as reported in the literature. The reduced grain size enhances the yield strength as per Hall-Petch relation. Strengthening is also possible by other structural features such as dislocations, subgrain boundaries, nanotwins and solute atoms. The sum of all these structural features are responsible for strengthening mechanisms. .

The performance of structural components in nuclear power reactors depends on tensile, creep and corrosion resistance properties. These properties are heavily influenced by microstructure of the material fabricated through different thermo mechanical treatments. SPD processing along with apt post heat treatment could produce multimodal microstructures in the materials, which can provide simultaneous improvement in strength and ductility. Cryorolling is one of the novel deformation processing techniques used widely to produce ultrafine and nanostructures in the pure metals and alloys. In this technique, dynamic recovery is suppressed to accumulate high density of dislocation in the materials during processing at liquid nitrogen temperature. The literature on the influence of cryorolling and cross rolling on the mechanical behaviour of zircaloy-2 is limited. Therefore, the present work has been focused on producing ultrafine and nanocrystalline zircaloy-2, with improved mechanical properties, from its coarse grained alloy using the various thermomechanical processing such as cryorolling, room temperature rolling, room temperature cross rolling and cryo cross rolling.

The objectives of the present work was to investigate (i) Mechanical behaviour and microstructural characteristics of ultrafine grained zircaloy-2 processed by cryorolling; (ii)

Mechanical and microstructural evolution of ultrafine grained zircaloy-2 produced by room temperature rolling; (iii) Texture and mechanical behavior of zircaloy-2 rolled at different temperature; (iv) Development of ultrafine grained zircaloy-2 by room temperature cross rolling and cryo cross rolling; (v) Microstructure and mechanical behavior of room temperature rolled zircaloy-2 after water and mercury quenching; (vi) Experimental evaluation of mechanical properties and fracture-fatigue simulation of cryo and room temperature rolled zircaloy-2; (vii) Experimental and simulation study on the fracture toughness of zircaloy-2 processed by rolling and cross rolling at different temperatures A chapter wise summary of the thesis is given below.

Chapter 1 highlights a brief introduction to the material used in the present investigation, deformation mechanism of the material used, various SPD processes used to produce UFG materials, applications of UFG materials in various fields and pros and cons associated with the SPD techniques.

The literature relevant to the present research work on ultrafine grained zircaloy-2 is critically reviewed in **Chapter 2**. A brief description of the properties and application of zirconium alloys as well as the effect of alloying elements on mechanical and corrosion behaviour are made. Deformation mechanism and mechanical properties of UFG Zr and its alloy is reviewed. It forms a strong basis to formulate the key objectives pertaining to the development of ultrafine grained zircaloy-2 with improved strength and ductility as compared to their commercially available bulk counterpart.

All the related experimental techniques and procedures employed in the present work are outlined in the **Chapter 3**. The methodology for characterizations and mechanical behaviour of UFG materials are discussed. The simulation is performed by using FEM and XFEM software package Abaqus.

In Chapter 4, Section 4.1 describes the following experimental investigations performed on zircaloy-2. The mechanical properties and microstructural characteristics of ultrafine grained zircaloy-2 processed by cryorolling (CR) were investigated. The solutionised zircaloy-2 was rolled at liquid nitrogen temperature (77K) with different thickness reductions (25% to 85%). The dislocation density $\langle\rho\rangle$ in the cryorolled zircaloy-2 increases with increasing true strain due to the suppression of dynamic recovery. The CR 85% alloy showed hardness and yield strength values of 282 HV and 891 MPa, respectively. The annealed CR 85% alloy showed higher ductility (9.5% and 11.2%) in rolling and transverse direction, respectively, as compared to CR 85% alloy.

In **section 4.2,** the effect of deformation strain at room temperature on the microstructural and mechanical properties of zircaloy-2 is discussed. The deformed alloy reveals the misorientation of incidental grain boundaries (IDBs) due to large plastic strain induced in the sample. The hardness of the alloy after 85% room temperature rolling (RTR) is found to be 269 HV, while the tensile strength is 679MPa and 697 MPa, in the rolling and transverse direction, respectively. The deformed alloy subjected to annealing at 400^{o} C for 30 minutes sample shows increase in ductility (6% and 7.2% in rolling and transverse direction respectively) due to the annihilation of dislocations as evident from the TEM study.

In **section 4.3,** the microstructural characteristics, texture, and mechanical properties of the zircaloy-2 processed by CR and RTR are described. Texture results show the activation of basal slip at higher strains in room temperature rolled zircaloy-2. In cryorolled zircaloy-2, only activation of prism slip is observed. Grain refinement, sub-structures, and texture in the deformed alloy contribute for the improvement in mechanical properties.

Effect of change in strain path by cross rolling at 300 K up to a true strain of 1.89 and at 77K upto 0.69 true strain has been studied and reported in **section 4.4**. The texture and mechanical properties of cross rolled zircaloy-2 at 77K and 300 K temperature are discussed. The fragmentation of near basal grains due to change in strain path is evident from the EBSD micrographs. $\{10\bar{1}2\}$ extension twins are observed initially up to 25% reduction, with the further reduction in thickness, near basal grains are oriented towards the normal direction. These basal grains are fragmentated due to changes in strain path upon room temperature cross-rolling as observed from KAM and EBSD images. TEM results of the room temperature cross rolled sample confirm the formation of ultrafine and nanograins in the alloy due to orientation of incidental dislocation boundaries (IDB) in the direction of macroscopic plastic flow and post-annealing treatment of the deformed alloy. A tensile strength of 991 MPa with 7.5% ductility is observed in the 85% room temperature cross rolled alloy. Annealing at 673K for 30 minutes recrystallizes the deformed microstructure and forms ultrafine grains. Evolution of deformed microstructure occurs by the activation of prismatic slip, $\{11\bar{2}2\}$ contraction and $\{10\bar{1}2\}$ extension twin at 77K. Probability of basal slip <a> at 77K is also observed by Taylor and Schmid factor analysis. The deformation at 300K occurs by prismatic, basal <a> and Pyramidal <c+a> slip predicted by texture images. Stored energy and dislocation density in the deformed alloy is calculated with the help of KAM.

In **section 4.5,** the effect of water and mercury quenching on the microstructural and mechanical behavior of room temperature rolled zircaloy-2 is discussed. Solution treatment of zircaloy-2 at 1073K, followed by quenching in mercury and water has been made prior to rolling. Different reduction from 25% to 85% of the quenched alloy was given for characterizing their microstructures and mechanical properties. Rolling reduction accumulates high dislocation density inside the materials, thereby enhancing the mechanical strength. Initial deformation has occurred by the activation of extension twinning as can be seen from EBSD microstructure. By optimizing the annealing temperature (400^o C for 30 minutes), ultrafine grains are produced in 85% room temperature rolled zircaloy-2. The mechanical properties of ultrafine grained zircaloy-2 is found to be better than the coarse grained zircaloy-2.

Chapter 5 describes the results of compact tension test, FEM and XFEM simulation performed for zircaloy-2. **Section 5.1** describes Finite element method used to study the 2-D quasi static crack analysis. *J*-integral and internal energy of the processed alloys are evaluated and compared with each other. Fatigue simulations are performed by using ANSYS software to find the S-N curve of mercury quenched, CR and RTR zircaloy-2.

In **section 5.2,** the fracture toughness of zircaloy-2 processed under rolling conditions is discussed. The rolled sample shows better crack arresting capabilities due to larger back stress produced during loading. Xtended finite element simulation is performed by using Abaqus software package to evaluate the fracture toughness of the alloy. CT results obtained after XFEM simulation show a good match for undeformed samples (MQ), while for severely deformed samples, the values obtained are less because dislocations are not modeled in the simulation.

The conclusions of the present investigation and scope of the future work are reported in **chapter 6.**

ACKNOWLEDGEMENTS

God has been exceptionally kind to me and without His blessings, this thesis would not have been completed. This thesis is part of a most remarkable journey of my life.

I could keep this thesis on the correct path only with the support and encouragement of numerous people, including my supervisors, my family members, my friends, associates and various institutes. It is challenging to recollect every person who has contributed to this thesis, but I would like to acknowledge everyone who has touched my life in any way.

First and foremost, I am highly grateful to my respected supervisor Prof. R. Jayaganthan, Department of Metallurgical and Material Engineering, Indian Institute of Technology, Roorkee who is the main inspiring source for me to choose and move in this pursuit of knowledge. He has always been a guiding spirit for me and helped me to do my work with his valuable suggestions on various important critical issues so that I could start my journey in the field. He has a place of an icon in my life.

I am highly delighted to express my gratitude to my loving, caring respected co-supervisor Dr. Indra Vir Singh, Associate Professor, Department of Mechanical and Industrial Engineering, Indian Institute of Technology, Roorkee. It is very difficult for me to express how many important ideas I got from him. All the moments I spent with him were auspicious moments for my research work especially. Without his scholarly guidance, it would not have been possible for me to pursue my research in such a way.

Beside the two respected personalities, it is a great privilege for me to pay my deep gratitude to Prof. B. K. Misra, Professor, Department of Mechanical and Industrial Engineering, Indian Institute of Technology, Roorkee who inspired me all along the course of work in spite of his busy schedule.

I wish to thank the Head Department of Metallurgical and Material Engineering for providing me with a nice working environment and fellowship. I express my deep sense of gratitude to my SRC members Prof. Satya Prakash and Prof. Anjan Sil for being there and encouraging in all my research endeavors. I thank all the faculty members of the Department of Metallurgical and Material Engineering for generously providing guidance whenever required. R. K. Sharma and Rajendra Sharma in the labs made sure that research sources are available in time.

I wish to express my gratitude to Board of Nuclear Sciences (BRNS), Mumbai and Nuclear Fuel Complex, Hyderabad for providing funding and material for the completion of my research.

I want to pay my special thanks to Dr. D. Srivastava, Scientist, BARC and Mr. S. K Jha, Manager, NFC, for their support to complete the work.

I will ever remember the support and affection given to me by Dr. Dharmendra Singh and Dr. Abhishek Kumar, my friends Ashish Selokar, Sandan Sharma, Himanshu Panjiyar, Deepa Mudgal, Paritosh Dubey, Kuldeep Saxena and Surendra Chandaniha who were great support for me to accomplish my work regularly, with patience. Without their help and support it would not have been possible for me to complete my work.

I would like to thank my lab mates Kamal Sharma, Sachin Chaudhary, Gagandeep Bharadwaj, Amit Sharma, Dr. Somnath Bhattacharya, P. Nageshwar Rao, Nikhil Sishodhiya, Nidhi Rana, Devasri Fuloria and Vipul Tiwari for their co-operation in lab.

Last but not the least, I am extremely grateful to my father Mr. K. L. Goel and my mother Smt. Kusum Rani Goel, along with my younger brothers and sisters for their unfailing love and support.

SUNKULP GOEL

TABLE OF CONTENTS

LIST OF TABLES

LIST OF FIGURES

LIST OF ABBREVIATIONS AND SYMBOLS

SPD	Severe Plastic Deformation
UFG	Ultra-Fine Grained
GNBs	Geometrically Necessary Boundaries
IDBs	Incidental Dislocation Boundaries
HCP	Hexagonal Closed Packed
TEM	Transmission Electron Microscopy
FE-SEM	Field Emission Scanning Electron Microscope
EBSD	Electron Back Scattered Diffraction
XRD	X-Ray Diffraction
BCC	Body Centered Cubic
GPa	Giga Pascal
BWR	Boiling Water Reactor
PWR	Pressurized Water Reactor
ECAP	Equal Channel Angular Pressing
HPT	High Pressure Torsion
ARB	Accumulative Roll Bonding
MAF	Multi Axial Forging
TE	Twist Extrusion
ASR	Asymmetric Rolling
SSMR	Super Short Interval Multi-Pass Rolling
CFAE	Continuous Frictional Angular Extrusion
FSP	Friction Stir Processing
STS	Severe Torsion Straining
CCDF	Cyclic Close Die Forging
RCS	Repetitive Corrugation And Straightening
CCM	Cone-Cone Method
CCDF	Cyclic Close Die Forging
NECAP	Non-Equal Channel Angular Pressing
HPTT	High-Pressure Tube Twisting
CEE	Cyclic Expansion–Extrusion
XFEM	Xtended Finite Element Method
RTCR	Room Temperature Cross Rolling

CCR	Cryo Cross Rolling
FEG-SEM	Field Emission Gun Scanning Electron Microscopy
UTM	Universal Testing Machine
CT	Compact Tension
NC	Nanocrystalline
CANDU	Canadian Deuterium Uranium
LWR	Light Water Reactors
NFC	Nuclear Fuel Complex
SAED	Selected Area Electron Diffraction
ICSD	Inorganic Crystal Structure Database
FEM	Finite Element Method
RTR	Room Temperature Rolling
CR	Cryo Rolling
MPa	Mega Pascal
Hf	Hafnium
Zr	Zirconium
Å	Armstong
HV	Hardness Vickers
KAM	Kernal Average Misorientation
M	Taylor Factor
CRSS	Criticaly Resolved Shear Stress
CI	Confidence Index
µm	Micro Meter
OIM	Orientation Imaging Microscopy
Annld	Annealed
TD	Transverse Direction
RD	Rolling Direction
Cu	Copper
Al	Aluminium
Ni	Nickel
Ti	Titanium
CPE4R	4-node bilinear plane strain quadrilateral, reduced integration, hourglass control

CPS4R	4-node bilinear plane stress quadrilateral, reduced integration, hourglass control
MQ	Mercury Quenched
KN	Kilo Newton
K_{IC}	Critical Stress Intensity Factor
USA	United States of America
Sn	Tin
Fe	Iron
O	Oxygen
Cr	Chromium
Ti	Titanium
Zn	Zinc
Mg	Magnesium
K	Kelvin
T_m	Melting temperature
^oC	Degree Celcius

CHAPTER 1

INTRODUCTION

1.1 General Introduction

Zirconium was first discovered in 1789 by a German Scientist Klaproth of Ceylon. In the early time of discovery, it was isolated from its metallic form until 1824 when Berzelius obtained an impure metal powder by reducing potassium fluorozirconate with potassium. Hafnium is always associated with zirconium in ore form (about 2%) and it was not isolated until 1923. In 1925, Van Arkel and de Boer developed an iodide process to reduce Hf from Zr and produced a high purity crystal bar of Zr. It showed good ductility and also used in electronic industry for residual gas gettering. In 1947, Krolls process was developed to produce Zr sponge by US Bureau of mines (J. H Schemel, 1977). However, initial studies suggested that Zr is not applicable for nuclear application due to absorption of high thermal neutrons until it was observed that Hf is responsible for high thermal neutron cross section which was reported, by Oak Ridge. In the late 1950's, Zr was available in industries and it was used by many chemical industries in various severe corrosion environment. Admiral Rickover in Naval Nuclear Propulsion program at Pennsylvania, USA was the first person to use Zr in nuclear application for the water cooled reactor of the submarine nautilus (Rickover, 1975). However, its use took an upward swing when Canadian scientists developed CANDU nuclear reactor in which natural uranium was utilized, making neutron absorption a major consideration. Thus, Zr became attractive and necessary material in the structural components of reactor core due to its low neutron absorption cross section (Figure 1.1).

Initially, when zirconium was selected for nuclear applications, scientists were trying to produce zirconium as pure as possible but the problem with corrosion at high temperature was not solved. Later, they found that purity was not the issue as even the impure zirconium crystal exhibited better corrosion resistance. Finally, they found that Sn, Fe, Cr and Ni are helpful in improving the corrosion resistance. The first alloy of zirconium for nuclear application produced was zircaloy-1 in which tin was 2.5%. The problem of corrosion was still observed in zircaloy-1. Then, zircaloy-2 was produced with lesser tin (1.5%), iron (0.15%), nickel (0.05%) and chromium (0.10%). Chromium was accidentally picked up from the stainless steel reactor vessel. Zircaloy-2 was found to have equal strength with better corrosion properties than zircaloy-1 (Krishnan *et al.*, 1981; Lemaignan *et* *al*., 1984). Subsequently, zircaloy-3 and zircaloy-4 alloys with better properties were produced by eliminating nickel.

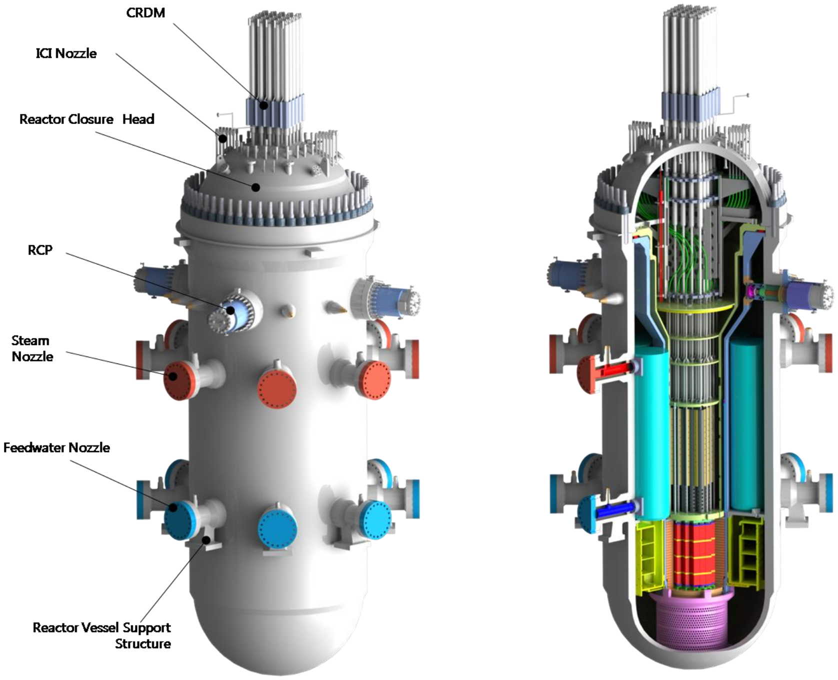

Figure 1.1 Small Modular Reactor (SMR) Showing Core of a Nuclear Reactor (http://ansnuclearcafe.org/)

1.2 Applications of Zirconium Alloys in the Nuclear Industry

Zircaloy-4 is used in light water reactors (LWR) and pressurized water reactors (PWR). Zircaloy-2 is used in boiling water reactors (BWR). The zircaloy-2 in the form of tubes is used for the following applications.

- Tubes with 60 mm diameter with a wall thickness of 1 to 2 mm are used as Calandria tubes in PWR.
- Tubes less than 30 mm diameter are used as fuel cladding in BWR.

These components are exposed to temperature of 400^{o}C to the inner surface and outer surface temperature of 280 to 350^{o}C. The heat flux in the cladding is in the range of 30-50 W cm^{-2} (Lemaignan et.al., 1984).

The total production of zirconium in the world is estimated to be 1,250,000 metric tons with India itself producing about 38000 metric tons in 2010 as reported by United States Geological

Survey Mineral Resources Program in 2011. With increasing demand of zirconium, its production is ever increasing as shown in Figure 1.2 (a), while Figure 1.2(b) shows the production percentage in 2010. The zirconium used as fuel cladding material is not recycled, which is treated as radioactive waste for removal and stored for long term without reconditioning (Gusakov-Stanyukovich *et al.*, 2010). As almost 90% of the zirconium produced is used in nuclear plants, it cannot be recycled. Even the cost of recycling is very high. There is ever growing demand to increase efficiency of the alloy in terms of mechanical properties, which can be easily achieved by engineering the microstructures.

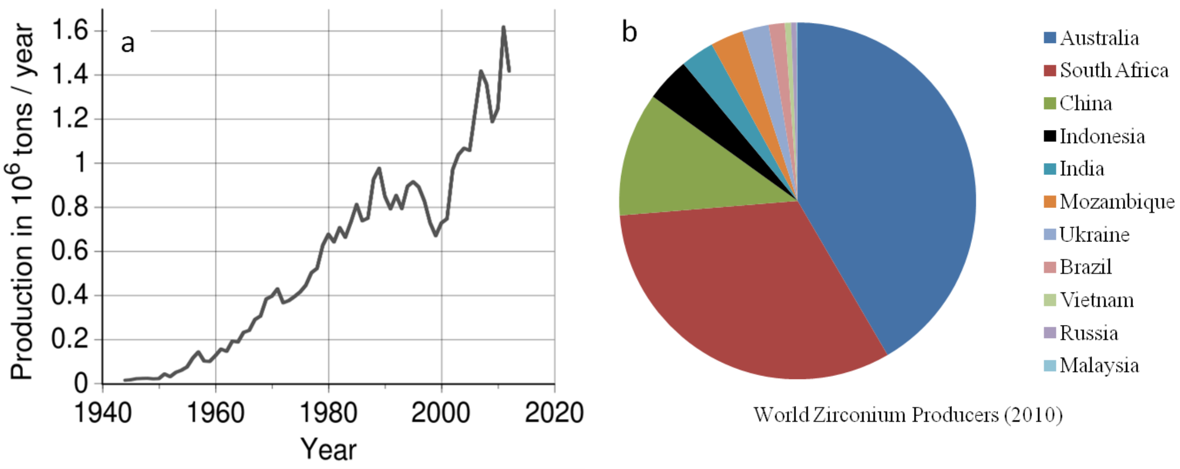

Figure 1.2(a) Graph Showing Trend of Zirconium Production in the World and **(b)** Pie Chart Showing the Countries Producing Zirconium in Year 2010 (U.S Geological survey)

With the reduction in grain size, during deformation, mean travelling distance of the dislocations is reduced and dislocation pile up near the grain boundary occurs. Thus, strength of the material increases in accordance with the Hall-Petch relationship (Hall, 1951; Petch, 1953). The ultrafine (<1 μm) and nanocrystalline (>100 nm) zirconium alloys exhibit better mechanical properties and could be used for producing structural components of nuclear reactors. There are basically two types of approaches for the development of ultra fine grained materials (i) Top down and (ii) Bottom up approach.

1.3 Ultrafine Grained Materials

Severe Plastic Deformation (SPD) techniques (Valiev *et al.*, 2000; Valiev *et al.*, 2006; Estrin *et al.*, 2013) have been used to produce ultrafine grained materials with improved mechanical and functional properties. Iwahashi *et al.*, (1998) have explained the phenomenon of grain refinement in which dislocation cells formed during deformations are transformed into high angle grain boundary. On increasing strain, dislocations get arranged in the form of boundaries with high misorientation angle known as geometrically necessary boundaries (GNBs) and trapping incidental dislocation boundaries (IDBs) inside it. The GNBs are formed during initial deformation and with increasing strain, IDBs gets oriented along the macroscopic orientation where the macroscopic plastic flow occurs. The subdivision of grain takes place with further increase in strain leading to the formation of newly developed cells, thus forming nanocrystalline and ultrafine grains (Hansen, 2001; Hughes *et al.*, 2003; Jiang *et al.*, 2012).

Due to hexagonal closed packed (HCP) structure, the deformation occurs by twinning and slip in zircaloy-2. The primary deformation mechanism is prismatic <a> slip $\{10\bar{1}0\}\langle 1\bar{2}10\rangle$ and can be seen at all temperatures. According to the Von-mises criteria, at least five independent slip systems are needed for a material to deform (Mises, 1928). Therefore, other deformation systems (slipping and twinning) should be present along with prism <a> slip. For examples, deformation can be accommodated by pyramidal and basal slips, which results in a small homogeneous strain without change in volume (Groves *et al.*, 1963). The prismatic and <c+a> pyramidal slip could be activated at low strain easily, while basal <a> slip gets activated when prismatic becomes strain hardened and cross slip operates at high strain in zirconium alloys (Akhtar, 1973a; Tome *et al.*, 2001).

Twinning is another mode of deformation in zirconium alloy and is independent of temperature due to which at low temperature, the deformation occurs mostly by twinning (Akhtar 1973a; Luan *et al.*, 2013). In extension, loading along 'c' axis, $\{10\bar{1}2\}\langle\bar{1}011\rangle$ twin gets activated and $\{11\bar{2}1\}\langle\bar{1}\bar{1}26\rangle$ twins get activated less often. During contraction loading along 'c' axis, $\{11\bar{2}2\}\langle\bar{1}\bar{1}23\rangle$ twins are active while, $\{10\bar{1}1\}\langle\bar{1}012\rangle$ twins are often seen (McCabe *et al.*, 2009). At liquid nitrogen temperature, deformation is governed mainly by prismatic slip, extension twinning $\{10\bar{1}2\}\langle\bar{1}011\rangle$, $\{11\bar{2}1\}\langle\bar{1}\bar{1}26\rangle$ and contraction twinning $\{11\bar{2}2\}\langle\bar{1}\bar{1}23\rangle$ (McCabe *et al.*, 2006; McCabe *et al.*, 2009; Akhtar, 1973b; Luan *et al.*, 2013).

Vanitha *et al.*, (2009) have reported the formation of equiaxed fine grains for the alloy rolled up to 60% followed by recrystallisation at 710^{o} C due to recovery process, strain localization, deformation bands, and by extended recovery for selected grain orientations. Mukherjee et al.,

(2004) investigated microstructural characteristics of zircaloy-2 rolled at room temperature up to 70% after annealing it at 750° C for 10 hours in a sealed quartz tube under vacuum and cooled at the rate of 5° C per hour. The domain size, microstrain, dislocation density and stacking fault probabilities were evaluated by simplified breadth method, Williamson-Hall technique and the modified Rietveld method, respectively. The dislocation density ‹ρ› was found to be 10^{-15} /m^2. The relationship between domain size and dislocation density in hexagonal closed packed (HCP) material was established. The maximum strength of room temperature rolled zircaloy-2 after annealing at 750° C for 20 hours in vacuum was found to be approx 689 MPa (Whitmarsh, 1962). Sahoo et al., (2007) have investigated the heterogeneous deformation characteristics of single phase zircaloy-2 subjected to plane strain deformation. They showed the existence of deformed and non-deformed grains (equiaxed) in the alloy cold rolled to 20% and 50% reductions through ESBD measurements. The near basal grains are not fragemented as reported in their work. Ballinger and Pelloux (1981) have studied the influence of anisotropy on the mechanical properties of zircaloy-2 and reported that the deformation mechanisms such as prism slip, <c+a> slip and twinning contribute for the texture dependent mechanical properties.

Zircaloy-2 has been cryorolled up to 70% and the deformed sample exhibit tensile strength of 795.9 MPa as reported in the literature. (Kamalanath *et al.*, 2012; Guo *et al.*, 2012a; Guo *et al.*, 2012b; Guo *et al.*, 2012c) have investigated the mechanical properties of cryorolled Zr and reported the formation of ultrafine grains in the metal, which exhibit ultimate tensile strength of 658 MPa and 20.7% elongation at break after annealing at 450°C for 1 hour. The multimodal structure obtained after annealing the cryorolled pure Zr with rolling strain of ~2.87 at 400°C for 1 hour contains 63% grains having size less than 100nm and 37% grains having size between 100 and 1000nm. The sample annealed at 450°C contains 20% nano crystalline, 56% ultrafine and 24% coarse grains as estimated from TEM images. Dislocation density of cryorolled sample with 92% rolling thickness reduction was estimated to be $1.4\text{x}10^{-14}$ /m^2 (Guo *et al.*, 2012b, Guo *et al.*, 2012c).

The limited literature is available on tensile and fracture behaviour of Zr alloys processed by SPD techniques Hence,the present work has been envisaged to develop ultrafine grained zircaloy-2 processed through rolling at room temperature and cryo temperature (normal rolling and cross rolling) and substantiate the grain refinement mechanisms through detailed microstructural investigations by TEM, FE-SEM/EBSD, XRD. Optimization of annealing conditions for deformed zircaloy-2 has been made to achieve a best combination of strength and ductility in the present work.

1.4 Outline of Thesis

The outline and contents of various chapters of the thesis are summarized as follows:

The brief description of zirconium and its alloys, properties of ultrafine grained/nanocrystalline materials, different techniques of their synthesis and introduction to cryorolling followed by literature review are summarized in **Chapter 2.** Based on literature review, the problem for present research work was formulated and listed in S**ection 2.5**. Materials selection, different processing techniques adopted and their experimental procedures, methodology pertaining to their microstructural characterization, texture analysis and mechanical testing are discussed in detail in **Chapter 3.** Different experimental investigations performed on zircaloy-2 processed through rolling and cross rolling at different temperatures and their results are discussed in **Chapter 4.** Mechanical behaviour and microstructural characterizations of ultrafine grained zircaloy-2 processed by cryorolling are discussed in **Section 4.1.** Mechanical and microstructural characterizations of ultrafine Grained zircaloy-2 processed by room temperature rolling are discussed in **Section 4.2.** Texture and mechanical behavior of zircaloy-2 rolled at different temperature are discussed in **Section 4.3.** Development of ultrafine grained zircaloy-2 by room temperature cross rolling and texture evolution and ultrafine grain formation in cross cryorolled zircaloy-2 are discussed in **Section 4.4.** Microstructure and mechanical behavior of room temperature rolled zircaloy-2 upon subjected to solutionising treatment followed by water and mercury quenching are discussed in **Section 4.5.**

The mechanical behavior of deformed zircaloy-2 has been substantiated using microstructural and texture characteristics investigated through FE-SEM, EBSD, TEM, and XRD. The conclusions drawn from experimental investigations of zircaloy-2 are also reported at the end of each section of **Chapter 4.** Experimental studies and FEM simulation of fracture toughness of zircaloy-2 were made and the results are discussed in **chapter 5**. Experimental Evaluation of Mechanical properties and Fracture Fatigue Simulation are discussed in **Chapter 5.1**. Effect on Fracture Toughness of zircaloy-2 after rolling and cross rolling at different temperatures by experiments and simulation are discussed in **Chapter 5.2**.

The final conclusions are summarized in **Chapter 6** with future scope followed by references in the present work.

CHAPTER 2

LITERATURE REVIEW

In this chapter, a brief description of zirconium and its alloys, various properties of the alloy, and processing techniques used for producing ultrafine/nanocrystalline materials are discussed. Literature pertaining to cryorolling and other severe plastic deformation techniques used for producing ultrafine grain microstructure in zircaloy-2 and other materials are discussed. The formulation of problem for the present dissertation work has been made based on the existing literature. The scope, objectives, and outline of the dissertation work are discussed in this chapter.

2.1 Properties of Zirconium

Zirconium is a hexagonal close packed (HCP) metal at room temperature with anisotropic mechanical properties. In ‘a’ and ‘c’ axes, the stress free lattice spacing at room temperature (RT) are 3.23118 Å and 5.14634 Å and 3.22977 Å and 5.14173 Å at 77k , respectively, and c/a ratio is 1.59271 at RT and 1.59198 at 77K, respectively (Hurst 1997). The elastic constants of single crystal Zr at room temperature and 77K are shown in **Table 2.1** (Fischer *et al*., 1964). The stiffness is calculated from the elastic constants by Nye’s equation (1957).

At 865^o C, Zr undergoes allotropic transformation from HCP α phase to BCC β phase. On cooling, the transformation takes place, either martensitic or banitic which depends on the cooling rate. The melting occurs at 1860^o C. Due to low thermal neutron capture cross section of zirconium, which is 30 times less than iron, imparts the nuclear reactor with high thermal efficiency (Lemaignan *et al*., 1984).

Table 2.1 Stiffness Values of Single Crystal Zircaloy-2

Temp. ^{o}K	**C11**	**C33**	**C44**	**C66=½(C11-C12)**	**C13=C23**	**C12**	**Ea (Gpa)**	**Ec (Gpa)**
73	154.2	171.6	31.8	43.2	64.8	67.8	115.26	133.77
298	143.4	164.8	32	35.3	65.3	72.8	98.79	125.35

2.2 Alloys and Alloying Elements

Zr alloys currently used are of two types: i) The first type is for nuclear applications and ii) The second type is for industrial applications. In nuclear applications, four reactor grades of Zr and its alloys are used (C Lemaignan *et al*., 1984) as given below.

1. Pure unalloyed zirconium (UNS R-60001) used as inner lining of zirconium alloy fuel cladding tubes. It is corrosion resistant in steam and hot water environment.
2. Zircaloy-2 (UNS R-60802) is Zr-Sn alloy with some amount of Fe, Cr, and Ni. It is highly resistant to corrosion in steam and hot water. It is used as cladding and structural material, such as guide tubes in boiling water reactor (BWR) and pressurized water reactor (PWR) and channel boxes in BWR and structural material in CANDU reactors.
3. Zircaloy-4 (UNS R-60804) is a modified version of zircaloy-2 with no nickel but contains iron in a controlled way. It is better than zircaloy-2 in terms of its lesser ability to absorb hydrogen. It is used for similar applications as given above for zircaloy-2.
4. Zr-2.5Nb (UNS R-60901) has high corrosion resistance to supersaturated water and is used as pressure water tubes in heavy water reactors.

Zirconium shows excellent corrosion resistance to various acids, alkalies, salts and organic compound. The few chemicals which corrode zirconium are hydrofluoric acid, ferric or cupric chloride, aqua regia, concentrated sulphuric acid and chlorine gas. Due to better corrosion resistance to chemicals, the following zirconium alloys are used in chemical industries.

1. UNS R 60702- commercially pure zirconium similar to reactor grade.
2. UNS R 60704- a Zr-1.5 Sn similar to zircaloy-2.
3. UNS R 60705 and 60706- Zr-2.5 Nb a high strength alloy and the latter having low oxygen contents.

The safety concerns restrict the development of new alloy because a large amount of data is needed to verify the safety in nuclear applications. The alloys used currently are broad enough to optimize the properties within the present ranges in composition. The microstructure of the alloy can be changed by altering the composition of the alloys and hence changing the α-β phase transformation. The main alloying elements, which affect the microstructure and phase transformation of the alloys, are discussed below.

2.2.1 Oxygen and Tin

Oxygen is not considered as impurity but as an alloying element. Zirconium is added in the form of ZrO_2 powder before melting. The oxygen contents increase the yield strength by solution strengthening and its content are in the range of 800 to 1600 ppm. A concentration of 1000 ppm oxygen addition increases the yield strength by 150 MPa. Oxygen is also an α stabilizer and forms an interstitial solid solution. The phase diagram of Zr-O is shown in **Figure 2.1**. High concentrations of oxygen stabilize α phase to liquid temperature.

Tin is also an α stabilizer and it forms a substitutional solid solution in α and β phase. It mitigates the effect of nitrogen in deteriorating corrosion behavior when present in the range of 1.2 to 1.8%. Due to better control in processing parameters usually in terms of controlling nitrogen content, use of tin is reduced in alloys. Tin also affects the tensile yield strength of the alloy.

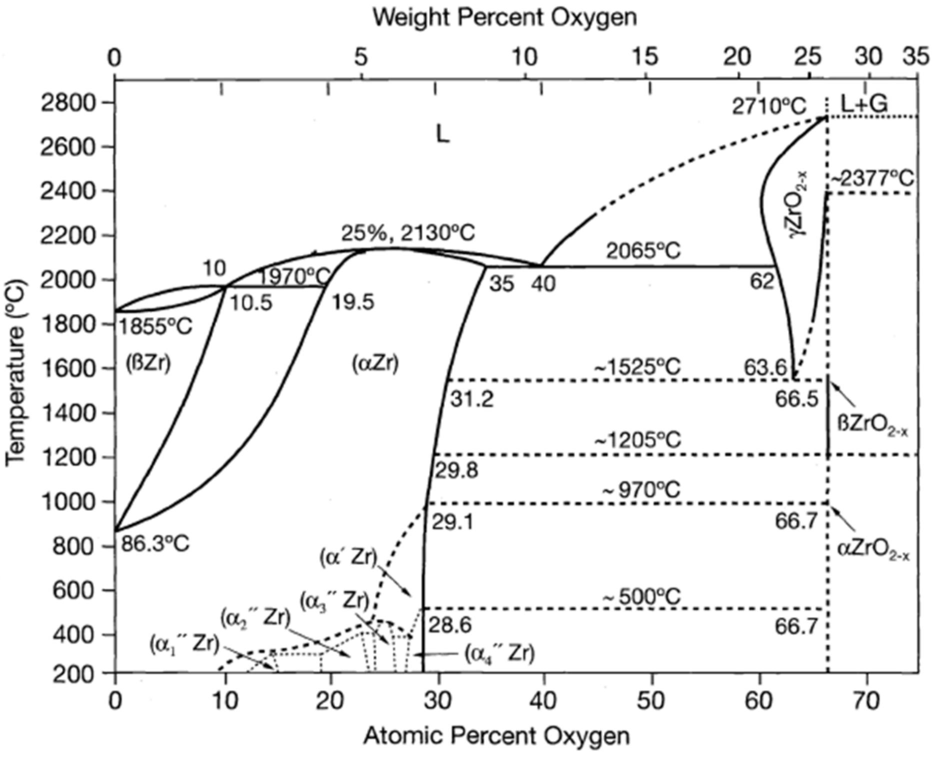

Figure 2.1 Zirconium-Oxygen Phase Diagram (Abriata *et al.*, 1986)

2.2.2 Iron, Chromium and Nickel

These elements in phase diagram have a eutectoid composition of β phase due to which they are known as β eutectoid. The eutectoid phase diagram of Fe, Cr and Ni can be seen from **Figure 2.2-2.4**. As discussed in **Chapter 1**, they are accidentally introduced into the alloy, which showed enhanced corrosion resistant property leading to the formation of zircaloy-2 and zircaloy-4. The dissolution of these elements in zirconium takes place in the range of 835^{o} to 845^{o} C, in upper α -β range (Miquet *et al*., 1982). The solubility of Fe and Cr in α phase is very low, in the range of 120 ppm and 200 ppm respectively (Charquet *et al*., 1989). For Zr-Cr and Zr-Ni binary alloys, Zr_2Ni and $ZrCr_2$ are the stable forms of the second phase. The Zr_3Fe phase which appears in Zr-Fe phase diagram is not found in Zircaloy (Bhanumurthy *et al*., 1991).

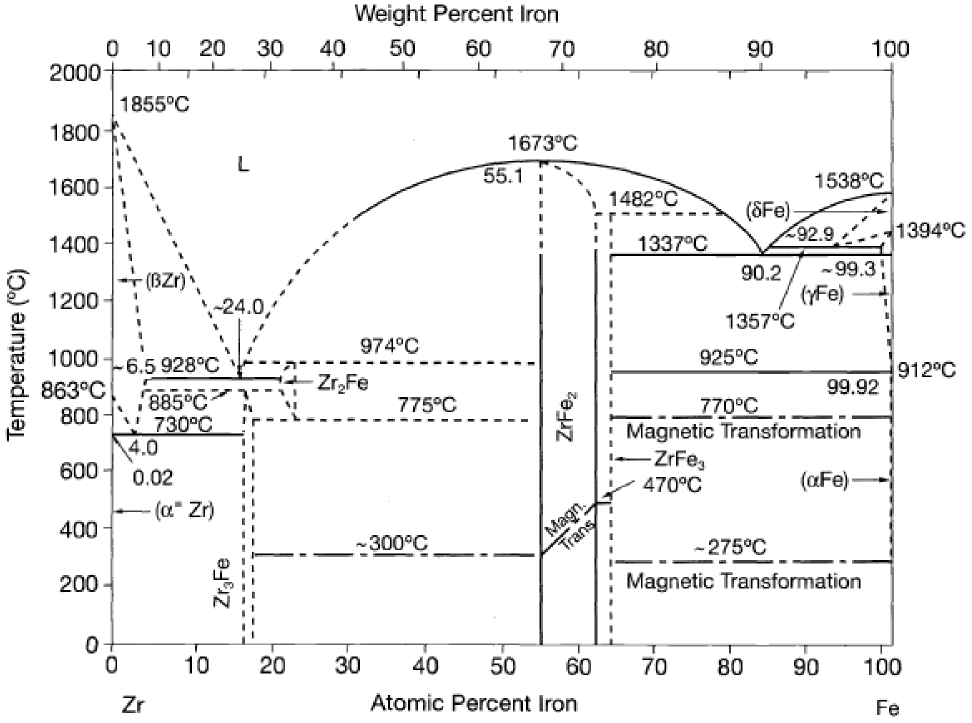

Figure 2.2 Zirconium-Iron Phase Diagram (Arias and Abriata 1988)

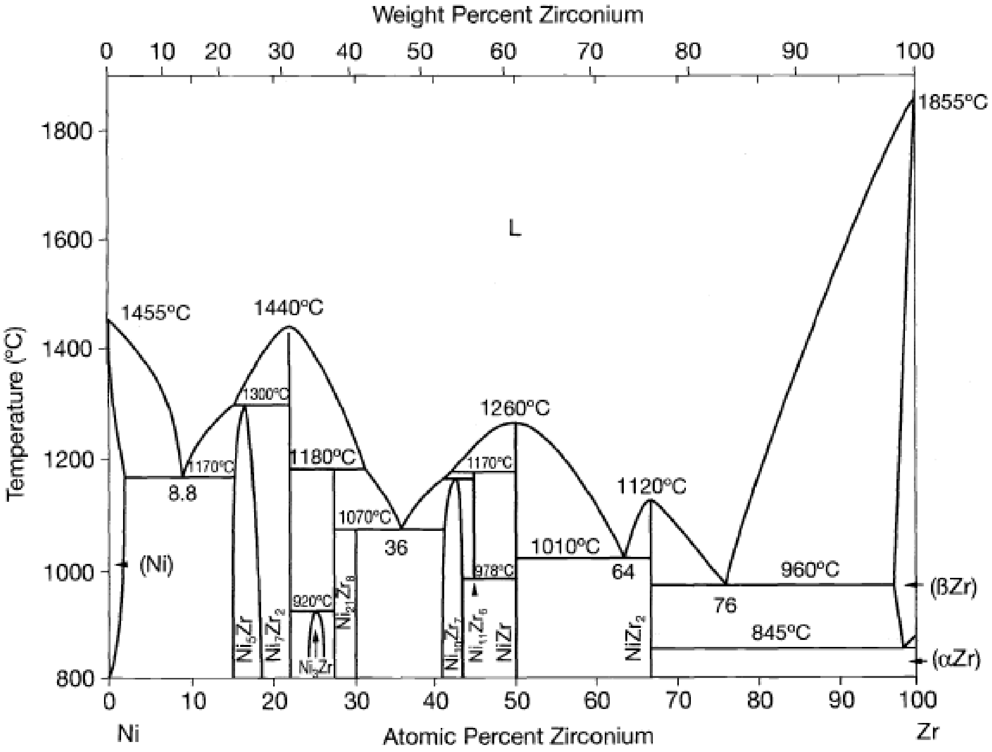

Figure 2.3 Zirconium-Nickel Phase Diagram (Nash *et al*., 1984)

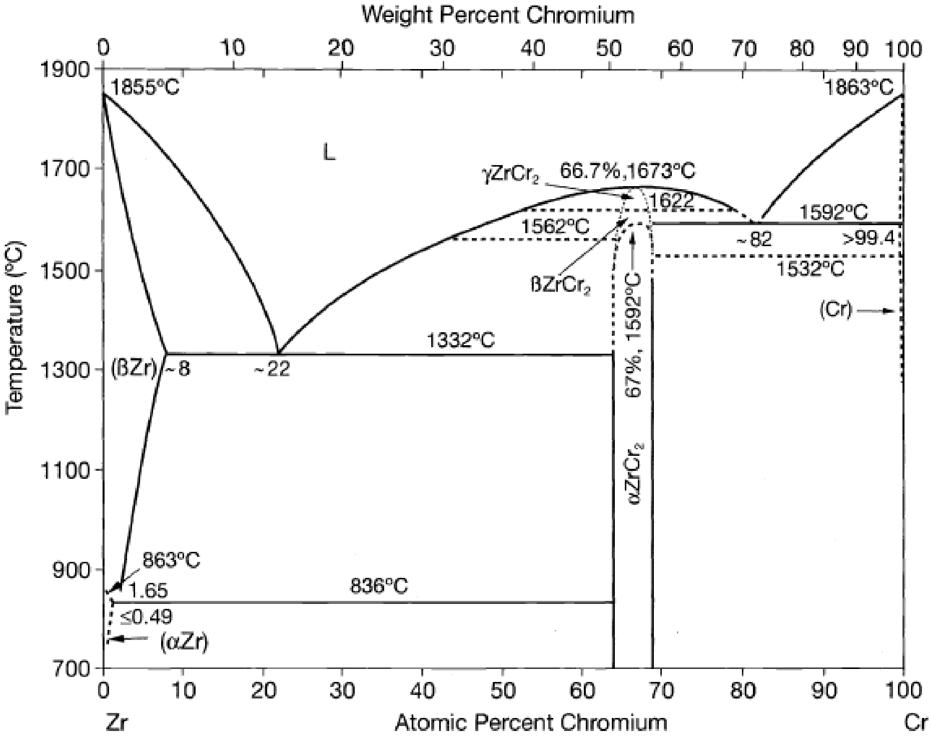

Figure 2.4 Zirconium-Chromium Phase Diagram (Arias and Abriata 1986)

Therefore, the intermetallics formed in zircaloy are Zr$_2$(Ni, Fe) and Zr(Cr, Fe)$_2$. In zircaloy-4, there is a nominal composition of Fe/Cr ratio, while in Zircaloy-2, the partitioning of Fe between two intermetallic phase causes a more complex relationship between the precipitate composition and nominal composition (Charquet *et al.*, 1985). Crystal structure of Zr(Cr, Fe)$_2$ depends on composition and heat treatment. The crystallographic structure depends on the ratio of composition of Fe/Cr (FCC below 0.1 or above 0.9) and HCP in between (0.1< HCP >0.9) (Shaltiel *et al.*, 1976). Zr$_2$(Ni, Fe) phase exhibits body centered tetragonal structure. The size of precipitates is also of great importance for corrosion resistance, larger precipitates are good for uniform corrosion resistance and uniformly distributed small precipitates are desirable for localized corrosion resistance.

2.2.3 Niobium

Niobium is a β stabilizer, from pure β zirconium to pure niobium, a substitutional solid solution forms at high temperature. There is a monotonic phase transformation at 620^{o} C as seen from **Figure 2.5**. On water quenching from β or α+β region, the β-Niobium rich grains transform by martensitic decomposition to supersaturated $\alpha^{'}$ HCP phase, subsequent heat treatment below monotectoid temperature leads to precipitation of niobium $\beta^{'}$ precipitates at twin boundaries of $\alpha^{'}$ needles (Williams *et al.*, 1966). By slow cooling β or by ageing the quenched material, a metastable phase ω can be obtained (Dawson *et al.*, 1970).

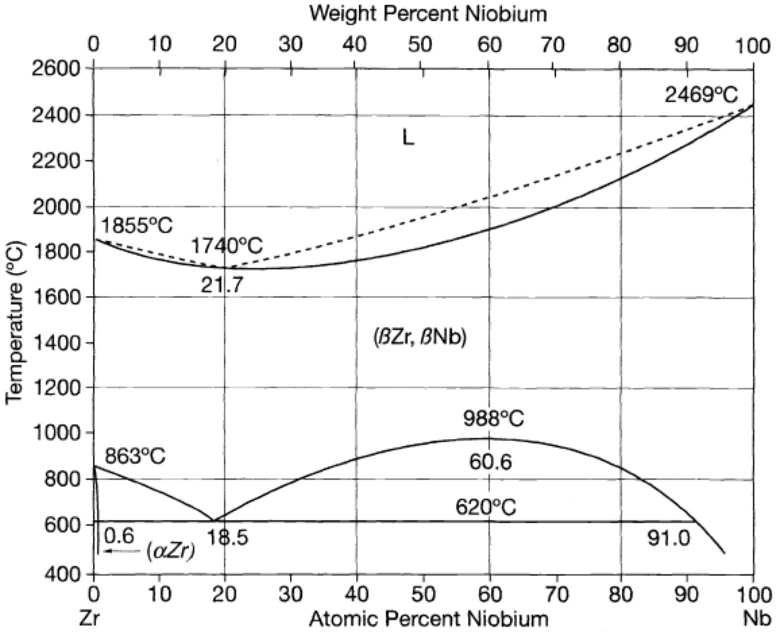

Figure 2.5 Zirconium-Niobium Phase Diagram (Abriata *et al.*, 1982)

2.2.4 Hydrogen

Hydrogen is not an alloying element but it causes corrosion once it is absorbed from water. Hydrogen is located on the tetrahedral site of the HCP cell of zirconium matrix and is soluble to about 15 ppm at 200^{o}C to about 200 ppm at 400^{o}C. As the solubility increases, hydrogen forms a δ face centered cubic (FCC) phase i.e. $Zr\ H_{1.66}$, which can be seen from phase diagram shown in **Figure 2.6**. Metastable body centered tetragonal γ phase (ZrH) is formed when cooling rate is high (Weatherly 1981).

Precipitation of hydride causes volume expansion, due to which this new phase tends to reduce its strain energy by nucleating low index crystallographic planes (Bradbrook *et al*., 1972). Further growth of the hydride clusters takes place in basal plane or plane of maximum tensile stress (Kearns *et al*., 1966). Other minor constituents such as carbides, phosphides and silicides are also found in the form of precipitates.

2.3 Deformation Mechanism in Zirconium Single Crystal

The mode of deformation (slip or twinning) in Zr depends on the combination of stress applied and temperature. Various deformation modes of zirconium crystal can be seen from **Figure 2.7**. Slip on the prism plane $\{10\bar{1}0\}$ along the direction $\langle 11\bar{2}0\rangle$ (denoted as prism <a> slip) is the primary deformation mode in zirconium crystal up to 500^{o}C (Tenckhoff 1974, Akhtar 1975, Akhtar 1973a). It is also reported that prism slip is easiest slip system and is active at all temperatures (Akhtar 1973a). Slip on the {0002} basal and $\{10\bar{1}1\}$ pyramidal <a> plane in the direction $\langle 11\bar{2}0\rangle$ is also reported by Tenckhoff (1974). Basal <a> slip {0002} $\langle 11\bar{2}0\rangle$ in a single crystal takes place at high temperature, 575^{o} C when crystal has unfavorable orientation for prism slip (Akhtar 1973b). Slip on the $\{10\bar{1}1\}$ and $\{11\bar{2}1\}$ pyramidal planes in the $\{11\bar{2}3\}$ <c+a> direction are also reported (Tenckhoff 1974, Akhtar 1973a). $\{11\bar{2}1\}$, $\{11\bar{2}2\}$, $\{11\bar{2}3\}$ and $\{10\bar{1}2\}$ are the four twinning mechanisms, which are found to be active in single crystal (Rapperport 1959, Rapperport 1960). The most active twin is $\{11\bar{2}1\}$ found at all temperature (77K to 1075K), while $\{11\bar{2}2\}$, $\{11\bar{2}3\}$ and $\{10\bar{1}2\}$ active in deceasing order of their importance. At 77K, the $\{11\bar{2}1\}$ twin was found to be most dominant while at 293 K, $\{10\bar{1}2\}$ is most dominant (Reed Hill *et al*., 1968; Akhtar *et al*., 1971).

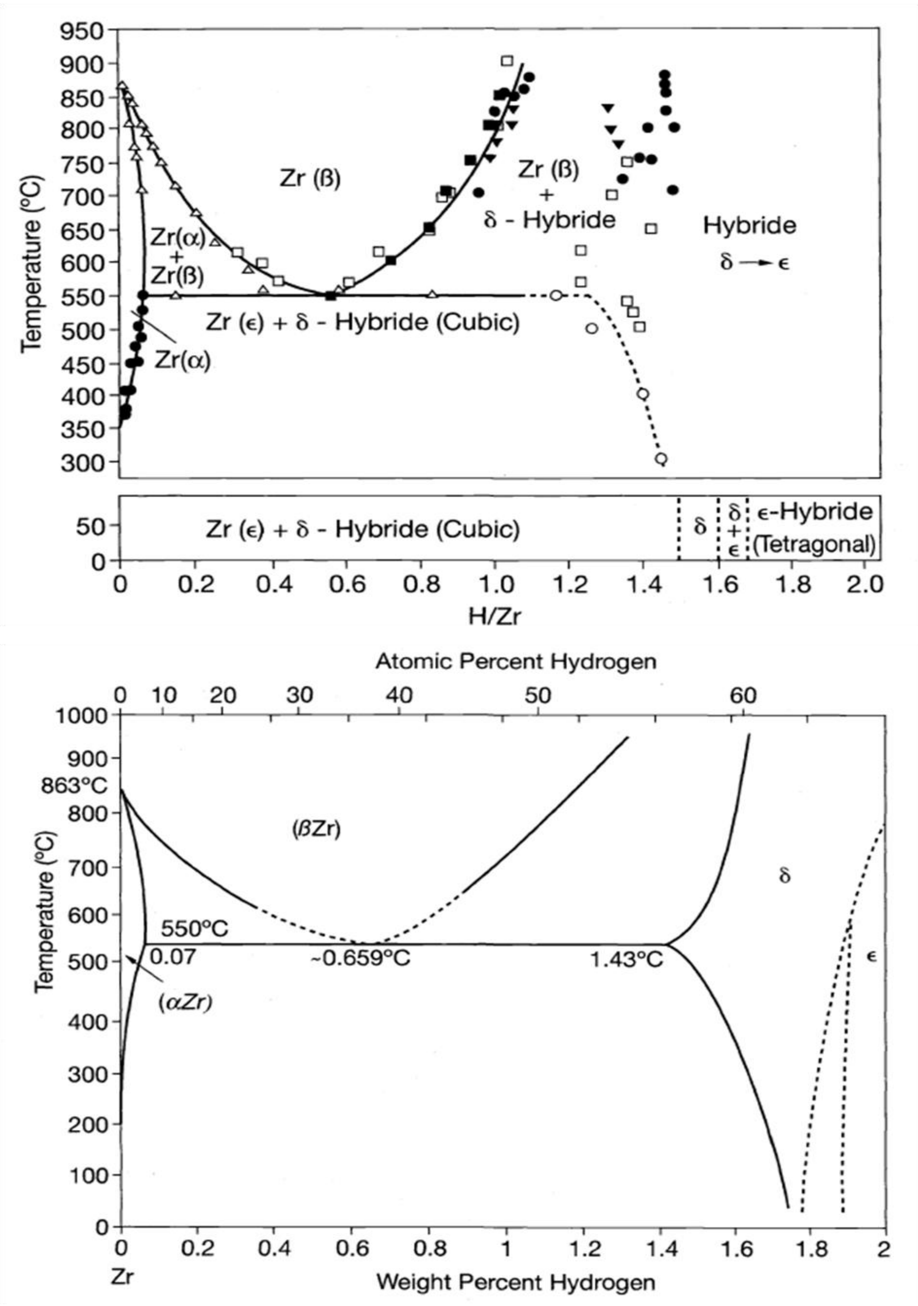

Figure 2.6 Zirconium-Hydrogen Phase Diagram (Zuzek et al, 1990)

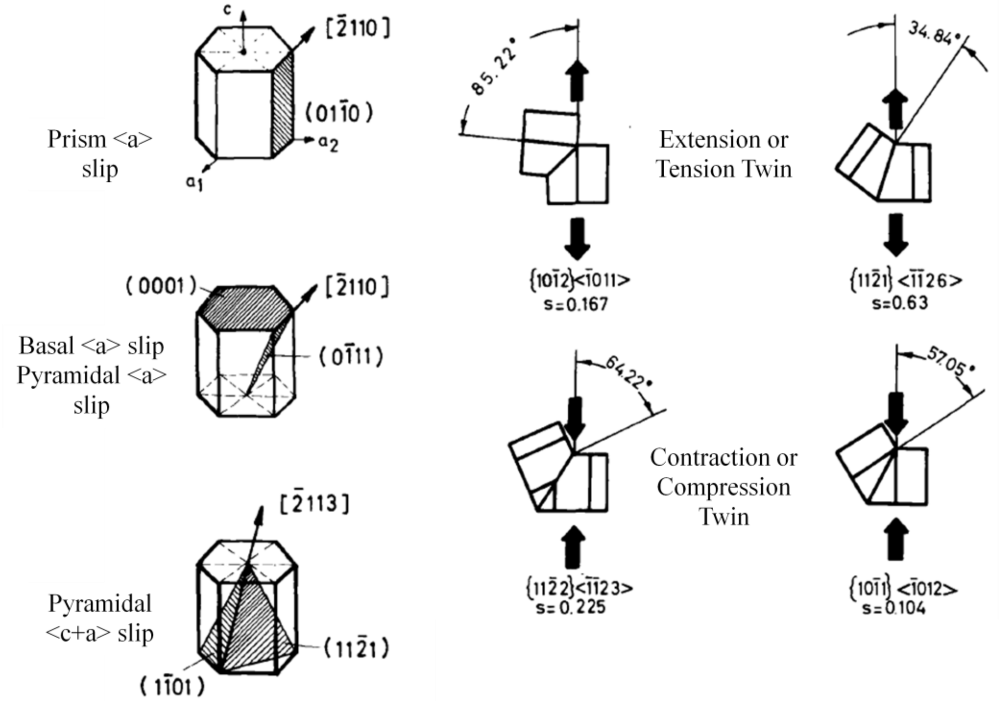

Figure 2.7 Deformation Mechanism of Zirconium or Zircaloy Single Crystal (Prism <a> Slip, Basal and Pyramidal <a> Slip, Pyramidal <c+a> Slip, Extension and Contraction Twin) (Tenckhoff 1988)

2.4 Deformation in Polycrystalline Zirconium and its Alloys

Prism slip $\{10\bar{1}0\}\langle 11\bar{2}0\rangle$ is the primary deformation mode in polycrystalline Zr. The slip contains only two independent slip system, thus at least five independent slip systems are required to fulfill the Von Mises criteria (Mises 1928). At room temperature, compression along the c-axis pyramidal (c+a) slip gets activated in polycrystalline zirconium rather than $\{11\bar{2}2\}$ contraction twinning (Picklesimer 1966; Ballinger *et al.*, 1984). At room temperature, $\{10\bar{1}2\}$extension twinning, prism <a> slip, and pyramidal <c+a> slip are the most commonly reported deformation mechanisms in polycrystalline zirconium (Westlake 1964; Dickson *et al.*, 1971; McCabe *et al.*, 2006). At higher stresses, dislocations begin to accumulate and local stress concentrations are developed, in which cross slip tends to operate (Xu *et al.*, 2008b). Cross slip is the likely mechanism where basal <a> slip and pyramidal <a> slip can operate. At higher strain, basal <a> slip can operate at room temperature (Xu *et al.*, 2008a). At cryo temperature, the deformation is governed by prism<a> slip, extension twinning $\{10\bar{1}2\}\langle\bar{1}011\rangle$,

$\{11\bar{2}1\}\langle\bar{1}\bar{1}26\rangle$ and contraction twinning $\{11\bar{2}2\}\langle\bar{1}\bar{1}23\rangle$ (Knezevic *et al.*, 2013; Luan *et al.*, 2013; McCabe *et al.*, 2009).

2.5 Crystallographic Texture

Zircaloy-2 due to its deformation history the crystals have some preferred crystallographic orientation or texture. Polycrystalline materials are made up of grains with random crystallographic orientation, but they are rarely randomly distributed. Mostly, the crystals tend to follow a one or more specific crystallographic orientation relative to an external coordinate system. This is known as texture (Cullity 1978). Mechanical and thermal processing routes in manufacturing process affect texture of the Zr alloy. The texture of zirconium alloys greatly influences the processing route of fabrication and service of the part obtained after fabrication in terms of its strength, irradiation

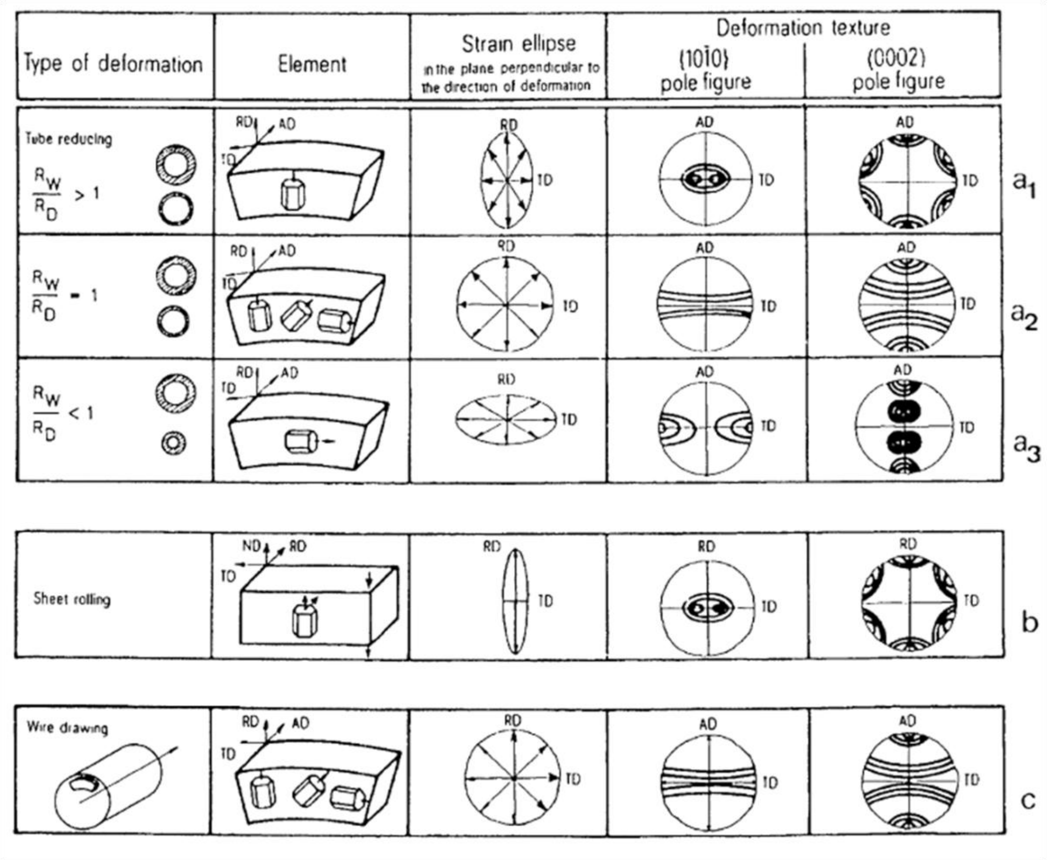

Figure 2.8 Deformation Texture Development of Zirconium and its Alloys after **(a_1-a_3)** Tube Reduction, **(b)** Rolling and **(c)** Wire Drawing Operations (Murthy *et al.*, 2006)

growth, hydride formation and corrosion cracking (Murthy *et al.*, 2006; Nieh *et al.*, 2006; Rogerson *et al.*, 1979; Kim *et al.*, 2001; Knorr *et al.*, 1982, Habibi *et al.*, 2012).

In zircaloy tube deformation, tube reduction involves triaxial stresses. The main influence of this process alters the stable basal pole peak according to the thickness to diameter reduction ratio (R_w/R_d). Tubing having $R_w/R_d > 1$ attains a texture in which basal poles are aligned normally to the radial direction. If $R_w/R_d = 1$, a random distribution of basal poles in the radial tangential plane is observed and if $R_w/R_d < 1$, the basal poles align parallel to tangential direction as can be seen from **Figure 2.8(a_1-a_3)**.

During sheet rolling, compressive load acts on the normal direction making the sheet to elongate towards the rolling direction and a little in the transverse direction. Since, basal poles always align parallel to the loading direction, it aligns towards the normal direction and slightly inclined 20^o to 40^o towards the transverse direction due to small compressive force acting on it as seen from **Figure 2.8(b)** (Tenckhoff 1988). In wire drawing of tube, the load is applied concentrically due to which the texture is developed as shown in **Figure 2.8(c)**.

2.6 Nanocrystalline and Ultrafine Grained Materials

Grain size is one of the key microstructural factors, which affect the physical and mechanical behavior of the materials. The unique functional and structural properties of ultrafine and nanocrystalline materials have gained ever growing importance among materials scientists and industries. Nanocrystalline (< 100 nm) and ultrafine grained (100-1000 nm) materials contain high volume fraction of grain boundaries, which may affect their mechanical, chemical, physical, and functional properties. Bridgman has introduced SPD processing with combination of hydrostatic pressure and shear deformation (Bridgman, 1935a). In 1981, Gleiter has introduced inert gas condensation to produce nanocrystalline powders and reported in situ consolidation. Later on, more techniques have been developed to produce bulk ultrafine and nanostructured materials.

2.6.1 Synthesis of Ultrafine and Nanocrystalline Materials

The increase in demand of ultrafine (UFG) and nanocrystalline materials (NC) has enabled continuous development of new processing routes for producing them in a large quantity. There are basically two approaches to produce ultrafine and nanocrystalline materials. The first is “top to down approach” in which processing of bulk materials is carried out by plastic deformation at high strain for producing UFG grains and the second is “bottom up approach” in which deposition of atoms by various physical and chemical methods are performed to produce UFG/NC materials. The UFG materials produced by both the techniques differ by their grain boundaries, dislocation density, the distribution of elements, grain shape and size, which affect their texture and mechanical properties. The schematic showing various processing methods and procedures to produce UFG and NC materials are shown in **Figure 2.9**.

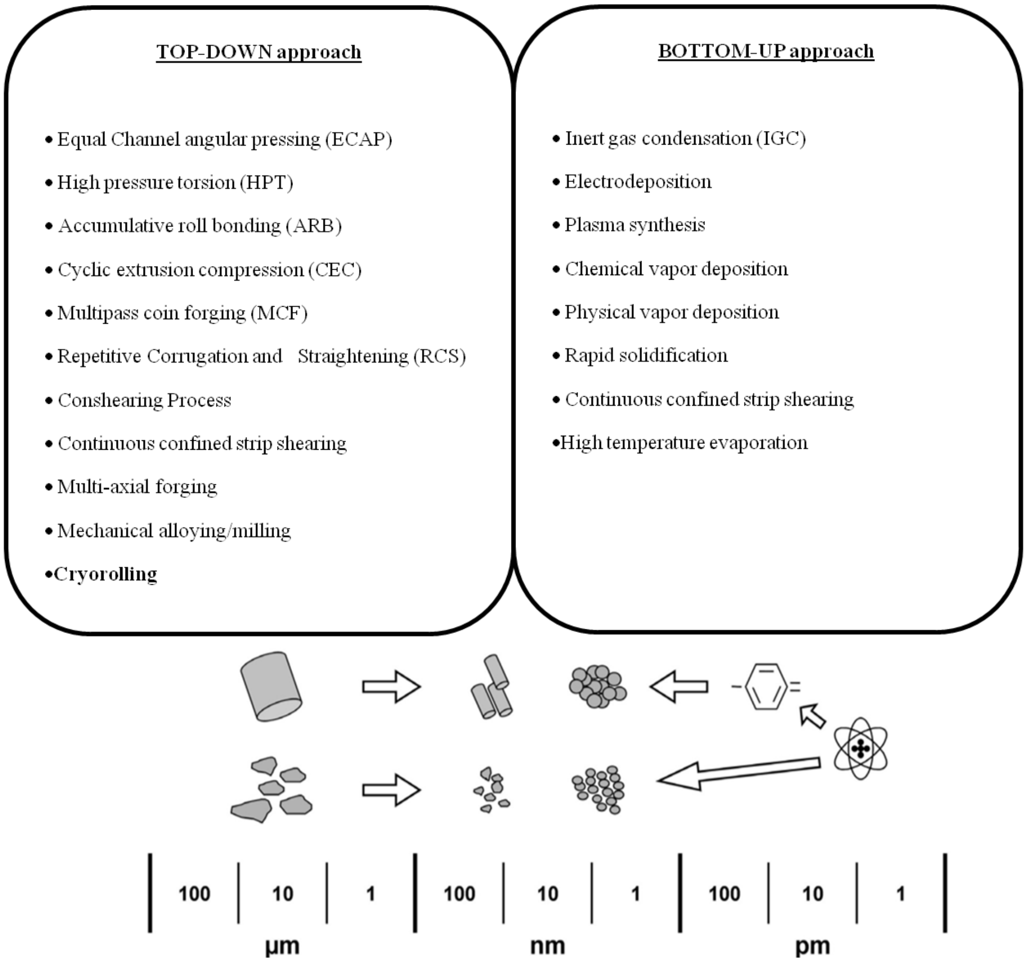

Figure 2.9 Schematic Representation of Building up of Ultrafine Grained and Nanostructured Materials

2.6.1.1 Top Down Approach

In this approach, bulk starting material on application of large strain leads to the formation of ultrafine/nanostructures. Typical examples are severe plastic deformation techniques (SPD) (Valiev et al., 1991; Horita et al., 1996, Avettand-Fènoël *et al.,* 2014) and mechanical alloying through ball milling/cryomilling and consolidation of powder (Koch 1997; Dybiec 2007). HCP materials have received considerable attention and UFG were developed in these alloys through these techniques. The need of large plastic strain in SPD processing to produce UFG materials makes it energy intensive and expensive tool design.

2.6.1.2 Bottom Up Approach

In the “bottom-up” approach, synthesis of nano powders is carried out several techniques such as electro deposition (Erb *et al*., 1995; Lu *et al*., 2005), inert gas condensation (Gleiter 1981; Gleiter 1989), chemical vapor deposition (Jaeger et al., 2002; Choy 2003), crystallization from amorphous materials (Tong et al., 1992; Liu et al., 1993), etc. The materials produced by these techniques possess fine grains even less than 100 nm, which can be used for fabricating electronic devices.

2.6.2 Severe Plastic Deformation (SPD) Methods

Among various techniques developed for grain refinement, SPD techniques are of great interest as they can produce ultrafine or nanostructures in the bulk materials. The metals subjected to SPD can induce very high plastic strains in the materials and can break the micron sized grains to produce grain size as fine as 50-100 nm, containing mainly high angle grain boundaries (Valiev et al., 2000). Nanostructured metals produced by SPD are 100% dense, contamination free, and sufficiently large. These materials are found to have high strength, superior superplasticity, a low friction coefficient, high wear resistance and enhanced high cycle fatigue life (Zhu et al., 2005). A lot of papers are published explaining the various SPD techniques by various researchers. The various SPD techniques are given below.

1. Equal channel angular pressing (ECAP)(Segal 1995)
2. High pressure torsion (HPT) (Bridgman 1937)
3. Accumulative roll bonding (ARB) (Geist *et al*., 2011)
4. Multi axial forging (MAF) (Lee *et al*., 1999)

5. Twist extrusion (TE) (Kaibyshev 2001)

Derivative Process

6. Repetitive side extrusion (Orlov *et al*., 2009; Orlov *et al*., 2011)
7. Rotary die ECAP (Azushima *et al*., 2002)
8. Cyclic extrusion compression (CEC) (Zhu *et al*., 2001)
9. Cyclic close die forging(CCDF) (Lee at. al., 2002)
10. Repetitive corrugation and straightening (RCS) (Kurzydlowski 2006)
11. Cone-cone method (CCM) (Bouaziz *et al*., 2007)
12. Cryorolling (Wang *et al*., 2002)
13. Transverse rolling (Alexander 2007)
14. Asymmetric rolling (ASR) (Lapovok *et al*., 2009)
15. Super short interval multi-pass rolling (SSMR)(Etou *et al*., 2008)
16. Helical rolling (Kolobov 2009)
17. Continuous frictional angular extrusion (CFAE)(Huang *et al*., 2007)
18. Friction stir processing (FSP)(Mishra *et al*., 2005)
19. Severe torsion straining (STS) (Nakamura et.al., 2006)
20. Torsion extrusion (Mizunuma 2006)
21. Simple shear extrusion (Pardis *et al*., 2010)
22. Vortex extrusion (Shahbaz *et al*., 2011)
23. ECAP with rotation tooling in which the conventional fixed die is replaced by rotating tools (Alexander 2007)
24. Reversed shear spinning (Alexander 2007)
25. Non-equal channel angular pressing (NECAP) for plate shaped billets (Toth *et al*., 2009a)
26. Tube channel pressing (Farshidi *et al*., 2012)
27. KOBO forming (Bochniak 2005)
28. High-pressure tube twisting (HPTT) for thin-walled tubes (Toth *et al*., 2009b)
29. Cyclic expansion–extrusion (CEE)—a modified CEC process(Pardis *et al*., 2011)
30. High-pressure sliding (Fujioka *et al*., 2009)

Integrated Process

31. Integrated extrusion + ECAP (Estrin *et al*., 2008)
32. Parallel channel ECAP (Nishida *et al*., 2001)

Continuous Process

33. ECAP-conform (Segal *et al*., 1994; Etherington 1974)
34. Con shearing (Raab *et al*., 2004)
35. Continuous confined strip shearing (Saito *et al*., 2000)
36. Continuous repetitive corrugation and straightening(Huang *et al.*, 2004)
37. Incremental ECAP (Lapovok *et al*., 2008)
38. Continuous high pressure torsion (Edalati *et al*., 2010)
39. Continuous manufacturing of bolts (Jin *et al*., 2007)

From the above mentioned SPD methods, it can be noted that most of the methods are developed recently within the period of 10 to 12 years and there is scope for further development. Cryorolling, because of its simplicity, less expensive process, no die design requirement, lesser wear problems during processing, low maintenance cost, makes it easy to produce ultrafine and nanocrystalline structures in the bulk materials. Wang et.al., (2002) have processed copper plate by cryorolling up to 93% reduction and succeeded in producing ultrafine and nanocrystalline structures in the bulk metal. They reported that after annealing deformed Cu at low temperature, multimodal grain structure with bulk, ultrafine and nanocrystalline grains in the bulk metal was observed. They showed large ductility without losing strength. Literature on cryorolling of Cu, Al, Ti, Steel, Zn, Mg, Ni and their alloys are plenty (Sauvage *et al*., 2012; Valiev *et al*., 2000; Estrin *et al*., 2013; Lee *et al*., 2005; Rangaraju *et al*., 2005; Zherebtsov *et al*., 2013, Alhamidi *et al.*, 2014, Shivamurthy *et al.*, 2013, Gopala *et al.*, 2011, Um *et al.*, 2014, Hunag *et al.*, 2010, Manna *et al.*, 2011).

2.6.3 Ultrafine Grained Zirconium and its Alloys

Zirconium and its alloys are widely used in nuclear reactors in the form of cladding tube as discussed in section 2.2. The need to impart better mechanical property to the alloy with the limitation of adding more alloying elements, makes researchers to achieve this goal by severe plastic deformation (SPD) techniques. Cryorolling is one of the potential techniquesto produce ultrafine grains ad nanostructures in the bulk materials. A lot of efforts and optimization of several SPD techniques are required to realize their applications in nuclear industries.

Generally, the alloy is quenched at β temperature i.e. greater than 1250K and process annealed during rolling (Ballinger *et al*., 1981; Vanitha *et al*., 2009; Xu *et al*., 2008b; Lee 1972). β quenching of the alloy leads to the formation of Widmanstätten structure. Vanitha *et al* (2009) have reported the formation of equiaxed fine grains for the alloy rolled up to 60% followed by recrystallisation at 710^{o} C due to three types of recrystallisation/recovery process, strain localization, deformed bands, and by extended recovery for selective grain orientations.

Edalati *et al.*, (2009) processed pure zirconium using HPT at pressure ranging from 1-40 GPa. Above 4 GPa pressure, phase transformation from α to ω takes place, which leads to grain refinement, strength and hardness enhancement and reduction in ductility. The ‘c’ axis expanded to 0.6% and the phase is stable up to 400 days at room temperature. ECAP of pure zirconium was performed and microstructural evolution by subsequent annealing treatment was studied. It was found that when the samples were annealed at 873 K, grain size reduced from 40 µm to 3 µm by four ECAP passes, while the grain size reduced to 0.2 µm when annealed at 773 K (Lee *et al.*, 2007). The textured pole figure shows rotation of {0001} poles by 70^{o} for rod cross section. X-ray data reveals that after first pass of ECAP at 350^{o} C, due to dynamic recovery, the substructure condition is intermediate between annealed and cold rolled cladding tubes, while after fourth pass, it is near to substructure condition (Perlovich *et al.*, 2006).

The ARB of pure zirconium at 0.3 T_m temperature with 75% reduction in each pass results leads to the formation of equiaxed ultrafine grained structure with grain size of 400 nm and 242 nm. With 75% reduction given in each pass, the grain fragmentation occurs due to geometrical thinning and subdivision of grains due to formation of geometrically necessary dislocations (Jiang *et al.*, 2008; Jiang *et al.*, 2007). Polycrystalline zirconium is subjected to high shear strain (25-100) deformed by split Hopkinson bar with strain rate of 10^4 s^{-1} in hat shaped specimen. A narrow region (10-20 µm) of intense plastic deformation is formed with equiaxed grains having grain size of 2000 nm. The deformation occurred by three processes, firstly, elongated cells and substructure is formed and then increase in misorientation results in breakup of elongated grains and finally, rotation of grain boundaries leads to formation of equiaxed grain structure (Kad *et al.*, 2006).

2.6.4 Rolling of Zirconium and its Alloys at Different Temperature

Zircaloy-2 has been cryorolled up to 70% and the deformed sample exhibits tensile strength of 795.9 MPa as reported in the literature (kamalanath *et al.*, 2012). Mukherjee *et al.*, (2004) investigated microstructural characteristics of Zircaloy-2 rolled at room temperature up to 70% after annealing it at 750^{o} C for 10 hours in a sealed quartz tube under vacuum and cooled at the rate of 5^{o} C per hour. The domain size, microstrain, dislocation density and stacking fault in the alloy were evaluated by simplified Breadth method, Williamson-Hall technique and the modified Rietveld method, respectively. The dislocation density ‹ρ› was found to be 10^{15} /m^2. The relationship between domain size and dislocation density in HCP material was established (Mukherjee *et al.*, 2004). The maximum strength of room temperature rolled Zircaloy-2 after annealing at 750^{o} C for 20 hours in vacuum was found to be approximately 689 MPa (Whitmarsh 1962). Sahoo *et al.*, (2007) have investigated the heterogeneous deformation characteristics of single phase Zircaloy-2 subjected to plain strain deformation. They showed the existence of deformed and non-deformed grains (equiaxed) in the alloy cold rolled to 20% and 50% reductions through ESBD measurements. The near basal grains are not fragmented as reported in their work. Ballinger and Pelloux (1981) have studied the influence of anisotropy on the mechanical properties of Zircaloy-2 and reported that the deformation mechanisms such as prism slip, <c+a> slip and twinning contribute for the texture dependent mechanical properties. Tabachnikova *et al.*, (2010) studied the evolution of microstructure and mechanical properties of ultrafine fine grained zirconium (200 nm) during deformation at 4.2 – 300 K produced by extrusion, wire drawing and annealing. They found that twinning activity is lower in UFG zirconium as compared to coarse grained zirconium at ambient and lower temperatures but at 4.7 K, twinning increases with decreasing grain size.

Guo *et al.*, (2012a; 2012b; 2012c) have investigated the mechanical properties of cryorolled Zr and reported the formation of ultrafine grains in the metal, which exhibit ultimate tensile strength of 658 MPa and 20.7% elongation at break after annealing at 450^{o}C for 1 hour. The multimodal structure obtained after annealing the cryo rolled pure Zr with rolling strain of ~2.87 at 400^{o}C for 1 hour contains 63% grains having size less than 100nm and 37% grains having size between 100 and 1000nm. The sample annealed at 450^{o}C contains 20% nano crystalline, 56% ultrafine and 24% coarse grains as estimated from TEM images. Dislocation density of cryo rolled sample with 92% rolling thickness reduction was estimated to be $1.4\text{x}10^{-14}$ /m^2 (Guo *et al.*, 2012b; Guo *et al.*, 2012c). Formation of dislocation cells in cryorolled zirconium is studied by Shi *et al.*, (2013a). They found that at high strain, dislocation lamellas formed during cryo rolling gets fragmented to dislocation cells during annealing at 100^{o}-200^{o} C temperatures. While at low strain, dislocation cells after annealing is formed by fragmentation or necking of dislocation tangles. It is also reported that the formation of these dislocation cells plays a significant role on microstructural and mechanical behavior of materials (Shi *et al.*, 2013a). Shi *et al.*, (2013b) reported multimodal grain structure comprising of nano, ultrafine (78%) and coarse (22%) grains ranging from 200 nm to 1.6 µm obtained through cryo rolling followed by thermal annealing. It showed a good combination of tensile strength (650 MPa) and ductility (13.4%). Guo *et al*., (2014) performed mechanical annealing and explained movement of pre existing dislocation by application of high stress on cryo rolled zirconium. A good combination of high strength (843 MPa) and ductility (6.7) is achieved by applying 0.5 GPa mechanical annealing pressure. The increase in ductility is due to restoration of work hardening and grain boundary related deformation, while high tensile strength is due to ultrafine and nano structured grains. Guo *et al*., (2014) reported the formation of (2-3 µm) fine grained zirconium structure produced by annealing the cryo rolled zirconium at 500^{o} C for 1 hour and obtained a yield strength (415 MPa) and tensile strength (510 MPa)with 15.5% ductility as compared to coarse grained zirconium (Yield strength (317 MPa), Tensile strength (370) and 13.3% ductility). Li *et al*., (2014) reported the higher fracture toughness of ultrafine and nanostructured zirconium produced by cryorolling (117 MPa $m^{1/2}$) as compared to coarse grained zirconium (78 MPa $m^{1/2}$). Sarkar *et al*., (2015) cryo rolled zircaloy-4 up to 70% rolling reduction and found that the increase in dislocation density due to suppression of dynamic recovery is the primary source of strengthening. The tensile strength obtained is 800 MPa with 17% ductility on comparing with the annealed condition, which showed tensile strength (500 MPa) and 40% ductility.

2.6.5 Fracture Behaviour of Ultrafine Grained Materials

In a polycrystalline material, the crack propagates in three stages such as void nucleation, void growth, and finally void coalescence. The crack initiation inside the material takes place by formation of void, which forms due to decohesion of particle or matrix interface and fracture of particle (Garrison *et al*., 1987). During static loading of ultrafine and nanocrystalline grained material, the fracture occurs by dimple formation, with size much smaller as compared to coarse grained material. In some cases, the dimple size is much greater than grain size of the UFG and NC materials due to shear localization (Meyers *et al*., 2006). In case of fatigue loading, the crack formation and propagation take place in the shear bands. In some cases, with the reduction in grain size, the fatigue crack threshold decreases and thus fatigue crack growth was enhanced. The high cycle fatigue life of ultrafine and nanocrytalline grains is much more as compared to coarse grained materials (Mughrabi *et al*., 2010). Das *et al*., (2011) reported that fracture toughness of the UFG Al alloy has increased 78% as compared to coarse grained alloy due to precipitation hardening and subgrain coarsening. The enhanced fracture toughness is due to disclination shielding effect on the crack tip as reported by Shimokawa *et al.*, (2011). Disclination shielding is activated in two conditions: firstly, transition of dislocation takes place from the crack tip to grain boundary and secondly, transformation of grain boundary in to an energetically stable neighbouring boundary occurs when dislocations are emitted from the grain boundary (Shimokawa *et al.*, 2011). Zhu *et al.*, (2012) reported that the strength and ductility of biomodal structure is sensitive to the volume fraction of constituents and distribution of nano and micro cracks. The micro and nano cracks during loading release elastic stress near the crack and in between dislocations produced near the cracks are stopped by the grain boundary resulting in back stress, which acts on kinematic strain hardening. Increase in fracture toughness of multimodal grain structure of zirconium processed by cryo rolling is reported by Li *et al.*, (2014). The fracture toughness of multimodal grain structured zirconium calculated by using small punch test technique was found to be 117 MPa $m^{1/2}$ as compared to coarse grained (78 MPa $m^{1/2}$).

2.6.6 Fracture Simulation using Xtended Finite Element Method (XFEM)

The basic idea and mathematical model of partition of unity method (PUFEM) is proposed by Melenk *et al.*, (1996) and Duarte *et al.*, (1996). Later, a minimal remeshing finite element method is reported by Belytschko *et al.*, (1999) in which discontinuous enrichment function is added to finite element approximation to find the presence of the crack. Further, this method was improved by Moes *et al.*, (1999) and Dolbow (1999) and named it Xtended Finite element method (XFEM). This method allows entire crack to be represented independent of mesh and constructed an enriched approximation that can predict the interaction of crack geometry with the mesh.

Later on, Jirásek (2001a, 2001b) combined damage theory with XFEM and modeled the transition from a smeared to embedded discrete crack. Sukumar *et al.*, (2003) presented two dimensional problem on the effect of microstructure on brittle fracture, while Dumstorff *et al.*, (2003) and Patzak *et al.*, (2003) presented a model for the analysis of brittle crack in post cracking regime. Further, Ventura *et al.*, (2005) proposed a model for simulating displacement and stress field produced by dislocation.

2.7 Problem Formulation

Zirconium alloys are extensively used in nuclear industry due to its high strength, ductility, creep strength and high corrosion resistance. The formulation of a research problem is made based on research gap identified from the literature review in the present work. The following are summary of literature review on Zr alloys:

- With increasing demand for energy production through nuclear reactors,, the requirement of zirconium alloys is ever increasing for producing pipes and various components of reactors. Therefore, emphasis on enhancing the material properties without altering composition of the alloying contents is growing, which can be achieved through microstructural engineering..
- The development of new techniques is required to produce the ultrafine grained zirconium and its alloy, so that high strength of products can be achieved and thus increasing life of the products.
- Apart from tailoring the alloying contents, reducing grain size to ultrafine and nanocrystalline range through SPD techniques has been studied extensively in the last two decades.
- Cryorolling is one of the simple techniques for producing UFG material with a good combination of high strength and ductility.
- New advancements such as cross rolling at cryo temperature and room temperature, is also very effective in producing UFG zirconium alloys.

Based on the literature review, the following objectives are proposed in the present work:

- To study the hardness and tensile properties of Zircaloy-2 subjected to rolling at liquid nitrogen temperature. The microstructural features of the deformed samples are characterized by using techniques such as XRD, FE-SEM, EBSD, and TEM. The formation of ultrafine grains in the Zicaloy-2 has been explained using EBSD and TEM results.
- To investigate the maximum grain refinement achievable in Zircaloy-2 by room temperature rolling and study its hardness and tensile properties correlated through the microstructures of the heavily deformed alloys. TEM and ESBD techniques were used to substantiate the mechanisms of formation of ultrafine grains in the Zircaloy-2.
- To study anisotropic mechanical behavior and textures of ultrafine grained zirconium alloy processed by cryorolling and room temperature rolling. XRD and EBSD techniques were

used to characterize the macro and micro textures of the cryorolled Zircaloy-2 and correlated with its anisotropic deformation behavior.

- To study the texture, microstructure, and mechanical properties of Zircaloy-2 processed by room temperature cross rolling (RTCR) and cryo cross rolling (CCR). The Schmidt and Taylor factor of the deformed alloy was estimated to substantiate the formation of texture and stored strain energy, respectively.
- To differentiate the effect of quenching in water and mercury, respectively, on the grain size and mechanical behavior of room temperature rolled zircaloy-2.
- To simulate the fracture toughness and fatigue life of the zircaloy-2 by applying finite element method (FEM) using the mechanical data obtained from the tensile test.
- To focus on the fracture toughness obtained after normal rolling and cross rolling at cryo and room temperature and to simulate the fracture toughness of the large strained zircaloy-2 of normal and cross rolled zircaloy-2 samples using XFEM.

CHAPTER 3
EXPERIMENTAL DETAILS: MATERIAL AND METHODS

In the present chapter, material selection, experimental techniques used for producing ultrafine grains and various characterization techniques including mechanical testing are discussed.

3.1 Material Selection

Zircaloy-2 plate with 4mm thickness is procured from Nuclear Fuel Complex, Hyderabad, India. The chemical composition of alloy is shown in **Table 3.1**. The samples were cut from the received plate and were solution treated at 800^{o}C temperature for 2 hours in argon environment and then quenched in water and mercury. The obtained material after solution treatment was free from any defect and homogenized microstructure with an average grain size of 20µm and 10µm, respectively. The sample dimensions used for different processing routes are described below.

- Samples with dimensions of 40 X 30 X 4.3 mm were used for Cryorolling (CR) and Room Temperature Rolling (RTR). They are deformed at liquid nitrogen temperature and room temperature up to 25%, 50%, 75% and 85% reductions with a true strain of 0.28, 0.69, 1.38 and 1.89, respectively.
- Samples with dimension 40 X 40 X 4.3 mm were used for cryo cross rolling and room temperature cross rolling. The samples are deformed at liquid nitrogen temperature and room temperature up to 25%, 50%, 75% and 85% reductions with a true strain of 0.28, 0.69, 1.38 and 1.89 respectively.

Table 3.1 Chemical Composition of Zircaloy-2 (Weight %)

Component	Sn	Fe	Cr	Ni	N	Zr
Wt %	1.3-1.6	0.07-0.20	0.05-0.16	0.03-0.08	0.006	Balance

3.2 Experimental Techniques

3.2.1 Experimental Set Up for Rolling

Cryorolling (CR) is one of the potential techniques for producing ultrafine grains in the bulk materials. Different rolling reductions up to 85% at cryo and room temperature were performed and cross rolling at cryo and room temperature was performed in the present study. The initial dimensions of the samples are discussed in the previous section. The experimental set up used to perform rolling and cross rolling is shown in **Figure 3.1**. The details of the equipment and accessories used during rolling are given below:

- Two high laboratory rolling mill was used to perform rolling with rolling speed and roll diameter of 8 rpm and 110 mm, respectively.
- Molybdenum disulphide was used during rolling to reduce frictional and heat losses.
- A cryocan is used to procure and store liquid nitrogen.
- A stainless steel container to dip samples in liquid nitrogen was prepared consisting of tubular stainless steel container covered with glass wool and was kept in thermocole box to minimize evaporation of liquid nitrogen.
- Container filled with water was used to perform room temperature rolling.
- To measure thickness of the sample during rolling, digital Vernier caliper was used. Gloves were also used for handling the samples.

3.2.2 Cryorolling Procedure

Machined sample with the required dimension was subjected to solution treatment prior to rolling at different temperatures. Illustration of the rolling setup for normal rolling and cross rolling at cryo and room temperature is shown in **Figure 3.2**. The image of the microstructure of zircaloy-2 before and after solution treatment is shown in **Figure 3.3**.

Procedure used to perform rolling and cross rolling at different temperatures is given below in detail.

- Prior to rolling, the rollers of the rolling mill was cleaned properly using emery paper and acetone to remove the unwanted particles such as rust, oxides, oil and grease etc on the surface.
- Prior to rolling and cross rolling at cryo temperature, the samples were dipped into liquid nitrogen (-196^{o} C) for 15 minutes and the process is repeated till the required strain is achieved.
- The time span required to achieve the desired temperature is visualized by observing the bubbles formation, these bubbles got reduced as the desired temperature of the sample is

reached. The temperature of the sample is measured before and after the rolling pass and is found to be -175 ^{o}C and -50 ^{o}C.

Figure 3.1 Experimental Set Up of Cryorolling

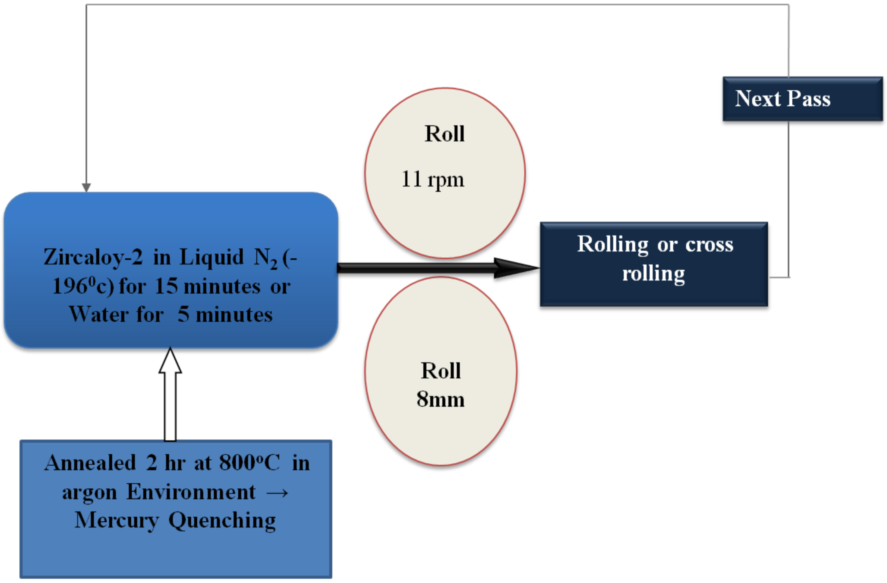

Figure 3.2 Schematic Diagram of Cryorolling and Cross Rolling

- Rolling at room temperature was performed by dipping the samples in water for 10 minutes prior to rolling and then 5 minutes with each pass up to the desired strain is achieved. The sample dimension after achieving the required strain is measured using the Vernier caliper.
- Total true strain after rolling is measured using the formula given below.

$$\mathrm{E} = \frac{\ln(\text{Thickness after cryorolling})}{\text{Initial thickness before cryorolling}} \qquad \textbf{(3.1)}$$

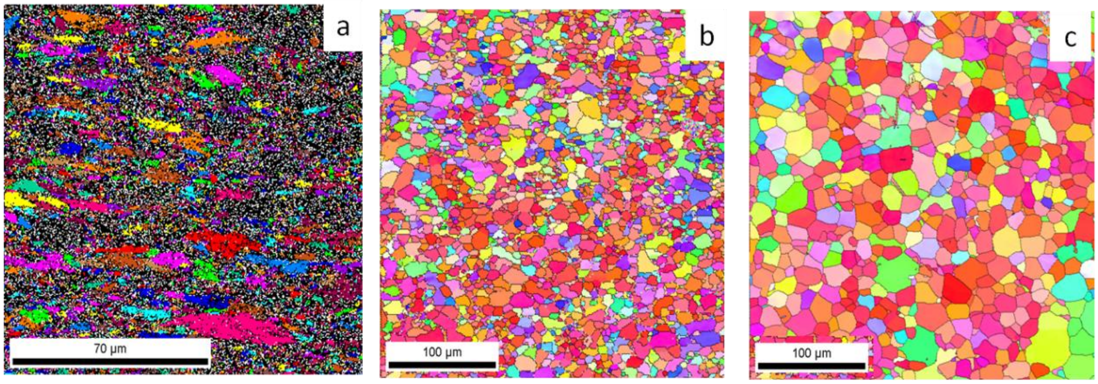

Figure 3.3 Microstructure of **(a)** As received, **(b)** Mercury Quenched and **(c)** Water Quenched Zircaloy-2 samples

3.3 Characterization Techniques

3.3.1 Electron Back Scatter Diffraction (EBSD) Analysis

Electron backscatter diffraction (EBSD) with a high resolution field emission gun scanning electron microscope (FEGSEM) is used to characterize local grain misorientation, local texture, phase identification, point to point orientation on the surface of polycrystalline material. The ability to examine large surface of the sample has made it a potential technique for analyzing microstructure in detail. The deformed microstructure along with probability of the activation of various slip mechanisms and mechanism of ultrafine grains formation can easily be examined using the EBSD technique. Therefore, in the present work, samples after solution treatment, rolled and cross rolled samples at different temperatures are characterized using EBSD technique. Figure 3.4 shows the image of the EBSD machine along with FEG-SEM.

The samples is placed 70^o inclined to the horizontal in front of the EBSD detector, which is equipped with the phosphor screen. The phosphorous screen is used to convert diffracted electron in to light signals, which are further processed in charge coupled device (CCD) to collect Kikuchi patterns. A schematic diagram for EBSD setup is shown in **Figure 3.5**. To analyze the obtained EBSD pattern, computer software is used for detecting the Kikuchi pattern by using an optimized hough transform. The data is further analysed using the TSL OIM software package for determining texture and misorientations of individual grains in addition to microstructural characteristics such as grain size, grain size distribution, etc.

Sample preparation is very important to get relevant Kikuchi bands pattern. The selected area of the sample is cut using the diamond cutter in which coolant is used to avoid heating during cutting. The samples were then polished using emery paper of different grit sizes, usually 320, 600, 800, 1200 and 2000. The samples were then cloth polished using the velvet cloth on a high speed wheel and a colloidal solution of aluminium oxide with water is used. Electropolishing of the cloth polished sample is performed at -20 °C by using (80:20) methanol: perchloric acid solution at potential of 20 volts.

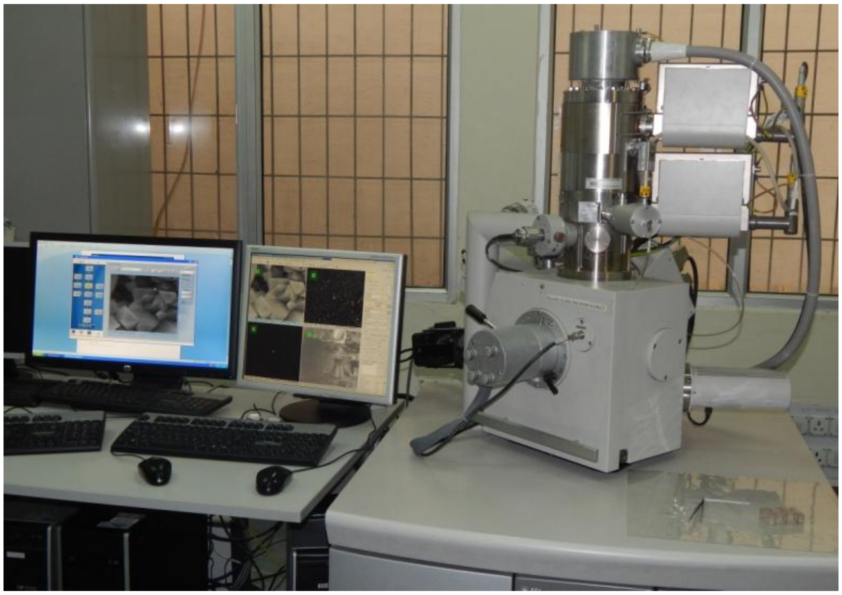

Figure 3.4 Photograph of FEI Quanta 200 FEG-SEM

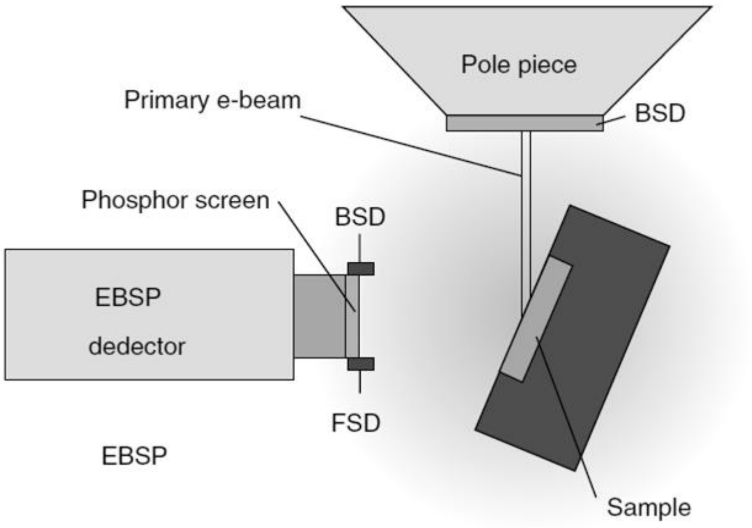

Figure 3.5 Schematic Diagram of a Typical EBSD Sample Installation (A. P. Day *et al.*, Channel 5 User Manual, HKL Technology A/S, Hobro, Denmark (2001)

EBSD scan was performed from the middle place of the rolled sheet. For solution treated samples, scan rate of 1 μm was used while for deformed samples, 0.1 μm scan rate was used. The EBSD was performed in FEI, Quanta 200 F using TSL OIM analysis 4.6 software developed by TEXSEM laboratories Inc. A confidence index (an approximate measure of accuracy of indexing) of 0.03 was partitioned so that the completely deformed region can be seen as dark.

3.3.2 Field Emission Gun Scanning Electron Microscopy (FEG-SEM)/ SEM

To analyse the fracture morphology of the zircaloy-2 samples, fracture surface of the broken sample is studied in scanning electron microscope (FEG SEM). Before placing the samples in SEM, the broken samples were ultrasonically cleaned to remove the unnecessary particles from the fractured surface. **Figure 3.4** shows the FEG SEM image used for fractography.

3.3.3 Transmission Electron Microscopy (TEM)

Transmission Electron Microscopy (TEM) is used to characterize specimens for very high magnification to atomic resolution (10^6 to 10^9) by transmission of electrons from the thin sample. The higher resolution of the TEM owing to small De Broglie wavelength of electron makes it useful in scientific fields such as physical and biological sciences. TEM is used to characterize crystal structures, specimen orientations, dislocation density, chemical compositions and precipitation morphology through diffraction pattern, X-ray and electron-energy analysis. In the present work, microstructural changes after deformation (rolled and cross rolled) and annealing were characterized by using a FEI Technai 20 TEM operated at 200 KV as shown in **Figure 3.6(a)**. The various hardware components inside the closed chamber in the TEM are shown in **Figure 3.6(b**).

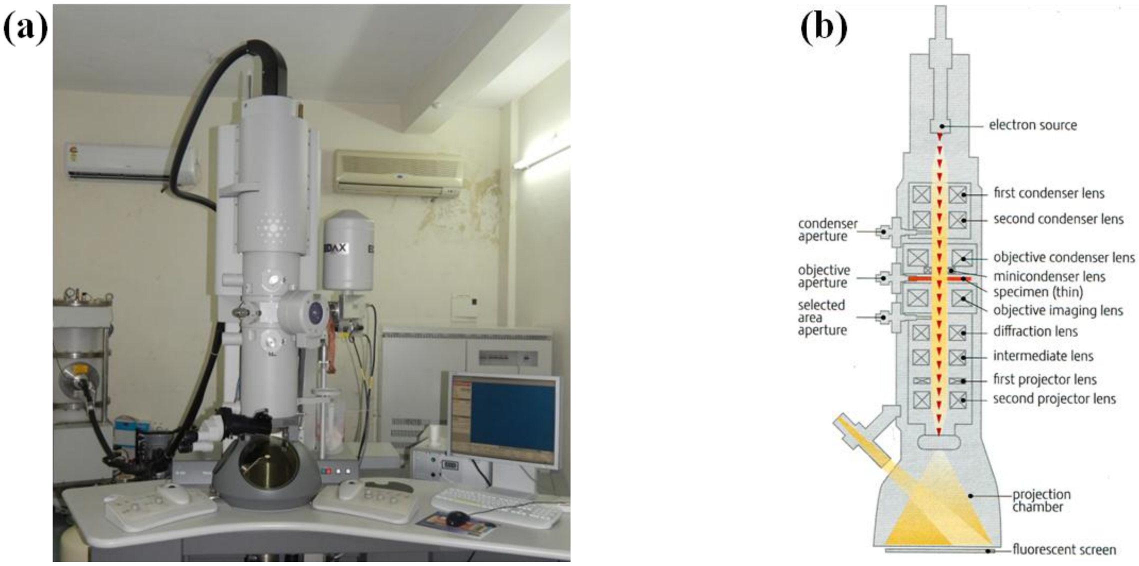

Figure 3.6 (a) Photograph of TEM Unit (FEI Tecnai-20), **(b)** Schematic Diagram of TEM (*micron.ucr.edu/public/manuals/Tem-intro*).

The sample for TEM characterization was prepared by initially cutting the sample in to 10 mm × 10 mm dimension. The samples were then thinned from both sides using emery papers of 220, 400, 600,800, 1000, 1200 and 1500 and 2000 grit sizes. Thin foil of the sample is then washed with methanol and acetone and 3mm disc was punched from the sample. The final thinning of the samples was made using twin jet polishing using the solution of 20% perchloric acid and 80% methanol at a temperature of -40 °C and at potential of 20 volts. The electropolished samples were washed in methanol to remove the etchant and unwanted particles formed during polishing.

3.3.4 X-ray Diffraction

XRD is a technique used to characterize the phases, unit cells and the dislocation density of the material. In the present study, the XRD is used to find the phases and dislocation density of the deformed zircaloy-2 before and after rolling. XRD (Bruker AXS D8 Advance instrument) using Cu Kα radiation for the analysis is shown in **Figure 3.7(a)**.

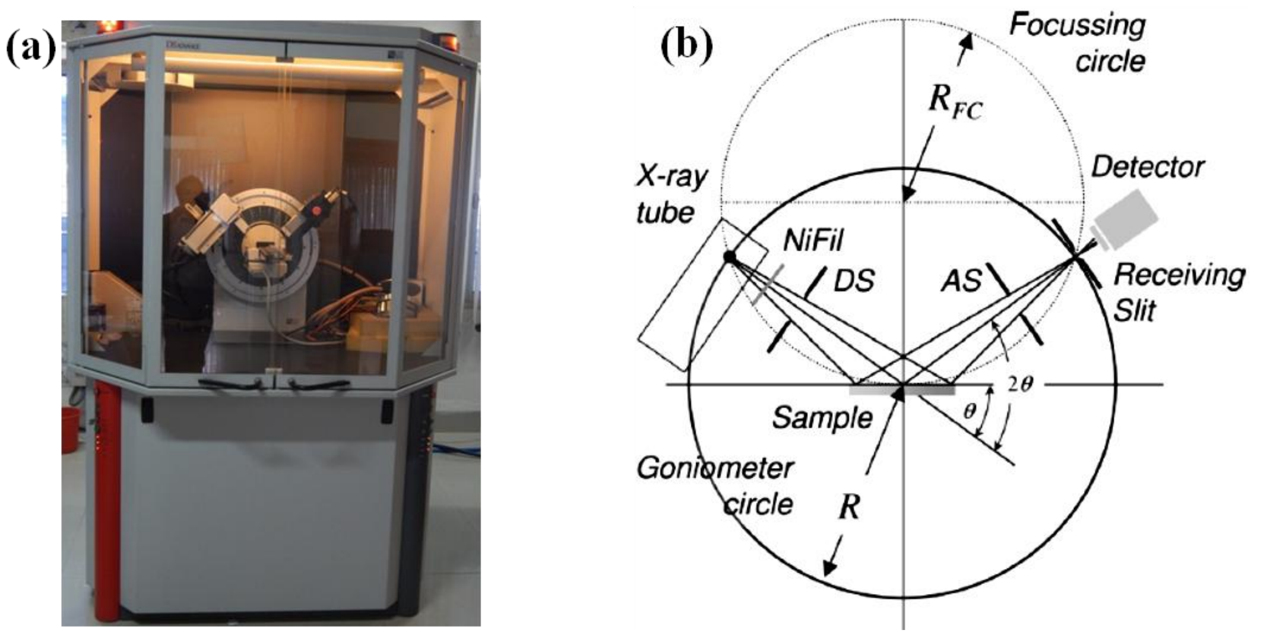

Figure 3.7 (a) Photograph of XRD Unit θ/2θ (Bruker AXS D8 Advance diffractometer, **(b)** Schematic Representation of Diffraction in Bragg–Brentano Geometry (WILEY-VCH Verlag GmbH & Co. KGaA, weinhei)

The working principle of the setup is shown in **Figure 3.7(b)**. The X-rays produced by the X-ray tube are filtered to get monochromatic radiation, which is directed towards the sample. The arrangement is made in such a way that the sample rotates in path of the collimated X ray beam by an angle ‘θ’ and the diffracted beam is collected by the X-ray detector. Constructive interference takes place whenever $2d \sin \theta = n\lambda$ condition is satisfied which leads to change in the peak intensity. The data obtained is further analysed using the Xpert High score software.

3.3.5 Texture Analysis through X-ray Diffraction

X-ray diffraction technique is one of the most common methods used to measure texture of the materials and the method is known as Schultz reflection method. To measure the texture, the measurement is taken along four axis due to which the apparatus is also known as four angle diffractometer. In the present work, texture of the samples was carried out by Pan analytical MRD system instrument using Cu Kα radiation with a step size of 0.0017^{o} and an integration time of 400 seconds. The initial sample preparation is same as that of the EBSD sample preparation. The machine used to perform texture XRD is shown in **Figure 3.8**.

Figure 3.8 Image Showing Pan Analytical MRD System Used to Measure Texture

3.4 Mechanical Testing Procedures

3.4.1 Bulk Vickers Hardness Test

Hardness is defined as the property by which the material shows resistant to localized plastic deformation. The hardness test is carried out using a diamond indenter having pyramidal shape and an angle of 136^{o} between the opposite faces. Applied load varies with the type of material ranging from 1 to 30 Kgf. Hardness test of the zircaloy-2 samples were performed before and after rolling and cross rolling at different temperatures with an applied load of 20Kgf and holding time of 15 seconds. The test is important as it can be used to predict tensile values of the materials. The image of instrument used in the present study is shown in **Figure 3.9**.

Figure 3.9 Photograph of Vickers Hardness Testing Machine

The samples of dimension (15 × 15 mm^2) were used and polished using emery paper up to 2000 grit size and then cloth polished as explained above in EBSD section. An average value of ten readings was taken to obtain a hardness (HV) value of sample.

3.4.2 Tensile Test

Tensile test was performed to investigate the mechanical behavior of the deformed as well as annealed sample. The tensile yield strength and ductility of the samples were estimated from the test. The tests were performed on S-Series, H25K-S universal testing machine (UTM) with a strain rate of $5 \times 10^{-4} S^{-1}$. The samples were machined in rolling and transverse direction according to the ASTM E-8 standard with a sub size specimen having a gauge length of 16 mm. The sample surface was polished properly before testing so as to remove the burrs and scratches formed during machining. Five samples of each condition were tested and analyzed to get average values. The UTM used to perform tensile test is shown in **Figure 3.10**.

Figure 3.10 Photograph of Vickers Hardness Testing Machine

3.4.3 Compact Tension Test

The compact tension test was performed on 25 KN servo hydraulic universal testing machine. The sample was prepared according to the ASTM Standard E-1820-09E1 as shown in **Figure 3.11**. Micro crack on the edge is developed by loading the sample under cyclic load in sinusoidal form at 1 KN for 1000 cycles. Static loading is applied to carry out the compact tension test and value of critical fracture toughness (K_{IC}) is calculated. The image of the CT sample loaded is shown in **Figure 3.12**.

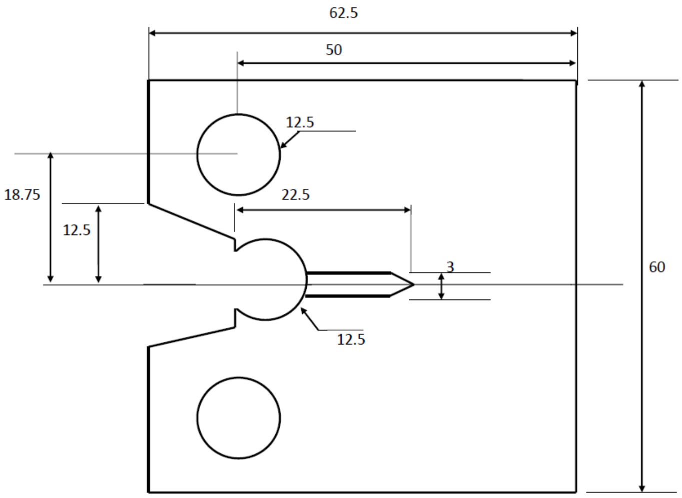

Figure 3.11 Schematic Diagram of CT Sample (All Dimensions in mm)

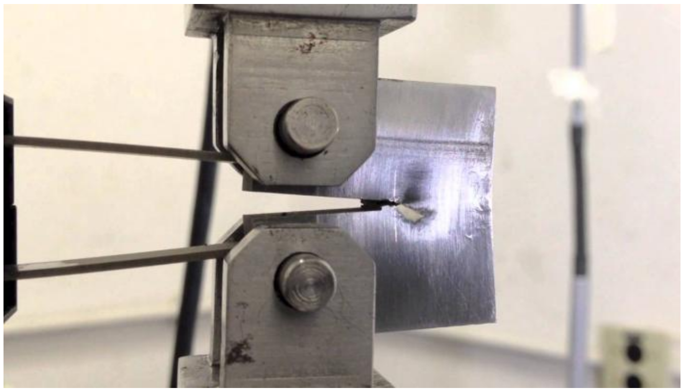

Figure 3.12 Photograph Showing CT Specimen during Testing on Servo Hydraulic Machine

CHAPTER 4

PROCESSING AND CHARACTERIZATION OF ZIRCALOY-2

In this chapter, the results obtained on characterization and mechanical behaviour of ultrafine grained zircaloy-2 processed by rolling and cross rolling at different temperatures are discussed. The present research work was focused on various experimental investigations of the alloy such as: (i) Mechanical behaviour and microstructural characterizations of ultrafine grained zircaloy-2 processed by cryorolling; (ii) Mechanical and microstructural characterizations of ultrafine grained zircaloy-2 processed by room temperature rolling; (iii) Texture and mechanical behaviour of zircaloy-2 rolled at different temperature; (iv) Development of ultrafine grained zircaloy-2 by room temperature cross rolling and cryo cross rolling; (v) Effect on the microstructure and mechanical behavior of RTR zircaloy-2 after water and mercury quenching. The results of each study are substantiated using detailed microstructural characterizations of the samples processed under different conditions.

4.1 Mechanical Behaviour and Microstructural Characterizations of Ultrafine Grained Zircaloy-2 Processed by Cryorolling

---

4.1.1 Introduction

In recent years, ultrafine grained (UFG) and nanostructured (NC) materials are produced by severe plastic deformation techniques such as ECAP, accumulative roll bonding (ARB), high pressure torsion, and multiaxial forging and they impart high strength, ductility and superplasticity to various metals such as Cu, Al, Mg and Ni and their alloys (Sauvage *et al.*, 2012; Valiev *et al.*, 2000; Estrin *et al.*, 2013, Bhowmik *et al.*, 2009). However, the productivity of UFG and NC material is limited by these techniques. Recently, deformation of metals at liquid nitrogen temperature with very less amount of plastic strain has been successfully shown to produce UFG and NC materials. Rolling at cryo temperature results in the suppression of dynamic recovery, which suppresses dynamic recovery, hence increases dislocation density (Zhao *et al.*, 2006; Wang *et al.*, 2002; Panigrahi *et al.*, 2011; Guo *et al.*, 2012a; Guo *et al.*, 2012b; Guo *et al.*, 2012c). Subsequently, annealing of CR samples at low temperature results in formation of bimodal structure containing nano and ultrafine grains, possessing high strength and ductility (Wang *et al.*, 2002; Guo *et al.*, 2012b; Guo *et al.*, 2012c).

Zircaloy-2 is widely used in light water reactors (LWR) as a structural material as well as to fabricate pressure tubes of the Canadian deuterium Uranium (CANDU) power reactors due to its excellent mechanical properties, superior corrosion resistance, and low neutron cross section (Macewen *et al.*, 1983; Mehan *et al.*, 1961; Ibrahim *et al.*, 1969). It is composed of α-phase (HCP), β-phase (BCC), and γ (intermetallic phase) (Corchia *et al.*, 1981; Massih *et al.*, 2006; Massih *et al.*, 2003; Sell *et al.*, 2002).Two types of precipitates present in zircaloy-2 are $Zr_2(Ni,Fe)$ and $Zr(Fe,Cr)_2$, both exhibit elliptical shape (Chemelle *et al.*, 1983; Meng *et al.*, 1989; Degueldre *et al.*, 2008; Jayakumar *et al.*, 1998). Zircaloy-2 absorbs hydrogen and forms the hydride phase, which decreases its ductility and promotes crack propagation (Ostberg *et al.*, 1968). Generally, the alloy is quenched at β temperature (>1250K) and process annealed during rolling as reported in the literature (Ballinger *et al.*, 1981; Vanitha *et al.*, 2009; Xu *et al.*, 2008b; Lee, 1972). Vanitha *et al* (2009) have reported the formation of equiaxed fine grains for the alloy rolled up to 60% followed by recrystallisation at 710^o C due to recrystallisation/recovery process, strain localization, deformed bands, and by extended recovery for the selective grain orientations. The zircaloy-2 has been CR up to 70% and the deformed sample exhibit tensile strength of 795.9 MPa as reported in the literature (Kamalanath *et al.*, 2012). Guo *et al.*, (2012a; 2012b; 2012c) have investigated the mechanical properties of CR Zr up to 90% thickness reduction and reported the formation of ultrafine grains in the metal. The CR Zr subjected to annealing for 1 hour at 450^{o}C exhibit ultimate tensile strength and elongation of 658 MPa and 20.7%, respectively as reported in their work.

Zircaloy-2 shows limited slip systems due to its HCP structure and therefore plastic deformation is difficult in this alloy. Zr has a c/a ratio of less than 1.633, thus prismatic slip is more dominant on $\{10\bar{1}0\}$plane along $\langle 1\bar{2}10\rangle$ direction. During cold working, prismatic slip becomes harder, thus making twinning to get activated. Basal slip becomes active in $\{0002\}$/ $\langle 1\bar{2}\bar{1}0\rangle$ slip systems in the samples deformed above 0.5 true strain (Vanitha *et al.*, 2009; Tenckhoff, 1988; Murthy *et al.*, 2006). The prismatic slip could also occur in (c+a) Burger vector direction. As slip planes are limited, deformation of Zr also occurs by twinning. It provides oriented planes favorable for further slipping. Under tensile loading in c-direction of HCP crystal, $\{10\bar{1}2\}\langle\bar{1}011\rangle$ and $\{11\bar{2}1\}\langle\bar{1}\bar{1}26\rangle$ twinning gets activated; while in compressive mode, $\{11\bar{2}2\}\langle\bar{1}\bar{1}23\rangle$ gets activated and at high temperature, $\{10\bar{1}1\}\langle\bar{1}012\rangle$ twins is observed. At room temperature, $\{10\bar{1}2\}\langle\bar{1}011\rangle$ tensile twinning is active up to 17% strain and with further increasing strain, $\{11\bar{2}2\}\langle\bar{1}\bar{1}23\rangle$ compressive twinning gets activated as reported in the literature (Murthy *et al.*, 2006).

The literature on mechanical properties of cryo rolled (CR) ziraloy-2 is scarce. Therefore, the present work has been focused to study the hardness and tensile properties of zircaloy-2 subjected to rolling at liquid nitrogen temperature. The microstructural features of the deformed samples are characterized by using techniques such as XRD, FE-SEM, EBSD, and TEM. The formation of ultrafine grains in the zicaloy-2 has been explained using EBSD and TEM results.

4.1.2 Experimental Procedure

Zicaloy-2 sample has been obtained in the form of 4mm thick sheet hot rolled at 800^{o}C from Nuclear Fuel Complex (NFC), Hyderabad, India. The chemical composition of the material is shown in **Table 3.1** in **Chapter 3**. The sheet was cut in 30 X 50 mm size and heat treated at 800^{o}C in argon environment for 2 hours and quenched in mercury at room temperature to get the coarse grain structure. The quenched sample was then surface ground and washed in methanol. Cryorolling was performed as discussed in **Chapter 3**. The solid lubricant $MoSi_2$ was used to avoid the friction losses. Initially, the thickness of the sample was 4.35mm. A reduction of 0.2 mm per pass was given to the sample with a roller speed of 8 rpm and roller diameter of 110mm. The temperature of the sample was less then -150°C during rolling. The true strain induced in to the samples subjected to 25%, 50%, 75%, and 85% reductions, is 0.28, 0.69, 1.38 and 1.89, respectively. After rolling, tensile test, hardness, TEM, EBSD and XRD was performed to characterize the samples as discussed in **Chapter 3**.

4.1.2.1 Dislocation Density Calculation by X-Ray Diffraction

CR samples were characterized by using XRD (Bruker AXS D8 Advance instrument) with Cu Kα radiation at a scan rate of 1^{o} per minute. Expert high score plus (2.2.5) software is used to identify the formation of different phases in the samples using the XRD data. Here, dislocation density of deformed zircaloy-2 has been estimated using XRD in the present work using the equation 4.1. It is assumed that the broadening of peak is due to size effect and strain effect. Variance method is based on the asymptotic behavior of the second and fourth order moment of the peak profile. Dislocation density is measured by variance method where 4th order moment of the peak profile is related to the dislocation density of zircaloy-2 (Borbely *et al.*, 2001; Groma, 1998; Sarkar *et al.*, 2008).

$$\frac{M_4(q)}{q^2} = \frac{1}{3\pi^2\varepsilon_f} + \frac{\Lambda\langle\rho\rangle}{4\pi^2} + \frac{3\Lambda^2\langle\rho^2\rangle}{4\pi^2 q^2}\ln^2\left(q/q_1\right) \tag{4.1}$$

Where $M_4(q)$– moment of peak profile

$\langle\rho\rangle$ – Average dislocation density

Λ – Geometrical constant describing strength of dislocation contrast

ε_f – Average column length

$q = 2/\lambda (\sin(\theta) - \sin(\theta_o))$

Where

θ – Diffraction angle

θ_0 – Bragg's angle

q_1 – Fitting parameter

By fitting the straight line to $M_4(q)$curve, average dislocation density is determined.

4.1.3 Result and Discussion

The micrograph of as received sample is shown in **Figure 4.1(a)**. It shows severely elongated grains with heterogeneous structure obtained upon hot rolling at 800^{o}C without any post-annealing treatment. The coarse grain structure was obtained by heat treating zircaloy-2 for 2 hours in Argon environment followed by quenching it in mercury. The temperature of the mercury after quenching was 70^{o}C. The quenching is found to be useful as the sample does not come in contact with hydrogen, which results in increase in ductility to 25% with tensile strength of 499 MPa. Zircaloy-2 quenched in Hg after heat treatment for 2 hours at 800^{o}C exhibits α grains with equiaxed grain morphology (average grain size of 10µm) as shown in **Figure 4.1(b)**. It showed 25% improvement in ductility as compared to the starting alloy, which has not been reported in the literature so far. The quenched sample with initial grain size of 10 µm is well suited for getting ultrafine grained structure upon cryorolling as small grains require less strain to generate high dislocation density.

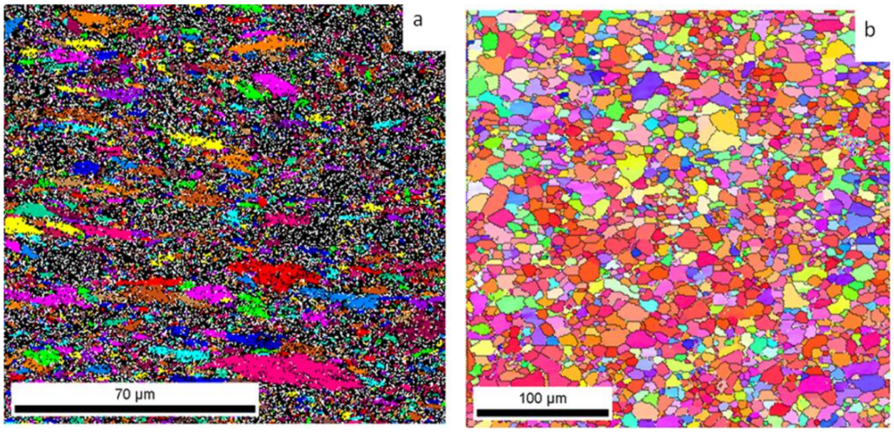

Figure 4.1 EBSD Image of **(a)** As Received and **(b)** 800^{o}C Mercury Quenched Zircaloy-2

The XRD of zircaloy-2 quenched in Hg upon 2 hours heat treatment at 800^{o}C in Argon environment shows the presence of α-phase as shown in **Figure.4.2**. The XRD peaks are in tandem with the pattern having reference code of 98-007-1958 reported for Zr. The α-phase exhibits hexagonal closed pack structure.

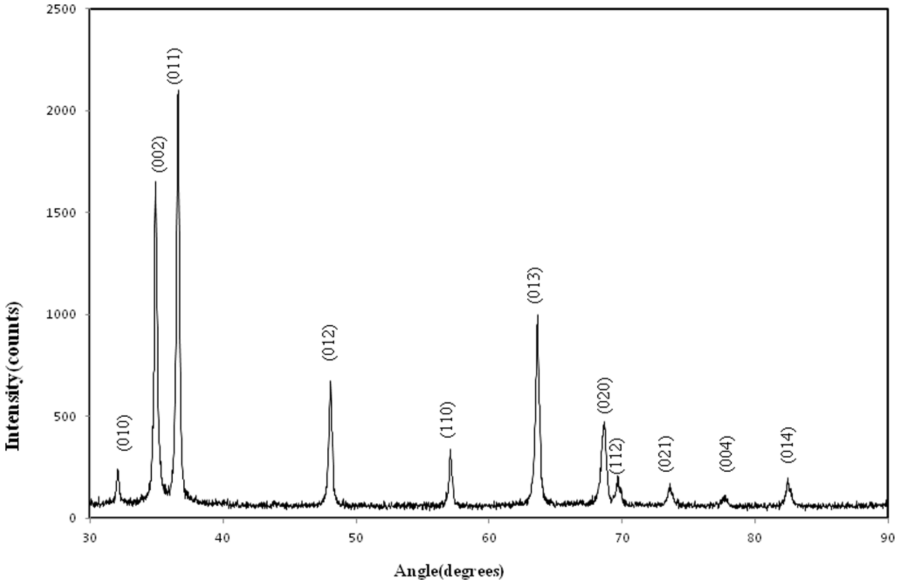

Figure 4.2 X-Ray Diffraction (XRD) Analysis of the 800^{o}C Mercury Quenched Sample

It shows that precipitates are completely dissolved in the matrix as the there is no peak showing its presence. The hydride phase is also not present in the XRD pattern, which is also validated by the EBSD microstructure as shown in **Figure 4.1**.

4.1.3.1 Dislocation Density

The 2θ positions at 34.79^{o} and 47.87^{o} represent (020) and (012) peaks of α-phase as can be seen from **Figure 4.3**. The intensity of the peak changes with increasing plastic strain in the samples due to change in fraction of grain orientation. The broadening of peak at (020) and (012) occurs due to increase in dislocation density in the material. Variance method is used to estimate the dislocation density in the CR zircaloy-2. Initially, the mercury quenched sample has $\langle\rho\rangle$ of 1.608687 x 10^{15} /m^{2}. After cryorolling, the sample contains $\langle\rho\rangle$ of 4.363240 x 10^{15} /m^{2}, 9.150664 x 10^{15} /m^{2}, 1.678539 x 10^{16} /m^{2} and 2.086366 x 10^{16}/m^{2} for thickness reduction of 25%, 50%, 75% and 85%, respectively. The increase in dislocation density with increasing plastic strain is due to suppression of dynamic recovery at cryo temperature (-190^{o}C), as confirmed from TEM and EBSD characterizations.

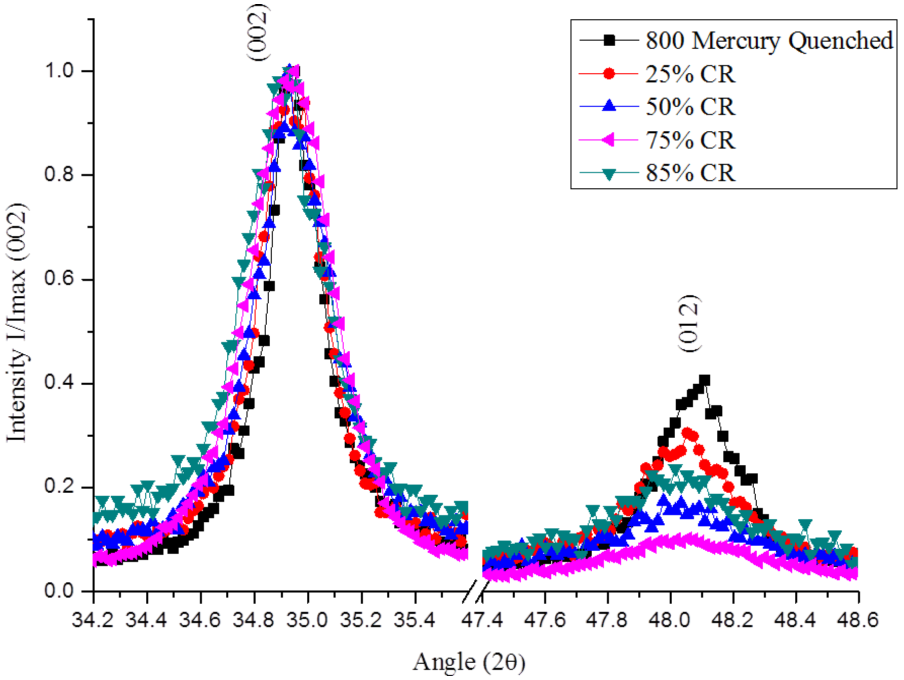

Figure 4.3 XRD Peaks of Mercury Quenched 25% CR, 50% CR, 75% CR and 85% CR Zircaloy-2

4.1.3.2 Mechanical Properties

The effect of cryorolling on the tensile and hardness properties of zircaloy-2 is shown in **Figure 4.4**. The increase in hardness, yield strength, and tensile strength is due to increase in dislocation density caused by the suppression of the dynamic recovery during plastic deformation at cryo temperature, which is validated by finding ‹ρ› by applying variance method using XRD results shown in **Figure 4.3** (Sauvage *et al*., 2012; Valiev *et al*., 2000; Wang *et al*., 2002; Rangaraju *et al*., 2005; Zherebtsov *et al*., 2013; Valiev *et al*., 1993). The hardness of CR samples has increased from 182 HV to 282 HV (54%) with 85% reduction, while the tensile strength has increased from 499 MPa to 891 MPa (78%) in case of 85% rolling direction and 967 MPa (92%) in case of transverse direction, which can be seen in **Figure** 4.4. The ductility is reduced due to increase in immobile dislocation density in the CR sample.

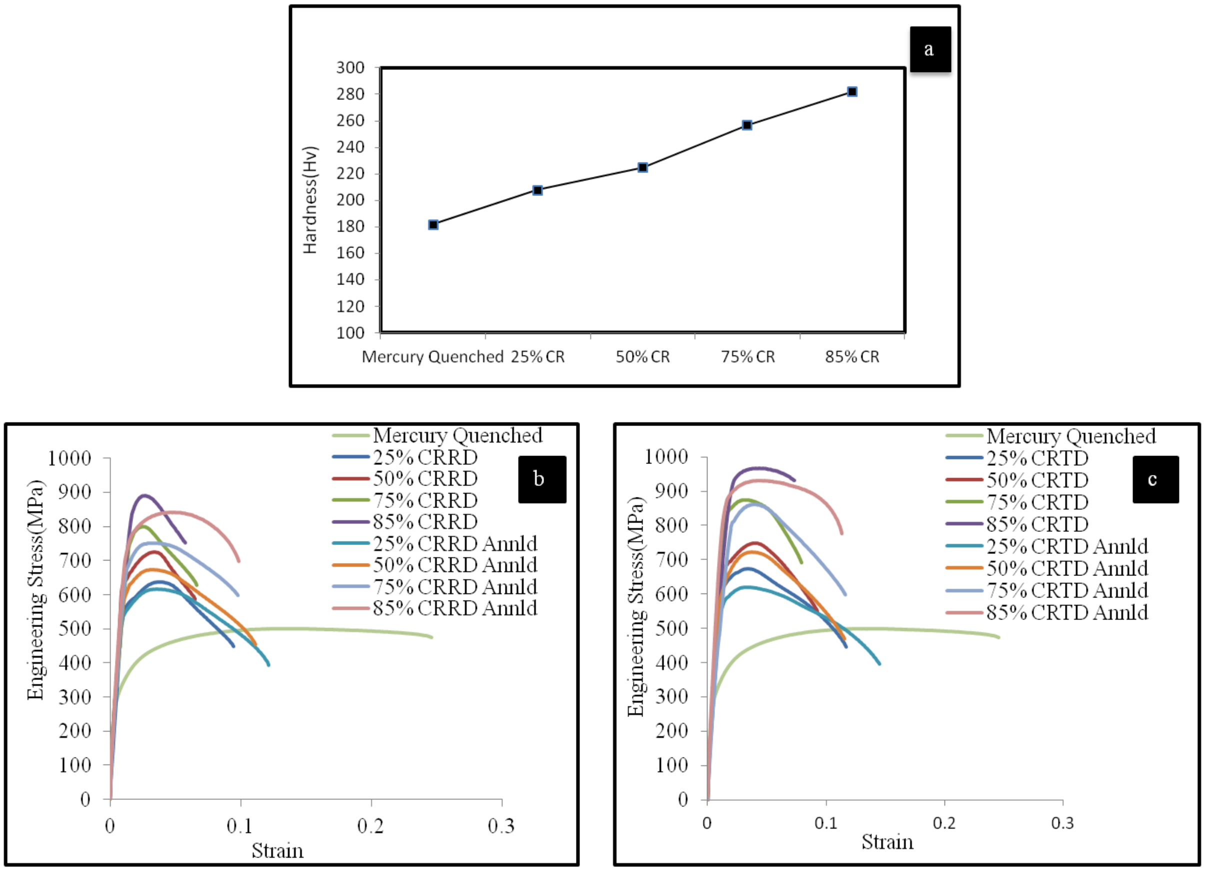

Figure 4.4 (a) Effect of Cryorolling on Hardness of Zircaloy-2, **(b)** Effect on Mechanical Properties after Cryorolling and Annealing at 400^o C for 30 minutes in Rolling Direction, **(c)** in Transverse Direction

The ductility and tensile strength (4.1% and 891MPa) in the rolling direction after 85% reduction is less as compared to the transverse direction (5.1% and 967 MPa), which is due to mechanical anisotropy and texture properties of the material (Ballinger *et al.*, 1981; Tenckhoff, 1988; Proust *et al.*, 2007, Rittenhouse, 1967). The higher strength of CR samples (85% thickness reduction) subjected to annealing at 400^{o}C for 30 minutes as compared to mercury quenched sample, can be explained by Hall-Petch relation.

Annealing of CR samples results in the removal of internal stress and enables dislocations to rearrange themselves and forms sub-grain structures. Short-annealing limits the grain growth and facilitates the formation of sub-grain boundaries. So, the samples annealed at 400^{o}C for 30 min led to increase in ductility (9.5%) with slight reduction in yield strength (841MPa) as compared with

85% CR zircaloy-2 is due to stress relieving, reduction in dislocation density and recrystallisation as shown in **Figure 4.6(e and f)**.

In case of Zircaloy-2, it contains limited number of slip system due to its HCP structure and therefore some grains with insignificant average misorientations, near basal grains are unable to deform completely up to 0.5 true strain (Whitmarsh 1962), as can be seen in **Figure 4.5(b)**. The grains, which are deformed completely leads to the formation of nanocrystalline, ultrafine and coarser grains upon annealing (**Figure 4.6 (e)**). The variation in grains size is also due to the HCP structure of zircaloy-2. These grains play a very important role for the improvement in elongation and strength of the material. Coarse grains provide ductility while the nano and ultrafine grains provide strength as explained by Hall-Petch relation. The microstructure with the formation of UFG and NC grains for CR alloy subjected to annealing is evident from the TEM results (**Figure 4.6 (e)**). The tensile strength and yield strength of zircaloy-2 have decreased while the elongation increases after annealing, as shown in **Figure 4.4(b and c)**. The above explanations are evident from the EBSD and TEM images of CR and annealed samples.

4.1.3.3 Electron Back Scatter Diffraction (EBSD)

The effect of cryorolling after various percentage of reduction of the zircaloy-2 can be seen in **Figure 4.5**. The minimum confidence index is taken to be 0.05 such that the completely deformed grains are having very low confidence index and can be seen as dark. Heterogeneous microstructure is observed with increasing percentage of thickness reduction in the samples. The increase in rolling reduction causes elongation of grains along the rolling direction (**Figure 4.5(a, b and c)**). At 25% thickness reduction, small quantity of $\{10\bar{1}2\}\langle\bar{1}011\rangle$ tensile twins orient softer grains into harder orientation as shown in (**Figure 5(a)**). This twin restricts dislocation movement and causes strain hardening in the deformed samples. The $\{10\bar{1}2\}\langle\bar{1}011\rangle$ tensile twin is dominant up to 25% thickness reduction and with further increasing strain, deformation occurs mainly by slip. With the thickness reduction of sample up to 50%, $\{11\bar{2}2\}\langle\bar{1}\bar{1}23\rangle$ compressive as well as $\{10\bar{1}2\}\langle\bar{1}011\rangle$ tensile twins are observed. These $\{11\bar{2}2\}\langle\bar{1}\bar{1}23\rangle$ compressive twins are activated at low temperature and high strain, which orient near basal grains to softer orientations as seen from **Figure 4.5(b)**. At 75% reduction, elongation of grains along the rolling direction is observed (**Figure 4.5(c)**). It shows the

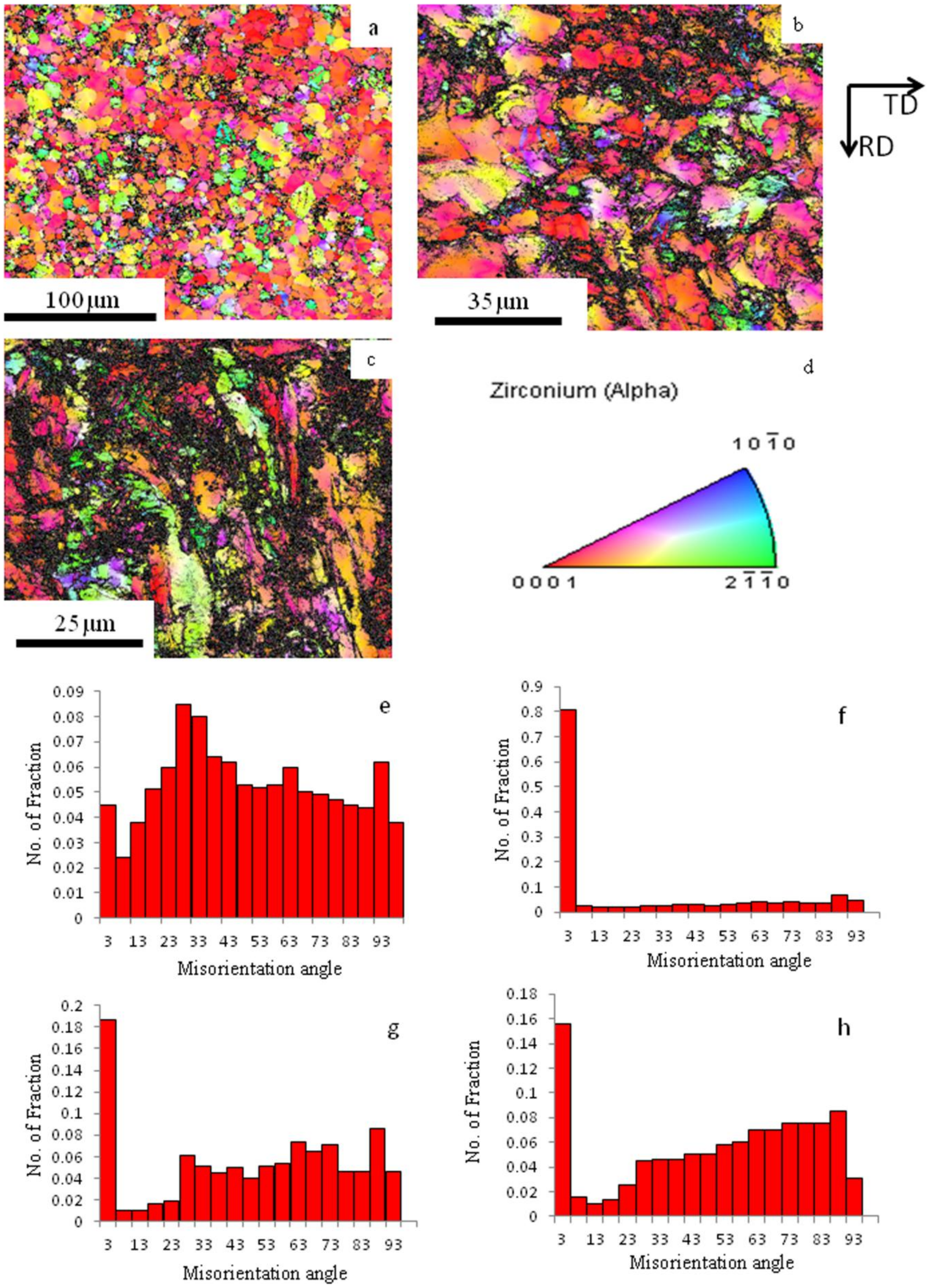

Figure 4.5 EBSD Image for **(a)** 25%, **(b)** 50% and **(c)** 75% Cryorolled Zircaloy-2. A Minimum Confidence Index (.05) is taken to show the Completely Deformed Portion as Dark **(d)** Orientation of Crystals. The Fraction of Low and High Angle Grain Boundaries of **(e)** Mercury Quenched, **(f)** 25% CR, **(g)** 50% CR and **(h)** 75% CR Zircaloy-2, respectively

deformation of near basal grains indicating the activation of basal slip at large strain (Knezevic *et al*, 2013). The elongated near basal grains as observed in **Figure 4.5(c)** is due to non linear distribution of strain in the highly anisotropic structure of zircaloy-2. The basal slip might have got activated due to the high strain, which leads to the elongation of near basal grains. The twinning observed up to 25% deformation gets vanished on further reduction as it causes grain fragmentation and favors further slipping. The twinning causes change in grain orientation, which is favorable for further slipping (Murthy *et al*., 2006). There are some near basal grains, not deformed completely at low strain (**Figure 4.5(b)**), which is due to insignificant grain average misorientation and being elastically harder (Sahoo *et al*., 2007). The misorientation angle shows that initially 800^{o}C mercury quenched sample exhibit high fraction of high angle grain boundaries because the grains are completely recrystallised as observed in the present work (**Figure 4.5(e)**).

For the CR 25% samples, the fraction of low angle grain boundaries has increased as can be seen in **Figure 4.5(f)**. With further increase in reduction to 50% and 70%, the fraction of high angle grain boundaries has increased due to recrystallisation of some elongated grains as shown in **Figure 4.5(g and h)**.

4.1.3.4 Transmission Electron Microscopy (TEM)

TEM observations of CR samples show that as the deformation increases, the formation of dislocation cells and dislocation tangles occurs. Dislocation cells can be seen as dark patches indicated by triangles i.e. agglomerated dislocations which is due to suppression of dynamic recovery. The dislocation tangles indicated by arrows can be seen in the form of dark thick lines, which is due to the interaction of dislocations with each other at different strain rates. It is evident from **Figure 4.6(a, b, c and d)**, that as the deformation increases, the dislocation cells get reduced and dislocation tangles are increasing, showing suppression of dynamic recovery. The dislocation cells can also be identified in selected area diffraction (SAD) pattern indicated by triangles which can be seen as discontinuous arc and dislocation tangles indicated by arrows can be seen as continuous arc. The inset picture of (SAD) pattern in **Figure 4.6(a, b, c and d)** shows that the discontinuous arc in the SAD pattern is increasing with increasing thickness reduction of the sample. In **Figure 4.6(d)**, it can be seen that the dislocation tangles are getting denser showing highly deformed structure with very high internal stresses, which are in accordance with the results of measured dislocation density and EBSD image of deformed samples in the present work.

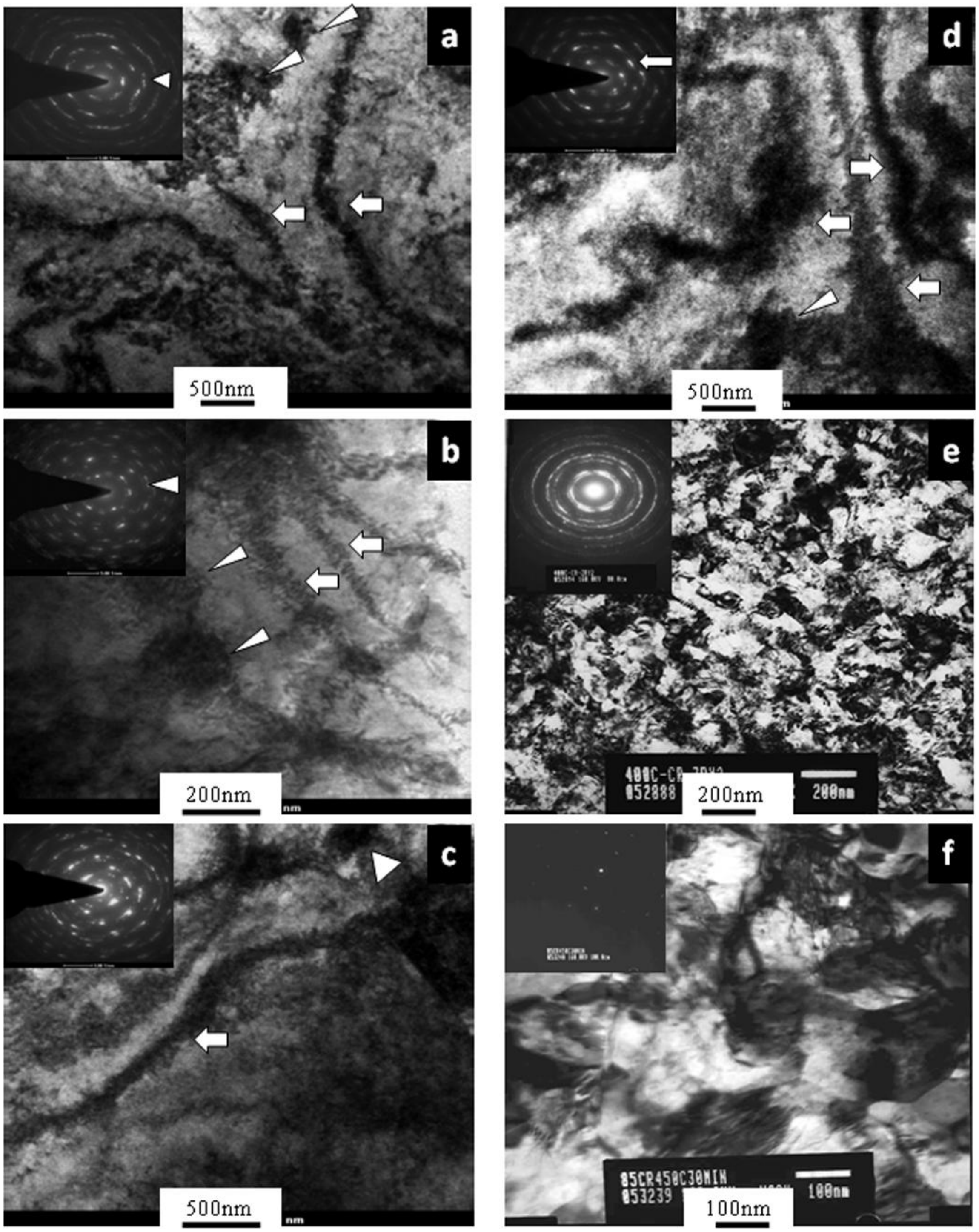

Figure 4.6 TEM Image of Cryorolled Zircaloy 2 with **(a)** 25%,**(b)** 50%,**(c)** 75%,**(d)** 85% Reductions respectively, **(e)** TEM Image of Annealed Zircaloy-2 at 400^{o} C for 30 min after 85% Cryorolling, **(f)** TEM Image of Zircaloy-2 Annealed at 450^{o} C for 30 min. Inset shows the Selected Area Diffraction Pattern (SAD) of respective Images

It is evident from **Figure 4.6(e and f)** that the formation of nanocrystalline grains with an average grain size of 150 nm occurs due to the rearrangement of dislocations. Annealing of deformed samples at low temperature (400^{o} C for 30minutes) results in the nucleation of subgrain structure followed by bimodal grain structure comprising of both nanocrystalline and ultrafine grains. Due to anisotropy in HCP crystals, distribution of stress inside them is nonlinear, which also causes formation of multimodal structure after annealing. The high dislocation density in the CR zircaloy-2 acts as nucleation sites for the formation of sub grain structures and subsequently, the bi-modal structure, when it is subjected to annealing at 400^{o} C for 30 minutes.

4.1.4 Summary

The hardness and tensile behavior of CR zircaloy-2 has been investigated in the present work. The microstructural features of the deformed alloy and CR alloy subjected to annealing at 400^{o}C for 30 minutes were characterized by FESEM/EBSD and TEM. The following conclusions are made based on the present study.

- The microstructure of solutionised zircaloy-2 followed by quenching in mercury at 800^{o}C exhibits homogenous microstructure with α phase present in the alloy as evident from EBSD and XRD study.
- CR zircaloy-2 with different thickness reductions such as 25%, 50%, 75%, and 85% shows heavily deformed grains and the dislocation density in the alloy increases with increase in plastic strain induced in the alloy.
- With increase in strain up to 50%, $\{10\bar{1}2\}\langle\bar{1}011\rangle$ tensile twins are replaced by $\{11\bar{2}2\}\langle\bar{1}\bar{1}23\rangle$ compressive twins. After 50% reduction, twins get vanished from the structure but the deformation in near basal grains occurs due to basal slip in them.
- EBSD study reveals that the volume fraction of low angle boundaries is found to be higher in 25% CR due to the generation of dislocations during cryorolling but it decreases with increasing plastic strain. The volume fraction of high angle boundary is higher in zircaloy-2 subjected to thickness reduction of 75%. zircaloy-2 subjected to annealing exhibits heterogeneous microstructure comprised of ultrafine grains and nanocrystalline grains.
- The hardness and tensile strength of CR zircaloy-2 increases with increase in induced plastic strain during cryorolling due to the accumulation of dislocation density, formation of sub-grain structure followed by ultrafine grains in the alloy. The hardness and tensile strength of

85% CR is found to be 282 HV and 891 MPa, respectively, and for the annealed alloy, it is observed to be 282 and 841 MPa in rolling direction and 931 MPa in transverse direction. The ductility improvement in the annealed zircaloy-2 upon cryorolling with plastic strain (1.89) is due to the recovered ultrafine grains, which exhibit higher work hardening rate.

4.2 Mechanical and Microstructural Characterizations of Ultrafine Grained Zircaloy-2 Processed by Room Temperature Rolling

4.2.1 Introduction

During rolling, the zircaloy-2 sheet undergoes compressive load in normal direction, while friction forces in the rolling direction due to which it elongates more in the rolling direction. There is small compressive force exerted in transverse direction due to which less elongation occurs in the transverse direction. The basal pole {0002} prefers to align parallel to the compressive direction (normal direction) and spread 20-40^o towards the transverse direction because of the small compressive force in the transverse direction (Murthy *et al.*, 2006). Rolling is performed by quenching zircaloy-2 at β temperature with Widmanstätten type of structure and process annealed during rolling as reported in the literature (Vanitha *et al.*, 2009; Xu *et al.*, 2008a; Lee *et al.*, 1972; Ballinger *et al.*, 1981). Rolling reduction up to a maximum of 70% at room temperature is obtained by annealing zircaloy-2 in a seal quartz tube for 10 hours at 750^o C and cooling with a rate of 5^o C per minute. The dislocation density was investigated using Williamson Hall technique and it was found to be of the order of 10^{-15}/m^2 (Mukherjee *et al.*, 2004).

It is well known that grain size influences physical and mechanical response of a structural material. Development of a material with desired properties include its grain size control through optimized thermo mechanical processing conditions. Ultrafine and nanocrystalline materials provide high strength, super plasticity at elevated temperature and good fracture strength properties. These materials are produced by severe plastic deformation techniques (SPD) such as ECAP, Multiaxial forging, ARB, etc (Sauvage *et al.*, 2012; Valiev *et al.*, 2000; Estrin *et al.*, 2013; Vedani *et al.*, 2004). The formation of ultrafine grained microstructures in the material during SPD can be briefly explained as follows.

During deformation, dislocations are created in the material and it moves with a very high velocity and get adhered inside the grains in the form of dislocation cells and tangles with low strain. On increasing strain, dislocations get arranged in the form of boundaries with high misorientation angle known as geometrically necessary boundaries (GNBs) and trapping incidental dislocation boundaries (IDBs) inside it. The GNBs are high angle misorientation while IDBs are low angle misorientation from 1.5 to 15^o. Dislocations with less than these angles are distributed naturally inside the grains. The GNBs are formed during initial deformation and with increasing strain, IDBs gets oriented along the macroscopic orientation where the macroscopic plastic flow occurs. The subdivision of grain takes place with further increase in strain leading to the formation of newly developed cells, thus forming nanocrystalline and ultrafine grains (Hansen, 2001; Hughes *et al*., 2003; Jiang *et al*., 2012; Wilsdorf *et al*., 1991; Liu *et al*., 1995).

The literature is scarce on the influence of room temperature rolling on the grain refinement and mechanical properties of zircaloy-2. Therefore, the present work has been focused to investigate the maximum grain refinement achievable in zircaloy-2 and study its hardness and tensile properties correlated through the microstructures of the heavily deformed alloys. TEM and ESBD techniques were used to substantiate the mechanisms of formation of ultrafine grains in the zircaloy-2.

4.2.2 Experimental Procedure

The material for the present study was procured from NFC, Hyderabad, India in the form of 4mm thick rolled sheets. The chemical composition of the material is shown in **Table 3.1** in Chapter 3. The alloy was then heat treated at 800^{o}C in argon environment and then quenched in mercury at room temperature. The quenched sample was then surface ground and rolled at room temperature. Initially the thickness of the sample was 4.35mm. A reduction of 0.2 mm to 0.05 mm per pass was given using 2 high rolling mill having 8 rpm with 110 mm roller diameter. After rolling, the sample was immediately dipped in water so that the sample temperature does not exceed room temperature for another pass. $MoSi_2$ was used to avoid the frictional and heat losses. Further characterization of the samples are performed such as Tensile test, hardness, EBSD, TEM, XRD. The method of the named characterization technique is already discussed in chapter 3.

4.2.2.1 Dislocation Density Calculation by X-Ray Diffraction

Room temperature rolled (RTR) zircaloy-2 samples was characterized by advanced X-ray diffraction instrument using Cu Kα radiation with a scan rate of 1^{o} per minute. Expert high score plus (2.2.5) software is used to identify the formation of different phases in the samples using the XRD data. Dislocation density of the RTR zircaloy-2 was calculated by using variance method based on the XRD peaks (Borbely *et al*., 2001; Groma, 1998; Sarkar *et al*., 2008).

4.2.3 Result and Discussion

4.2.3.1 Microstructure

Microstructure of as received and solutionised zircaloy-2 is discussed in chapter 4.1. XRD results show the presence of α-phase obtained in solutionised zircaloy-2 (Chapter 4.1). All the peaks in the pattern is matching with reference pattern (98-007-1958) reported for α-phase of Zr in inorganic crystal structure database (ICSD). During room temperature rolling, dislocation density increases with various thickness reductions up to 25%, 50%, 75% and 85% in zircaloy-2. Dislocation density was calculated by finding fourth order moment of peaks profile at 34.79^{o} and 47.87^{o} 2θ position as can be seen from **Figure 4.7**. The dislocation density ‹ρ› of mercury quenched zircaloy-2 is 1.608687×10^{15} /m^{2}. After room temperature rolling, dislocation density ‹ρ› of 25%, 50%, 75% and 85% zircaloy-2 is 4.168184×10^{15} /m^{2}, 5.124711×10^{15} /m^{2}, 1.168889×10^{16} /m^{2} and 1.546860×10^{16} /m^{2}, respectively.

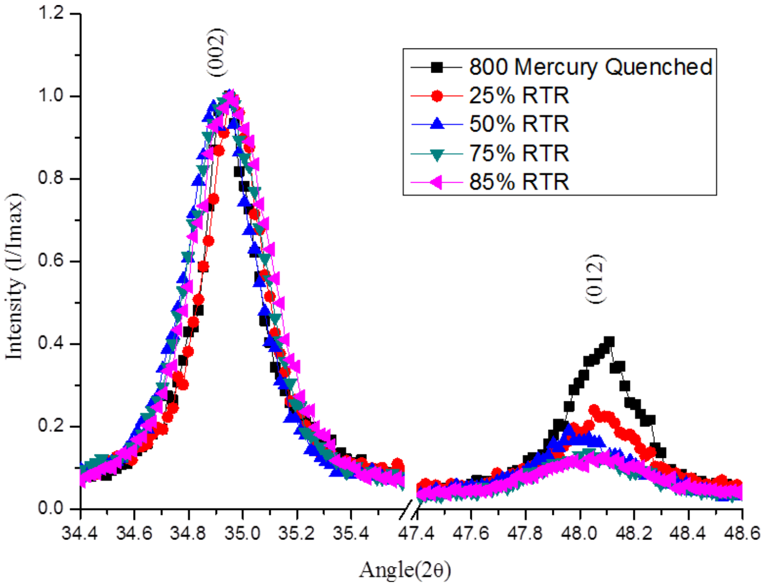

Figure 4.7 XRD Peaks of Mercury Quenched 25% RTR, 50% RTR, 75% RTR and 85% RTR Zircaloy-2 showing the effect of Rolling on the Broadening of (002) and (012) Peaks

4.2.3.2 Transmission Electron Microscopy (TEM)

Deformed microstructure obtained after various thickness reduction can be seen in **Figure 4.8**. The dislocation density is increasing with increasing true strain in the material. The dislocations get accumulated initially in the form of tangles and on further reduction, dislocation cells are formed, shown by arrows and triangles in the **Figure 4.8**. During rolling, a reduction of 0.2mm per pass was given due to which, work done over the material is transferred to move dislocation inside the crystal and it increases internal stresses at different point of the grains. All the work performed was not utilized to introduce dislocation as part of them converted in to heat. On further reduction, the materials become harder due to strain hardening. Heat dissipation during plastic deformation can be understood using the following relation

$$\dot{q} = \eta \bar{\sigma} \dot{\bar{\varepsilon}} \qquad \textbf{(4.2)}$$

Where

$\dot{q}$ is heat dissipation

η is heat generation efficiency (fraction of plastic strain energy that is converted to heat)

$\bar{\sigma}$ is equivalent stress

$\dot{\bar{\varepsilon}}$ is equivalent plastic strain

It is evident from equation **(4.2)** that heat dissipation is directly proportional to the plastic strain induced in each pass during rolling. There is always some heat effect, despite using lubricant, which directly affects recovery of zircaloy-2 during deformation. The recovery is also proportional to the plastic strain induced during rolling (Kobayashi *et al.*, 1989). Initially on applying strain, initially cell blocks are developed with high angle grain boundaries (GNBs). With further increasing strain, dislocations accumulate near the cells in the form of cell boundary with low angle misorientation (IDB). Initially, these IDBs follow a specific orientation but with further increase in strain, they get oriented along macroscopic planes along the induced macroscopic plastic flow. At higher strains, these misorientation increases further. By this process, grain subdivision occurs in which group of cells get oriented in different orientation and formation of ultrafine and nanocrystalline grains occurs as shown in **Figure 4.8(d)**, which are in tandem with the published literature (Guo *et al.*, 2014; Sauvage *et al.*, 2012; Valiev *et al.*, 2000; Estrin *et al.*, 2013; Vedani *et al.*, 2004). Multimodal structure with 60% nanocrystalline and rest of it ultrafine grains are observed from **Figure 4.8(d)**. Rings in the diffraction pattern clearly indicate the formation of large number of grains seen from the inset of **Figure 4.8(d)**.

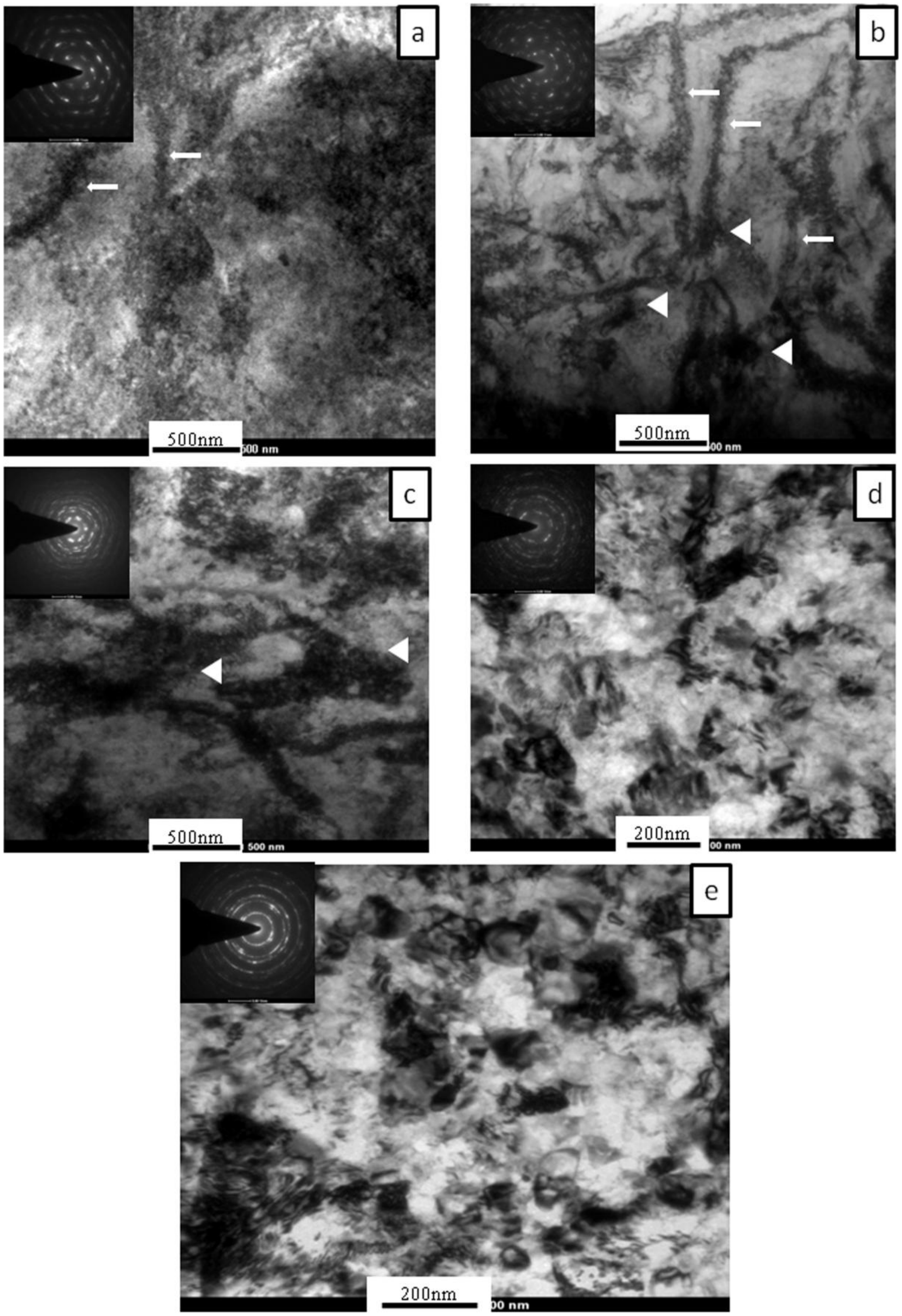

Figure 4.8 TEM Image of Room Temperature Rolled Zircaloy-2 after **(a)** 25%, **(b)** 50%, **(c)** 75% and **(d)** 85% Reduction respectively **(e)** Showing the effect of Annealing at 400^o C for 30minutes after 85% Reduction

On annealing at 400^{o} C for 30 minutes, 85% RTR zircaloy-2 reveals the formation of sub grain boundaries due to the rearrangement of dislocation. The deformed grains during annealing undergo recovery and forms stress free ultrafine grains. Multimodal grain structure with a combination of nano and ultrafine grains can be seen from the **Figure 4.8(e)**, which is also indicated by the diffraction pattern shown in the inset of **Figure 4.8(e)**.

4.2.3.3 Hardness and Tensile Properties

The effect of room temperature rolling on the tensile and hardness properties of zircaloy-2 is shown in **Figure 4.9(a-c)**. The plastic deformation during repeated rolling, increases dislocation density inside the grains and it forms tangles at room temperature. There is a limit for achieving maximum dislocation density in the material due to recovery effect. The hardness of RTR samples has increased from 182 to 269 MPa (47%) with 85% reduction, and the tensile strength has increased from 499 to 679 MPa (36%), 697 MPa(39%) in case of transverse direction. The ductility and tensile strength observed in the rolling direction after 85% reduction is less as compared to the transverse direction. It is due to mechanical anisotropy and texture properties of the material (Tenckhoff, 1988, Ballinger *et al*., 1981; Proust *et al*., 2007; Rittenhouse *et al*., 1967). 85% RTR zircaloy-2 after annealing at 400^{o} C for 30 minutes shows better ductility (6% in rolling direction, 7.2% in transverse direction) due to partial annihilation of dislocations and its rearrangement leading to the formation of nanocrystalline and ultrafine grains as shown in **Figure 4.8(e)**. These ultrafine grains are responsible for strength increment of RTR zircaloy-2 as can be understood using Hall-Petch relation. It is evident from **Figure 4.9(b and c)** that 85% RTR annealed zircaloy-2 shows 33% increment in tensile strength (664 MPa) in rolling direction, while 35% increment (674 MPa) in transverse direction. The increment in yield strength is 93% in rolling direction (634 MPa) while 97% in transverse direction (653 MPa). The increment is more in yield strength as compared to tensile strength. With increasing thickness reduction, strain hardening occurs which decrease ductility of the alloy. It diminishes the difference between yield strength and tensile strength but there is a less increment in the tensile strength after rolling.

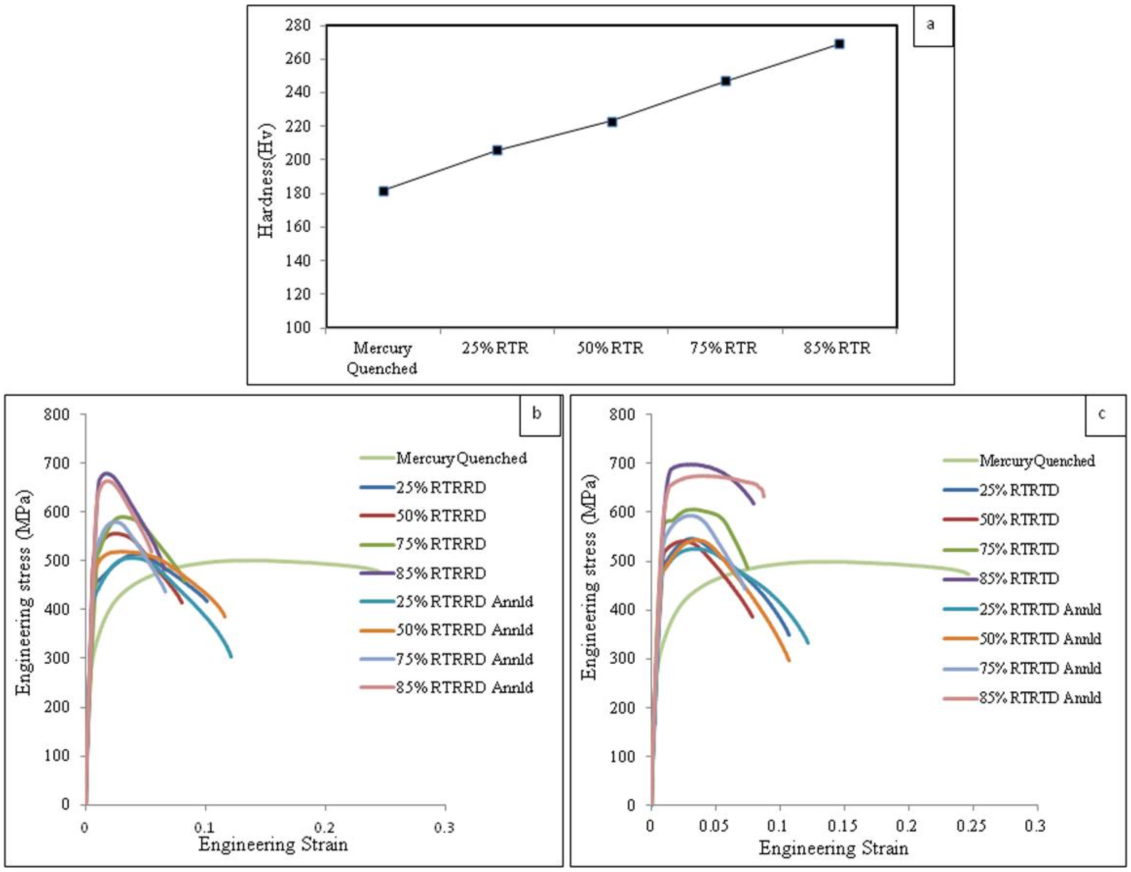

Figure 4.9(a) Effect of Room Temperature Rolling on Hardness of Zircaloy-2, **(b)** Effect on Mechanical Properties after Room Temperature Rolling and Annealing at 400^{o} C for 30 minutes in Rolling Direction, **(c)** in Transverse Direction

4.2.3.4 Electron Back Scatter Diffraction (EBSD)

The deformed microstructure of 25%, 50% and 75% RTR zircaloy-2 is shown in **Figure 4.10(a-c)**. Signal with a minimum confidence index of .05 is excluded from the image so that deformed part can be seen as dark. It can be clearly seen that deformation in the grains is increasing with increasing thickness reduction. In 25% and 50% RTR condition, most of the grains red in colour are {0002} plane having orientation perpendicular to normal rolling direction. The grains blue in color with $\{10\bar{1}0\}$ planes parallel to rolling direction are shown in **Figure 4.10(a and b)**. Heterogeneous structure with some undeformed grains in 75% RTR sample is due to insignificant grain misorientation and is elastically harder (Sahoo *et al*., 2007). The inverse pole, **Figure 4.10(d)** shows that most of the grain after 75% deformation shows its basal plane perpendicular to normal

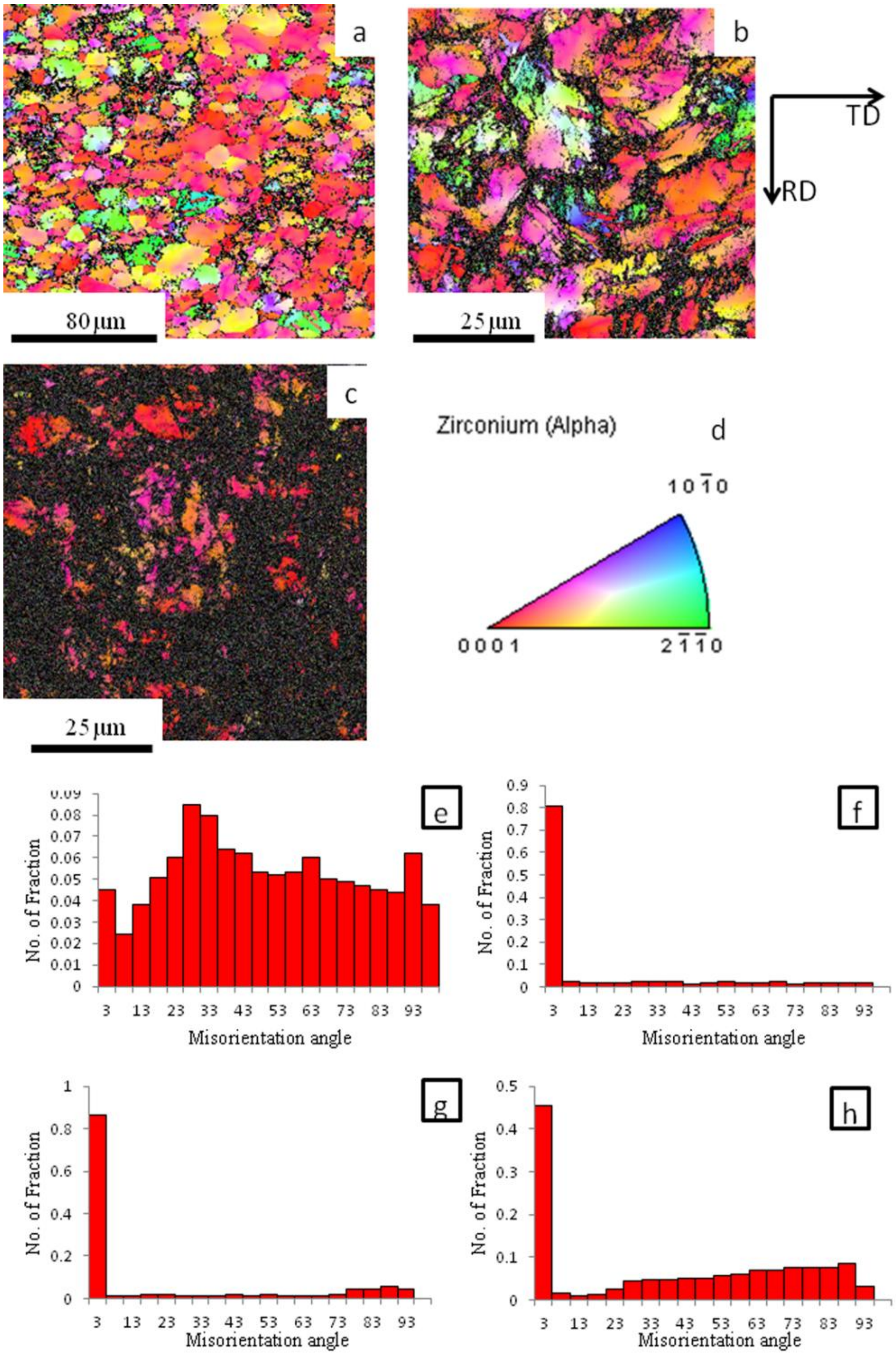

Figure 4.10 EBSD Image of **(a)** 25%,**(b)** 50% and **(c)** 75% Room Temperature Rolled Zircaloy-2 **(d)** Orientation of Grains. A Minimum Confidence Index (.05) is taken to show the Completely Deformed Portion as Dark. The Fraction of Low and High Angle Grain Boundaries of **(e)** Mercury Quenched, **(f)** 25% RTR, **(g)** 50% RTR and **(h)** 75% RTR Zircaloy-2 respectively

direction with some grains (pink and purple colour). The basal plane i.e. (0002) is rotated approximately 0-30^{o} outward to the normal direction because of some compressive load exerted by the grains in the transverse direction (Murthy *et al*., 2006) as shown in **Figure 4.11**. During room temperature rolling, fraction of low angle grains boundaries is increasing as shown in **Figure 4.10 (e-h)** due to dislocation introduced inside the grains, during deformation. After 50% and 75% thickness reduction, a fraction of high angle grain boundary gets increased due to the formation of new grains.

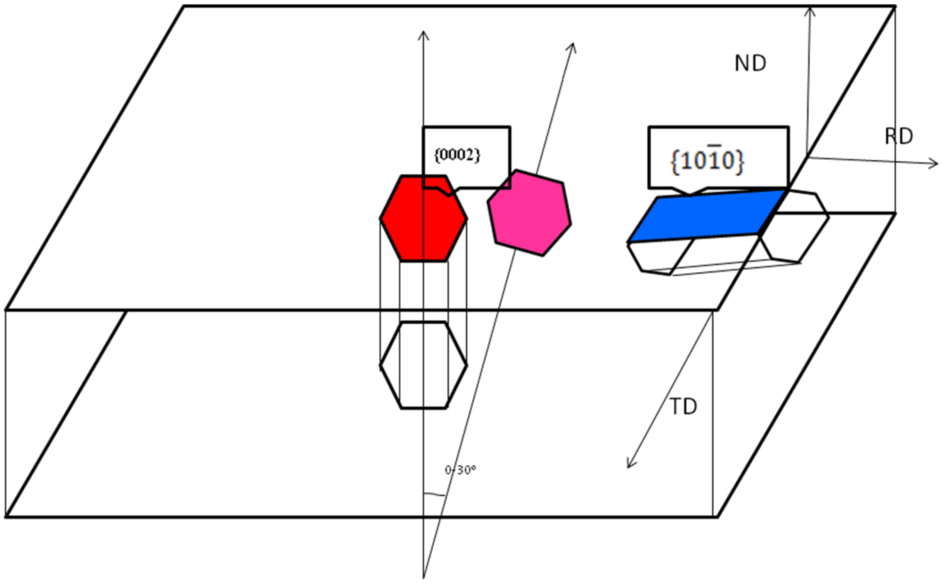

Figure 4.11 Orientation of Planes after Rolling

4.2.4 Summary

Zircaloy-2 was subjected to room temperature rolling with true strain of (1.89) and its hardness and tensile properties were measured in the present work. The following conclusions are made based on the study.

- The heavily deformed microstructure in the zircaloy-2 shows the presence of high dislocation density and it shows the increment in tensile strength from 499 to 679 MPa (36%) in case of 85% rolling direction and 697 MPa (39%) in case of transverse direction.

- The rolled samples subjected to annealing at 400^{o} C for 30 minutes showed the tensile strength value of (664 MPa), 33% increment in rolling direction, while (674 MPa), 35% increment in transverse direction.

- EBSD results shows the orientation of basal plane {0002} up to $20\text{-}30^{o}$ outward to the normal direction of rolling. Microstructure reveals the presence of bulk nanostructured zircaloy-2 with average grain size of 60nm in RTR, while 110 nm in 400^{o} annealed condition.

- TEM study reveals the formation of high dislocation density with increasing thickness reduction of the Zicaloy-2. The alloy subjected to annealing at 400^{o} C for 30 minutes leads to the formation of ultrafine and nanostructured grains.

4.3 Texture and Mechanical Behaviour of Zircaloy-2 Rolled at Different Temperature

4.3.1 Introduction

The HCP structure of Zr alloy significantly affects its deformation behavior due to the formation of different textures during thermo mechanical processing, resulting in anisotropic behavior in mechanical properties. The lack of slip systems and twinning plays an important role in the plastic deformation of the HCP materials. Twinning causes non reversal reorientation of c axis due to which strong crystallographic texture is formed, imparting anisotropy to HCP material (Ballinger *et al.*, 1981; Tenckhoff, 1988; Murthy *et al.*, 2006). Generally, texture in the materials is formed during various processing such as casting, welding, thermo mechanical processing, and even heat treatment.

At room temperature and above, both slip and twinning affect the plastic deformation of zircaloy-2. Low c/a ratio causes slip more on $\{10\bar{1}0\}$ plane with $\langle 1\bar{2}10\rangle$ direction. In {0002} plane, slip is rarely observed but cold working makes the prism slip strain hardened and the activation of basal slip. Von-Mises criteria of plastic deformation and large plasticity of zircaloy-2 is validated by pyramidal slip. It is observed in first $\{10\bar{1}1\}$ plane and second order in $\{11\bar{2}2\}$ plane along $\langle 11\bar{2}3\rangle$ (c+a) directions as reported in the literature (Tenckhoff, 1988; Murthy *et al.*, 2006; Wang *et al.*, 2003). When 'c' axis is parallel to normal direction, prism slip is not possible. Therefore, the grains in HCP materials can only deform either by <c+a> pyramidal slip or by $\left(\{11\bar{2}2\}\langle\bar{1}\bar{1}23\rangle\right)$ compressive twinning. It was reported that at room temperature, <c+a> pyramidal slip is easier to activate than $\left(\{11\bar{2}2\}\langle\bar{1}\bar{1}23\rangle\right)$ compressive twinning (Mccabe *et al.*, 2006). At large strain greater than 0.5, basal slip gets activated at room temperature (Knezevic *et al.*, 2013).

Twinning is one of the deformation modes in HCP structured materials as it may provide favorable planes for further slip. Twinning modes depend on the type of resultant load which the crystal experiences, whether it is tensile or compressive. In tensile loading along c axis, $\left(\{10\bar{1}2\}\langle\bar{1}011\rangle\right)$ twin gets activated and $\left(\{11\bar{2}1\}\langle\bar{1}\bar{1}26\rangle\right)$ twin gets activated less often. During compressive loading along c axis, $\left(\{11\bar{2}2\}\langle\bar{1}\bar{1}23\rangle\right)$ twins are active, while at high temperature, $\left(\{10\bar{1}1\}\langle\bar{1}012\rangle\right)$ twin is observed. The deformation modes which are observed at liquid nitrogen temperature are prismatic slip, tensile twinning $\left(\{10\bar{1}2\}\langle\bar{1}011\rangle\right)$, $\left(\{11\bar{2}1\}\langle\overline{11}26\rangle\right)$ and compressive twinning $\left(\{11\bar{2}2\}\langle\overline{11}23\rangle\right)$ (Mccabe *et al.*, 2009).

Microstructure of zircaloy-2 after deformation exhibits fragmented and non fragmented type of grains. There is also formation of twins after deformation of this alloy. Realignment and annihilation of dislocation and formation of high angle grain boundary are responsible for fragmentation of grains. At the same time, plastic deformation leads to misorientation of prior twins causing annihilation of twins (Sahoo *et al.*, 2010). The tilting of crystal towards transverse direction is due to $\{10\bar{1}0\}\langle 11\bar{2}0\rangle$ prismatic and $\{0001\}\langle 11\bar{2}0\rangle$ basal slip. In polycrystalline materials with HCP structure, anisotropic deformation occurs in the direction of loading to which the applied load is either tensile or compressive. If load applied to the crystal is parallel or perpendicular to the c-axis, the results found are; Compressive stress II c-axis, σ_{yield} = 2150 N/mm, Tensile stress II c-axis, σ_{yield} = 1430 N/mm, Tensile or compressive stress ⊥ c-axis, σ_{yield} = 650 N/mm^2 (Tenckhoff, 1988). Depending on the type of loading, ratio between the strength of the above cases is found to be 3:2:1. This is due to the deformation mode, twinning gets activated when the load is applied parallel to the c-axis but slip gets activated if it is perpendicular to the c-axis (Tenckhoff, 1988).

The literature on the texture of CR zircaloy-2 is limited as discussed in earlier sections. Therefore, the present work has been focused to study anisotropic mechanical behavior and textures of ultrafine grained zirconium alloy processed by cryorolling and room temperature rolling. XRD and EBSD techniques were used to characterize the macro and micro textures of the CR zircaloy-2 and correlated with its anisotropic deformation behavior.

4.3.2 Experimental Procedure

Rolled sheet of zircaloy-2 with 4mm thickness has been obtained from Nuclear Fuel Complex, Hyderabad, India. Chemical composition of the alloy is shown in **Table 3.1** in **Chapter 3**. The sheet was heat treated in vacuum at 800^o C in argon environment and then quenched in mercury at room temperature. After quenching, zircaloy-2 sheet was surface ground and washed in methanol. Cryorolling was performed by dipping the 40mm x 30mm piece into liquid nitrogen for 10 minutes prior to rolling. Liquid nitrogen was continuously poured to maintain rollers at low temperature during rolling. Room temperature rolling (RTR) was performed by dipping the sample in water after every pass to maintain sample temperature during rolling. A 0.2mm to 0.05mm reduction was given in every pass using baby rolling mill with 8rpm speed and 110mm roller diameter. MiSo$_2$ was used to avoid the frictional and heat losses during rolling of the alloy. Further characterization such as Tensile test, Bulk hardness, EBSD, TEM, texture XRD was performed as discussed in Chapter 3.

4.3.3 Result and Discussion

As received and initial microstructure after heat treating zircaloy-2 for 2 hours at 800^o C for 30 minutes exhibit equiaxed grains with an average grain size of 10μm as reported in section 4.1. Mercury quenching found to be useful as it increases ductility up to 25% and tensile strength of 499 MPa. The XRD pattern also shows the presence of α phase. The **Figure 4.12** shows that even after annealing, {0002} pole is inclined 20^o to 30^o towards the transverse direction.

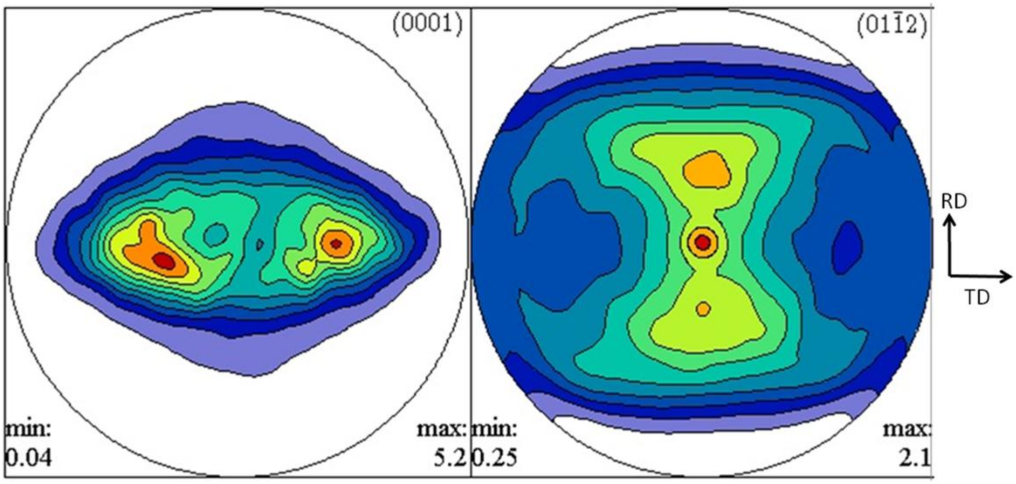

Figure 4.12 Texture {0002} and $\{01\bar{1}2\}$ Pole Figure of Mercury Quenched Zircaloy-2

4.3.3.1 Transmission Electron Microscopy (TEM)

TEM results of CR and RTR zircaloy-2 are already discussed in **Section 4.1** and **4.2**. An increase in dislocation density in CR and RTR zircaloy-2 with increase in reduction during rolling was observed. Formation of dislocation cells and dislocation tangles are seen in CR zircaloy-2.In CR samples, dislocations tangles are getting thicker, which prove suppression of dynamic recovery and formation of ultrafine grains did not occur even at 85% reduction. RTR zircaloy-2 samples show dynamic recovery due to increase in sample temperature during rolling. With increasing thickness reduction of RTR zircaloy-2, dislocation cells are formed. At 85% reduction, dislocation cells get oriented along macroscopic planes due to macroscopic plastic flow inside the RTR sample. This results in grain subdivision, leading to the formation of nanocrystalline and ultrafine grain structure in zircaloy-2.

During rolling at cryo temperature, critical resolved shear stress in the slipping planes becomes large in zircaloy-2 (Derep *et al*., 1980; Beyerlein *et al*., 2008). However, dislocations get trapped inside the grains with increasing rolling passes as dynamic recovery is suppressed at cryo temperature. Because of lesser plastic flow at cryo temperature during deformation, edge cracks are formed after rolling more than 75% thickness reduction (85% CR), proving the material is less ductile and still rollable at low temperature, as evident from **Figure 4.13**. Although, cracks can also be seen in 85% RTR zircaloy-2 (**Figure 4.13**), activation of {0002} basal slip may occur near the cracks (Dickson *et al*., 1971). The formation of ultrafine grains does not occur during rolling at cryo temperature but it is facilitated upon annealing CR zircaloy-2.

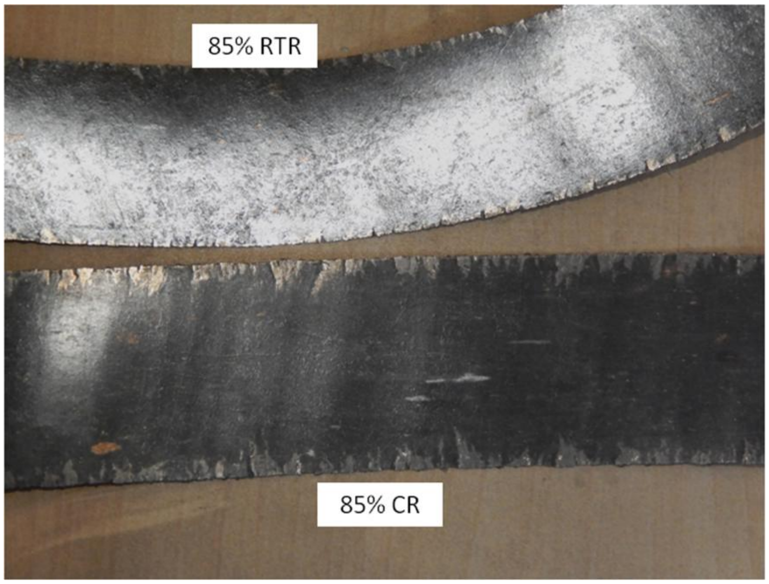

Figure 4.13 Image of Crack Formation at the Edge of 85% CR and RTR Zircaloy-2

On annealing the 85% CR and RTR zircaloy-2 at 400^{o} C for 30 minutes, ultrafine and nanocrystalline grains with average grain size of 150nm and 110 nm are formed, which are in tandem with the reported literature (Guo *et al*., 2012; Guo *et al*., 2012b; Zhao *et al*., 2006, Panigrahi *et al*., 2011). Annealing treatment of 85% CR zircaloy-2 at 400^{o} C for 30 minutes causes recrystallization leading to the formation of ultrafine and nanocrystalline grains (Humphreys *et al*., 2004). However, in RTR samples, dislocation annihilation occurs in the deformed grains. Dislocations rearrange themselves in the grains, which are already formed due to dynamic recovery, thus forming stress free ultrafine grains.

4.3.3.2 Texture Study

Bulk texture of mercury quenched zircaloy-2 is seen from **Figure 4.12** with {0002} and $\{01\bar{1}2\}$ plane orientation. It shows strong texture away from normal direction. Large volume fractions of {0002} basal grains are oriented towards 20^o to 40^o along the transverse direction from the normal direction. The same texture is also evident from EBSD data (Section 4.1 and 4.2). After 25% rolling, {0002} basal plane aligns parallel to normal direction with a little spread 30^o to 50^o towards the transverse direction. Rolling causes the sheet to get compressed in the normal direction. Hence, it is elongated towards the rolling direction and a little towards the transverse direction. During rolling, compressive forces act on the normal direction and small compressive force is exerted towards transverse direction. The basal pole always aligns parallel to the compressive forces (Murthy *et al*., 2006). In RTR and CR sample up to 25% reduction, $\{10\bar{1}2\}$ tensile twins are seen which orients softer orientation to harder orientation, as seen from **Figure 4.14(a-b)**. Generally, up to 17% strain $\{10\bar{1}2\}$ tensile twins and $\{10\bar{1}0\}$ prismatic slip play an important role in the deformation of zircaloy-2. Fewer fractions of tensile twins are due to initial texture of mercury quenched plate. Tensile twins orient softer orientation of crystal to harder orientation due to which work hardening is more up to lesser true strain (Mccabe *et al*., 2006). Deformation up to 25% rolling reduction is possible by tensile twinning and prismatic slip as observed in EBSD and pole **Figure**. Accumulation of grains towards transverse away from normal direction occurs in both RTR as well as CR condition, as evident from **Figure 4.15(a)** and **Figure 4.16(a)**. $\{01\bar{1}2\}$ pole is also getting textured towards the transverse direction.

On further increasing the thickness reduction up to 50% (0.69 true strain), split basal texture is formed, the crystal orientation in RTR condition is getting close to the normal direction (5^o to 30^o) as can be seen from **Figure 4.15(b)**. $\{01\bar{1}2\}$ pole is getting more textured towards the transverse direction. EBSD microtexture image shows that grains are elongated and are oriented towards basal plane as shown in **Figure 4.14(d)**. Due to high true strain i.e. above 0.5, {0002} basal slip gets activated as reported in the literature (Knezevic *et al*., 2013) and split basal texture in titanium also

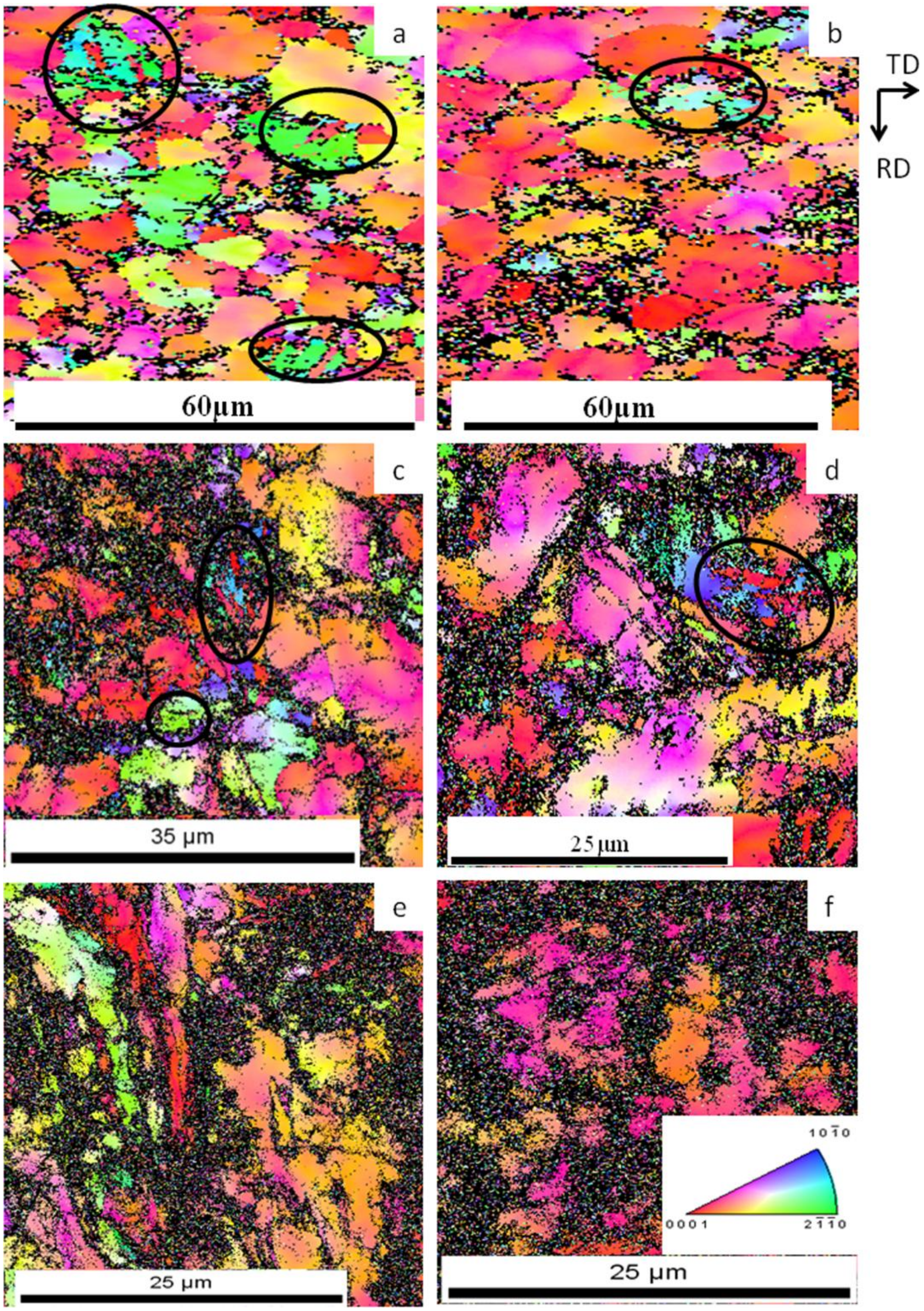

Figure 4.14 EBSD Image of **(a)** 25%, **(c)** 50% and **(e)** 75% CR Zircaloy-2, EBSD Image of **(b)** 25%, **(d)** 50% and **(f)** 75% RTR Zircaloy-2 with Circles Showing the Twins Formed after Deformation

explains that prismatic and pyramidal slip is active (Chun *et al*., 2005). Basal slip is unlikely when the ‘c’ axis is aligned towards the normal direction. Hence, activation of prismatic and pyramidal slip could be the reason for 50% rolling reduction in the alloy. In CR condition, the orientation of basal plane is more towards the transverse direction around 25^{o} to 30^{o} away from normal. At cryo temperature, CRSS of materials increases due to which larger value of stress is required for the movement of dislocations. Hence, softer grains deform easily, while in harder grains i.e. grains with near basal orientation does not deform. There is little split in $\{01\bar{1}2\}$ texture (**Figure 4.16(b)**). $\{11\bar{2}2\}$ compressive twinning in near basal grains (red) with purple color can be seen from **Figure 4.14(c)**. Although, from TEM results, no twinning was noticed but in EBSD results $\{11\bar{2}2\}$ compressive twinning is seen. At cryo temperature, deformation in zircaloy-2 only occurs by $\{10\bar{1}0\}$ prism slip, $\{10\bar{1}2\}$tensile twinning and $\{11\bar{2}2\}$ compressive twinning (Mccabe el. al., 2006; Knezevic *et al*., 2013; Mccabe *et al*., 2009).

After 75% thickness reduction (1.38 true strain) in RTR condition (**Figure 4.15(c)**), the {0002} texture is aligning close to the normal direction. The poles are getting closer to the normal direction due to prism slip, but pyramidal slip cause poles to move apart (Tenckhoff, 1988). A large lattice rotation of the basal plane can be seen due to activation of secondary twinning at room temperature. EBSD image shows that the grains are completely deformed but some of the grains having orientation near basal i.e. {0002} are not deformed completely (**Figure 4.14(f)**). It is because the ‘c’ axis always aligns parallel to the direction of maximum force and near basal grains is elastically harder (Sahoo *et al*., 2007). In CR condition (**Figure 4.16(c)**), {0002} texture is strong at 15^{o} to 20^{o} towards the rolling direction and around 30^{o} to 40^{o} towards transverse direction away from the normal direction. Since any slip system cannot cause such large lattice rotation of basal poles, it can only be due to activation of secondary twining. EBSD image (**Figure 4.14(e)**) shows that grains with basal orientation as well as some grains having near prismatic orientation are not deformed completely. It may be due to compressive twinning which orients basal planes away from normal direction and is not visible in EBSD because of step size (Mccabe *et al*., 2006). No evidence of basal and pyramidal slip has been found yet at cryo temperature (Mccabe *et al*., 2006; Knezevic *et al*., 2013; Derep *et al*., 1980). $\{01\bar{1}2\}$ pole in both RTR and CR sample is almost same i.e. towards transverse direction.

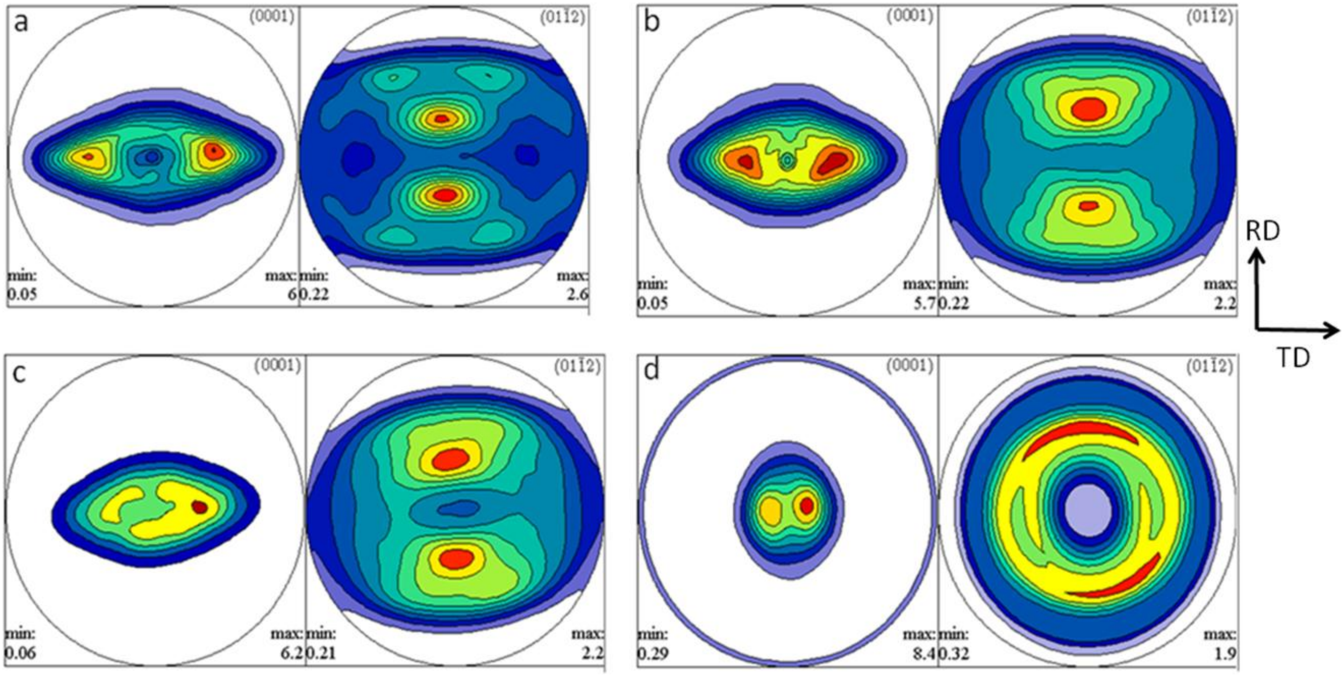

Figure 4.15 Texture {0002} and $\left\{01\bar{1}2\right\}$ Pole Figure of RTR Zircaloy-2 after **(a)** 25%, **(b)** 50%, **(c)** 75%, **(d)** 85% Thickness Reductions, respectively

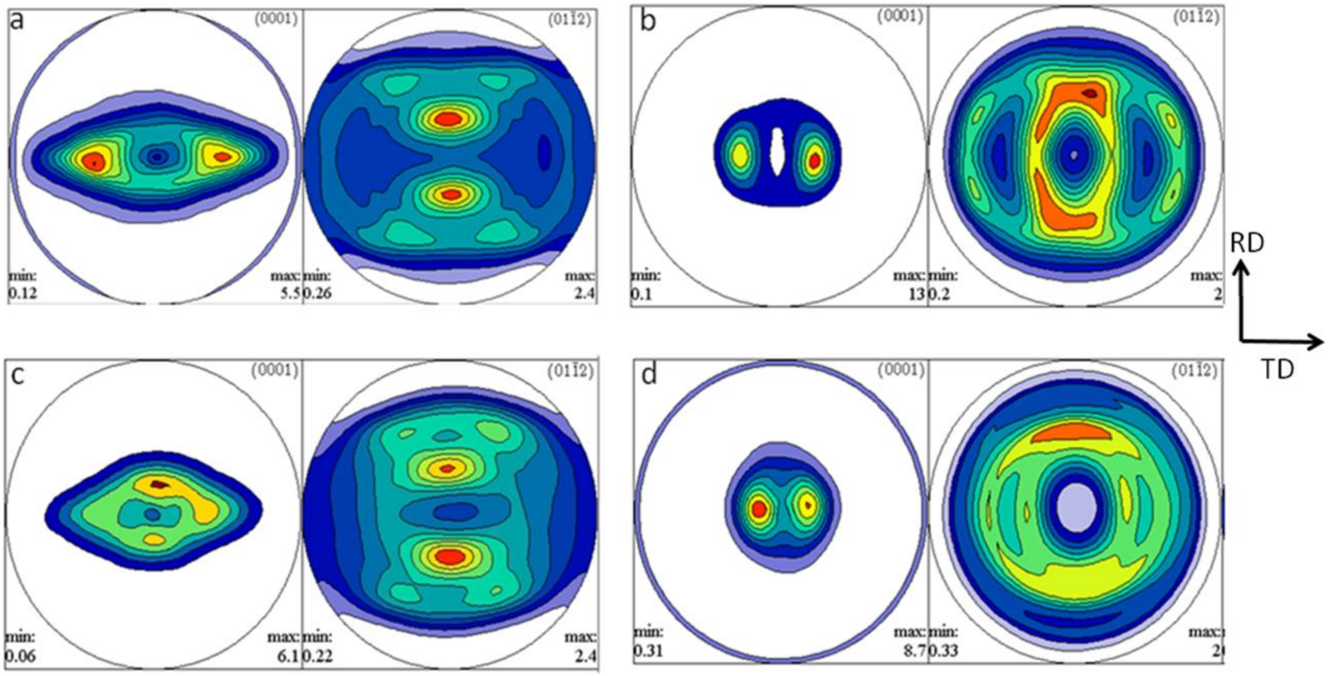

Figure 4.16 Texture {0002} and $\left\{01\bar{1}2\right\}$ Pole Figure of CR Zircaloy-2 after **(a)** 25%, **(b)** 50%, **(c)**75%, **(d)** 85% Thickness Reductions, respectively

On further increasing the thickness reduction to 85%, the {0002} texture in RTR condition is strong along 0^o to 15^o towards the transverse direction, as observed from **Figure 4.15(d)**. This is due to very high compressive forces exerted by the grains at room temperature and strain per pass has also increased as the thickness gets reduced to 0.6mm. The pole figure of 85% RTR sample clearly indicates the activation of basal, pyramidal and prismatic slip (Knezevic *et al.*, 2013). Although 75% RTR texture shows that secondary twinning is also responsible to obtain the 85% RTR texture. In case of CR samples, the texture is strong 15^o to 20^o from normal to transverse direction as seen from **Figure 4.16(d)**. The deformation is only possible by prismatic slip and compressive twinning in 85% CR zircaloy-2 (Mccabe *et al.*, 2006).

After 85% thickness reduction, annealing was performed at 400^o and 450^o C for 30 minutes due to which grain refinement has occurred. Annealing at 400^o C is better condition as it imparts higher tensile strength and ductility to the alloy. The {0002} and $\{01\bar{1}2\}$ texture of annealed RTR and CR zircaloy-2 can be seen from **Figure 4.17(a-d)**. It reveals that texture is moving away from the normal direction showing the effect of recrystallization on the grains. Even on increasing temperature, $\{01\bar{1}2\}$ texture is expanding. In RTR condition, the texture orientation is very close to the normal direction, while in CR condition, texture is strong away from the normal direction lying towards transverse direction and spreading slightly towards the rolling direction with increase in annealing temperature. In both RTR and CR condition, texture is getting stronger with increase in annealing temperature. $\{01\bar{1}2\}$ texture in CR zircaloy-2 is not spread much as compared to RTR after annealing. After annealing, $\{11\bar{2}0\}$ plane became parallel to the rolling direction in CR as well as in RTR condition (Tenckhoff, 1988).

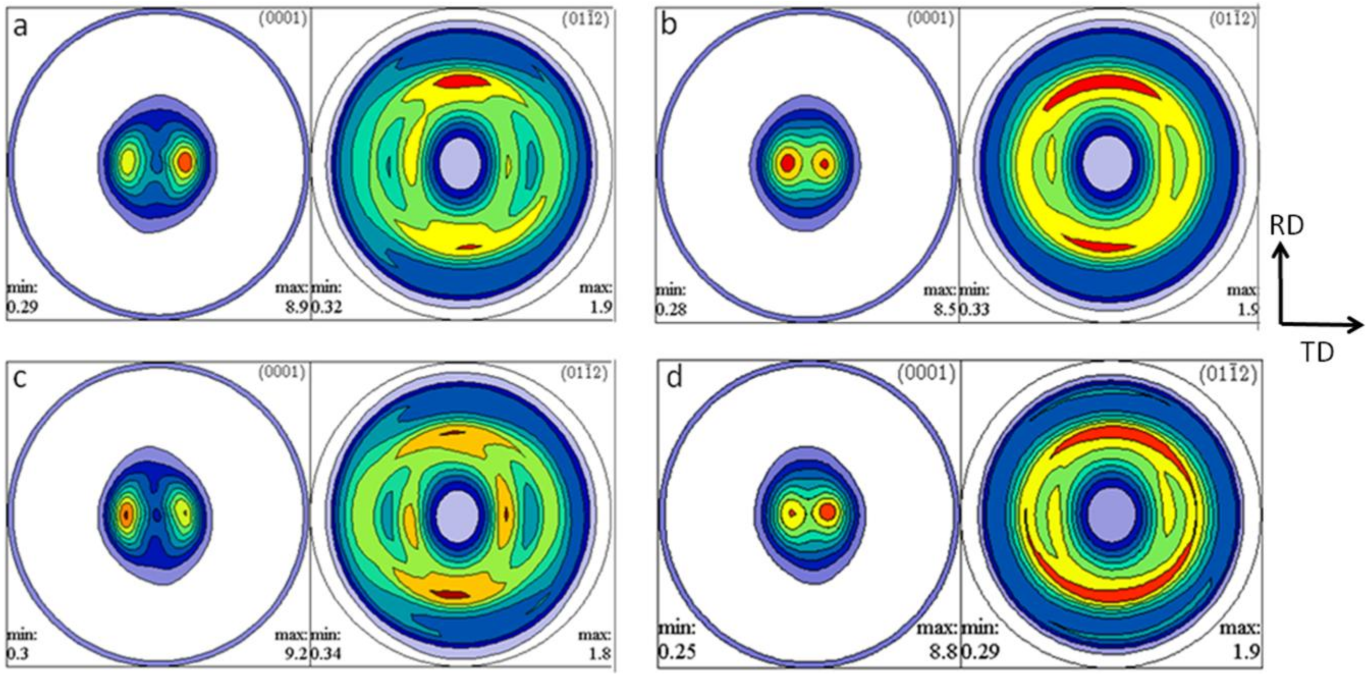

Figure 4.17 Texture {0002} and $\left\{01\bar{1}2\right\}$ Pole Figure of Annealed Zircaloy-2 after **(a)** 85% CR Annealed at 400^{o}C, **(b)** 85% RTR Annealed at 400^{o}C **(c)** 85% CR Annealed at 450^{o}C and **(d)** 85% RTR Annealed at 450^{o}C Zircaloy-2

4.3.3.3 Mechanical Behaviour

Deformation of zircaloy-2 by cryorolling causes increase in yield and tensile strength due to the accumulation of dislocations inside the crystals. The difference between yield strength and tensile strength gets reduced with increasing strain due to increase in strain hardening. It decreases the plasticity in the material and hence yield strength reaches closer to the tensile strength. In CR condition, tensile and yield strength (891MPa and 835 MPa) increment is much more as compared to RTR condition (679 MPa and 666 MPa). It is due to the suppression of dynamic recovery in the former as compared to the latter (**Table 4.1(a and c)**) (Panigrahi *et al*., 2011). At room temperature, dynamic recovery occurs due to which tensile strength becomes less as compared to CR condition.

Table 4.1(a) Mechanical Properties of CR and Annealed Zircaloy-2 in Rolling Direction, **(b)** Mechanical Properties of CR and Annealed Zircaloy-2 in Transverse Direction, **(c)** Mechanical Properties of RTR and Annealed Zircaloy-2 in Rolling Direction, **(d)** Mechanical Properties of RTR and Annealed Zircaloy-2 in Transverse Direction

A	Hardness (Hv)	Tensile strength (MPa)	Yield strength (MPa)	% elongation at break
Mercury Quenched	182	499	331	25
25% CR	208	638	541	8.55
50% CR	225	724	625	5.625
75% CR	257	800	765	5,07
85% CR	282	891	835	4.1
25% CR Annld	208	615	535	12
50% CR Annld	225	673	604	11
75% CR Annld	257	750	694	9.6
85% CR Annld	282	841	747	9.5

B	Hardness (Hv)	Tensile strength (MPa)	Yield strength (MPa)	% elongation at break
Mercury Quenched	182	499	331	25
25% CR	208	673	595	10.7
50% CR	225	749	666	8.025
75% CR	257	875	820	6.41
85% CR	282	967	931	5.1
25% CR Annld	208	620	562	14.4
50% CR Annld	225	721	602.5	11.5
75% CR Annld	257	862	801	11.4
85% CR Annld	282	931	878	11.2

C	Hardness (Hv)	Tensile strength (MPa)	Yield strength (MPa)	% elongation at break
Mercury Quenched	182	499	331	25
25% RTR	206	512	444	9.5
50% RTR	223	541	508	7.25
75% RTR	247	591	541	6.4
85% RTR	269	679	666	5.5
25% RTR Annld	206	505	421	12.4
50% RTR Annld	223	519	486	10.5
75% RTR Annld	247	579	516	7.5
85% RTR Annld	269	664	634	6

D	Hardness (Hv)	Tensile strength (MPa)	Yield strength (MPa)	% elongation at break
Mercury Quenched	182	499	331	25
25% RTR	206	546	481	10
50% RTR	223	557	519	7.45
75% RTR	247	607	577	6.5
85% RTR	269	697	688	5.6
25% RTR Annld	206	524	447	12.5
50% RTR Annld	223	543	472	10.8
75% RTR Annld	247	594	543	8.1
85% RTR Annld	269	674	653	7.2

After annealing, ductility of the CR zircaloy-2 is 9.5% and 11.2% in rolling and transverse direction, respectively. It is much more than RTR alloy with 6% and 7.2% ductility in rolling and transverse direction, respectively (**Table 4.1(a, b, c and d)**). The ductility of CR and RTR zircaloy-2 sample increases because of rearrangement of dislocations during annealing regains strain hardening capacity of the alloy, which delays necking. The dislocation density inside CR sample is much higher than that of RTR zircaloy-2. The presence of high fraction of undeformed grains as compared to RTR imparts higher ductility to CR zircaloy-2. However, in RTR condition, annihilations of dislocations during deformation and undeformed grains with near basal orientation are responsible for ductility (**Figure 4.14(f)**).

In transverse direction, the tensile strength (697 MPa and 967 MPa) as well as ductility (5.7 % and 5.1 %) of zircaloy-2 is more in both RTR and CR condition, respectively, as compared to their values in rolling direction (679 MPa with 4.1% ductility and 891 MPa with 5.5 % ductility. It is because of most of the crystal alignment is between 20^o to 40^o towards the transverse direction away from the normal direction. If 'c' axis of the crystal is perpendicular to the loading direction, $\left\{10\bar{1}0\right\} < 11\bar{2}0 >$ (prism slip) having 6.4 N/mm^2 CRSS under compression is active and if the 'c' axis is parallel to the loading direction, $\left\{10\bar{1}2\right\}$ tensile twining having 9.6 N/mm^2 CRSS and $\left\{11\bar{2}1\right\}$ twinning is active with twice the strength as compared to the perpendicular case. Also, twinning can facilitate deformation by reorienting crystal for slip as reported in the literature (Ballinger *et al.*, 1981; Tenckhoff, 1988; Murthy *et al.*, 2006). Hence, during loading in the transverse direction, both twinning and slip is active due to which ductility is more while more strength is imparted by twinning (Ballinger *et al.*, 1981). In the rolling direction, the crystal is oriented perpendicular to the loading direction, which results in less strength and ductility because only prism slip is active (Ballinger *et al.*, 1981).

4.3.4 Summary

The zircaloy-2 was processed by cryorolling and room temperature rolling and its influence on microstructural characteristics, texture, and mechanical properties of the alloy was investigated in the present work. The following conclusions are made:

- Due to initial texture, deformation up to 25% RTR and CR zircaloy-2 is possible due to tensile and compressive twinning. Deformation up to 50% rolling reduction is achieved by prismatic and pyramidal slip in RTR, while compressive twinning and prismatic slip occurs in 50% CR zircaloy-2.

- Further deformation i.e. above 50% occurred due to the activation of prismatic, basal and pyramidal slip along with compressive and tensile twinning in RTR sample, while in CR, deformation is possible by prismatic slip, tensile twinning and compressive twinning.

- The tensile strength and ductility of CR zircaloy-2 is found to be 891 MPa and 4.1 %, respectively, as compared to the RTR zircaloy-2 (679 MPa and 5.5 %). The difference in observed mechanical properties of rolling and transverse direction of the sample is due to preferential inclination of ‘c’ axis of grain is 20^o to 50^o towards transverse in CR, while 10^o to 30^o towards transverse in RTR.

- 85% CR alloy upon annealing at 400^o C for 30 minutes shows higher ductility (9.5 and 11.2 in rolling and transverse direction, respectively, due to mobile dislocation after annealing.

4.4 Development of Ultrafine Grained Zircaloy-2 by Room Temperature and Cryo Cross Rolling

4.4.1 Introduction

Schmid factor is an important parameter, a link between applied stress to the critically resolved shear stress on a specific slip system. It is a relation between the applied loading directions to the slip direction of a crystal, given by the relation "**cosφcosα**" in which "**φ**" is the angle between slip direction and loading axis while "**α**" is the angle between slip plane normal and loading axis (Takayama *et al.*, 2004). The slip system with the highest Schmid factor would operate first. During plastic deformation, reorientation of the crystal occurs leading to texture development in the alloy, which affects mechanical behavior of the material and thus promotes anisotropy in property (Barrett *et al.*, 1966). In addition to texture, grain size influences the strength of the zircaloy-2 in accordance with the Hall-Petch effect. The individual grains behave independently within polycrystalline materials during plastic deformation as reported in the literature (Cox *et al.*, 1937). This causes difference in the mechanical properties predicted by using theoretical and experimental results (Cox *et al.*, 1937). Taylor found that during deformation, each crystal behavior depends on the neighboring crystal and a Taylor factor, 'M' was derived relating the applied stress and CRSS. This factor is widely used to predict the texture formation due to polycrystalline deformation (Takayama *et al.*, 2004; Bunge *et al.*, 1970; Shen *et al.*, 2013), which is defined as

$$M = \frac{\sigma_y}{\tau_0} \tag{4.3}$$

Where 'M' is Taylor factor depends on crystal orientation, σ_y represents yield strength of the sample and τ_0 represents CRSS of the activated slip system.

The stored strain energy inside low carbon steel upon plastic deformation depends on the crystal orientation, which results in recrystallisation texture as reported in the literature (Hutchinson 1984). The stored strain energy of deformed materials are estimated by using the techniques such as calorimetric and diffraction (Matsuo *et al.*, 1971; Averbach *et al.*, 1956). Diffraction method is further divided into X-rays line broadening and orientation distribution function (Every *et al.*, 1974; Kalland *et al.*, 1984). The relation between stored strain energy and Taylor factor has shown that the stored energy increases with increase in Taylor factor with some exception (Taheri *et al.*, 2006;

Godfrey *et al.*, 2005). There is no reported study on effect of cross rolling on texture, stored strain energy, microstructure and mechanical properties of zircaloy-2. Therefore, the present work has been focused to study the texture, microstructure, and mechanical properties of zircaloy-2 processed by room temperature cross rolling (RTCR) and cryo cross rolling (CCR). The Schmidt and Taylor factor of the deformed alloy was estimated to substantiate the formation of texture and stored strain energy, respectively.

4.4.2 Experimental Procedure

Zircaloy-2 was initially obtained in the form of 4 mm thick rolled sheet from Nuclear Fuel Complex, Hyderabad India. The chemical composition is shown in **Table 3.1** in **Chapter 3**. Small samples of 5 x 3 cm were cut and solutionised by heat treating them at 800^{o} C in argon environment, followed by quenching at room temperature in mercury. Solutionised samples were then surface ground and washed in methanol. Cross rolling of the alloy was performed at room temperature by simultaneously changing the axis by 90^{o} after every pass. To perform room temperature cross rolling s, the sample was dipped in water after every pass, so as to maintain the temperature of zircaloy-2 in between 23^{o}- 27^{o} C. Cross rolling at room temperature and cryo temperature is performed by changing the orientation by 90^{o} in every pass as shown in **Figure 4.18**. The samples were dipped in liquid nitrogen for 10 minutes before each pass so as to attain cryo temperature inside the samples. Liquid nitrogen was continuously poured over the rollers to attain cryo temperature in rollers. With every pass, a reduction varying from 0.2mm to 0.05mm was given. The reduction was reduced accordingly, with the change in thickness of the samples. The lab scale rolling mill with 8 rpm speed and 110 mm roller diameter has been used to perform cross rolling. To prevent friction losses, $MiSo_2$ was used as lubricant. Further characterization such as EBSD, TEM, Tensile test, XRD was performed, the procedure is discussed in detail in chapter 3.

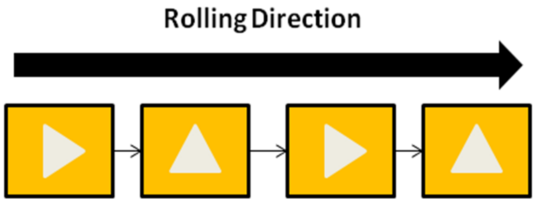

Figure 4.18 Schematic Diagram Showing the Cross Rolling Method

4.4.3 Results of Room Temperature Cross Rolled (RTCR) Zircaloy-2

4.4.3.1 Microstructure Study

The microstructure of rolled alloy is heterogeneous as can be seen from section 4.1. α phase with equiaxed grains (~ 10μm) were obtained after heat treating the sample at 800° C for 2 hours in argon environment followed by quenching it in mercury. The temperature of mercury rises to 70° C after quenching. Mercury quenching reduces the probability of hydride formation, which introduces cracks during loading and thus increases ductility up to 25% (Ostberg *et al.*, 1968). After solutionisation, tensile strength goes up to 499 MPa with an average grain size of 10 μm.

XRD peaks (reference pattern 98-007-1958) show the presence of α-phase in solutionised zircaloy-2. Rolling of the alloy leads to increase in dislocation density, which can be measured from XRD peak broadening through variance method (Borbely *et al.*, 2001; Groma, 1998; Sarkar *et al.*, 2008). Fourth order moment of the peak profile of the peaks with 2θ values at 34.79° and 47.87° were calculated to find the dislocation density ‹ρ› shown in **Figure 4.19**. The dislocation density calculated here can be compared to the initial mercury quenched sample. The dislocation density ‹ρ› of solutionised zircaloy-2 is 1.608687 x 10^{15} /m^2. After cross rolling at room temperature,

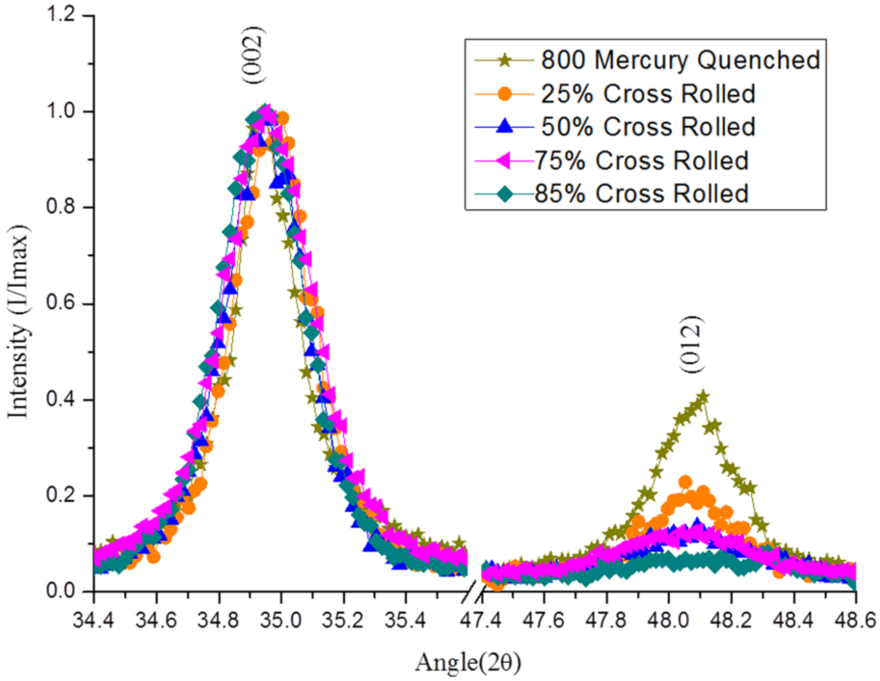

Figure 4.19 XRD Peaks of Mercury Quenched 25%, 50%, 75% and 85% RTCR Zircaloy-2

dislocation density ‹ρ› for 25%, 50%, 75% and 85% cross rolled zircaloy-2 is calculated to be 5.286423 x 10^{15} /m^2, 1.160324 x 10^{16} /m^2, 1.956432 x 10^{16} /m^2 and 2.806453 x 10^{16}/m^2, respectively.

4.4.3.2 Transmission Electron Microscopy (TEM)

TEM micrograph in **Figure 4.20(a)** reveals the formation of dislocation cells after 25% reduction in rolling as the dislocation is forming a net like structure due to which grain is divided into small segments (Hansen, 2001). Initially, during deformation, the dislocation get adhered near the grain boundary and further increase in plastic deformation results in the tangling of dislocations inside the crystals forming small boundaries, which are linked with each other. These are known as incidental dislocation boundaries (IDBs). Since the induced strain in the sample during rolling is less as compared to other SPD processes due to room temperature deformation, shear planes are not observed. Geometrically necessary Boundaries (GNBs), which are high angle boundaries from 15^o to $180^{o,}$ are formed near the grain boundary. IDBs are trapped inside the GNBs as reported in the literature (Hughes *et al.*, 2003; Liu *et al.*, 1995). With the increase in thickness reduction i.e., at 50%, dislocations content keep increasing and get trapped inside and near the boundaries of IDBs as can be seen from **Figure 4.20(b)**. The inset figure of selected area diffraction (SAD) pattern shows ring formation, which proves the presence of multiple grains, elongated discontinuous diffraction spots showing variation in lattice parameter as well dynamic recovery also. During rolling, all the work is not utilized to introduce dislocations inside the crystal, some of it is dissipated as heat, which causes dynamic recovery. After 75% reduction shown in **Figure 4.20(c)**, formation of nanostructured as well as ultrafine grains can be seen in the alloy. Hence, the IDBs have started orienting towards the macroscopic plastic flow due to which subdivision of the cells has started and thus forming a multimodal grain structure with nano and ultrafine grains. Due to the hexagonal crystal structure of zircaloy-2, grain formation is not symmetrical because of limited deformation mechanism in hexagonal crystal (Tenckhoff, 1988). Generally, grains having orientation near to basal i.e., {0002} normal to the rolling direction, does not deform because they are elastically harder (Sahoo *et al.*, 2007). Here, due to change in strain path, grains with {0002} basal orientation are getting fragmented, due to which ultrafine grains are formed even at lower strain. There are still grains which are bigger in size (µm) are seen from EBSD images. After 85% reduction, more cells

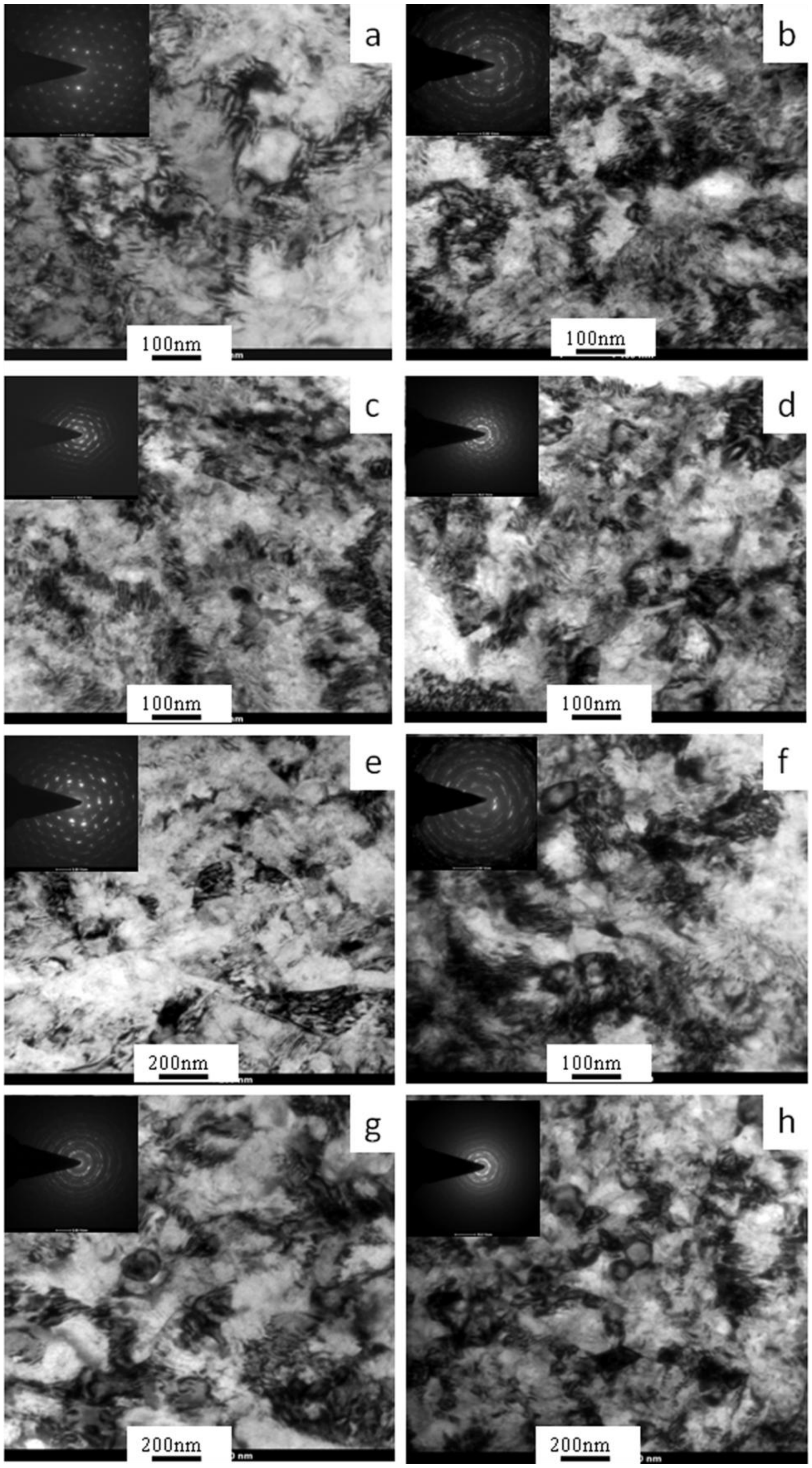

Figure 4.20 TEM Image of Cross rolled Zircaloy-2 after **(a)** 25%,**(b)** 50%,**(c)** 75% and **(d)** 85% Reduction, respectively. Effect of Annealing at 400^{o} C for 30 minutes after **(e)** 25%, **(f)** 50%, **(g)** 75% and **(h)** 85% Reduction, respectively

get oriented in macroscopic plastic flow, which results in increase in the fraction of nano and ultrafine grains. The average grain size obtained after 85% reduction is approx 180 nm, visible from **Figure 4.20(d)**. Inset SAD pattern also proves the presence of large number of grains in the captured area. The morphology obtained after 85% room temperature cross rolling is multi modal, which shows grains ranging from approx ≤ 50 nm to 6 µm. This imparts both high strength and ductility to the samples as discussed in mechanical properties.

Annealing of deformed alloy at 400^{o} C for 30 minutes proves to be helpful in removing internal strains and rearrangement of dislocations (Wang *et al.*, 2002; Guo *et al.*, 2012a; Guo *et al.*, 2012b). Due to plastic deformation, internal lattice strains are developed locally. On applying further strain over them, they move with the macroscopic plastic flow thus forming grains as explained above. Due to anisotropy in HCP crystal structure, there are some places inside the grains where the plastic flow is not possible due to which internal stresses remain as such inside the grains. The stored energy become high and provides the driving force for recrystallization. Both nucleation and grain growth therefore occurs at lower temperatures. Larger the strain causes increase in dislocation density, which serves as nucleation sites for the formation of fine grains in the alloy (Humphreys *et al.*, 2004). The grains which are already formed and having dislocation trapped inside them, their size gets increased and dislocations rearrange themselves after annealing. It is evident from **Figure 4.20(e-h)** that the recrystallisation increases with increasing strain causing high grain refinement in the materials. The 85% cross rolled annealed sample has an average grain size of 156 nm.

4.4.3.3 Mechanical Properties

The effect of RTCR on the mechanical properties of zircaloy-2 can be seen from **Figure 4.21**. With the decrease in thickness after RTCR, the dislocation density in the material gets enhanced. During deformation, the dislocations are generated and move in different direction inside the slip planes such as $\{10\bar{1}0\}$ prismatic, {0002} basal slip, which are active with respect to the applied strain. At room temperature, prismatic slip $\{10\bar{1}0\}$ in $\langle 1\bar{2}10\rangle$ direction is observed (Tenckhoff, 1988; Monnet *et al.*, 2004). Above 0.5 true strain, {0002} basal slip gets activated (Knezevic *et al.*, 2013). The moving dislocation gets tangled with each other due to which GNBs and IDBs are formed. With repeated plastic deformation, dislocation density becomes so high that further plastic deformation is not possible due to which material behave like brittle material imparting high strength and less ductility to the material. The formation of ultrafine and nano grains as seen in TEM image provide strength to RTCR zircaloy-2. Due to change in strain path during rolling, the dislocation density is higher as compared to normal rolling. The tensile strength of the cross rolled alloy is found to be 991 MPa, which is 98% higher than the mercury quenched alloy and 42% higher than the RTR alloy with 85 % thickness reduction . The ductility of RTCR alloys is 7.5%, which is 36% higher than the RTR alloy. The increase in ductility is due to the multimodal grain structure consisting of coarser, ultrafine, and nano grains. In addition to this, the movement of preexisting dislocation at higher value of stress applied during tensile loading also causes improvement in ductility (Monnet *et al*., 2004; Li *et al*., 2009; Gurao *et al*., 2009).

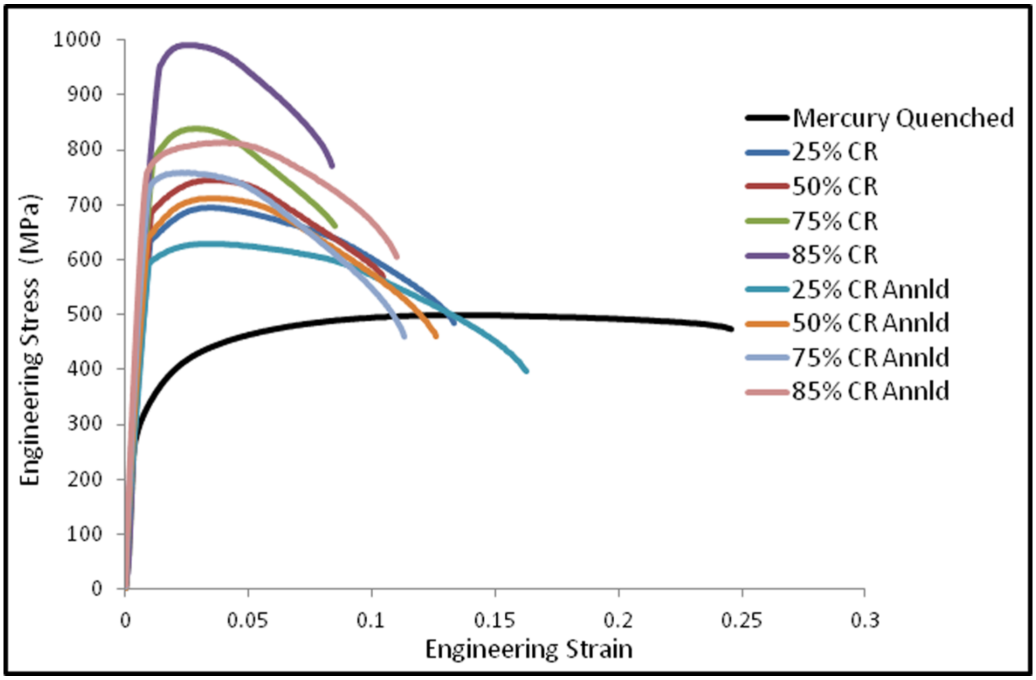

Figure 4.21 Effect on Mechanical Properties after RTCR and Annealing at 400^{o} C for 30 minutes

Annealing of the RTCR alloy at 400^{o} C for 30 minutes increases its ductility. Annealing a deformed material at optimized temperature increases the number of nucleation sites for recrystallization, causing the formation of ultrafine and nanocrystalline grains in the alloy. Anisotropy in hexagonal crystal is helpful in producing multimodal grain structure as some grains did not deform completely. After annealing 85% RTCR zircaloy-2, 46% increment in ductility (11%) is observed with a tensile strength of 812 MPa. The increase in tensile strength (812 MPa) as compared to solutionised sample (499 MPa) is due to the formation of ultrafine and nanocrystalline grains in the alloy.

4.4.3.4 Micro Texture Study

EBSD images of the deformed grains after 25%, 50% and 75% cross rolled zircaloy-2 and their respective pole figures can be seen from **Figure 4.22(a, b and c)**. Confidence index (CI) less than 0.03 has been excluded from the image so that the deformed area can be seen as white. As it has already been discussed in the experimental details that the plate is already rolled. The initial texture of the plate is basal. With increase in thickness reduction, the deformed grains are increasing in the sample. In 25% cross rolled zircaloy-2, extension twins of $\{10\bar{1}2\}$ plane in $\langle\bar{1}011\rangle$ direction are observed in grains having orientation near to $\{2\bar{1}\bar{1}0\}$ plane**.** $\{10\bar{1}2\}$ extension twins are formed extensively below 17% of deformation (Mccabe *et al*., 2009).

The $\{10\bar{1}2\}$ extension twins are efficient in accommodating strain as they reorient itself from soft to hard orientation as can be seen from **Figure 4.22(a)**. Some grains can be seen inside them the colour is changing which shows large misorientation inside the grain due to slip activity. The pole figure {0002} in **Figure 4.22(a)** indicates no twins as the fraction of these extension twins are very less. As in normal rolling, extension twins are formed up to 17% strain, due to the change in strain path. Large fractions of grains are oriented 30^o to 40^o towards the rolling direction. This happens due to the change in strain path as c-axis is always inclined perpendicular to the applied force (Tenckhoff, 1988).

After 50% thickness reduction, mostly all the grains show near basal orientation and no extension twins are seen, although traces of them are seen. The basal plane orientation is always perpendicular to the direction of load and the twinning reaches a transition as they orient the plane from soft orientation to the hard one as explained above. Twins can also be helpful in providing orientations, which may cause further slipping (Tenckhoff, 1988). Many grains having grain size equivalent to 10 µm can be seen as their orientation is near basal, due to which they are elastically harder (Sahoo *et al*., 2007). These near basal oriented grains are non deforming and non fragmenting. They do not deform because near basal dislocation in near basal orientation pin other dislocations, which result in no change in the dislocation density (Sahoo *et al*., 2010). Although in some of these near basal grains, large misorientations are found as the color in some grains is changing (**Figure 4.22(b)**). The reason can be the change in strain path due to which resultant load over the crystal is varying with each pass, thus causing deformation even in near basal grains. The {0002} basal pole are getting close, which also represents the activation of basal slip. The pole figure $\{10\bar{1}0\}$ reveals the orientation of the prism plane towards the rolling direction as in normal room temperature rolling (Tenckhoff, 1988).

During RTCR, strain path is changing in every pass. Also, after a particular reduction in thickness, all the grain orientation becomes near basal. It leaves only larger grains, which do not deform and have near basal 20^{o}-40^{o} orientation. Due to RTCR with the change in strain path, these near basal grains get deformed as the direction of force is changing (**Figure 4.22(c)**). It leads to increased dislocation density (2.806453 x $10^{16}/m^{2}$) as well as the tensile strength (991 MPa) of the alloy. Even misorientation can also be seen inside these near basal grains, which mean that more reduction up to 85% causes deformation of almost all the grains and those left would contain very large dislocation density inside them. These completely deformed grains after annealing at some optimized temperature can produce large volume of ultrafine grains with high strength and ductility. Even upon comparing **Figure 4.22(b)** and **Figure 4.22(c)**, it can be seen that the near basal grains in **Figure**. 4.22(b) has a larger size than **Figure 4.22(c)**, proving the above explanation. {0002} pole figure also shows grains having c-axis parallel to the normal direction are left, as others are deformed completely as seen in **Figure 4.22(c)**. The $\{10\bar{1}0\}$ pole figure shows the orientation is distributed towards both the rolling directions. Change in grain size at different rolling reduction can be seen from **Table 4.2**.

Table 4.2 Grain Size after Different Rolling Reduction

	Grain size undeformed area (EBSD)
25% RTCR	9.5 µm
50% RTCR	8 µm
75% RTCR	6.5 µm

Microstructure of 25%, 50% and 75% thickness reduced cross rolled zircaloy-2 along with their misorientation graph can be seen from **Figure 4.23(a, b and c)**. Misorientation less than 2^{o} is assumed as dislocation, 2^{o} to 15^{o} as low angle grain boundaries, which is IDBs and misorientations between 15^{o} to 180^{o} is high angle grains boundaries i.e., GNBs. After 25% reduction in thickness, it

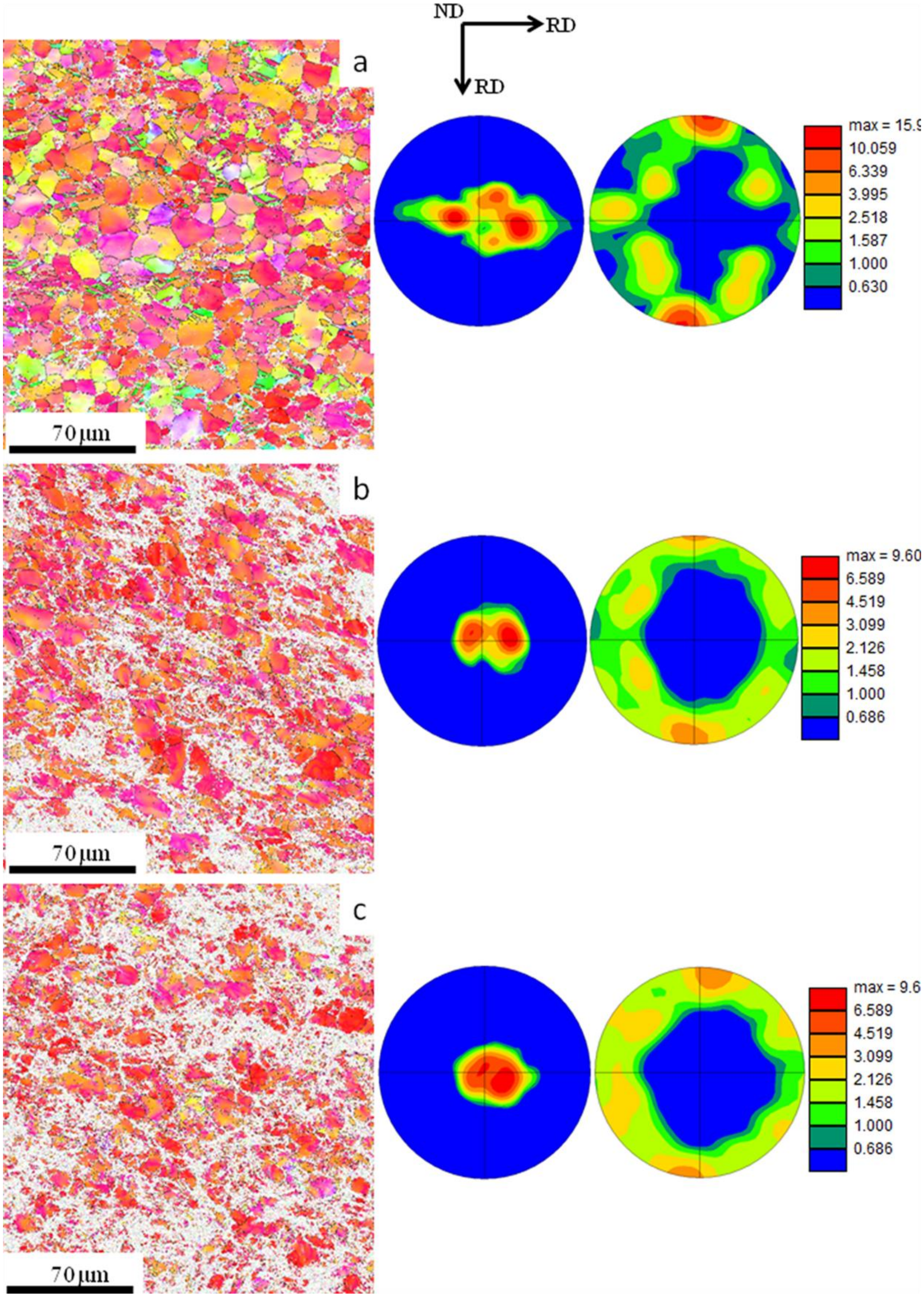

Figure 4.22 EBSD Image for **(a)** 25%, **(b)** 50% and **(c)** 75% RTCR Zircaloy-2. A Minimum Confidence Index (.03) is taken to show the Completely Deformed Portion as White, along with their Pole Figure, respectively

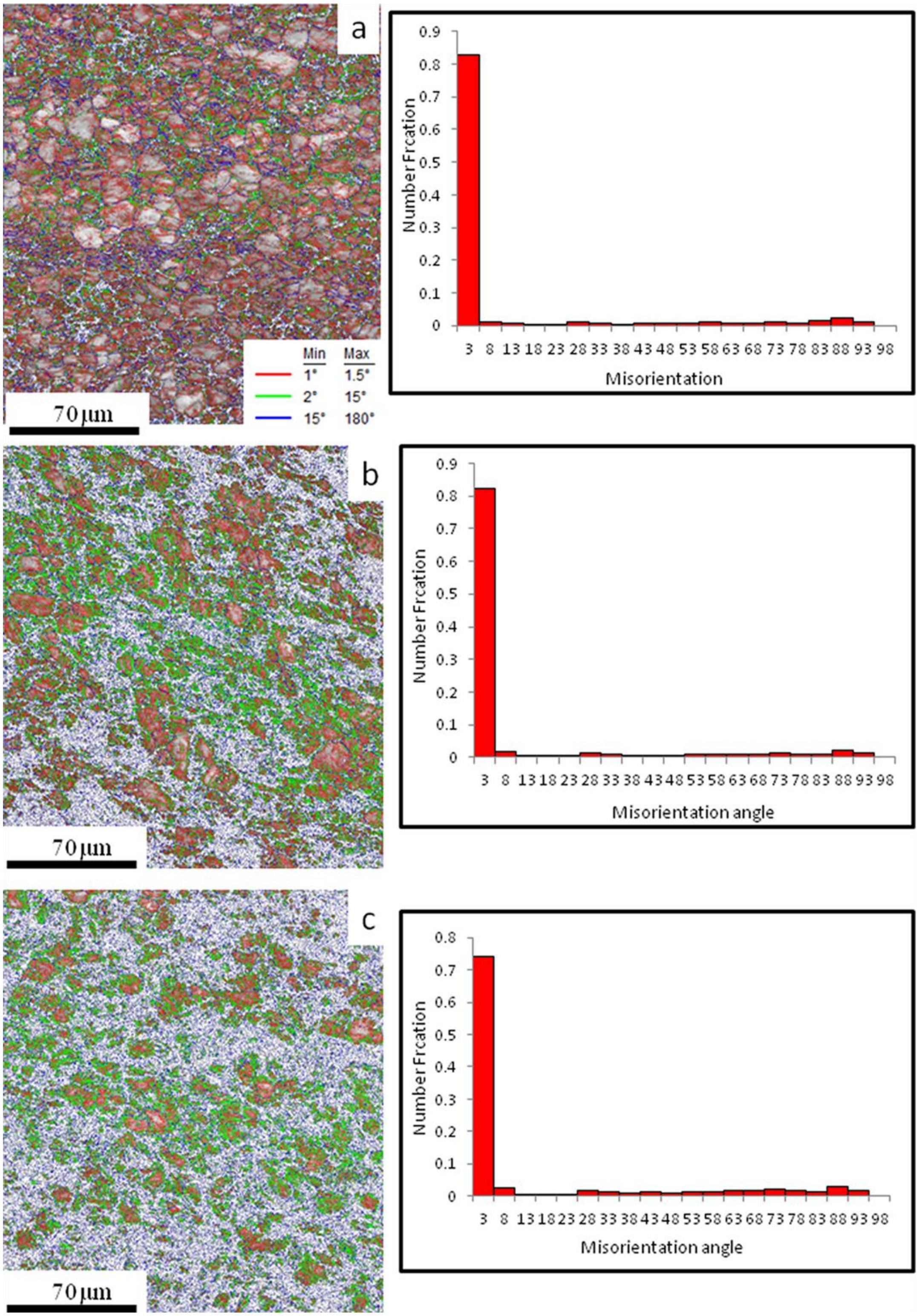

Figure 4.23 Fraction of Low and High Angle Grain Boundaries of **(a)** 25%, **(b)** 50% and **(c)** 75% RTCR Zircaloy-2 and their Misorientation Graph, respectively

can be seen from **Figure 4.23(a)** that there are some grains inside them with less dislocations, showing no deformation inside the crystal. This is near basal grain having orientation {0002}, which are non deforming and non fragmenting (Sahoo *et al.*, 2010). Only the softer grains get deformed first when the strain is less. It is seen that the fraction of low angle grain boundaries is more, which is due to deformation of softer grains. At 50% reduction in thickness, it is evident from **Figure 4.23(b)** that some of the undeformed near basal grains have dislocations inside them and IDBs are found near the grain boundary. This phenomenon of grain fragmentation has started due to the change in strain path already explained above. Comparison of the misorientation graphs of **Figure 4.23(a) and 4.23(b)** reveals that difference in the fraction of low angle grain boundaries is less, which is due to the formation of dislocations in near basal grains. However, the formation of ultrafine grain formation has already started as shown in **Figure 4.21(b)**.

After 75% reduction in thickness, it can be clearly seen from **Figure 4.23(c)** that grain fragmentation of near basal grain is taking place due to which the grain size of unreformed grain is reduced as well as large dislocations are formed inside the crystal. IDBs are formed near the grain boundary, which after dynamic recrystallisation are transforming to ultrafine and nanocrystalline grains. It can be observed from misorientation graph that fraction of high angle grain boundaries is not increasing even after 75% reduction, which proves the fragmentation of near basal grains due to change in strain path.

4.4.3.5 Dislocation Distribution

Kernel average misorientation (KAM) map is a tool in OIM analysis that can be used for estimating localized dislocation distribution in different grains of deformed material. Generally, distribution is in such a way that when the misorientation value is >1, high density of dislocation are present shown by light green colour, if >3, very high density of dislocations are present indicated by red colour. Undeformed grains are identified when misorientation is <1 shown by dark blue colour. From **Figure 4.24(a)**, 25% cross rolled zircloy-2, it is seen that the dislocation density is not evenly distributed as completely deformed part is having red colour, high dislocation density can be seen in grains, which are oriented along near prismatic planes i.e., $\{10\bar{1}0\}$ and $\{2\bar{1}\bar{1}0\}$ plane. As near basal grains are harder as compared to prismatic grains, the latter get deformed. After 50% thickness reduction, near basal grains shows dislocations near the boundary of the grains. It is due to the change in strain path during rolling, which leads to fragmentation of near basal grains. After 75%

thickness reduction, it is evident from **Figure 4.24(b) and (c)** that the undeformed grains seen in 50% thickness reduced zircaloy-2 have become small now. Some of the undeformed grains have large dislocation density inside them, undergo fragmentation upon 85% thickness reduction. The misorientation curve (**Figure 4.24(d)**) shows that initially at 25% reduction, misorientation is less than 1, while as the reduction is increasing, the KAM has been moving towards 5%, which shows that residual plastic strain is getting higher with the reduction in thickness.

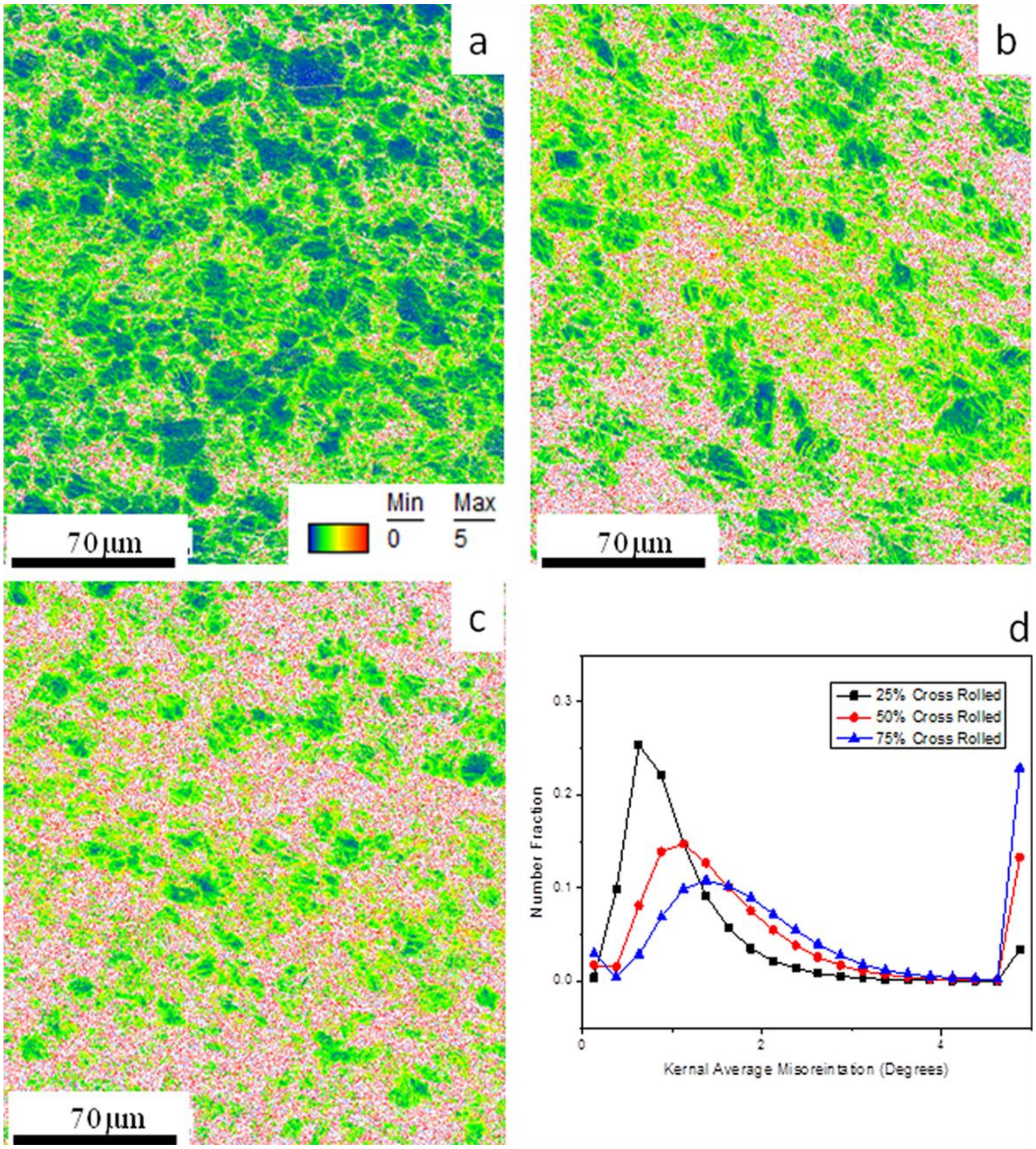

Figure 4.24 KAM of **(a)** 25%, **(b)** 50% and **(c)** 75% RTCR Zircaloy-2, **(d)** KAM Misorientation Graph, respectively

4.4.4 Comparison of Cryo Cross Rolled (CCR) and Room Temperature Cross Rolled (RTCR) Zircaloy-2

4.4.4.1 Transmission Electron Microscopy (TEM)

The TEM micrograph of 25% CCR is shown in **Figure 4.25(a)**. Dislocation cells with dislocation inside can be seen after 25% reduction of the alloy. At cryo temperature, dislocations formed are not able to neutralize due to which dislocation cells of very small size are formed and even some dislocations are also trapped inside them. The dislocation cells are low angle grain boundaries, which are also called incidental dislocation boundaries (IDBs). Since the true strain is very less, geometrically necessary boundaries (GNB) are not observed in CCR samples. When the strain is increased to 50%, dislocation density inside the cells has increased.

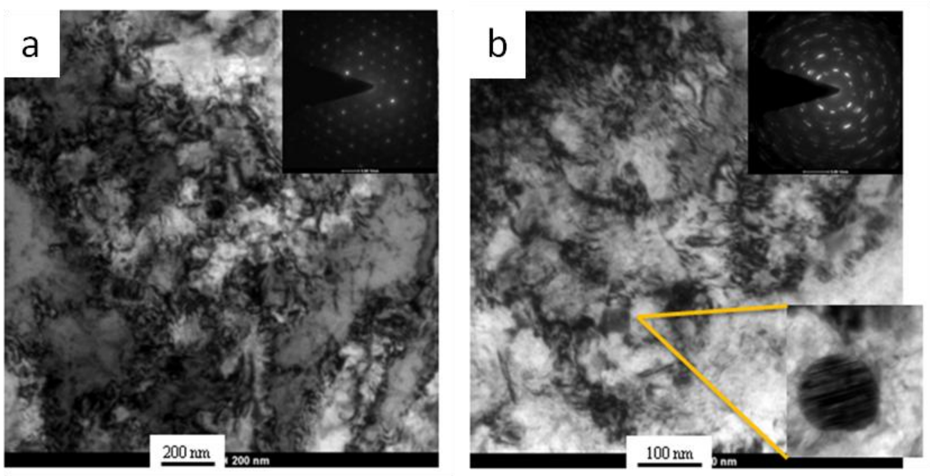

Figure 4.25 TEM Image of CCR Zircaloy-2 after **(a)** 25% and **(b)** 50% Reduction, respectively

In 50% CCR sample, ultrafine grains have formed in some locations due to change in orientation because of macroscopic plastic flow of the dislocation cells and stacking faults are observed as shown in inset of **Figure 4.25(b)**. RTCR zircaloy-2 after 50% strain showed dislocation cells with dislocations trapped inside these cells. Ultrafine grains are also formed in the alloy due to macroscopic plastic flow of dislocation cells stated above. Inset of **Figure 4.26(a)** shows selected area diffraction (SAD) pattern, which proves grain formation, while the elongated pattern shows the variation in lattice parameter. Further reduction up to 85% is possible only in RTCR sample as high CRSS of CR alloy causes cracking after 50% thickness reduction.

Annealing the rolled samples at 673K for 30 minutes leads to rearrangement of dislocation, which facilitates the nucleation of grains inside the crystals shown in **Figure 4.26(a-b)**. The internal stress inside the crystals increases with increasing plastic strain and it is developed locally due to the HCP structure and orientations of crystals. Annealing at low temperature provides the driving force for the nucleation of deformed grains in these places. The grains which are already formed due to dynamic recrystallisation transformed in to dislocation free grains upon annealing treatment. In 25% CCR sample, grains with low angle grain boundaries are observed (**Figure 4.26(a)**). The formation of ultrafine grains has increased with increasing strain followed by annealing as evident from **Figure 4.26(a-b)**.

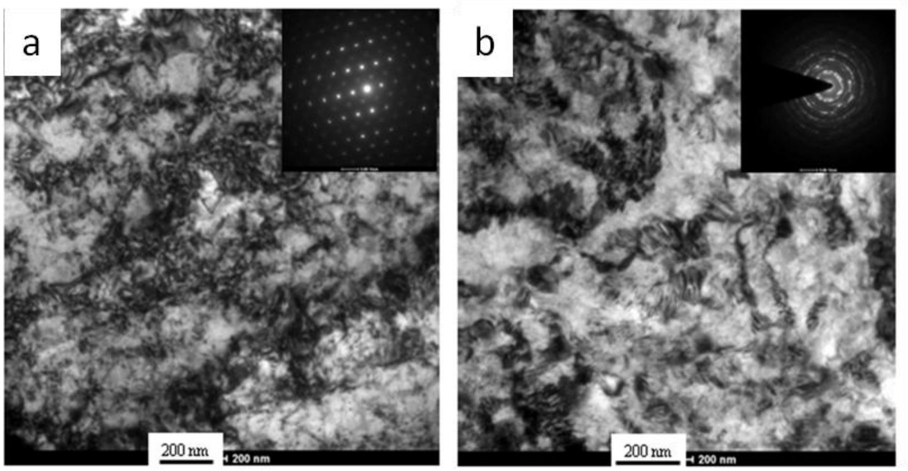

Figure 4.26 TEM Image of CCR Zircaloy-2 after **(a)** 25% and **(b)** 50% Reduction, respectively

4.4.4.2 Mechanical Properties

Mechanical properties upto 50% thickness reduction of CCR and RTCR is compared and shown in **Table 4.3**. When zircaloy-2 is deformed, the movement of slipping planes takes place due to which dislocations are generated. With every pass during cross rolling, the strain path and loading direction over the crystal get changed due to which more defects are generated. Due to suppression of dynamic recovery at cryo temperature, dislocation density becomes more in the crystals as compared to normal cryo rolling. CCR showed substantial improvement in strength compared to RTCR alloy due to its higher dislocation density achieved through suppression of dynamic recovery. The change in strain path during each pass also induces more plastic strain inside the crystals and therefore only for 50% reduction in thickness, the formation of ultrafine and nano grains has occurred inside the matrix, which are not observed for normal CR alloy. Large dislocation densities as well as ultrafine grains are responsible for strain hardening of the alloy. At cryo temperature, thickness reduction beyond 50% was not achieved due to fracture of samples owing to high CRSS. Tensile strength of 50% CCR was found to be 786 MPa with 8.7% ductility while the RTCR alloy showed strength of 727 MPa with 10.45% ductility at break. The strength and ductility of RTR zircaloy-2 after 85% reduction, showed 13% and 36% lesser, respectively, as compared CCR condition. The tensile strength and ductility of RTR alloy was less by 6.0% and 47.0 %, respectively, as compared to RTCR alloy in the present work. The increase in ductility may be due to multimodal grain structure and movement of preexisting dislocation at higher stress (Monnet *et al.*, 2004; Li *et al.*, 2009; Gurao *et al.*, 2009).

Table 4.3 Mechanical Properties of Zircaloy-2 after Cross Rolling

	Hardness(HV)	Tensile Strength(MPa)	Yield strength (MPa)	% elongation at break
Mercury Quenched	182	499	331	25
25% RTCR	211	693	632	13.3
50% RTCR	233	727	684	10.45
25% CCR	215	734	698	10.2
50% CCR	237	786	753	8.7
25% RTCR Annld	211	628	592	16.2
50% RTCR Annld	233	710	634	12.5
25% CCR Annld	215	659	621	12.8
50% CCR Annld	237	735	703	9.8

Annealing at 673K for 30 minutes results in nucleation and grain growth in deformed zircaloy-2 thus, forming ultrafine and nanocrystalline grains. Due to limited slip system in HCP crystals, the grain growth is not uniform inside the crystal, which leads to the formation of multimodal grain structure in the alloy. Annealing at low temperature improves the ductility without the drop in strength. The improvement in ductility of 50% CCR zircaloy-2 was 9.8% while 12.5% in RTCR zircaloy-2 after annealing. The tensile strength of CCR and RTCR was found to be 735 and 710 MPa, respectively. The 25% RTCR alloy upon annealing showed a ductility of 16.2% with tensile strength of 628 MPa. The improvement in ductility of 25% of RTCR zircaloy-2 observed in the present work is 62.9 % of 85% RTR annealed zirclaoy-2 with tensile strength almost equal.

4.4.4.3 Electron Back Scatter Diffraction (EBSD) and Kernal Average Misorientation (KAM)

It is observed from **Figure 4.27(a)** that after 25% CCR, grains with near basal orientation, in red color, are left non deformed as they are elastically harder (Sahoo *et al*., 2007). Low angle misorientations are increasing, which are dislocation cells and tangles as seen from TEM results. The misorientation chart in **Figure 4.27(c)** shows that the low angle grain boundaries are increasing with increase in reduction. Grains with some partitions in 25% CCR are seen from **Figure 4.27(a)** show orientation of about 20^{o}, which may be evidence of $\{11\bar{2}1\}$ tensile twinning and it has disappeared after misorientation due to activation of slip inside the crystal. In the 50% CCR sample (**Figure 4.27(b)**), only grains with near basal orientation are left undeformed because they are non fragmenting and elastically harder. However, due to change in strain during each pass, dislocations are formed inside these basal grains also, which can be seen from KAM (**Figure 4.27(f)**). CCR and

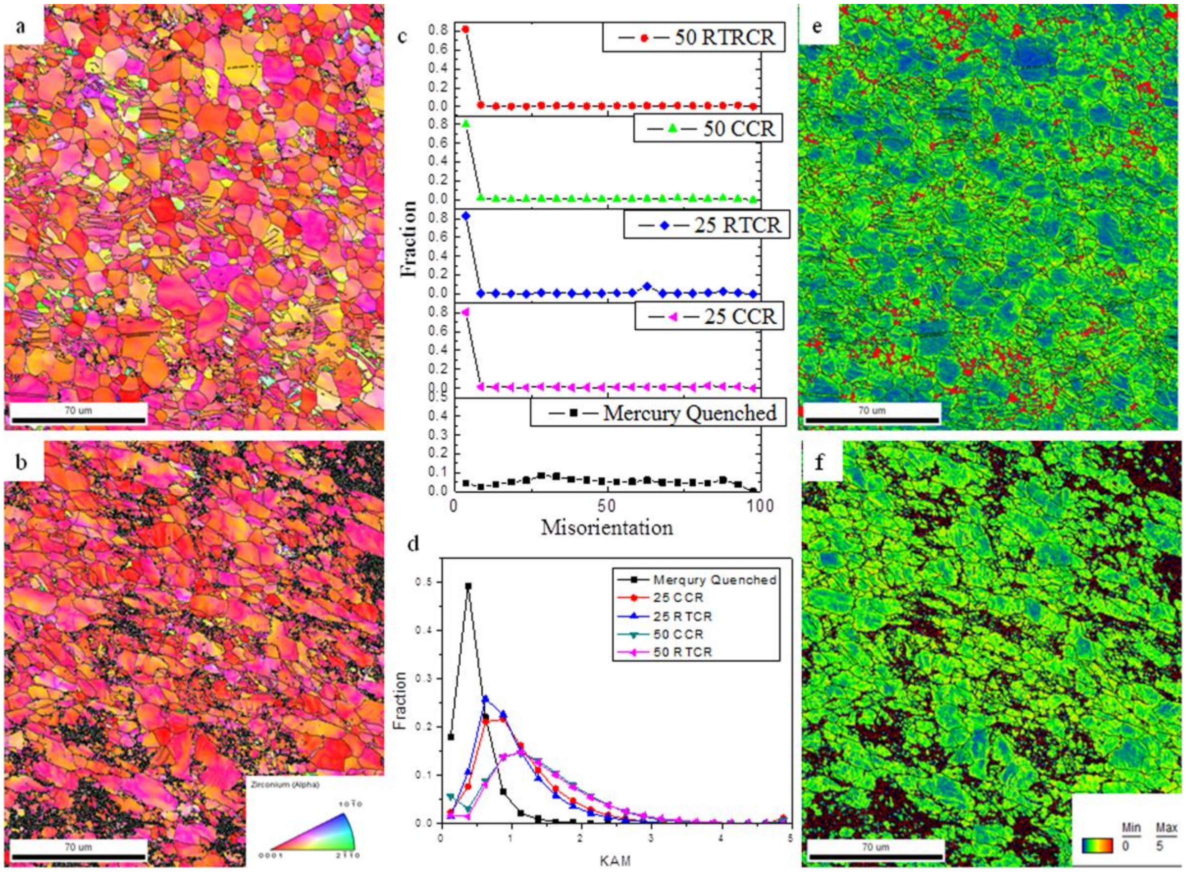

Figure 4.27 EBSD Image of **(a)** 25% and **(b)** 50% CCR Zircaloy-2. Average Misorientation and KAM Graph of **(c)** CCR and **(d)** RTCR Zircaloy-2. KAM Image of **(e)** 25% and **(f)** 50% CCR Zircaloy-2

RTCR samples (25% and 50%) show high and almost same fraction of low angle grain boundaries (**Figure 4.27(c)**), which also proves the effect of change in strain path resulting in more strain hardening.

KAM is defined as the average misorientation of the particular point with all its neighbors having misorientation exceeding 5^{o} is excluded (Takayama *et al.*, 2004). KAM generally signifies the dislocations and stored energy inside the crystals and it depends on the step size. The step size of 0.1 µm is taken for analyzing the EBSD results in the present work. The red region in the KAM shows very highly deformed regions, whose values are excluded from the graph (**Figure 4.27(d)**). As such a high misorientation near a value of 5^{o} on those places shows varying orientation with low CI index, leading to high. KAM value for 25% CCR sample. (**Figure 4.27(e)**) shows that most of the grains with large dislocation density inside. However, the KAM image of 50% CCR (**Figure 4.27(f)**) shows the presence of dislocations inside these near basal non fragmenting grains, due to change in strain path during rolling. It enables for improving the strength, hardness and ductility. Comparison of both 50% CCR and RTCR samples shows that there is no major difference in KAM and misorientation (**Figure 4(c-d)**) except little variation in their mechanical properties. Large KAM value can be seen near the grain boundary and in some grains, in 25% CCR sample. The high KAM value near the grain boundary shows that these grains should have hard orientation. In 50% CCR sample, almost all the grains with harder orientation show high KAM value, which reflects the effect of change in strain path.

4.4.4.4 Texture Study

{0002} and $\{01\bar{1}2\}$ pole figure (**Figure 4.28 (a)**) of mercury quenched zircaloy-2 shows a fully recrystallised structure with texture towards transverse direction, which are in tandem with the EBSD results. After 25% CCR, {0002} poles are aligning 30^{o} towards the rolling direction and $\{01\bar{1}2\}$ poles are shifted towards the transverse direction. They are spread towards the rolling direction as seen from **Figure 4.28(b)**, while in 25% RTCR (**Figure 4.29(a)**), the {0002} poles are towards rolling direction but they are expanded slightly towards the transverse direction. The texture is almost same in both the cases except the weak texture observed in 25% RTCR condition, as its intensity is 7.9 compared to 12 of 25% CCR condition. Difference in intensity shows that deformation in CCR sample occurred mostly by twinning, while in RTCR, it occurred by slip and twinning. In mercury quenched zircaloy-2, the texture is already showing basal orientation. Thus in CCR sample, apart from $\{10\bar{1}2\}$ tensile twinning, $\{11\bar{2}2\}$compressive twinning must be extensive, the same can be seen from EBSD image (Mccabe *et al*., 2006; Luan *et al*., 2013). Also, some traces of $\{11\bar{2}1\}$ tensile twin are also seen in EBSD (**Figure 4.27(a)**) (Mccabe *et al*., 2006). Since there is a change in strain path at each reduction during rolling, deformation due to activation of slip might have also taken place, which is prismatic slip. In RTCR sample, the initial texture is basal aligned $\{10\bar{1}0\}$prismatic slip and it is dominant in all the grains, while {0002} basal <a> slip in non basal grains and $\{11\bar{2}\bar{3}\}$pyramidal <c+a> slip in basal grains might have taken place (Gurao *et al*., 2013; Yu *et al*., 2013).

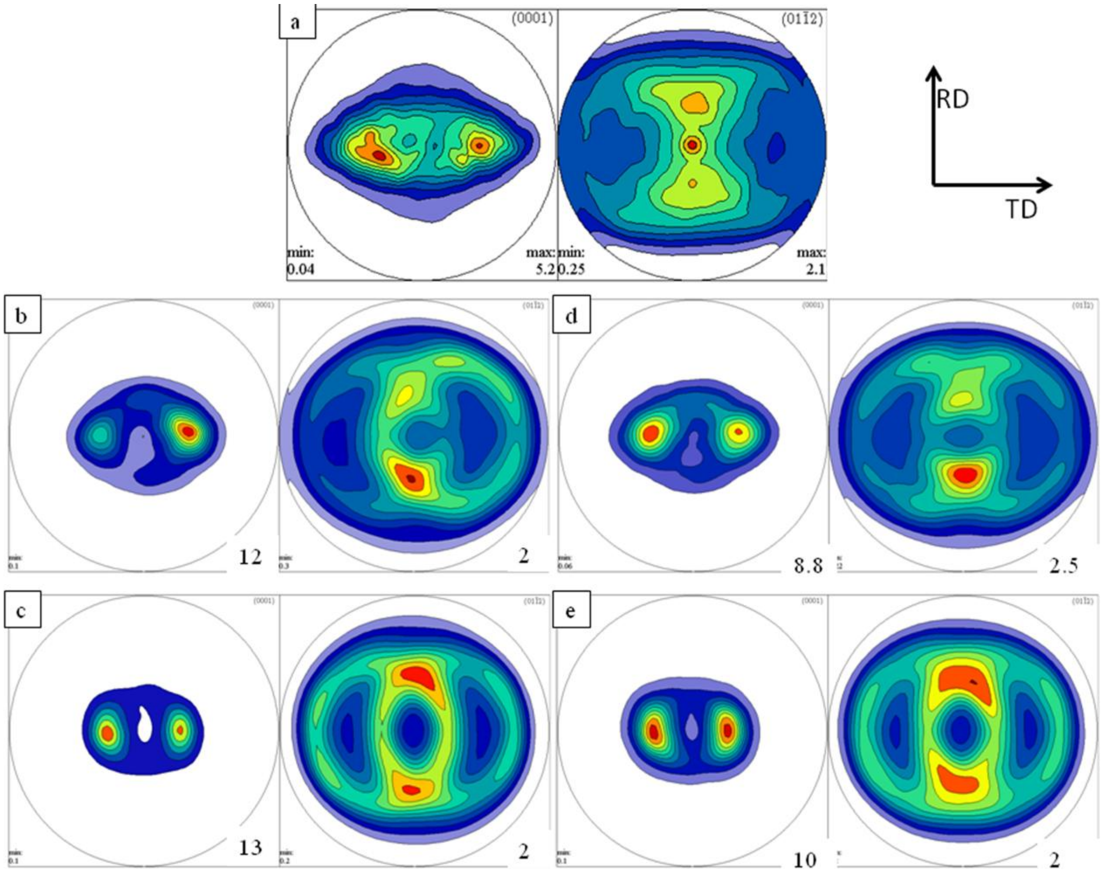

Figure 4.28(a) {0002} and $\{01\bar{1}2\}$ Pole Figure Image of Mercury Quenched Zircaloy-2, **(b)** 25% CCR **(c)** 50% CCR, **(e)** 25% CCR after Annealing at 400^{o} C for 30 minutes and **(f)** 50% CCR after Annealing at 400^{o} C for 30 minutes. Notation used as Transverse direction (TD) is only used to explain texture results otherwise TD is also the rolling direction

{0002} and $\{01\bar{1}2\}$ pole figure (**Figure 4.28(c) and 4.29(b)**) of 50% CCR and RTCR zircaloy-2 shows that these poles are spreading towards the rolling direction in both conditions, which may be due to change in strain path by cross rolling. Deformation in 50% CCR zircaloy-2 occurs by primary $\{11\bar{2}2\}$compressive twinning along with secondary $\{10\bar{1}2\}$tensile twinning in them because the poles are already inclined towards normal direction. There is very less chances of primary tensile twin to operate (Mccabe *et al.*, 2006). Basal grains with misorientation inside them can be seen (**Figure 4.27(b)**), showing activation of slip at cryo temperature. Prismatic slip might have taken place inside these grains; also probability of activation of {0002} basal slip <a>is also seen from Schmid and Taylor factor analysis discussed in next section (Judge, 2009). The intensity of 50% CCR zircaloy-2 has increased to 13 showing very large fraction of grains having orientation near basal due to which further reduction causes cracks resulting material failure. While, in 50% RTCR, reduction zircaloy-2 slip has played a major role in deformation, since most crystals are basal oriented prismatic, basal <a> and pyramidal <c+a> slip might have been activated (Gurao *et al.*, 2013). On further reduction in RTCR zircaloy-2 (**Figure 4.29 (c-d)**), the basal poles are inclined due to which pyramidal slip activity might have increased and due to change in strain path, basal and prismatic activity are also observed (Mccabe *et al.*, 2006; Gurao *et al.*, 2013).

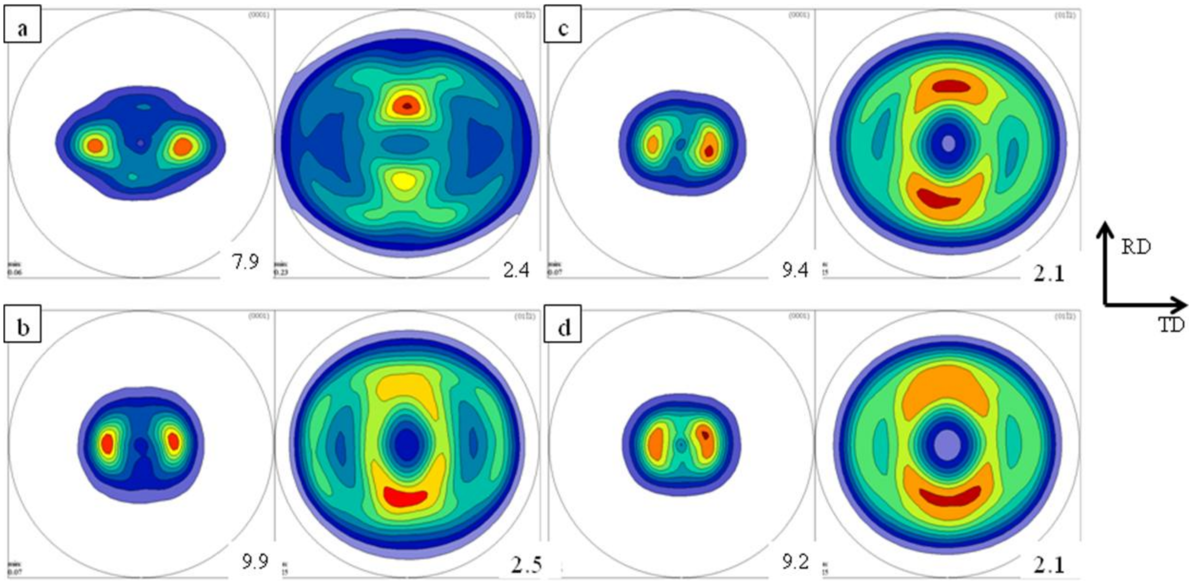

Figure 4.29 {0002} and $\{01\bar{1}2\}$ Pole Figure image of **(a)** 25%, **(b)** 50%, **(c)** 75% and **(d)** 85% RTCR Zircaloy-2. Notation used as Transverse direction (TD) is only used to explain texture results otherwise TD is also the rolling direction

Annealing causes recrystallisation as well as stress relieving to the deformed grains. The grains thus reorient themselves and prismatic plane align towards the transverse direction. Here, due to change in strain path, the prismatic planes get inclined in both the rolling directions. The effect of annealing on 25% and 50% CCR samples can be seen from **Figure 4.28(d-e)**. It clearly shows the weakening of basal texture as well as spreading of {0002} basal grains. There is no effect on the intensity after annealing on 25%-85% RTCR sample as seen from **Figure 4.30(a-d)**.

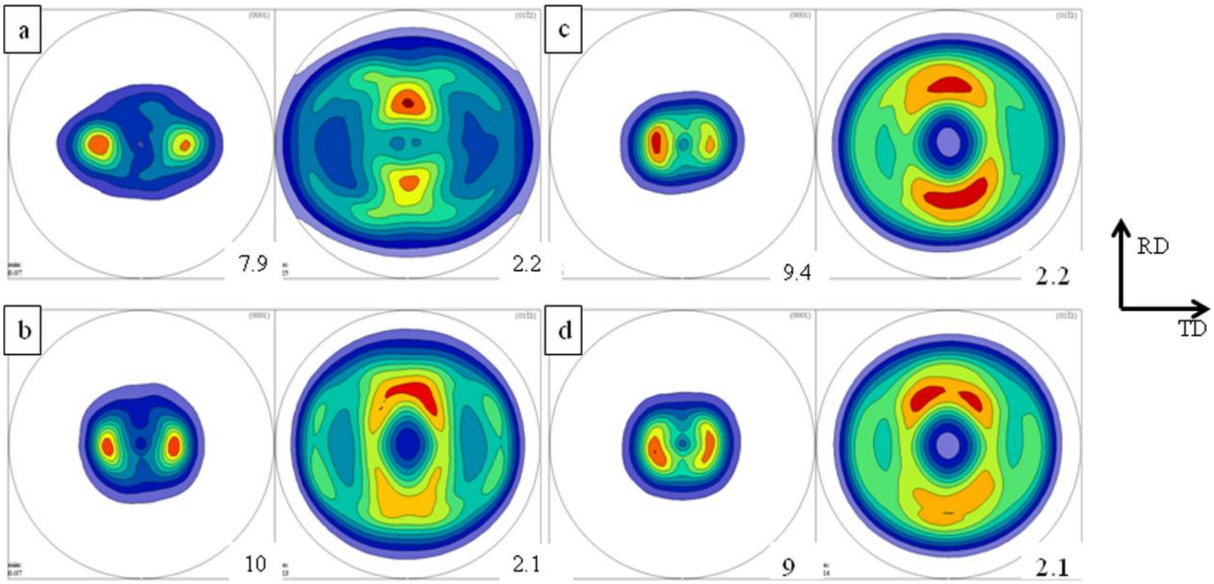

Figure 4.30 {0002} and $\{01\bar{1}2\}$ Pole Figure Image of **(a)** 25%, **(b)** 50%, **(c)** 75% and **(d)** 85% RTCR Zircaloy-2 after Annealing at 400^{o} C for 30 minutes

4.4.4.5 Schmid Factor and Taylor Factor

Deformation of a grain takes place in the plane, where CRSS value is minimum. The Taylor's theory is based on the assumption that plastic deformation is caused entirely by dislocation slip and deformation in the grains is almost identical to macroscopic deformation (Takayama *et al*., 2004). The Taylor factor is the energy required to deform the crystallite in the required orientation of active combination of slip systems (Bunge *et al*., 1970). Therefore, it relates yield strength of the material to its crystal orientation or texture. The Taylor Factor '**M**' is defined as

$$M = \sum_{s} \frac{d\gamma^{s}}{\varepsilon_{ij}} \qquad \textbf{(4.4)}$$

Where $d\gamma^{s}$ is the CRSS of a particular slip (s) in a given grain and 'ε_{ij}' is plastic strain applied externally (Shen *et al.*, 2013; Takayama *et al.*, 2004). Here, it is understood that 'M' depends on the lattice orientation of the crystal. If the value of 'M' is large, (near to 4.0), the large amount of slip is required to accommodate large plastic deformation, while low 'M' value indicates that more slip sets are available. Higher M value leads to, high hardening rate of a material (Cáceresa *et al.*, 2008).

Schmid factor is a parameter used to evaluate the ease to activate slip in a grain and it can be calculated by using the formula "**cosφcosα**" in which "**φ**" is the angle between slip direction and loading axis while "**α**" is the angle between slip plane normal and loading axis (Takayama *et al.*, 2004). During deformation, slip direction moves towards loading axis, while slip plane normal moves away from loading axis. Higher the Schmid factor shows a high probability of that slip. The Schmid factor is applicable for single crystal system and on comparing with Taylor factor, it can be applied to polycrystalline materials also. Schmid factor and Taylor factor can be calculated by defining the loading direction and deformation mechanism with CRSS values. The various CRSS values taken to calculate the Schmidt and Taylor factor are shown in **Table 2**. The Schmid factor and Taylor factor for 25% CCR with {0002} basal slip can be seen from **Figure 4.31(a-b)**. It can be seen that majority of grains have both large Schmid and Taylor factor values. These grains during deformation have the least probability to activate basal slip due to high Taylor factor. Hence, the basal slip gets strain hardened very fast. Some grains are seen whose Taylor factor is low << 2.4 but its Schmid factor is high >> 0.35, which are marked by circles in the image. The activation of basal slip will take place in these grains upon further increasing reduction (Judge 2009).

Table 4.4 Critically Resolved Shear Stress (CRSS) Values of Slip System at Room Temperature and Cryo Temperature

Slip	CRSS at 300K	CRSS at 77K
Prism<a>slip	0.1	0.220
Basal<a>slip	0.16	0.260
Pyramidal<c+a> slip	0.320	

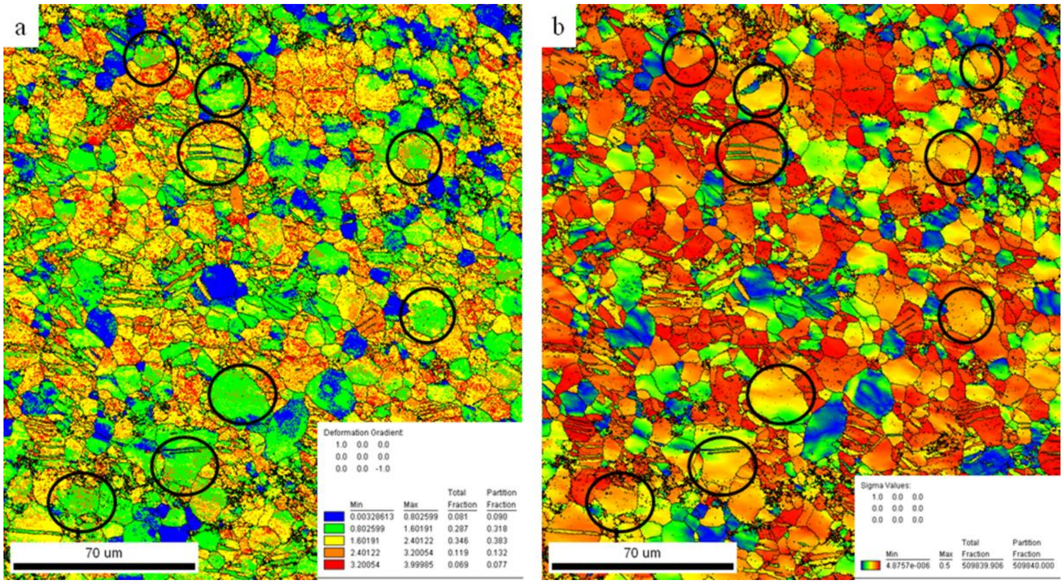

Figure 4.31(a) Basal Slip Taylor Factor and **(b)** Basal Slip Schmid Factor Image of 25% CCR Zircaloy-2

It has been found that the fraction of grains with low Taylor factor and high Schmid factor are much more in 25% RTCR as compared to 25% CCR. The curve in **Figure 4.32(a-b)** shows Taylor factor and Schmid factor of basal slip of CCR and RTCR condition up to 50% reduction. The image shows that 25% CCR and 25%, 50% RTCR have low average Taylor factor while high Schmid factor values. Mercury quenched and 50% CCR have low Taylor factor as well as low Schmid factor due to which basal slip will not take place in them on further deformation. The Taylor factor and Schmid factor image for basal slip of 50% CCR zircaloy-2 can be seen from **Figure 4.32(c-d)**. Schmid factor values were high for prism slip as it is always active, which is not shown. The CRSS value for pyramidal slip at cryo temperature is very high and therefore it is not active at low strain.

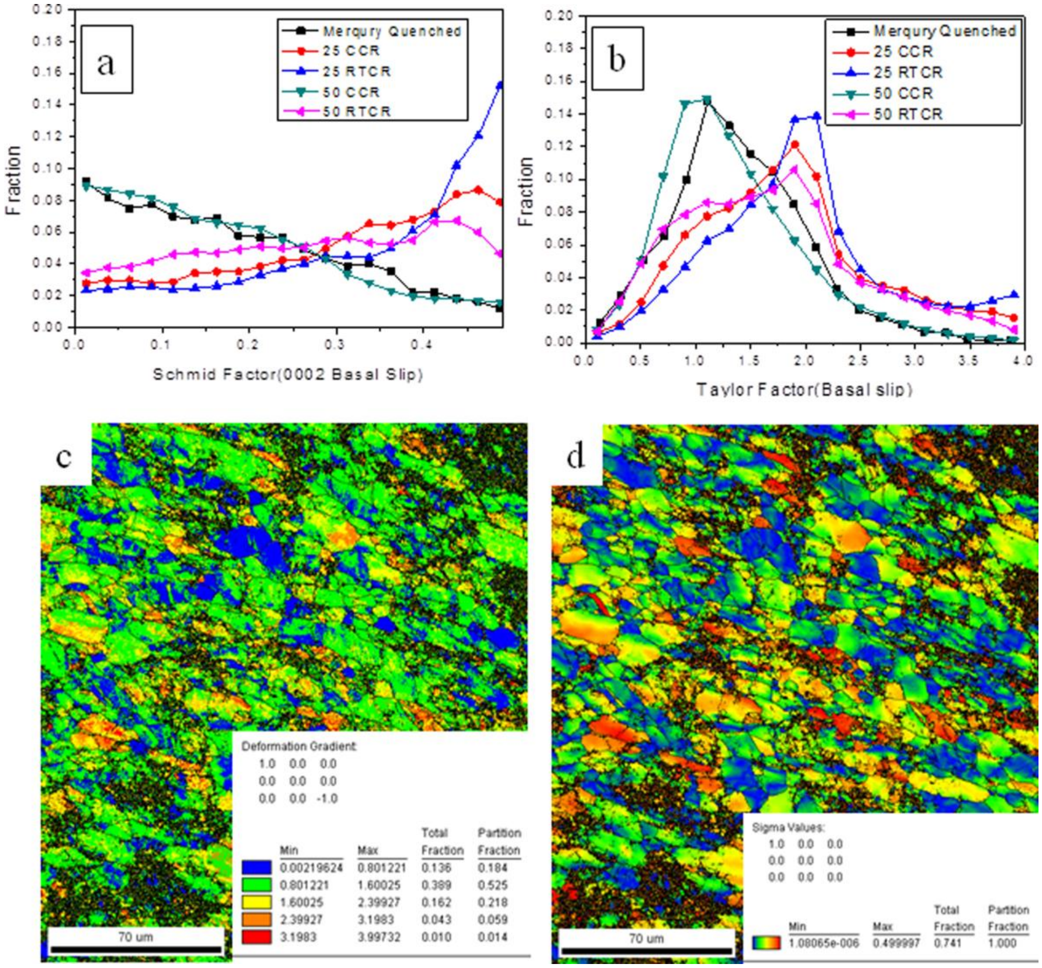

Figure 4.32(a and b) Graph Showing Basal Slip Taylor factor and Schmid Factor Values of CCR and RTCR Zircaloy-2, **(c and d)** Image Showing Basal Slip Taylor Factor and Schmid Factor of 50% CCR Zircaloy-2

4.4.4.6 Dislocation Density and Stored Strain Energy using KAM

KAM is average value of misorientation within 5^{o} with nearby grains, is used to find out the dislocation density and low angle grain boundary in the material. During deformation, low angle tilt and twist boundary consisting of screw dislocations and non screw dislocations are formed in zirconium (Monnet *et al*., 2004). If spacing between the dislocation with burger vector '**b'** having a boundary '**h'**, then the crystal on either side of low angle boundary is tilted by θ,

$$\theta \approx 2\sin\frac{\theta}{2} = \frac{b}{h} \tag{4.5}$$

This equation is also called Frank's formula (Frank, 1950). When distance between the misorientation (step size) is '**d',** area of the boundary planes with the neighbouring points per unit volume can be represented by the length 'l' and area 'a' of hexagon, in consideration of unit thickness as

$$\frac{(l/a)}{a} = \{2\sqrt{3}d/(\sqrt{3}d^2/2)\}/2 = 2/d \qquad \textbf{(4.6)}$$

Then, the α/h is the length of dislocation line per unit area, 'α' is constant depends on geometry of dislocation arrangement. Value of α is taken as '2' for tilt and '4' for twist boundaries. The dislocation line length per unit area and stored energy is given by (Takayama *et al.*, 2004; Godfrey *et al.*, 2005; Liu *et al.*, 1998)

$$\rho \approx \frac{\alpha\theta}{bd} \qquad \textbf{(4.7)}$$

$$E = \rho\frac{Gb^2}{2} \qquad \textbf{(4.8)}$$

$$E = \frac{\alpha Gb\theta}{2d} \qquad \textbf{(4.9)}$$

Where,

θ – Average KAM between dislocation boundaries
G – Shear modulus
b – Burger vector for dislocation
d – Step size

The value of 'α' is taken as 3 due to deformed structure, mostly at low temperature in zircaloy-2. Since $\langle a \rangle$ slip is dominant, the value of burger vector **b** corresponding to $\langle a \rangle$ slip is taken as 0.3232 nm. Shear modulus of 34.8 GPa for both CCR and RTCR samples is considered for comparison (Unga *et al.*, 2007). Step size for of EBSD scan is 0.1 µm. **Table 4.5** shows the value of dislocation density and energy of CCR and RTCR zircaloy-2. The variation in dislocation density and energy with increase in thickness reduction in RTCR and CCR shows that they are higher at cryo temperature due to suppression of dynamic recovery. Although, above mentioned method for calculation of energy gives more accurate results in case of medium and high stacking fault energy materials but variation of stored energy after deformation can be compared in case of zircaloy-2 (Godfrey *et al.*, 2005). The formation of ultrafine grain during annealing is influenced by the stored strain energy also. The locations where the KAM is high, stored energy is also high, which on annealing recrystallizes to form ultrafine grains.

Table 4.5 Energy and Dislocation Density of Cross Rolled Samples

	Mercury Quenched	25% CCR	25% RTCR	50% CCR	50% RTCR
Average KAM(radian)	0.008105	0.01951	0.017593	0.0276914	0.0233
Dislocation Density $\rho(m^{-2})$		9.944×10^{14}	8.805×10^{14}	1.818×10^{15}	1.41×10^{15}
Energy (J/mole)		29.02	25.7	53.06	41.15

4.4.5 Summary

The zircaloy-2 was subjected to RTCR and CCR with various thickness reductions and its mechanical, microstructural and microtexture were investigated in the present work. The following conclusions are made based on the present study.

- The dislocation density in the alloy is increasing with increasing strain during cross-rolling, which confirms the heavy deformation of the alloy as evident from EBSD results.
- Ultrafine and nano grains (~180 nm) are observed after 75% and 85% thickness reduction of the RTCR sample. The orientation of IDBs along the macroscopic plastic flow enables the alignment of dislocations for the formation of fine grain structures in the RTCR zircaloy-2.
- Large stored energy in the deformed alloy upon annealing at 400^o C for 30 minutes facilitates the large number of nucleation sites, which in turn enables formation of the ultrafine grains (average grain size of 156 nm) in the RTCR zircaloy-2. After 85% reduction in thickness, a tensile strength of 991 MPa with 7.5% ductility is observed. Annealing at 400^o C for 30 minutes results in annihilation of dislocations, thus improving ductility of RTCR zircaloy-2 up to 11%.
- $\{10\bar{1}2\}$ extension twinning is observed in the RTCR zircaloy-2after 25% thickness reduction. The fraction of low angle grain boundaries is seen inside near basal grains even after 75% thickness reduction, due to change in strain path. Hence, grains with near basal orientation are also deforming.

- KAM mapping reveals the high dislocation density in near basal crystals after 75% reduction in thickness. It confirms the mechanisms of grain fragmentation due to change in strain path during rolling in RTCR zircaloy-2.

- TEM reveals the formation of ultrafine grains after 50% CCR and after annealing at 673K for 30 minutes, the fraction of ultrafine grains has increased.

- Tensile strength of zircaloy-2 after 50% CCR is 786 MPa with 8.7% ductility, while after annealing at 673 K for 30 minutes, 9.8% ductility with tensile strength of 735 MPa is achieved.

- Evidence of $\{11\bar{2}1\}$ tensile twinning is seen in 25% CCR and deformed near basal grains are seen after 50% CCR reductions due to change in strain path.

- KAM analysis shows the presence of dislocations in near basal grains after 50% reduction proving slip activity inside the basal structure.

- Texture results shows that 25% CCR samples are deformed due to $\{11\bar{2}2\}$ compressive twinning active extensively with some traces of $\{11\bar{2}1\}$ tensile twinning. Although, in 25% and 50% RTCR, deformation takes place by activation of basal <a> slip, prismatic slip and pyramidal <c+a> slip.

- 50% reduction of CCR is possible by activation of secondary tensile twinning, primary compressive twinning and prismatic slip.

- 25% CCR and 25%, 50% RTCR shows low average Taylor factor while high Schmid factor values for basal slip. Mercury quenched and 50% CCR show low Taylor factor as well as low Schmid factor for basal slip.

- Texture, Taylor factor and Schmid factor analysis confirms the high probability of activation of basal<a> slip.

- Higher value of stored energy and dislocation density is obtained in CCR zircaloy-2 due to suppression of dynamic recovery at cryo temperature.

4.5 Effect on the Microstructure and Mechanical Behavior of Room Temperature Rolled Zircaloy-2 after Water and Mercury Quenching

4.5.1 Introduction

Grain size influences the physical and mechanical response of materials. Grain size can be controlled by optimizing mechanical and thermal processing of a material to get the desired properties. Ultrafine grain materials are produced mostly by severe plastic deformation techniques (SPD) such as ARB, ECAP, Multiaxial forging, repeated corrugation and straightening, etc (Sauvage *et al.*, 2012; Valiev *et al.*, 2000; Estrin *et al.*, 2013; Vedani *et al.*, 2004). It is difficult to perform mercury quenching of the starting alloy prior to SPD processing on industrial scale, it is essential to quench the alloy preferably in water. Therefore, the present work has been focused to differentiate the effect of quenching in water and mercury, respectively, on the grain size and mechanical behavior of RTR zircaloy-2.

4.5.2 Experimental Procedure

Zircaloy-2 has been brought from NFC Hyderabad rolled at 800^o C temperature with 4 mm thickness. Samples with 3 X 5 cm dimensions were cut from the plate and ground to remove the oxide layer on the surface of as received zircaloy-2. The samples are then heat treated in argon environment up to 800^o C for 2 hours followed by quenching in water. Similar heat treatment was given for another sample and quenched in Hg. Rolling was performed on 2 high baby rolling mill having 110 mm roller diameter with 8rpm rolling speed. A reduction of 0.4 mm was given in every pass and then quenched in water so that dynamic recovery is reduced. The characterisation such as TEM, EBSD and tensile test of the deformed alloy was performed as per the procedure discussed in Chapter 3.

4.5.3 Result and Discussion

4.5.3.1 Electron Back Scatter Diffraction (EBSD)

Initial microstructure contains homogeneous microstructure with an average grain size of 20 µm as seen from **Figure 4.33(a)**. The grains size of mercury quenched zircaloy-2 was 10 µm as discussed in **Section 4.1**. The difference in grain size can be due to the variation in cooling rate of water and mercury. Deformed structure of zircaloy-2 after rolling at (25% - 75%) reduction can be seen from **Figure 4.33(b-d)**. Minimum confidence index of 0.03 has been excluded from the image so that the completely deformed area can be seen as dark. The 25% rolled image shows basal texture with some undeformed grains having near basal orientation, which are elastically harder (Sahoo *et al.*, 2007). Extension twins are seen in some soft grains and are responsible for initial gain in strength. On further increasing reduction to 50%, larger fraction of deformed area can be seen with some undeformed near basal grains. The basal plane is always perpendicular to the direction of resultant force (Tenckhoff, 1988; Murthy *et al*, 2006). Even after 75% reduction in thickness, near basal grains are still left undeformed and non fragmented. The alignment of ‘c’ axis towards the normal direction makes the grains elastically harder (Sahoo *et al.*, 2007). Misorientation curves shows large fraction

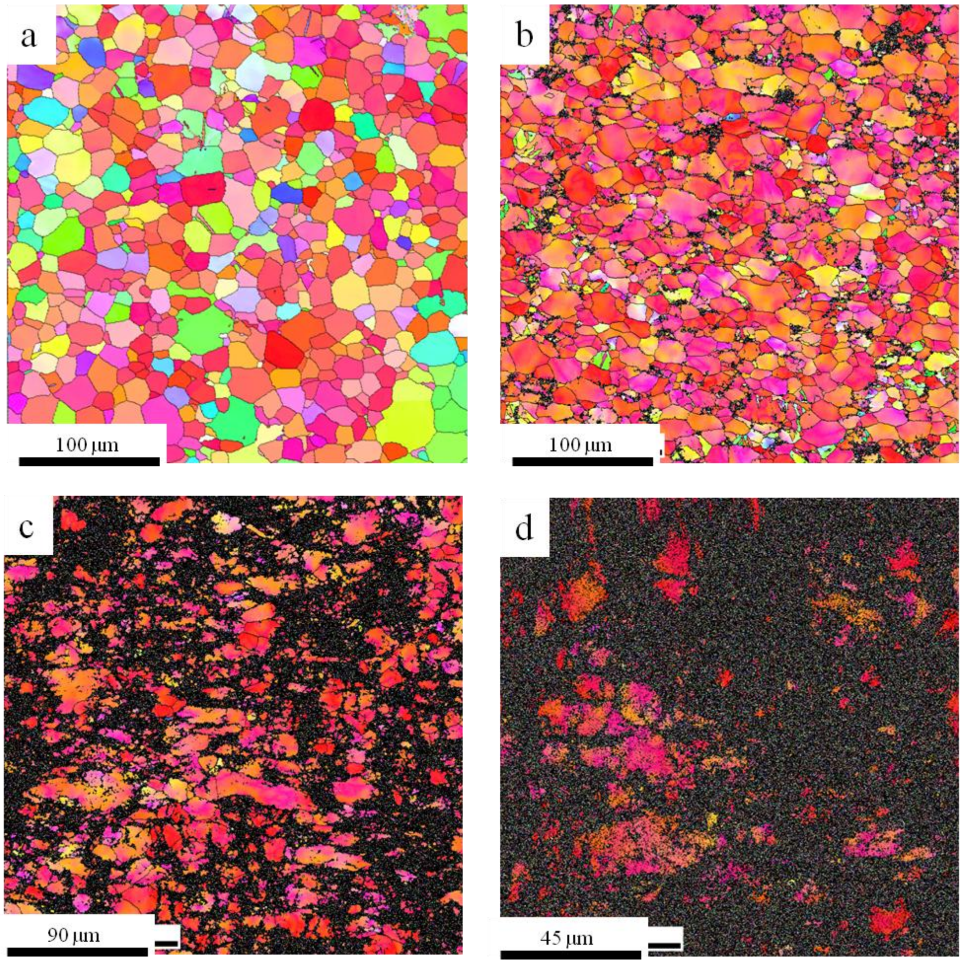

Figure 4.33 EBSD Image of **(a)** Water Quenched Zircaloy-2, **(b)** 25%, **(c)** 50% and **(d)** 75% RTR Zircaloy-2

of low angle grain boundary with no traces of twins in the graphs due to lesser fraction of twins as shown in **Figure 4.34(a)**. Even with the increase in reduction, the fraction of low angle grain boundaries is very high. This was not seen in mercury quenched zircaloy-2.

KAM image shown in **Figure** 4.34(b), shows that the average KAM value is increasing with rolling reduction. It explains that the energy stored and dislocation density in water quenched deformed zircaloy-2 is increasing with the increase in rolling percentage.

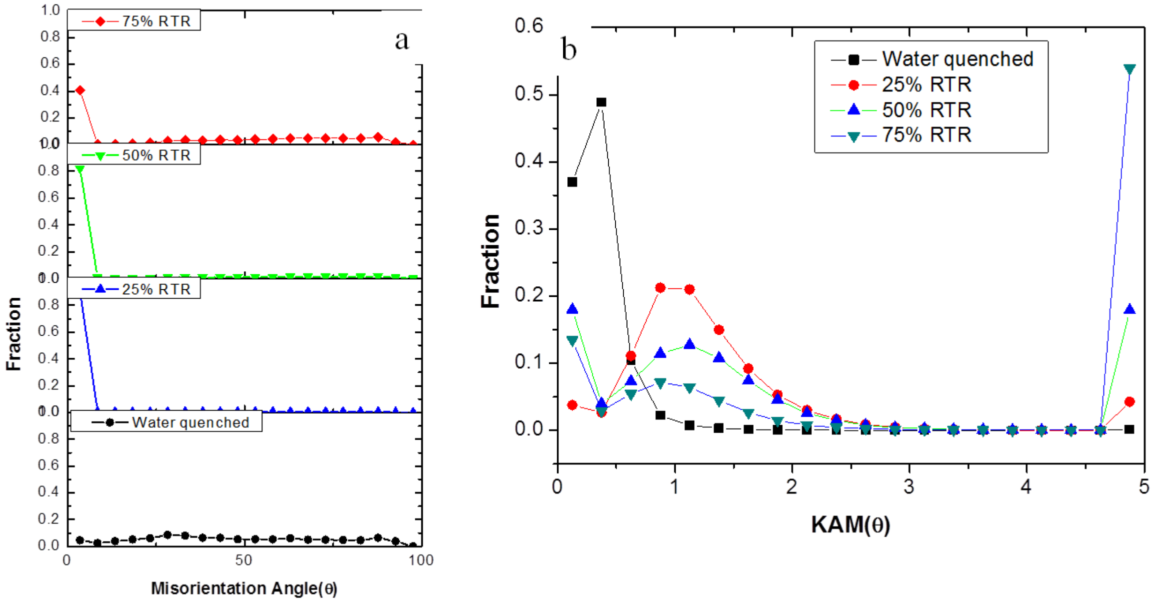

Figure 4.34 (a) Grain Boundary Misorientation **(b)** KAM of Water Quenched, 25%, 50% and 75% RTR Zircaloy-2

4.5.3.2 Transmission Electron Microscopy (TEM)

The TEM microstructure image of RTR water quenched zircaloy-2 is showing almost same feature as of RTR mercury quenched zircaloy-2, discussed in section 4.2. Dislocation cells and tangles can be seen in images shown in **Figure 4.35(a-d)**. Dislocation tangles are getting vanished and are converted to dislocation cells due to dynamic recovery at room temperature. Repeated plastic deformation causes the dislocation tangle to orient with very small angles thus causing to form dislocation cells, which are also known as low angle grain boundary (Hansen, 2001; Hughes *et al*., 2003; Jiang *et al*., 2012). These low angle grain boundaries are formed in almost 90% area, which is already seen in misorientation graph explained above. On repeated deformation, there are some locations in zircaloy-2 where large misorientation of dislocation cells are observed according to the resultant direction of force in grains. Thus, ultrafine grains are formed and the fraction of these grains keeps increasing with more deformation (Jiang *et al.*, 2012). The microstructures after 85% rolling reduction of zircaloy-2 consist of multimodal grain structure, which can be seen and compared with the EBSD and TEM image as shown. These images clearly show that the presence of

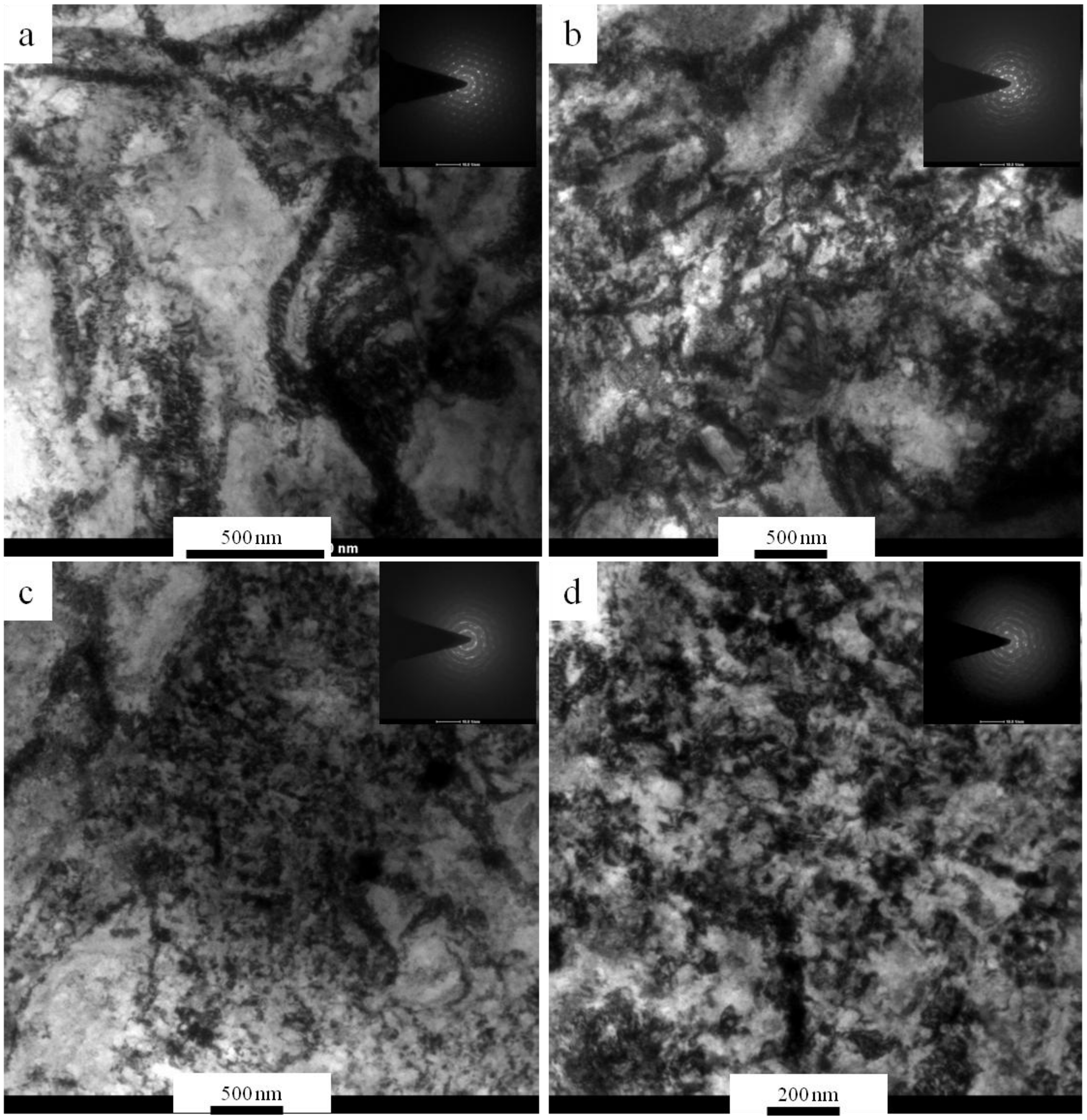

Figure 4.35 TEM Images of **(a)** 25%, **(b)** 50%, **(c)** 75% and **(d)** 85% RTR Zircaloy-2

grains with various sizes ranging from 50nm to even 10 µm. The grain with size above 5 µm contains dislocation tangles and cells. The structure obtained after RTR of zircaloy-2 exhibits high strength and ductility. The average grain size of the UFG regions, which is calculated using the TEM image is 167 nm.

On further annealing 85% RTR zircaloy-2 at different temperatures 400 and 500°C for 30 minutes, the grains size increases and dislocations get annihilated. **Figure 44.36(a-c)** shows the effect of annealing temperature on 85% RTR zircaloy-2. The average grain size increases to 220 nm after annealing at 400°C while annealing at 450° C increases the grain size to 320 nm. At 500° C, the grains size increases to an average of 800 nm size.

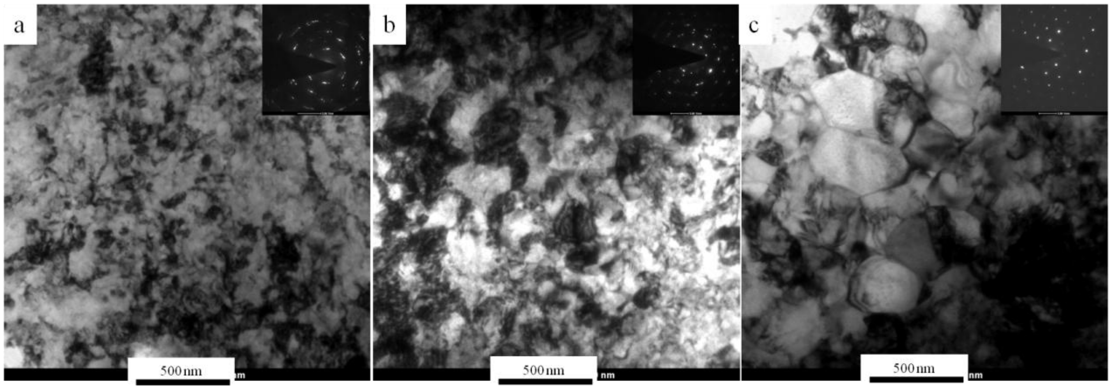

Figure 4.36 TEM Image of **(a)** 400°C, **(b)** 450°C and **(c)** 500°C Annealed Zircaloy-2 after 85% RTR

4.5.3.3 Mechanical Properties

The effect of room temperature rolling on the mechanical behavior is studied by performing tensile test and the results are shown in **Table 4.6**. The water quenched zircaloy-2 shows lesser tensile strength (389 MPa) and ductility (17%) as compared to mercury quenched zircaloy-2. Repeated rolling reduction increases the dislocation density and with higher reduction, the formation of ultrafine grains occurs as explained above. The reduction in grains size and stored dislocation density after RTR increases the strength of water quenched zircaloy-2. The improvement in tensile strength after 85% RTR increases from 389MPa to 745 MPa with 4 percent ductility in rolling direction. However, the 85% RTR mercury quenched sample shows tensile strength of 679 MPa with 5.5 percent ductility. The difference may be due to higher strain hardening capacity of water quenched zircaloy-2 compared to mercury quenched sample..

Annealing releases the stored energy of deformed zircaloy-2 by annihilating the dislocation density and formation of reoriented ultrafine grains of high angle grain boundary takes place. The temperature selected for annealing 85% RTR zircaloy-2 is 400° C for 30 minutes. On annealing above 400°C, a very sharp decrease in the tensile strength is seen. The tensile strength after annealing reduces to 669 MPa from 745 MPa with increase in ductility from 4 to 5 percent. On comparing it to 85% RTR mercury quenched sample, it shows almost same tensile strength of 664 MPa with 6% ductility.

Table 4.6 Mechanical Properties of Water Quenched and RTR Zircaloy-2

	Tensile Strength (MPa)	Yield Strength (MPa)	Ductility (%)
Water quenched	389	304	17
25% RTR	598	577	7.1
50% RTR	650	628	7
75% RTR	686	634	5.9
85% RTR	745	717	4
25% RTR Annld	580	559	10
50% RTR Annld	606	588	9
75% RTR Annld	621	595	7.1
85% RTR Annld	669	633	5

4.5.3 Summary

- Initial grain size of the zircaloy-2 after water quenching is 20 µm, which is higher than mercury quenched (10 µm) due to higher cooling effect of the latter.
- Initial deformation up to 25% rolling takes place by the activation of slip and extension twinning. After 25% reduction, non fragmented and undeformed near basal grains are left.
- With the increase in reduction, stored energy and dislocation density of material is increasing as seen by KAM results.
- The grain size of the zircaloy-2 range from 50nm to 5µm with areas where ultrafine grain with an average grain size of 167 nm is observed. Annealing at 400°C and 450° C for 30 minutes increases the average grains size to 220 nm and 320 nm, respectively. The grains size increases to 800 nm after annealing at 500° C for 30 minutes.
- Heterogeneous microstructure after 85% RTR shows high strength (745 MPa) along the rolling direction while after annealing, the tensile strength reduces to 664 MPa with 5 percent ductility.

CHAPTER 5

FRACTURE ANALYSIS OF ZIRCALOY-2 (EXPERIMENT AND SIMULATION)

In this chapter, the effect of rolling and cross rolling on the fracture toughness of zircaloy-2 has been investigated. Various experimental and finite element investigations of the alloy such as (i) Experimental Evaluation of Mechanical Properties and Fracture-Fatigue Simulation of Cryo and Room Temperature Rolled Zircaloy-2; (ii) Effect on the fracture toughness of zircaloy-2 after rolling and cross rolling at different temperatures (experimental and simulation). The results of each study are substantiated using detailed microstructural characterizations of the samples processed under different conditions.

5.1 Experimental Evaluation of Mechanical Properties and Fracture-Fatigue Simulation

5.1.1 Introduction

From the past 25 years, severe plastic deformation (SPD) has played a very important role for providing strength and ductility to the materials (Kawasaki *et al.*, 2012; Estrin *et al.*, 2013). The first person who studied SPD and conducted an experiment was Bridgman (Bridgman 1935b, Bridgman 1943). Since then, many methods for performing SPD has been developed such as high pressure torsion (HPT), equal channel angular pressing (ECAP), accumulative roll bonding (ARB), multi-axial forging, twist extrusion (TE) and many more (Estrin *et al.*, 2013).

Rolling at cryogenic temperature (-196 °C) came into study in 2002 (Wang *et al.*, 2002). Wang *et al.*, (2002) performed the CR of copper, and got inhomogeneous microstructure followed by annealing at 180^{o}C and 200^{o}C for 3 minutes containing nanocrystalline and ultrafine grains. In recent years, CR is extensively used by the researchers to provide strength to materials. CR has been used from past ten years for Cu, Al, Ni, Ti, Zr, and its alloy to obtain ultrafine grained structure (Wang *et al.*, 2002; Lee *et al.*, 2005; Rangaraju *et al.*, 2005; Zherebstov *et al.*, 2013; Guo *et al.*, 2012a). Ultrafine and nanocrystalline grains can be achieved at low strain rate by providing adequate annealing temperature after CR (Wang *et al.*, 2002).

Due to high temperature corrosion resistant, low neutron cross section and better tensile properties, zircaloy-2 is used in nuclear reactors such as boiled water reactor (BWR), Canadian Deuterium Uranium (CANDU) power reactors in the form of high pressure tubes (Mehan *et al.*, 1961, Ibrahim *et al.*, 1969). At different temperatures, Zircaloy-2 behaves as $\beta \geq 1250$ K; $1150 \leq \alpha+\beta \leq 1250$ K; $1080 \leq \alpha+\beta+\gamma \leq 1150$ K and $\alpha+\gamma \leq 1080$ K where α-phase having hexagonal closed pack (HCP) structure while β-phase having body centered cubic (BCC) structure and γ being intermetallic phase (Corchia *et al.*, 1981; Massih *et al.*, 2006; Massih *et al.*, 2003; Sell *et al.*, 2002). In the present work, zircaloy-2 has been CR, and its effect on the mechanical properties and microstructure has been studied. Further, the finite element method (FEM) is applied to simulate the fracture toughness and fatigue life of the zircaloy-2 using the mechanical data obtained from the tensile test.

5.2 Numerical Evaluation of *J*-Integral

Finite element method (FEM) was developed in early 1960’s to find the approximate solution of nonlinear equations with complex geometry, dissimilar materials and large deformations

(Veubeke *et al.*, 2001; Tong *et al.*, 1967; Eduardo *et al.*, 1968; Zamal, 1968). The use of FEM in fracture mechanics was started in 1969's for calculating the stress intensity factor using linear elastic fracture mechanic approach. Various methods were developed in 1970 to find the stress intensity factor at the crack tip such as stress method, displacement method and line integral method, collocation method, direct method and conformal mapping method (Chan *et al.,* 1970; Byskov *et al.,* 1970; Watwood, 1969). Hutchinson (1983) and Rice *et al.* (1968) worked for quasi static crack growth under monotonic loading conditions. *J*-integral was first introduced by Rice (1968) for fracture problem having large plastic deformation near the crack tip. *J*-integral for a cracked body on an arbitrary closed path is given by

$$J = \int_{\Gamma} (Wn_1 - T_i u_{i,1}) dS \tag{5.1}$$

where $W = \int \sigma_{ij} d\varepsilon_{ij}$ is strain energy density in which σ_{ij} and $d\varepsilon_{ij}$ are stress and strain tensor

T_i and u_i are i^{th} components of traction and displacement vector. *J*-integral is valid for linear and nonlinear materials, and is used to characterize the crack tip. In general, *J*-integral is calculated using domain type approach (Moran *et al.,* 1987). A contour integral used in Eq. (1) can be converted into area integral using divergence theorem. The values of *J*-integral for CR and RTR zircaloy-2 are calculated by FEM, and are compared with the mercury quenched zircaloy-2. The fatigue life of the materials can be evaluated by techniques including linear damage evolution, energy based approach, crack growth concept (Fatemi *et al.*, 1998). In this work, the fatigue life of the zircaloy-2 is evaluated by energy based approach.

5.3 Experimental Testing and Numerical Simulation

The zircaloy-2 was received from Nuclear Fuel Complex, Hyderabad, India in 4 mm thick rolled sheet. Chemical composition of the material is shown in **Table 1**. The sheet was annealed for 2 hours in Argon gas environment, and quenched in mercury at 800° C. After surface finishing, the rolling of annealed sheet having 3 x 6 cm dimensions was done at cryo-temperature by dipping the sample in liquid nitrogen for 15 minutes, while room temperature rolling was performed in air and after every pass, the sample was dipped into water at room temperature for 5 minutes so that temperature gets homogenized in the sample. The rollers were of 110 mm diameter rotating at 8 rpm. To reduce friction, solid lubricant $MiSO_2$ was used. Repetitive rolling was done with a thickness reduction of 0.02 mm per pass to achieve 75% and 85% reduction. After CR and RTR, tensile samples of sub-standard size having 16 mm gauge length were prepared using ASTM standard

E8/E8M along the rolling direction. Tensile test were performed on 5 samples for each condition using S series, H25K-S tensile testing machine. VMC 50 Vicker hardness testing machine with 20 kgf load was applied for 15 sec to get the hardness of the sample after taking the average of 5 readings at room temperature. To examine the microstructure and crystal structure, transmission electron microscopy (TEM) was performed using FEI Technai-20 machine at an operating voltage of 200 KV. After thinning the sample to 0.1 mm using emery paper ranging from 300 to 1200 grit size, the sample is further electro polished in twin jet polisher at 20V and -48 °C temperature using 80:20 solution of methanol and perchloric acid.

The FEM software package Abaqus has been used to calculate *J*- integral and internal energy, while Ansys package has been used to calculate the fatigue life of the mercury quenched, room temperature rolled and CR zircaloy-2.

5.4 Result and Discussion

5.4.1 Microstructure Study

Figure 5.1 shows the EBSD microstructure of the mercury quenched zircaloy-2 showing homogeneous grain with random texture orientation having an average grain size of 10 µm. TEM images in **Figures 5.2(a-c)** show the dislocations in the form of dark regions having dislocation tangles (shown by arrows) and dislocation cells (shown by triangles) in 75%, 85% CR and 75% RTR zircaloy-2. The nanostructured grains with an average grains size of 150 nm can be seen in 85% RTR (**Figure 5.2d**) zircaloy-2. The selected area diffraction pattern (SAED) can be seen from the inset showing discontinuous arc (triangle) due to dislocation cells. Dislocation cells are formed due to dynamic recovery. During deformation subdivision of grain occurs due to tangling of dislocation and formation of net like structure which is called as dislocation cells. The SAED pattern with continuous arcs (arrow) shows dislocation tangles which are formed because dislocations get tangled with each other inside the grain due to suppression of dynamic recovery. During deformation dislocation inside the crystal tangles with each other and becomes thicker with the increase in deformation at cryo-temperature, as neutralization of dislocation is not possible at this temperature known as dislocation tangles. As the plastic deformation in zircaloy-2 increases, internal stresses inside the crystal also increase. From **Figures 5.2(a-b),** one can see that the dislocations tangles are increasing with the thickness reduction in CR samples. In RTR sample (**Figure 5.2c**), dislocation cells are found more as compared to 75% CR sample due to dynamic recovery inside the sample at room temperature. Recovery in RTR sample can also be examined after comparing the tensile strength and dislocation density of 75% RTR zircaloy 2, which is less than 75% CR sample.

85% RTR zircaloy-2 in **Figure 5.2d** shows a large number of nanostructured and ultrafine grains having an average grain size of 150 nm which is also proved by the diffraction pattern showing rings in **Figure 5.2d** inset. The nanostructured and ultrafine grains are formed due to dynamic recrystalisation during room temperature rolling of zircaloy-2. During deformation dislocation cells get oriented in the direction of macroscopic plastic flow which results in nanocrystalline and ultrafine grains formation.

5.4.2 Dislocation Density

During the plastic deformation of the material, dislocations are introduced due to which, there is variation in the lattice parameters in crystals. The peak at any 2θ position in the X-ray diffraction pattern shows the plane of that particular grain. The intensity shows the density of the plane. In a completely undeformed material without any deformation, the peak should be a single line without any broadening but generally this does not happens due to some errors in measurement i.e. due to vibrations, sample height and other errors and that cannot be deducted. After proper heat treatment also, there are some dislocations left in the material due to which broadening generally occurs. By

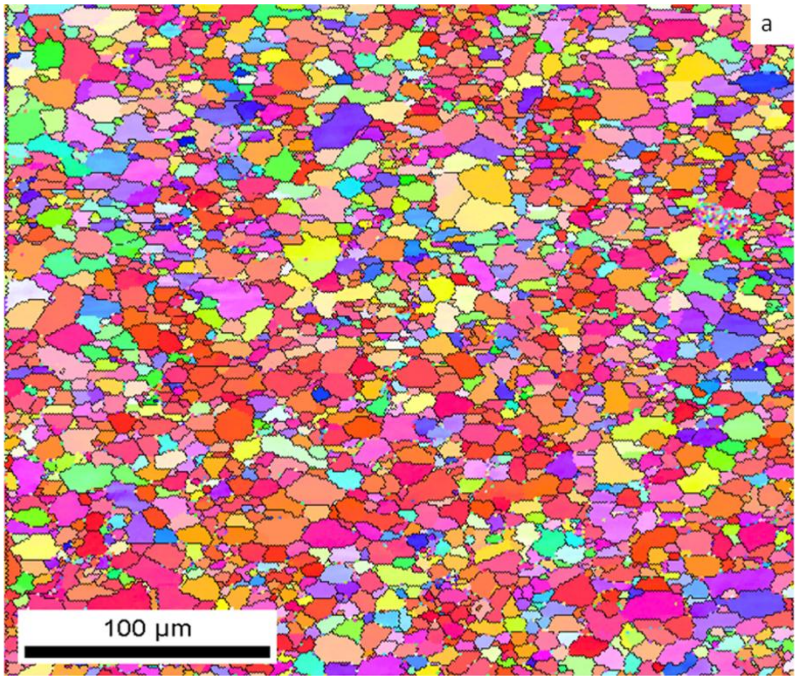

Figure 5.1 EBSD Microstructure after Mercury Quenching

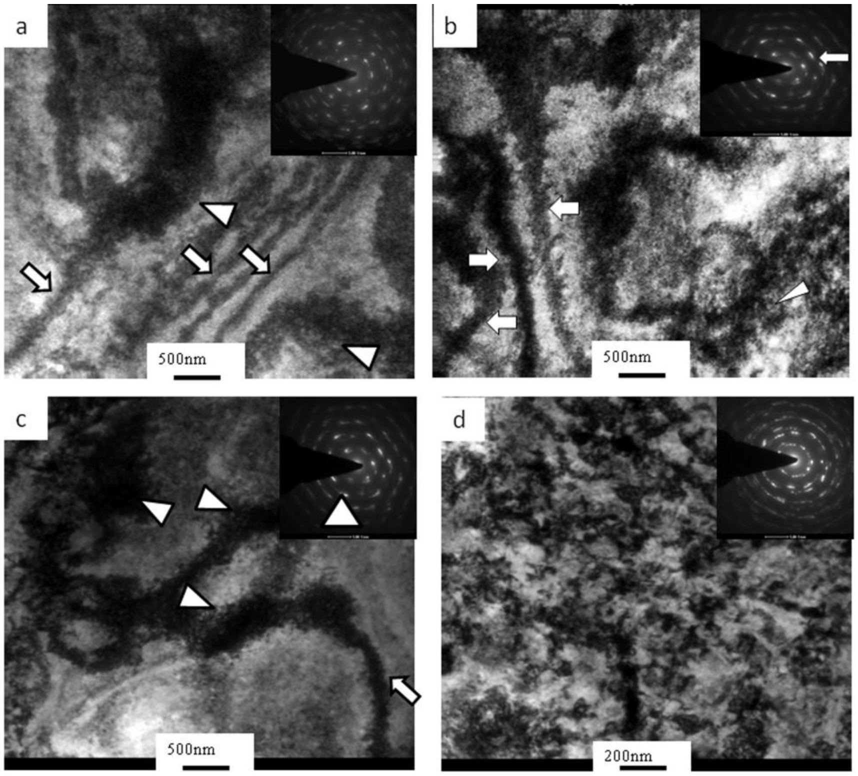

Figure 5.2 TEM Image of **(a)** 75% CR, **(b)** 85% CR, **(c)** 75% RTR and **(d)** 85% RTR Zircaloy-2 with Inset Showing the Diffraction Pattern

variance method, moment fourth order peak profile of Zircaloy-2 is calculated using X-ray diffraction which is related to the dislocation density of Zircaloy-2 as given by the Eq. (2) to estimate the dislocations present inside the material (Boebely *et al.,* 2001; Groma *et al.,* 1998; Sarkar *et al.,* 2008).

$$\frac{M_4(q)}{q^2} = \frac{1}{3\pi^2 \varepsilon_f} + \frac{\Lambda\langle\rho\rangle}{4\pi^2} + \frac{3\Lambda^2\langle\rho^2\rangle}{4\pi^2 q^2}\ln^2\left(q/q_1\right) \qquad \textbf{(5.2)}$$

where, $M_4(q)$– moment of peak profile

$\langle\rho\rangle$ – Average dislocation density

Λ – Geometrical constant describing strength of dislocation contrast

ε_f – Average column length

$q = 2/\lambda\ (\sin(\theta) - \sin(\theta_o))$

where, θ – Diffraction angle

θ_0 – Bragg's angle

q_1 – Fitting parameter

By fitting the straight line to $M_4(q)$ curve, average dislocation density is determined.

The effect of CR and RTR on the broadening of the selected peak can be seen from **Figure 5.3**. The peak at 34.79^o and 47.87^o represent the {002} and {012} planes of zircaloy-2 which are used to find the dislocation density. 75% and 85% CR zircaloy-2 is having more dislocations (1.678539 x 10^{16} /m^2 and 2.086366 x 10^{16}/m^2) as compared to the 75% and 85% room temperature rolled (1.168889 x 10^{16} /m^2 ,1.546860 x 10^{16} /m^2) due to suppression of dynamic recovery.

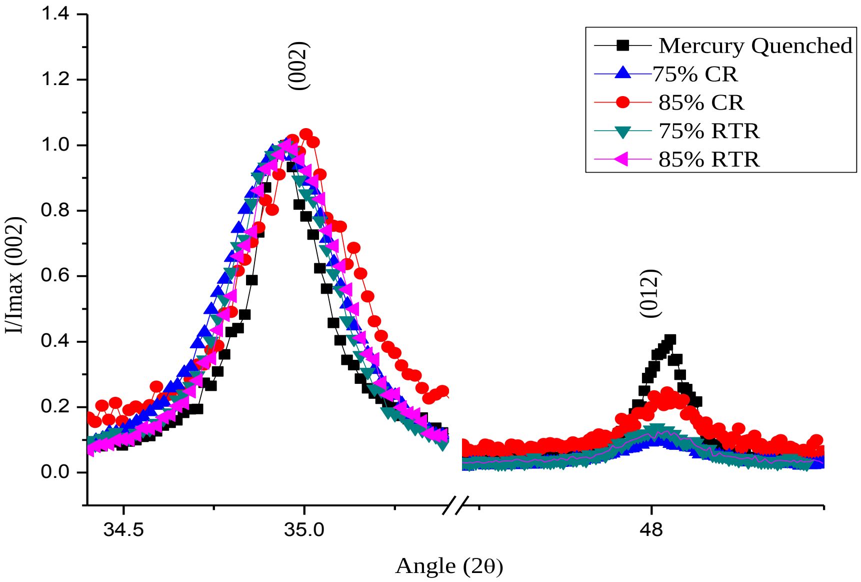

Figure 5.3 XRD Peak Showing the Effect of Cryorolling and Room Temperature Rolling

5.4.3 Tensile and Hardness Properties

Hardness and tensile behavior of the material can be seen from the **Table 5.1**. Hardness of the cryo rolled and room temperature rolled Zircaloy-2 increases gradually with the increase in thickness reduction. In comparison to mercury quenched Zircaloy-2, there is an increase of 35% and 47% in hardness with increase in thickness reductions in case of 75% and 85% room temperature rolled, while 41% and 54% increase in hardness with thickness reductions in case of 75% and 85% cryorolled as can be seen in **Table 5.1**. The room temperature rolled material has less increase in hardness as compared to cryorolled because at room temperature, there is some dynamic recovery occurs i.e. some of the dislocations are getting rearranged or the energy stored in the material during deformation is less. In case of cryorolling, the dynamic recovery is suppressed because of low temperature therefore more and more energy is stored. The results shown are validating the results obtained in TEM and by measured dislocation density of cryorolled and room temperature rolled zircaloy-2 using Variance method.

Table 5.1 Mechanical Properties of Mercury Quenched, CR and RTR Zircaloy-2

	Hardness (Hv)	Tensile strength (MPa)	Yield strength (MPa)	% elongation at break
800^{o}C Mercury Quenched	182	499	331	25
75% RTR	247	591	541	6.4
85% RTR	269	679	666	5.5
75% CR	257	800	765	5.07
85% CR	282	891	835	4.1

The yield strength of the 75% and 85% CR zircaloy-2 increases by 128% and 152% with increase in thickness reductions as compared to mercury quenched Zircaloy-2 while in room temperature rolled sample, there is an increase by 63% and 101% yield strength respectively (**Table 5.1**). There is an increase of 60% and 78% in tensile strength with thickness reduction in CR sample in comparison with mercury quenched sample while 18% and 36% increase in tensile strength in room temperature rolled zircaloy-2 respectively. The increment is more in yield strength as compared to tensile strength. This is beneficial also as larger the yield strength more will be the fracture toughness and fatigue life as compared to mercury quenched Zircaloy-2 under similar loading conditions.

5.4.4 Fracture Simulation

The tensile stress-strain data of zircaloy-2 is used for evaluating *J*-integral and internal energy values of mercury quenched, CR and RTR with 75% and 85% thickness reductions. The finite element software package Abaqus is used with elasto-plastic fracture mechanics approach. To compare the enhancement in the fracture properties of mercury quenched, 75% CR, 85% CR, 75% RTR and 85% RTR zircaloy-2, *J*-integral and internal energy are calculated for various two dimensional crack geometries having displacement control loading under plane stress and plane strain conditions. The different displacements were applied for evaluating the internal energy of the fractured specimens with constant crack length. An effective difference in the energy of CR and RTR zircaloy-2 has been observed due to increase in strength of CR and RTR zircaloy-2.

Figure 5.4 shows a comparison of mechanical properties of mercury quenched, CR and RTR zircaloy-2, which are improved after the suppression of dynamic recovery due to rolling at room temperature and cryo temperature. Two-dimensional quasi static crack growth analysis was performed using Ramberg Osgood relationship under displacement control loading condition. These simulations are performed under plane stress and plane strain conditions. Deformation plasticity model is used to develop Ramberg-Osgood material model given in Abaqus user's manual. In Ramberg-Osgood model, the elastic plastic properties of the material can be defined by a single function only. This model can be stated as,

$$E.\varepsilon = \sigma + \alpha\left(\frac{\pm\sigma}{\sigma_0}\right)^{n-1}\sigma \tag{5.3}$$

where, E is an elastic constant, ε is strain, σ is stress, σ_o is yield stress, α is yield offset and n is hardening exponent (nonlinear term (>1)) for the plastic material.

Strain energy can be derived by the relation

$$U = \int W \partial\varepsilon \tag{5.4}$$

For quasi static 2-D analysis, J integral is expressed as

$$J = \lim_{\Gamma\to 0}\int_{\Gamma} n.H.qd\Gamma \tag{5.5}$$

where, Γ is the contour beginning at the bottom of the crack surface and ending on to the top surface, n is the outward normal to Γ, q is the unit vector in the direction of virtual crack extension and H is given by

$$H = W\mathbf{I} - \sigma.\frac{\partial u}{\partial x} \tag{5.6}$$

where, W is defined as the elastic strain energy plus the plastic dissipation (Ref 2.16.1 Abaqus Theory Manual) for elasto-plastic behavior of the material and **I** is the identity matrix. Four 2-D crack problems are taken for the fracture simulations of mercury quenched, CR and RTR zircalloy-2.

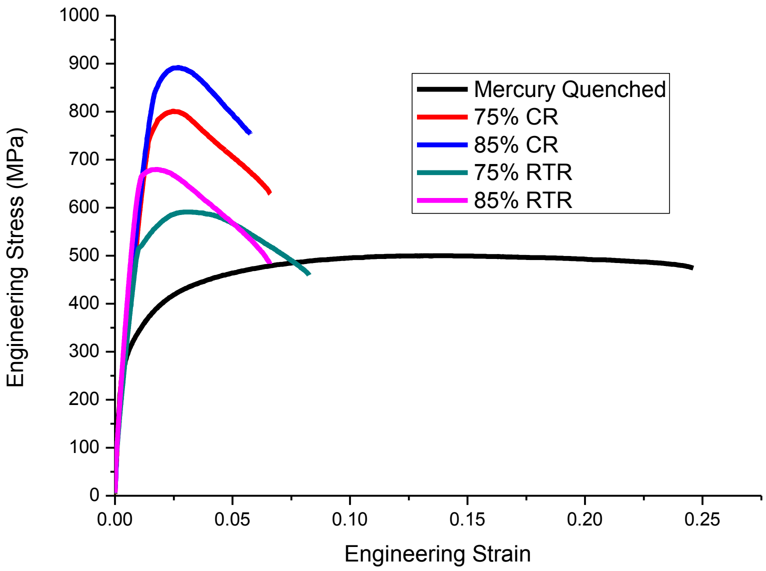

Figure 5.4 Stress Strain Curve for Mercury Quenched, CR and RTR Zircaloy-2

Case 1: Compact tension (CT) specimen

The dimensions of CT specimen are taken as per ASTM Standard E-1820-09E1 in **Figure 5.5**. An initial crack of length 15 mm is used to find the *J*-integral and strain energy of mercury quenched, CR and RTR Zircaloy-2 under plane stress and plane strain conditions. Unstructured mesh with 10 contours near the crack tip using CPS4R (4-node bilinear plane stress quadrilateral, reduced integration, hourglass control) element is used for analyzing plane stress, while CPE4R (4-node bilinear plane strain quadrilateral, reduced integration, hourglass control) is used for plane strain condition with displacement varying from 0.2 mm to 4 mm. **Figures 5.6(a-b) and 5.7(a-b)** show the effect of strengthening on internal energy and *J*-integral for mercury quenched, CR and RTR zircaloy-2 under plane stress and plane strain conditions. These figures clearly show that with the increase in yield strength, both *J*-integral and internal energy of zircaloy-2 are increasing. **Figures 5.8(a-e)** show the formation of plastic regions ahead of the crack tip after crack propagation under plane stress condition whereas **Figures 5.8(f-j)** show the formation of plastic regions ahead of the crack tip under plane strain condition. The 85% CR sample shows a large value of stress near the plastic zone as compared to mercury quenched and RTR zircaloy-2 which indicates a better crack arrest capabilities while the plastic region near the crack tip is decreasing as the strength of the zircaloy-2 is increasing which show that after rolling, the ductility of the zircaloy-2 is decreasing due to the increase in dislocations. These properties are visible in both plane stress and plane strain conditions.

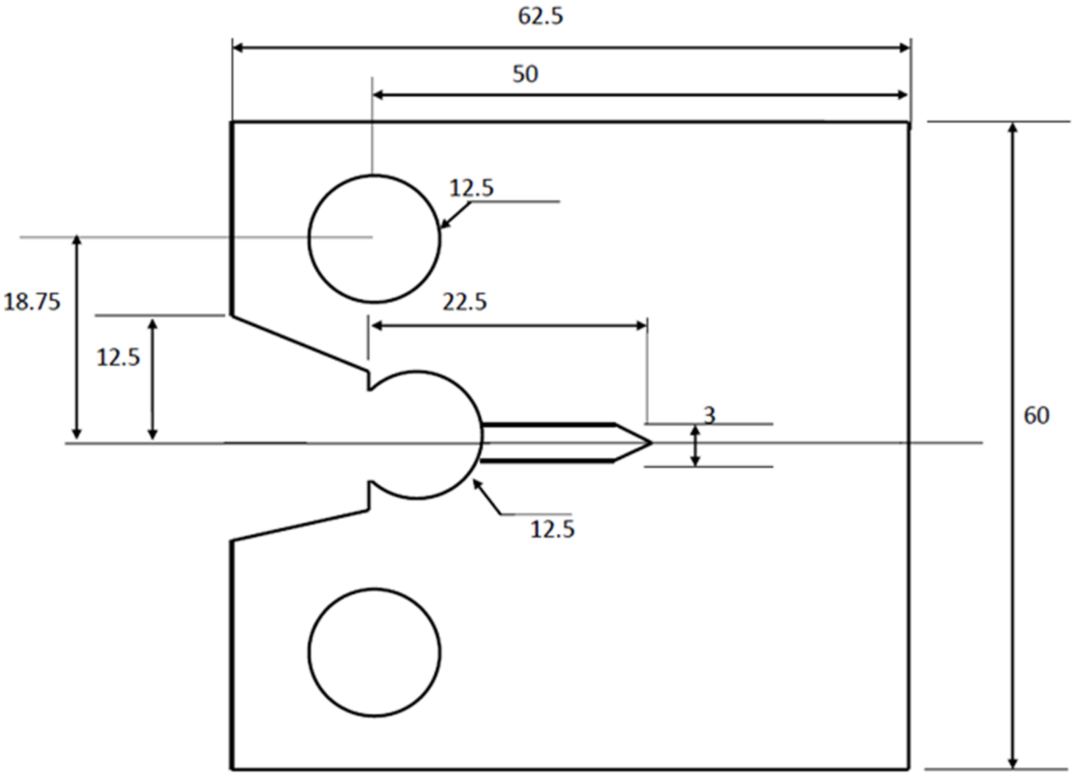

Figure 5.5 Geometry and Dimensions of the Compact Tension Specimen

Case 2: Edge crack under mode-I load

A 2-D 60mm x 50mm dimension specimen having a crack length of 15 mm on the edge has been used to analyze Mercury Quenched, CR and RTR zircaloy-2 with different thickness reductions. Unstructured mesh having 10 contours near the crack tip with CPS4R and CPE4R elements have been used to compare *J*-integral and strain energy. The edge cracks are generally developed on the surface of the material due to impact or rough polishing.

Figures 5.9(a-b) show the plots of internal energy for mercury quenched, CR and RTR zircaloy-2 under plane stress and plane strain respectively whereas **Figures 5.10(a-b)** show the plots of *J*-integral for mercury quenched, CR and RTR zircaloy-2 under plane stress and plane strain respectively. From these figures, it can be seen that both *J*-integral and internal energy are increasing as can be seen from **Figures 5.9(a-b) and 5.10(a-b)**. 85% CR zircaloy-2 sample shows the highest *J*-integral and internal energy values. These plots show that as the strength of the alloy is increasing, the crack arrest capability of the material is also increasing for a given displacement as more energy is needed to propagate the crack. The plastic region near the crack tip shows a decrease in plastic region for a given displacement of 0.2 mm, which shows strain hardening of the alloy due to rolling as can be seen from **Figures 5.11(a-e)** under plane stress condition while **Figures 5.11(f-j)** show the plastic region under plane strain condition.

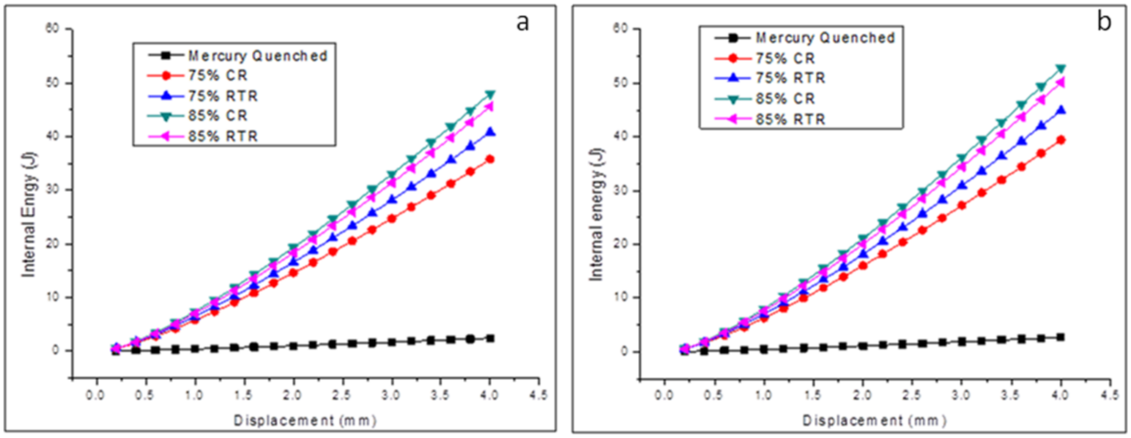

Figure 5.6: The Numerical Results for a CT Specimen **(a)** Internal Energy Under Plane Stress **(b)** Internal Energy Under Plane Strain

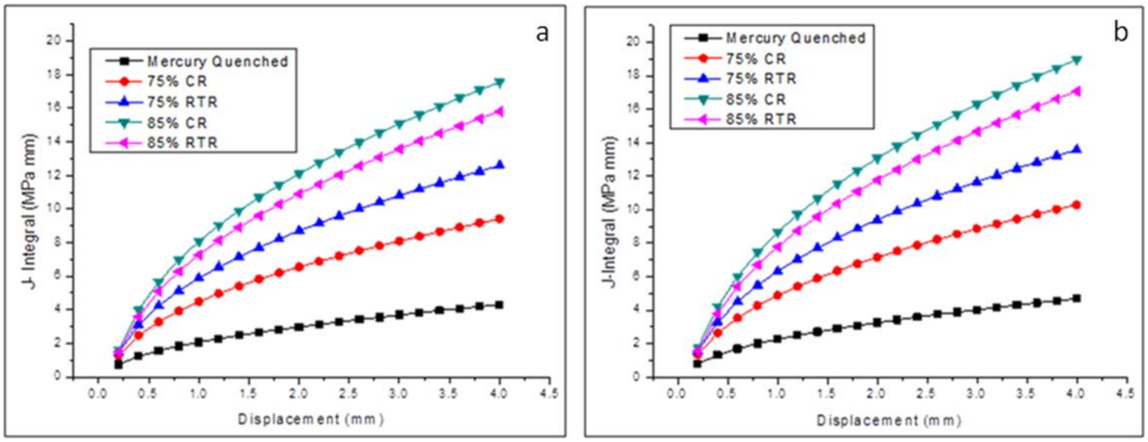

Figure 5.7 The Numerical Results for a CT Specimen **(a)** *J*-Integral Under Plane Stress **(b)** *J*-Integral Under Plane Strain

Case 3: Center crack under mode-I load

A 60 mm x 50 mm specimen having a crack length of 15 mm at the center has been taken to analyze mercury quenched, CR and RTR zircaloy-2. An unstructured mesh having 10 contours near the crack tip with CPS4R and CPE4R elements have been taken to compute *J*-integral and strain energy. The simulation of center crack in a specimen is quite common problem from the fracture mechanics point of view as these types of cracks are formed in the material during casting.

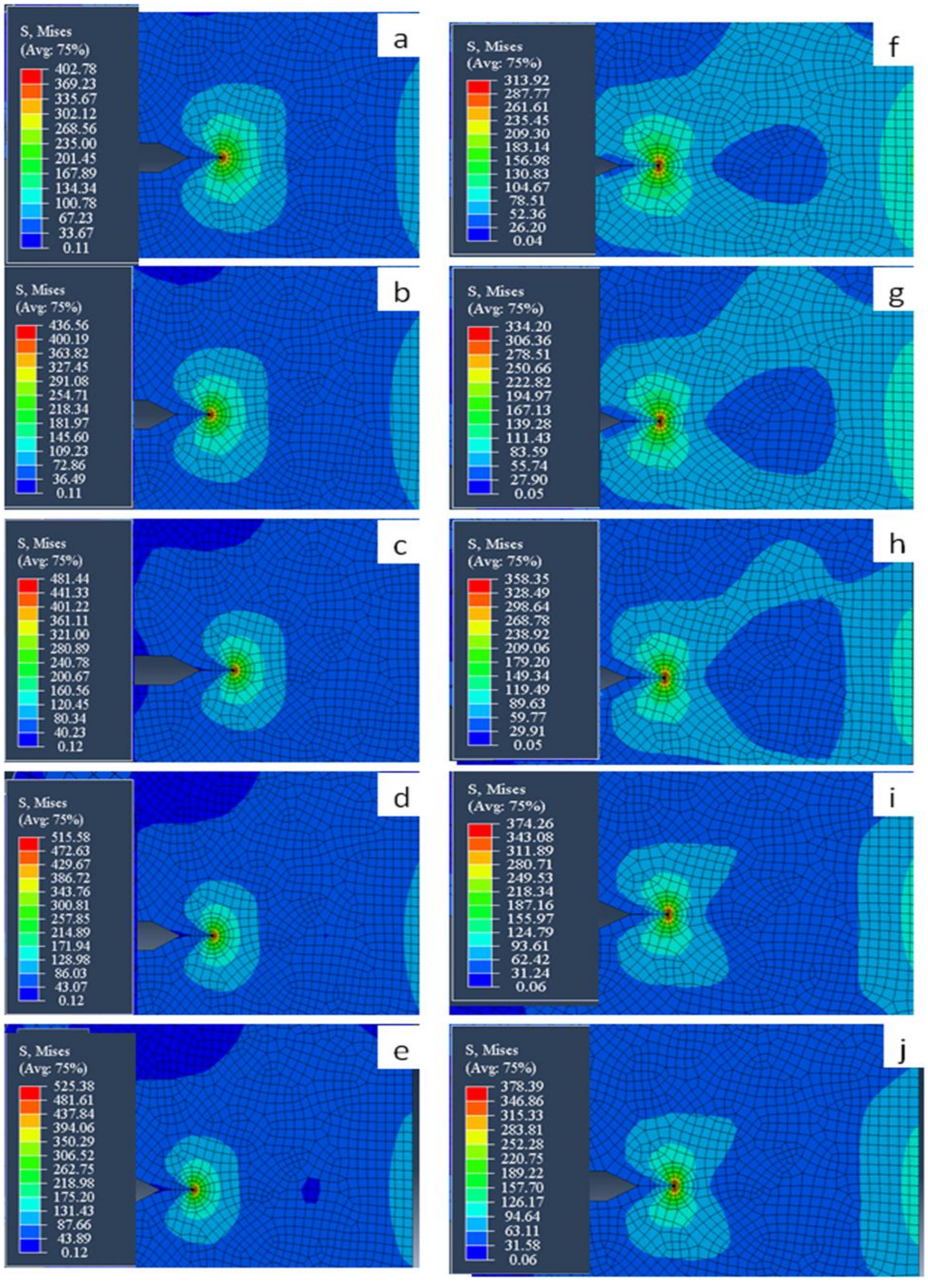

Figure 5.8 Crack Tip von-Mises Stress for a CT Specimen Corresponding to 0.2 mm Displacement at Different Processing Conditions **(a)** Mercury Quenched Under Plane Stress **(b)** 75% RTR Under Plane Stress **(c)** 75% CR Under Plane Stress, **(d)** 85% RTR Under Plane Stress **(e)** 85% CR Under Plane Stress **(f)** Mercury Quenched Under Plane Strain **(g)** 75% RTR Under Plane Strain **(h)** 75% CR Under Plane Strain **(i)** 85% RTR Under Plane Strain **(j)** 85% CR Under Plane Strain

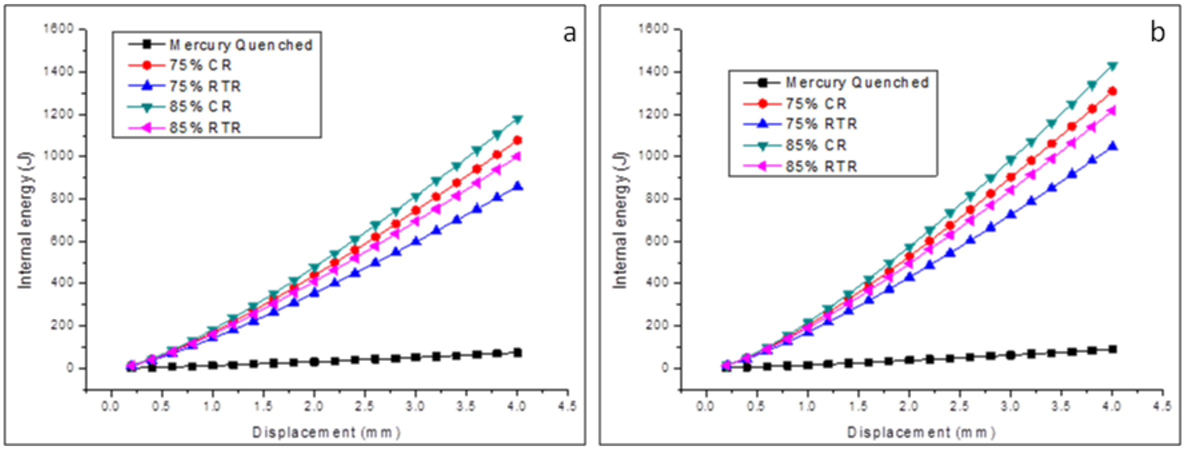

Figure 5.9 The Numerical Results for an Edge Crack Specimen **(a)** Internal Energy Under Plane Stress **(b)** Internal Energy Under Plane Strain

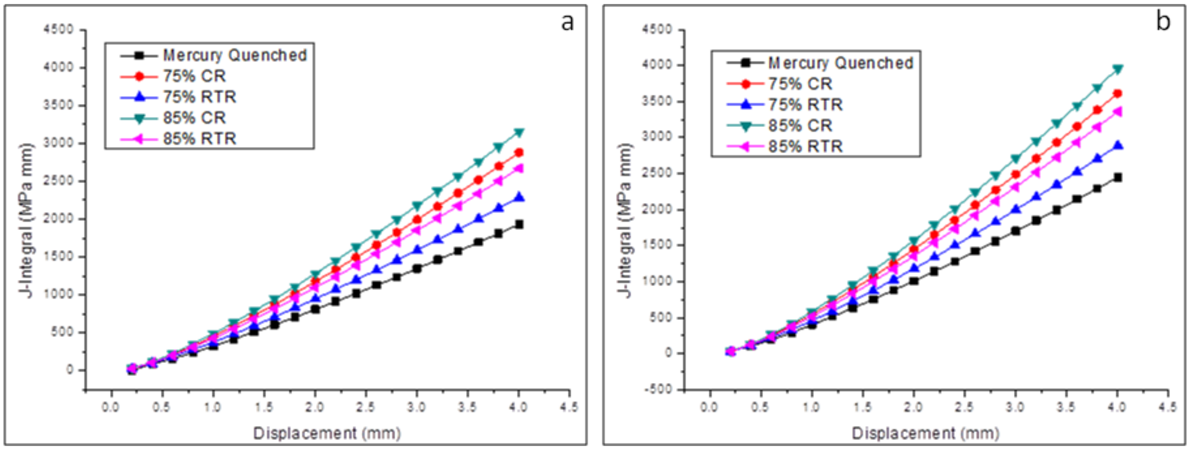

Figure 5.10 The Numerical Results for an Edge Crack Specimen **(a)** *J*-Integral Under Plane Stress **(b)** *J*-Integral Under Plane Strain

Figures 5.12(a-b) show the plots of internal energy for mercury quenched, CR and RTR zircaloy-2 under plane stress and plane strain conditions respectively whereas **Figures 5.13(a-b)** show the plots of *J*-integral for mercury quenched, CR and RTR zircaloy-2 under plane stress and plane strain conditions respectively. From the results presented in **Figures 5.12(a-b) and 13(a-b),** one can see that with the increase in displacement, *J*-integral and internal energy values of 85% CR zircaloy-2 are found more as compared to RTR and mercury quenched zircaloy-2 for both plane stress and plane strain conditions. The results show that 85% CR sample requires more energy for crack propagation as the size plastic zone of the plastic zone for 85% CR sample is small. The effect of strain hardening due to rolling on zircaloy-2 is shown in **Figures 5.14(a-e)** for plane stress

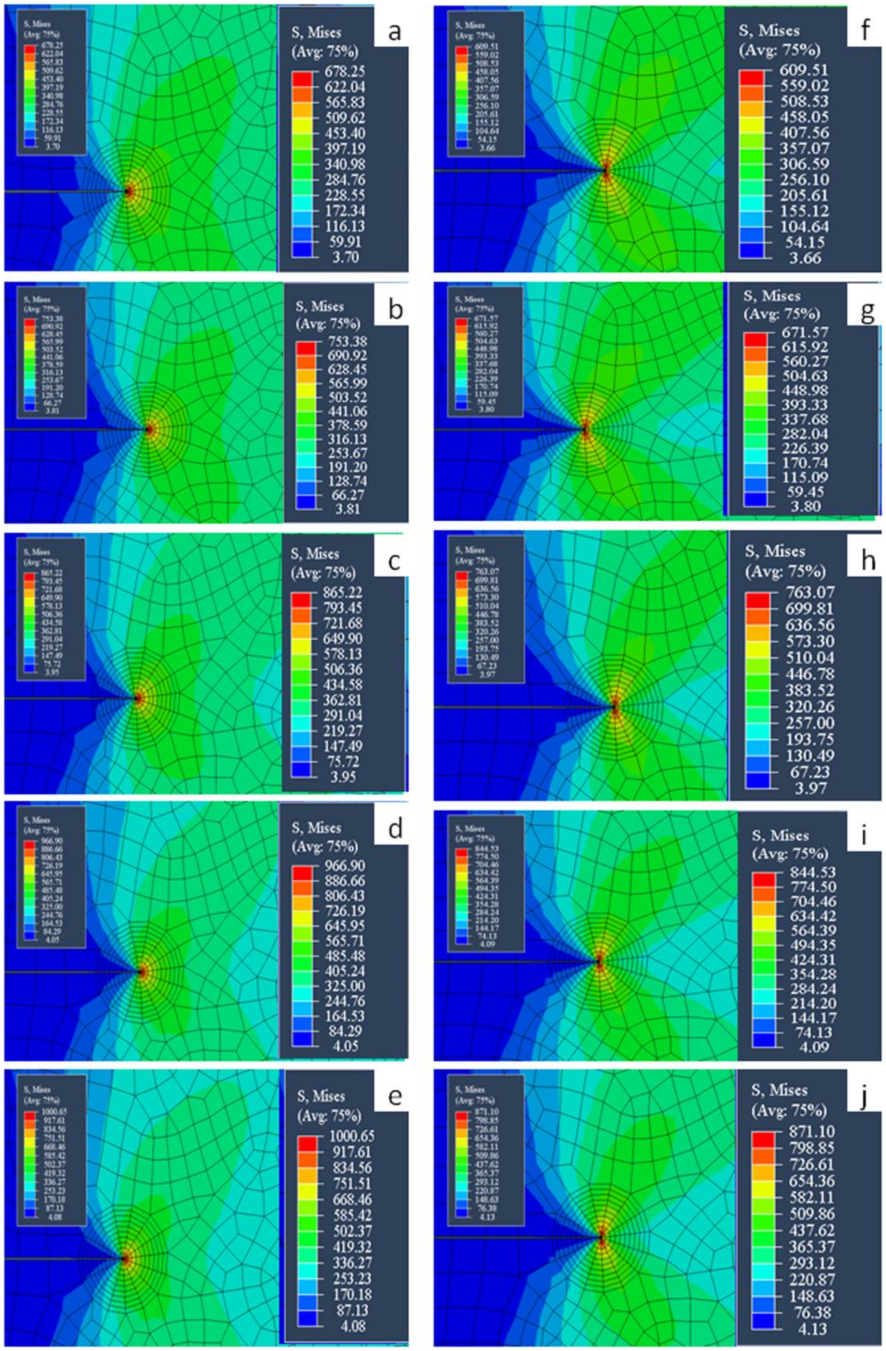

Figures 5.11 Crack Tip von-Mises Stress for an Edge Crack Specimen Corresponding to 0.2 mm Displacement at Different Processing Conditions **(a)** Mercury Quenched Under Plane Stress **(b)** 75% RTR Under Plane Stress **(c)** 75% CR Under Plane Stress, **(d)** 85% RTR Under Plane Stress (e) 85% CR Under Plane Stress (**f)** Mercury Quenched Under Plane Strain **(g)** 75% RTR Under Plane Strain **(h)** 75% CR Under Plane Strain **(i)** 85% RTR Under Plane Strain **(j)** 85% CR Under Plane Strain

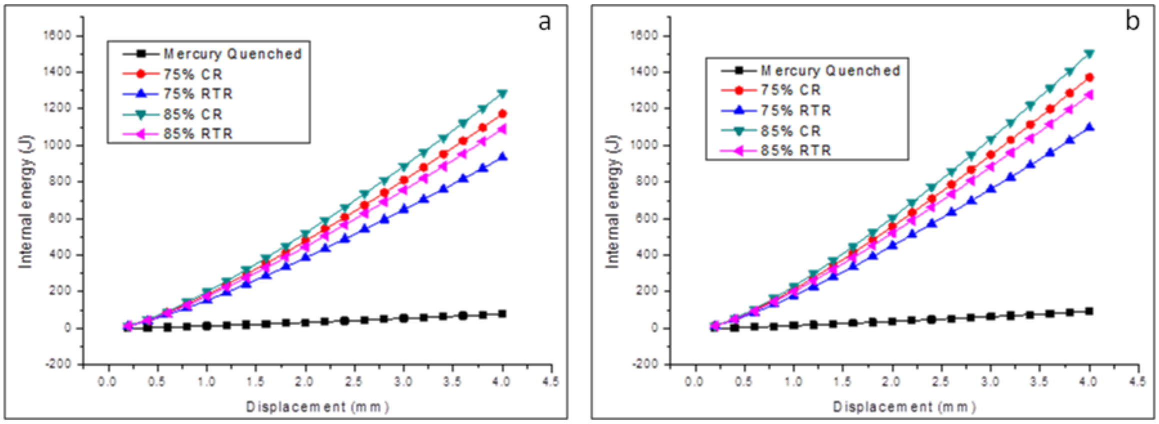

Figure 5.12 The Numerical Results for a Center Crack Specimen **(a)** Internal Energy Under Plane Stress **(b)** Internal Energy Under Plane Strain

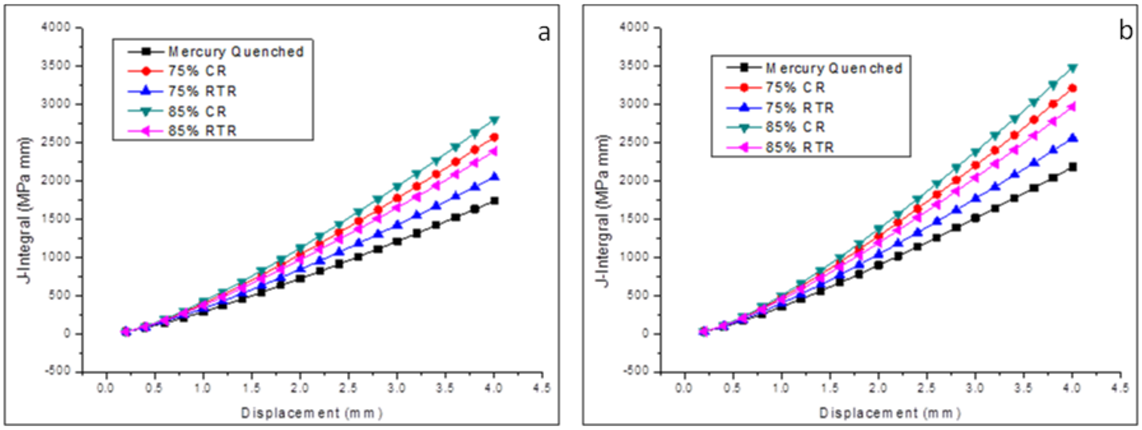

Figure 5.13 The Numerical Results for a Center Crack Specimen **(a)** *J*-Integral Under Plane Stress **(b)** *J*-Integral Under Plane Strain

condition while **Figures 5.14(f-j)** show the effect of strain hardening due to rolling on zircaloy-2 for plane strain condition. The values of *J*-integral for a center crack are found less as compared to an edge crack which shows that less amount of energy is required to propagate a center crack in the specimen as compared to propagate an edge crack in the specimen.

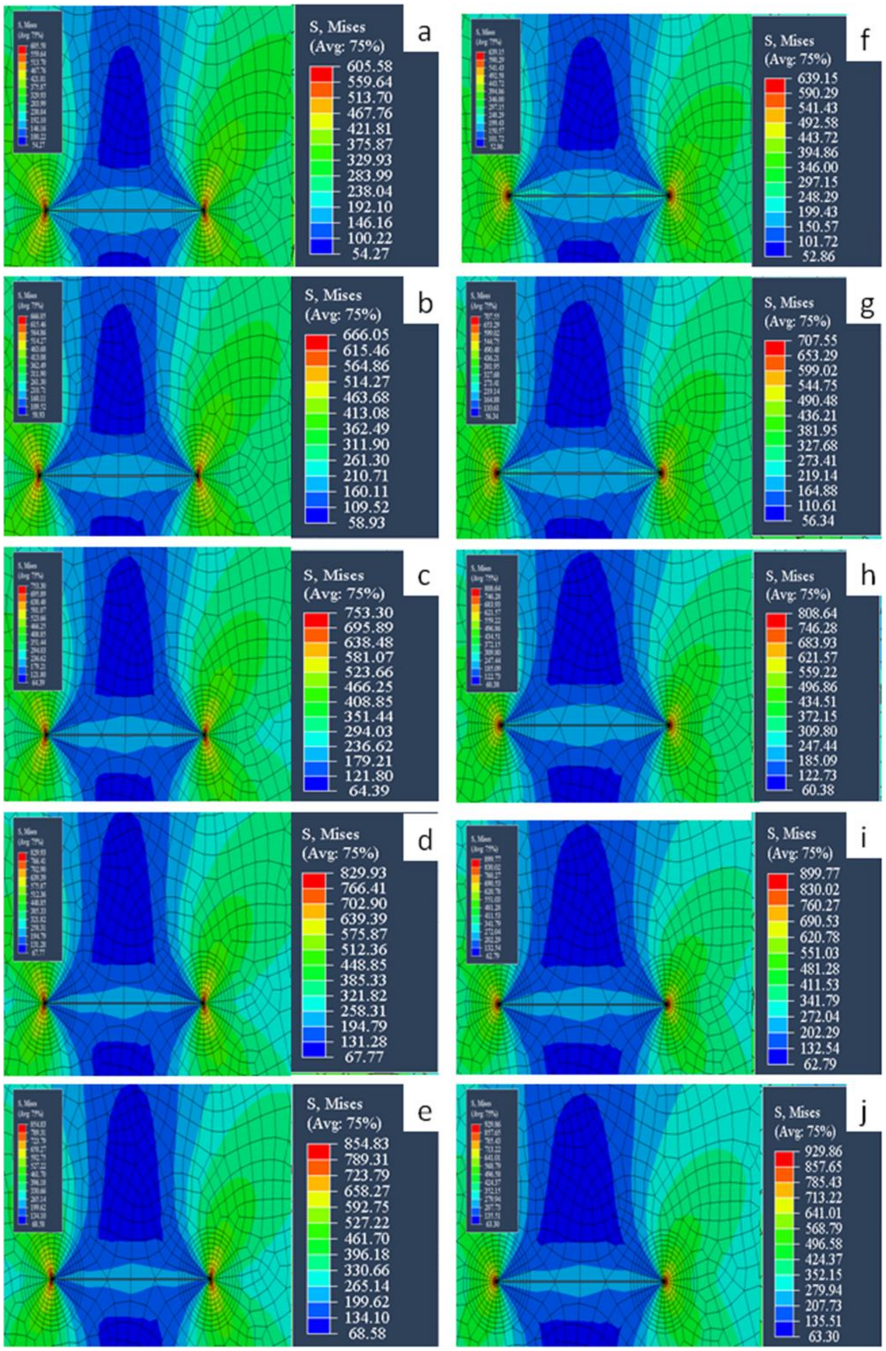

Figure 5.14 Crack Tip von-Mises Stress for a Center Crack Specimen Corresponding to 0.2 mm Displacement at Different Processing Conditions **(a)** Mercury Quenched Under Plane Stress **(b)** 75% RTR Under Plane Stress **(c)** 75% CR Under Plane Stress, **(d)** 85% RTR Under Plane Stress (**e**) 85% CR Under Plane Stress (**f)** Mercury Quenched Under Plane Strain **(g)** 75% RTR Under Plane Strain **(h)** 75% CR Under Plane Strain **(i)** 85% RTR Under Plane Strain **(j)** 85% CR Under Plane Strain

Case 4: Double Edge Crack Under Mode-I Load

A specimen of size 60 mm x 50 mm having a crack of length 10 mm on each edge has been used to analyze mercury quenched, CR and RTR zircaloy-2. An unstructured mesh having ten contours near the crack tip is used to compare *J*-integral and internal energy. If the length of anyone crack becomes more, then it keeps on propagating until failure. This case is not commonly seen as the casted alloy has lots of defects in which we try to reduce them by rolling or extrusion, and further by annealing.

Figures 5.15(a-b) show the plots of internal energy for mercury quenched, CR and RTR zircaloy-2 under plane stress and plane strain conditions respectively while **Figures 5.16(a-b)** show the plots of *J*-integral under plane stress and plane strain conditions respectively. From **Figures 5.15(a-b) and 5.16(a-b),** it can be seen that 85% CR zircaloy-2 show larger *J*-integral values as compared to mercury quenched and RTR samples for both plane stress and plane strain conditions. These results show that 85% CR zircaloy-2 is the best for reducing the possibility of crack propagation. The decrease in the size of plastic region in RTR and CR zircaloy-2 indicates strain hardening due to rolling which can be clearly seen in **Figures 5.17(a-e)** under plane stress condition and in **Figures 5.17(f-j)** under plane strain condition.

The study of crack propagation in various cracked specimens shows that the CR zircaloy-2 owns the better crack arrest capabilities as compared to mercury quenched and room temperature rolled zircaloy-2.

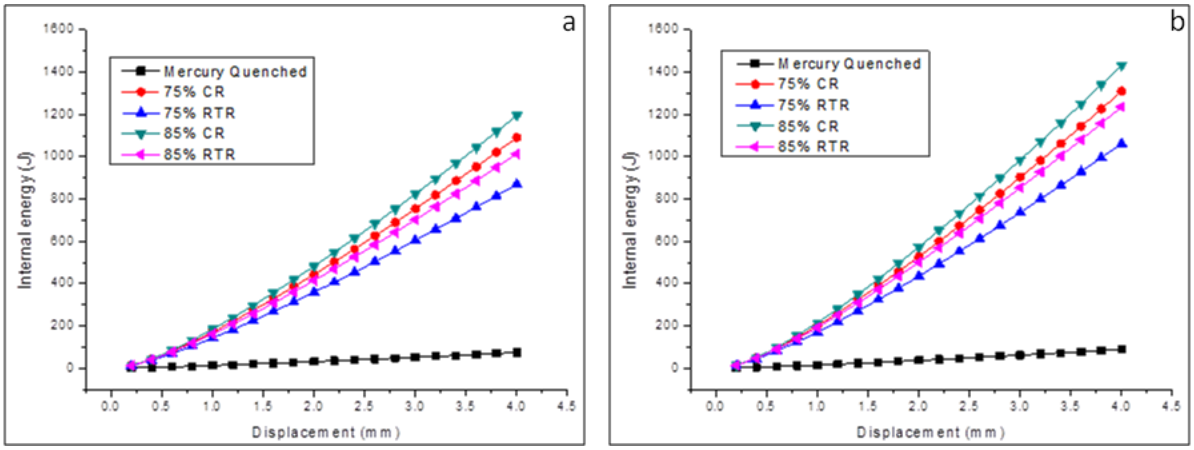

Figure 5.15 The Numerical Results for a Double Edge Cracked Specimen **(a)** Internal Energy Under Plane Stress **(b)** Internal Energy Under Plane Strain

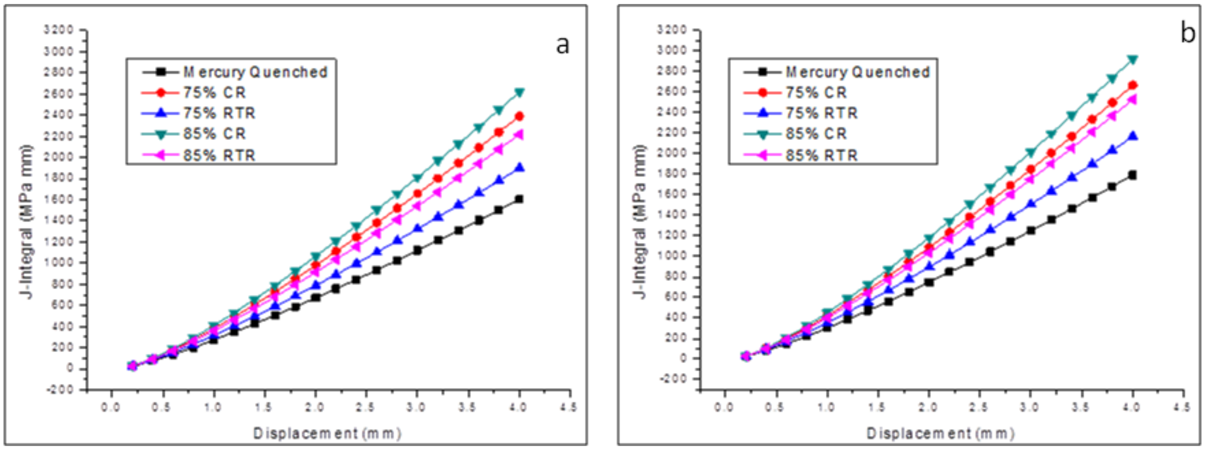

Figure 5.16 The Numerical Results for a Double Edge Cracked Specimen **(a)** *J*-Integral Under Plane Stress **(b)** *J*-Integral Under Plane Strain

5.4.5 Fatigue Simulation

Fatigue simulations of the mercury quenched, 75% and 85% CR and RTR zircaloy-2 are performed in ANSYS software. Gerber criterion for evaluating the fatigue life of the alloy is assumed to be good for ductile materials as it treats both negative and positive means stresses while others theory such as Goodman and Soderberg do not include both. Gerber criterion can be described by the following equation:

$$\frac{\sigma_{Alternating}}{\sigma_{Endurance\_Limit}} + \left(\frac{\sigma_{Mean}}{\sigma_{Ultimate\_Strength}} \right)^2 = 1 \tag{5.7}$$

The dimensions of the fatigue specimen (**Figure 5.18(a)**) are taken from ASTM E468-11 along with the different values of stresses to estimate the S-N curve. First of all, mercury quenched sample results are compared with the literature (Whitmarsh 1982). These results show that the S-N curve is found quite similar to the results of zircaloy-2 given in the literature (Whitmarsh 1982). The results of mercury quenched, 75% CR, 75% RTR, 85% CR and 85% CR zircaloy-2 are compared with each other. The S-N curve obtained from the simulations is shown in **Figure 5.18(b).** From **Figure 5.18(b)**, it can be seen that 85% CR sample requires maximum failure cycles as compared to mercury quenched and room temperature rolled samples. This is due to the increase in yield strength of the 85% CR zircaloy-2 due to the suppression of dynamic recovery at liquid nitrogen

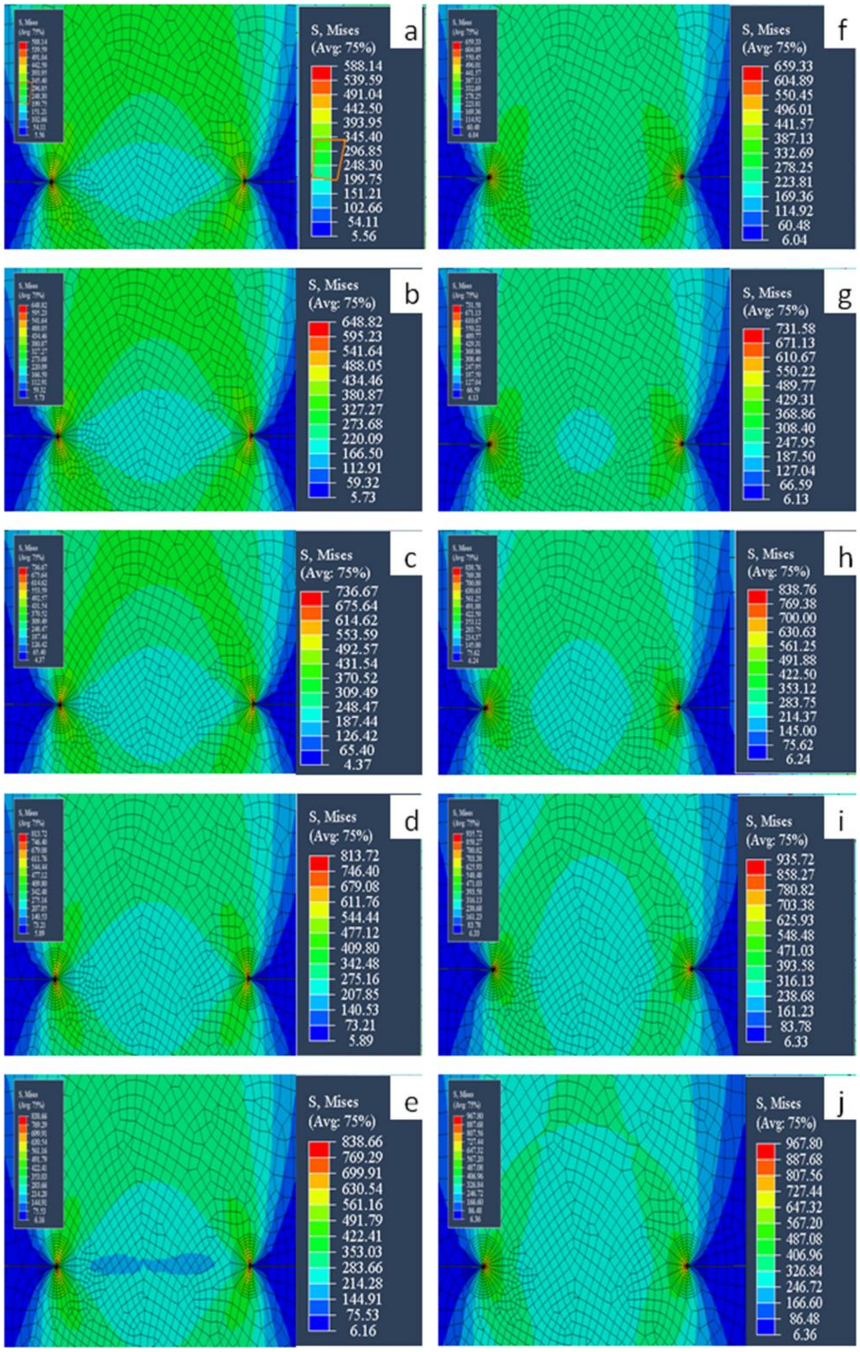

Figures 5.17 Crack tip von-Mises stress for a Double Edge Crack Specimen corresponding to 0.2 mm Displacement at Different Processing Conditions **(a)** Mercury Quenched Under Plane Stress **(b)** 75% RTR under Plane Stress **(c)** 75% CR Under Plane Stress, **(d)** 85% RTR Under Plane Stress (e) 85% CR Under Plane Stress (**f)** Mercury Quenched Under Plane Strain **(g)** 75% RTR Under Plane Strain **(h)** 75% CR Under Plane Strain **(i)** 85% RTR Under Plane Strain **(j)** 85% CR Under Plane strain

temperature during plastic deformation. Under cyclic load, many defects are developed due to the generation of dislocations inside the crystals, and they start accumulating and propagating. The process, in which the dislocations forms substructure inside the grain to minimize the energy of the crystal system (known as a strain hardening) results in the increase of material strength. In some materials, slip bands are formed to overcome the strain localization. These slip bands are responsible for the formation of cracks during loading. The formation of slip bands is possible in 75% RTR and CR zircaloy-2 due to larger size grain. This can also be stated that more is ductility, more will be the fatigue life. After strain hardening, the fatigue life of the alloy is reduced but if its is compared with a non-strain hardened material under same loading conditions, then the fatigue life of the strain hardended material will be more than a non-strain hardening material as can be seen from the simulations.

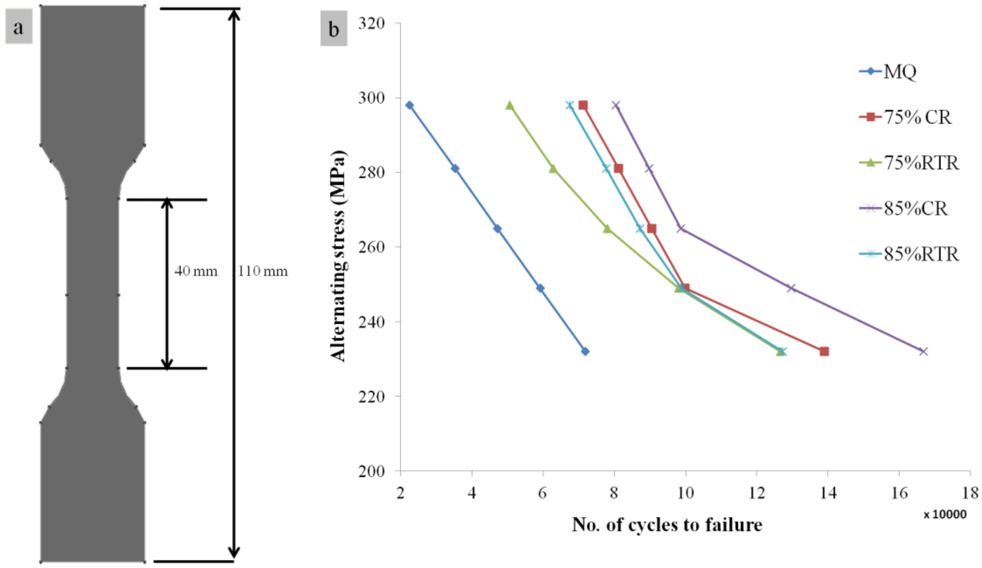

Figure 5.18(a) Dimensions of Fatigue sample, **(b)** S-N curve for Mercury Quenched, CR and RTR Zircaloy-2

5.5. Summary

On the basis of present study, the following conclusions are drawn

- 85% CR zircaloy-2 is found to have maximum dislocation density 2.086366x10^{16}/m^2 and tensile strength 891 MPa.
- TEM microstructure reveals the formation of dislocation cells and dislocation tangles inside the crystal due to plastic deformation in zircaloy-2.

- Due to dynamic recrystallisation, nanocrystalline grain formation has been observed in 85% room temperature rolled zircaloy-2 with an average grain size of 150 nm.
- In 85% CR zircaloy-2, large value of *J*-integral and internal energy has been found in different crack problems for both plane stress and plane strain conditions.
- With the decrease in thickness, the plastic zone size at the crack tip is reduced due to strain hardening.
- Fatigue simulations show that 85% CR zircaloy-2 has got maximum fatigue life.

5.2 Effect on the Fracture Toughness of Zircaloy-2 after Rolling and Cross Rolling at Different Temperatures: Experimental and Simulation Study

5.2.1 Introduction

Unstable and fast growth of crack leads to the sudden failure of components or structures. Various experimental and simulation techniques has been developed by various researchers to detect the crack growth in its early stages (Nurse and Patterson, 1990; Maiti *et al.*, 2003; Vadiraj *et al.*, 2006a, 2006b; Bind *et al.*, 2013; Singh *et al.*, 2014, Choubey *et al.*, 2006; Zhong *et al.*, 2007). The materials which are used to bear the load have various defects in the form of microscopic cracks and voids. These cracks after some time grow and results in the catastrophic failure of components, which can be very dangerous. After losing the life of people and failure of large structures, the scientists have now considered fracture toughness as relevant material parameter for designing. Over the last few decades better understanding of fracture mechanics has substantially reduced the risk of structure failure. The life of the components or structures in presence of crack growth can be accurately predicted through numerical simulations.

Over the years, the finite element method has been developed a very useful tool in solving various nonlinear problems of engineering and sciences (Chung *et al.*, 1998; Yoon *et al.*, 2004). But it has got some issues in analyzing the fracture mechanics problems which is mainly due to the requirement of conformal mesh to model and simulate the crack growth problems. In addition to this, true stress and strain field around the crack tip can only be captured by mesh refinement. To overcome these issues, extended Finite element method (XFEM) has been developed as an indispensable tool to solve fracture mechanics problems (Belytschko *et al.*, 1999). In XFEM, discontinuities can be handled without a need of conformal mesh (Sharma *et al.*, 2013; Liu *et al.*, 2014).

The cracks can be easily identified and handled through level set functions, which allows the discontinuity to be independent of mesh (Nguyen-Vinh *et al.*, 2012; Talebi *et al.*, 2013, Pathak *et al.*, 2013). Hence, XFEM is considered very useful tool for modelling problems involving discontinuities. The advantages of XFEM are listed below:

- A finite element mesh is used to describe and discretize the domain.
- Various discontinuities including cracks are modeled using the same mesh.
- Shape and size of discontinuity does not affect the finite element mesh.

- Conformal meshing is not required even for arbitrary discontinuity.
- There is no need to re-meshing for growing cracks.
- Mesh is independent of crack location so tracking the time history of points is not required.
- Higher accuracy can be achieved with less number of data points.
- The level sets are used for tracking the moving discontinuities such as cracks.
- Cracks, holes, inclusions, shear bands, and dislocations are modeled using various enrichment functions.

On the basis of above advantages, XFEM will be used in the present work for the fracture mechanics simulations.

5.2.2 Experimental Procedure for Fracture Toughness Testing

Rolled 4 mm thick zircaloy-2 sheet obtained from nuclear fuel complex, Hyderabad is heat treated at 800 ^{o}C in Argon environment and quenched in mercury. Samples of dimensions 60 mm x 60 mm are cut and rolled at different temperatures. Normal and cross rolling at room temperature and cryo temperature upto 25%, 50%, 75% and 85% thickness reductions have been done. Compact test (CT) specimens were prepared according to ASTM E-1820-09E1 standard and are tested under mode-I loading. Samples above 25% thickness reductions were not tested, as lower thickness leads to buckling during fracture toughness testing. Fatigue cracking with minimal load of 0.6 times of yield value is initially applied to generate micron cracks near the crack tip. The constant displacement loading is applied with a strain rate of 1 x $10^{-6}s^{-1}$. Fractures surface is ultrasonically cleaned and analyzed using FEI Quanta 200 FEG-SEM.

The critical value of stress intensity factor is calculated for different thickness reduction and rolling conditions using XFEM software package.

5.2.3 Experimental Results

5.2.3.1 Initial Microstructure with Texture Pole Analysis

Initial microstructure of as received, mercury quenched, 25% cryo rolled (CR), room temperature rolled (RTR), cryo cross rolled (CCR) and room temperature cross rolled (RTCR) can be seen from **Figure 5.19(a-f).** The microstructure of as received sample was heterogeneous, while mercury quenched, deformed 25% RTR and CR sample show an average grain size of 10 µm, while the deformed microstructure obtained after 25% RTCR and CCR is decreased to 9.5 due to twinning activity. The twinning activity is more in CCR and RTCR zircaloy-2 as compared to CR and RTR condition. Extension $\{10\bar{1}2\}$ twinning is present in most of the grains which provide initial hardening to the rolled CCR and RTCR zircaloy-2. Mis-orientations ranging from 20 to 25^{o} is also present in some grains in CCR and RTCR condition which shows the contraction twin activation.

Pole figure of as received, mercury quenched, 25% CR, 25% RTR, 25% CR and 25% CCR can be seen in **Figure 5.20(a-f)**. Since, the as received sample was already deformed as shown in **Figure 5.20(a**), the sample after mercury quenching is also textured {0002} pole. After CR and RTR, there is not much change in the texture but in case of CCR and RTCR {0002} poles are strongly textured. The difference in intensity can be seen in the order MQ<RTR<CR<RTCR<CCR. The variation in the intensity of {0002} pole also shows the effect on tensile strength. Although, $\{01\bar{1}2\}$ intensity does not changed much but the poles in RTR and CR are inclined towards the rolling direction and are got spread in case of CCR and RTCR.

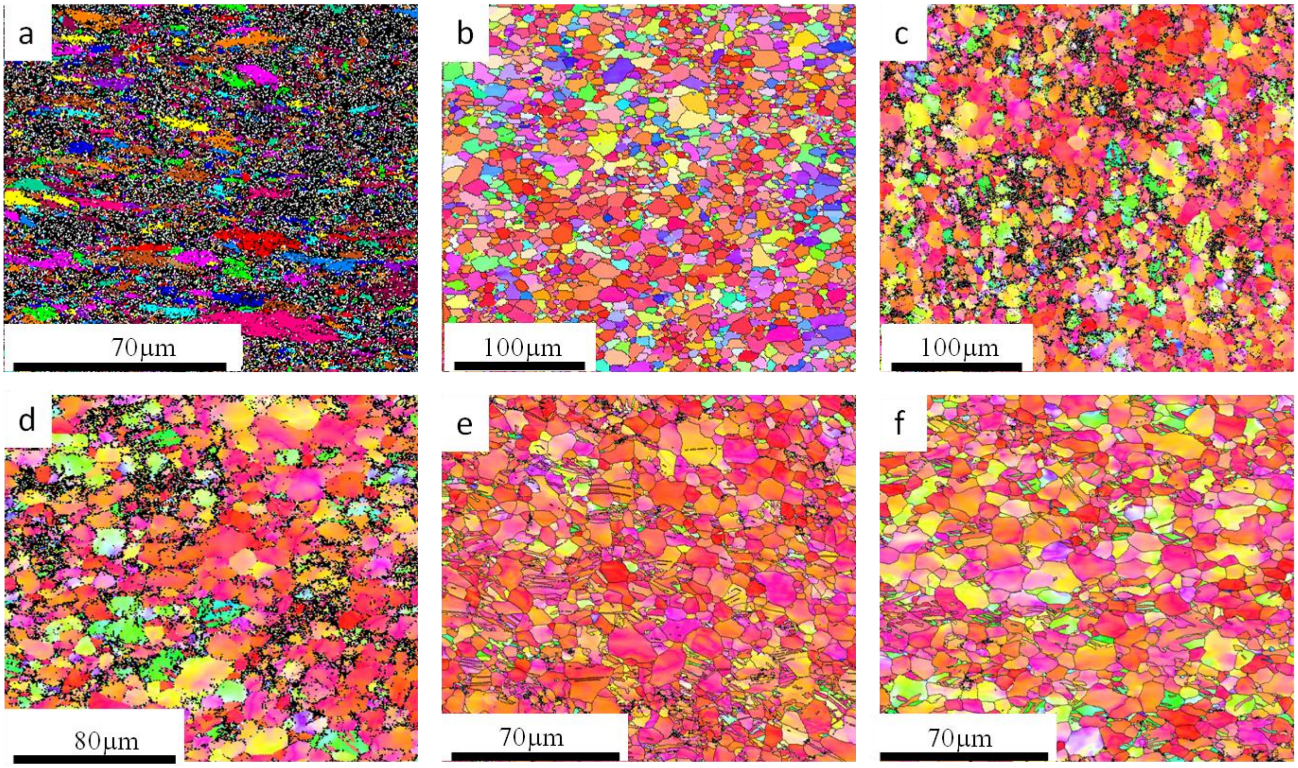

Figure 5.19 EBSD Microstructure of **(a)** As Received, **(b)** MQ, **(c)** 25% CR, **(d)** 25% RTR, **(e)** 25% CCR and **(f)** 25% RTCR Zircaloy-2

5.2.3.2 Load vs. Displacement Curve Analysis

The load vs. displacement curve for as received, MQ, 25% CR, 25% RTR, 25% CCR, 25% RTCR can be seen from **Figure 5.21**. The MQ and as received samples have thickness 4.3 mm; while 25% rolled samples have a thickness of 3.2 mm. The effect of thickness on the curve can clearly be seen in load displacement curve. Samples with 3.2 mm thickness showed plastic region in load vs. displacement curve as compared to 4.3 mm thick samples. The maximum load reached by MQ and as received samples is 10.3 KN and 12.5 KN respectively for 4.3 mm thickness. The maximum load reached by 25% CR, 25% RTR, 25% CCR and 25% RTCR are 12.4 KN, 11.1 KN, 13.2 KN and 12.2 KN respectively for with 3 mm thickness. Although, there is no grain refinement at 25% rolling reduction but the rolled zircaloy-2 showed the better crack arresting capabilities as compared to MQ. The reason is that the dislocations produced near the crack tip starts moving towards the grain boundary. Since, the dislocations are already present inside the grains, these dislocation produced are stopped by the pre-existing dislocations which results in the development

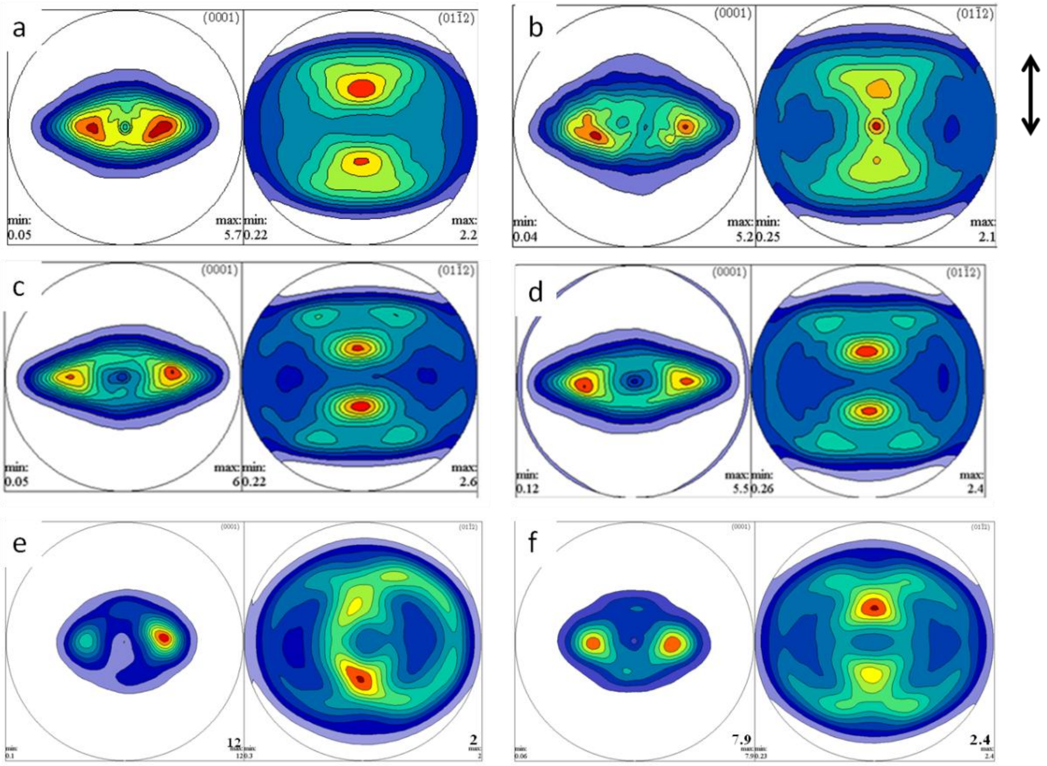

Figure 5.20 {0002} and $\{01\bar{1}2\}$ Pole figure image of **(a)** As received, **(b)** MQ, **(c)** 25% CR, **(d)** 25% RTR, **(e)** 25% CCR and **(f)** 25% RTCR Zircaloy-2, respectively with mark showing the Loading Direction during Fracture Toughness Testing

of back stress. Thus, it becomes hard for the dislocations to glide away from the crack tip and back stress becomes strong. Hence, the material fails by becoming brittle. This process is known as dislocation shielding (Becker *et al.*, 2002). Also, in case of CCR and RTCR, the plastic region is more as compared to CR and RTR, which may be due to the pre-existing dislocations are already reported. The experimental value of K_{IC} calculated from the load displacement curve can be seen in **Table.1**.

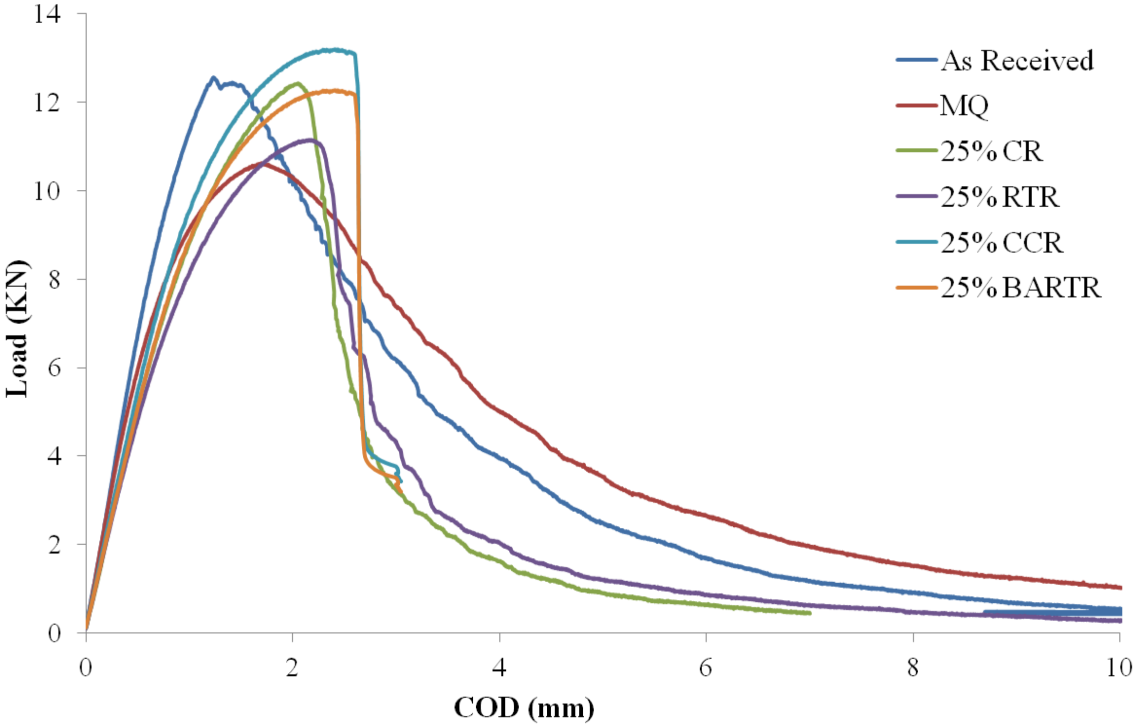

Figure 5.21 Load vs Crack Opening Displacement (COD) Curve obtained after CT Specimen Testing of As Received, MQ, 25% CR, 25% RTR, 25% CCR and 25% RTCR Zircaloy-2, respectively

5.2.3.3 Fracture Surface Analysis

From **Figure 5.22(a-f)**, crack formed by fatigue cracking can be seen in as received, MQ, 25% CR, 25% RTR, 25% CCR and 25% RTCR respectively. Cyclic cleavage mechanism observed from crack surface after fatigue cracking can be seen from **Figure 5.22**. This mechanism occurs in transgranular fracture mode behavior. **Figure 5.23(a-f)** shows fracture surface morphology of as received, MQ, 25% CR, 25% RTR, 25% CCR and 25% RTCR zircaloy-2 respectively. The fracture takes place by the formation of dimples showing plastic failure. Since, the fraction of secondary particles is very less, void coalescence is not seen on the fracture surface. It can be seen that dimple size of MQ is much larger as compared to rolled samples. The dimple size is small due to the formation of micro voids under severe strain induced during deformation by rolling. The decrease in size of dimples also explains the larger back stress near the crack tip as compared to mercury quenched and rolled samples. During loading, the movement of dislocations from crack tip towards the grain boundary occurs, if these dislocations are stopped in between then back stress is produced which help crack arresting. The loading at low temperature in deformed materials containing secondary precipitates particles, this process takes place, which enhances the fracture toughness of the material (Becker *et al.*, 2002).

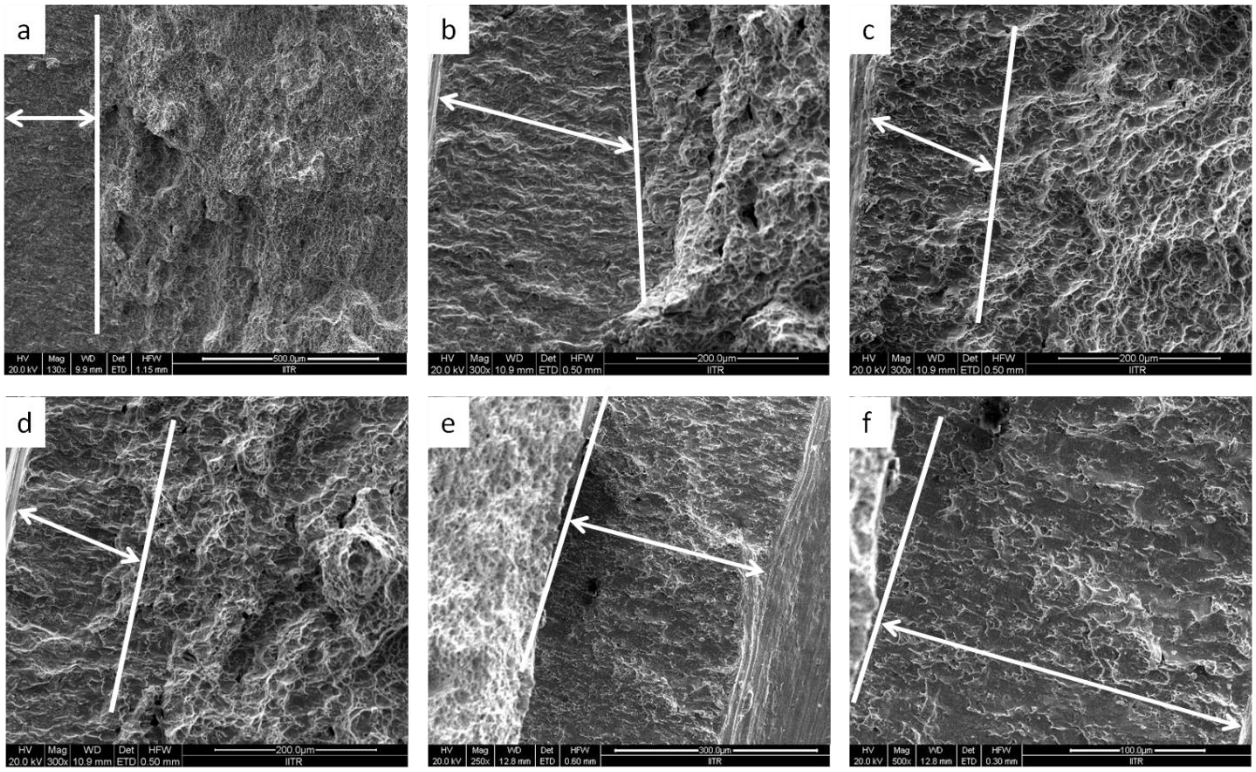

Figure 5.22 Micro Crack formation in CT Specimen during Fatigue Loading for **(a)** As Received, **(b)** MQ, **(c)** 25% CR, **(d)** 25% RTR, **(e)** 25% CCR and **(f)** 25% RTCR of Zircaloy-2

5.2.4 Methodology and Simulation

5.2.4.1 Xtended Finite Element Method (XFEM)

The extended finite element method is extrinsic partition of unity (PU) enriched finite element method. In XFEM, the local FE approximation is enriched using extrinsic PU approach to reproduce certain features of the problems under consideration. In XFEM, remeshing of the problem domain is not required if existing discontinuities such as crack or interface move with time. These discontinuities (crack or interface) are modelled by adding appropriate function in the standard FE approximation. The moving discontinuity are mainly handled by level set functions. Although, the use of level set function is not mandatory in XFEM. In past fifteen years, the XFEM has been successfully used to solve various problems involving geometric discontinuities in different areas of engineering and sciences.

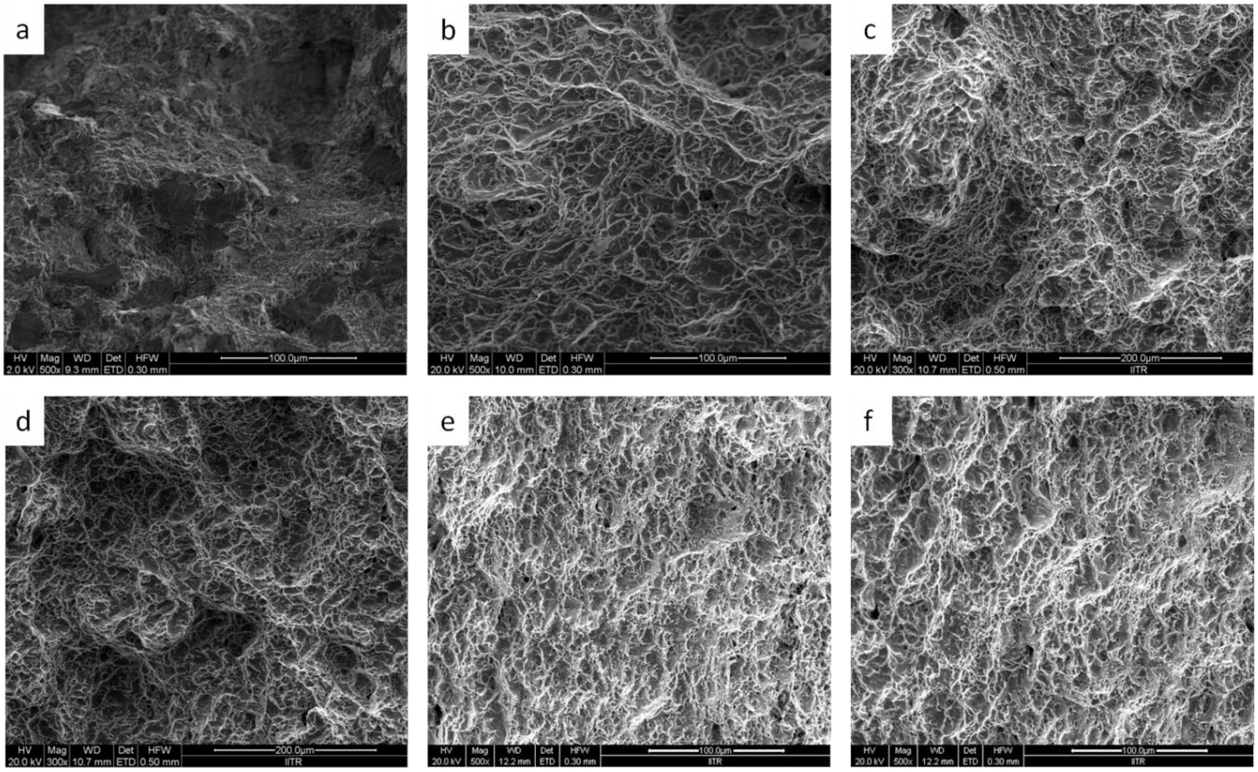

Figure 5.23 Fracture Surface of the CT Specimen after Failure **(a)** As Received, **(b)** MQ, **(c)** 25% CR, **(d)** 25% RTR, **(e)** 25% CCR and **(f)** 25% RTCR Zircaloy-2

5.2.4.2 Tensile Testing Simulation

A geometric model of sub-size tensile specimen created in Abaqus software with 16 mm gauge length is shown in **Figure 5.24(a)**. A structured mesh having total 840 element created using four-node bilinear plane stress quadrilateral element (CPS4R) is shown in **Figure 5.24(b)**. The displacement control loading with an amplitude of 1 mm per minute is applied. The one end of the specimen is fixed while displacement is applied on the other end during simulation. Elasto-plastic XFEM approach is used to calculate the tensile strength of MQ and other rolled samples. The engineering stress-strain curve is obtained in Abaqus using the experimentally obtained tensile properties. Elastic modulus and Poisson's ratio are taken as 100 GPa and 0.30 respectively. The von-Mises stress distributions corresponding to maximum load at the time of crack initiation, crack growth and final rupture are shown in **Figure 5.25(a, b and c)** and **Figure 5.25(d)** shows the stress strain curve obtained by experiment and simulation for MQ. The results show a good match between the XFEM results and experimental values. The stress-strain plot for CR, RTR, CCR and RTCR are shown in **Figure 5.26(a-d)**.

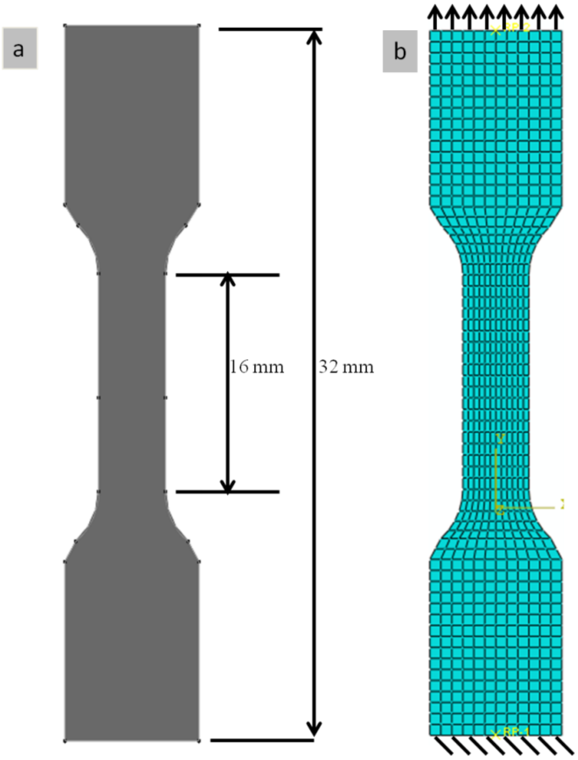

Figure 5.24(a) Geometry and **(b)** Mesh of Tensile Specimen

5.2.4.3 Fracture Toughness of Compact Tension (CT) Specimen

Compact tension (CT) specimen is prepared in Abaqus as per ASTM standard E-1820-09E1 with a crack length of 22.5 mm. A displacement control loading with strain of 10^{-6} is applied on the top edge of specimen. The boundary conditions are taken as per the experimental testing shown in **Figure 5.27(a)**. Four node bilinear plane stress quadrilateral (CPS4R) elements are used for the discretization. Tensile properties obtained from experimental tensile test are used as an input to obtain the load-displacement curve. A contour plot of von-Mises stress is shown in **Figure 5.27(b)**. A comparison of load vs. crack opening displacement is shown in **Figure 5.28** which shows a good agreement between experimental and XFEM results for MQ. From the load-displacement data, the fracture toughness of CR, RTR, CCR and RTCR samples is calculated, and compared with the experimental results in **Table 5.2**. It can be seen from **Table 5.2** that the experimentally obtained fracture toughness is found in good agreement with that obtained using XFEM but the deformed sample experimental results are not matching well with the simulation results. The reason may due to the back stress developed due to the existing dislocation present in experimental samples which are not accounted in the simulations.

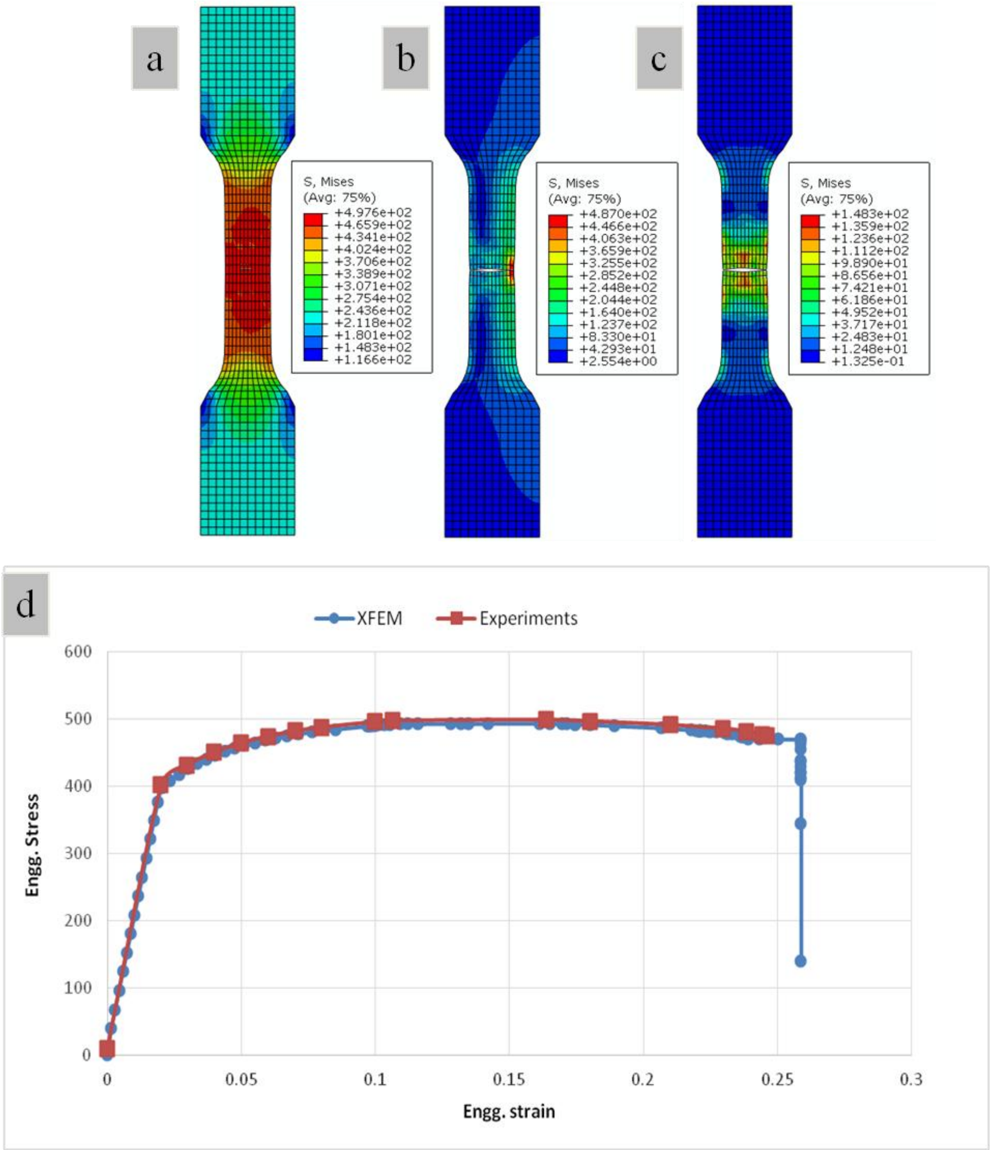

Figure 5.25 von-Mises Stress distribution of Tensile Specimen at **(a)** Crack Initiation, **(b)** Growth, **(c)** Rupture and **(d)** Stress Strain curve obtained by XFEM for MQ Zircaloy-2

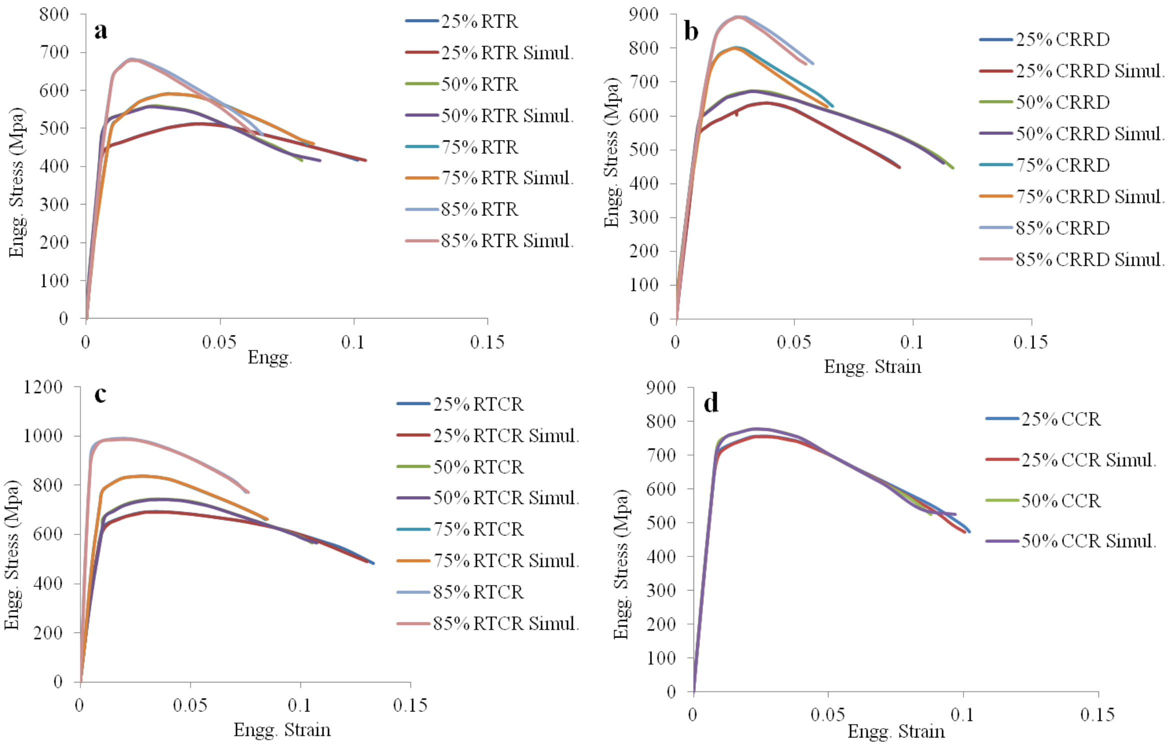

Figure 5.26 Stress Strain curves obtained by XFEM and Experimental Testing for **(a)** RTR **(b)** CRRD **(c)** RTCR **(d)** CCR Zircaloy-2

Table 5.2 Critical Stress Intensity Factor (K_{IC}) values for As Received, MQ and CR, RTR, CCR and RTCR Zircaloy-2 obtained through Experiments and XFEM Simulation

	CT Specimen (Experimental) (MPa m$^{1/2}$)	CT Specimen (XFEM) (MPa m$^{1/2}$)	Edge Crack (XFEM) (MPa m$^{1/2}$)	Center Crack (XFEM) (MPa m$^{1/2}$)	Three Point Bend (XFEM) (MPa m$^{1/2}$)
As received	33.11 (4.3 mm)	33.26 (4.3 mm) 36.15 (3.2 mm)	22.32	36.24	32.33
MQ	28.26 (4.3 mm)	27.99 (4.3 mm) 28.55 (3.2 mm)	16.67	28.15	26.27
25% CR	41.82 (3.2 mm)	35.26 (3.2 mm)	20.00	31.05	29.59
25% RTR	32.78 (3.2 mm)	28.9 0(3.2 mm)	17.79	29.2	24.18
25% CCR	40.96 (3.2 mm)	37.20 (3.2 mm)	21.12	34.51	35.98
25% RTCR	42.56 (3.2 mm)	39.04 (3.2 mm)	22.91	36.86	37.93

Buckling of CT specimens took place in samples rolled more than 25% i.e. samples with thickness less than 3.2 mm, due to which fracture toughness was not evaluated experimentally. However, the simulation performed using XFEM are presented in **Table 5.3** for 25% rolled samples.

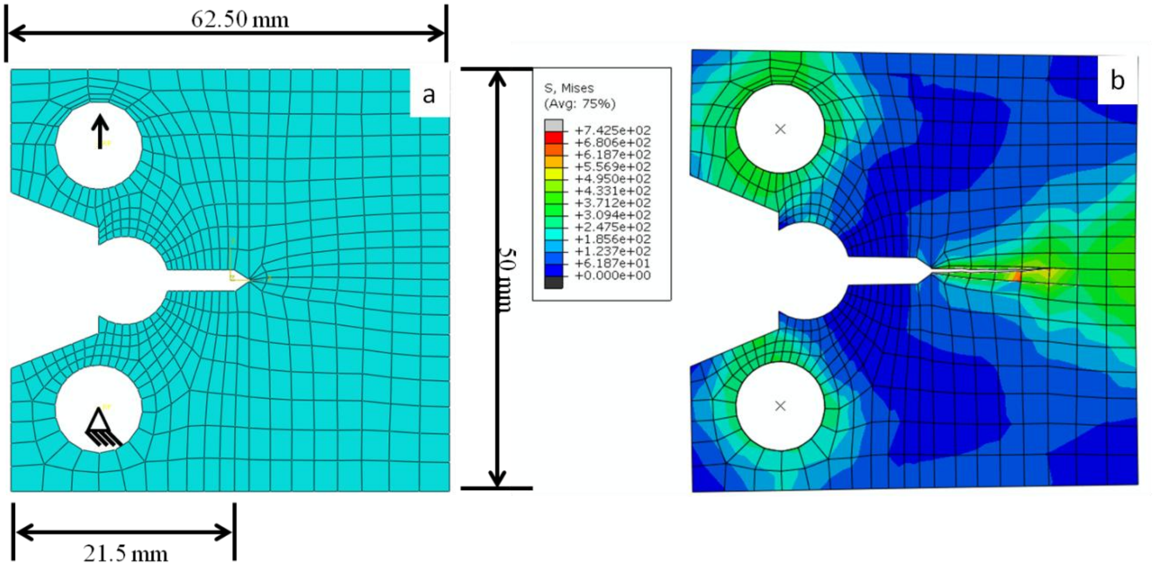

Figure 5.27 (a) Boundary Conditions, Dimensions and Mesh of CT specimen **(b)** von-Mises Stress distribution over the Geometry after Crack Growth

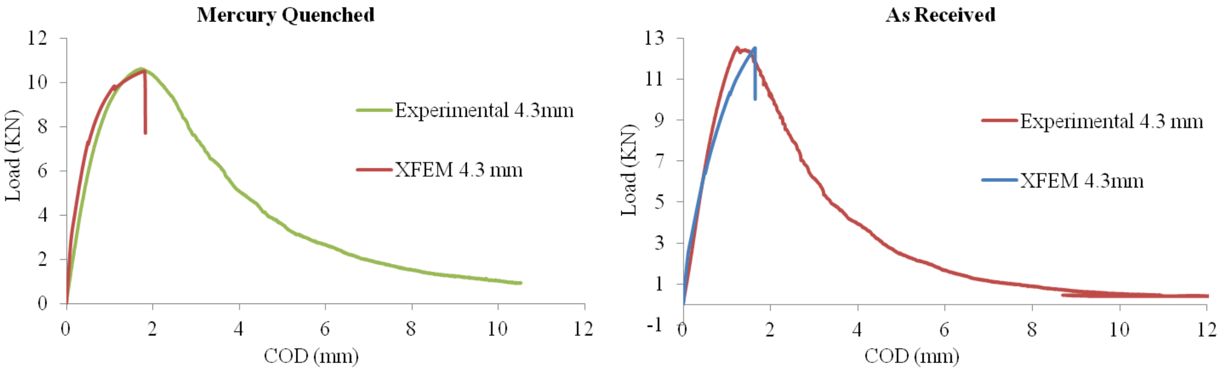

Figure 5.28 Load vs Crack opening Displacement (COD) curve obtained by XFEM and Experimental Testing for As Received and MQ Zircaloy-2

5.2.4.4 Edge Crack with Mode I Loading

XFEM simulation analysis on 40 x 20 mm rectangular plate with an edge crack of 5 mm with 1 mm thickness is performed. Displacement control loading with a strain of 1 x 10^{-6} applied on the specimen model. One side of the plate is fixed and displacement is applied on the other side. CPS4R elements are used in the model. Load vs displacement curves are computed from the XFEM results. The von-Mises stress distribution on the deformed plate after loading and propagation of crack of the MQ sample can be seen from **Figure 5.29 (a-b)**. The plastic zone size near the crack tip after loading can be seen in **Figure 5.29(a)**. The fracture toughness (K_{IC}) evaluated through simulation is presented in **Table 5.3, Table 5.4, Table 5.5** and **Table 5.6** for 25%, 50%, 75% and 85% rolled zircalloy-2 samples respectively. The fracture toughness values obtained through edge crack simulation are found low as compared to with those obtained through CT simulation.

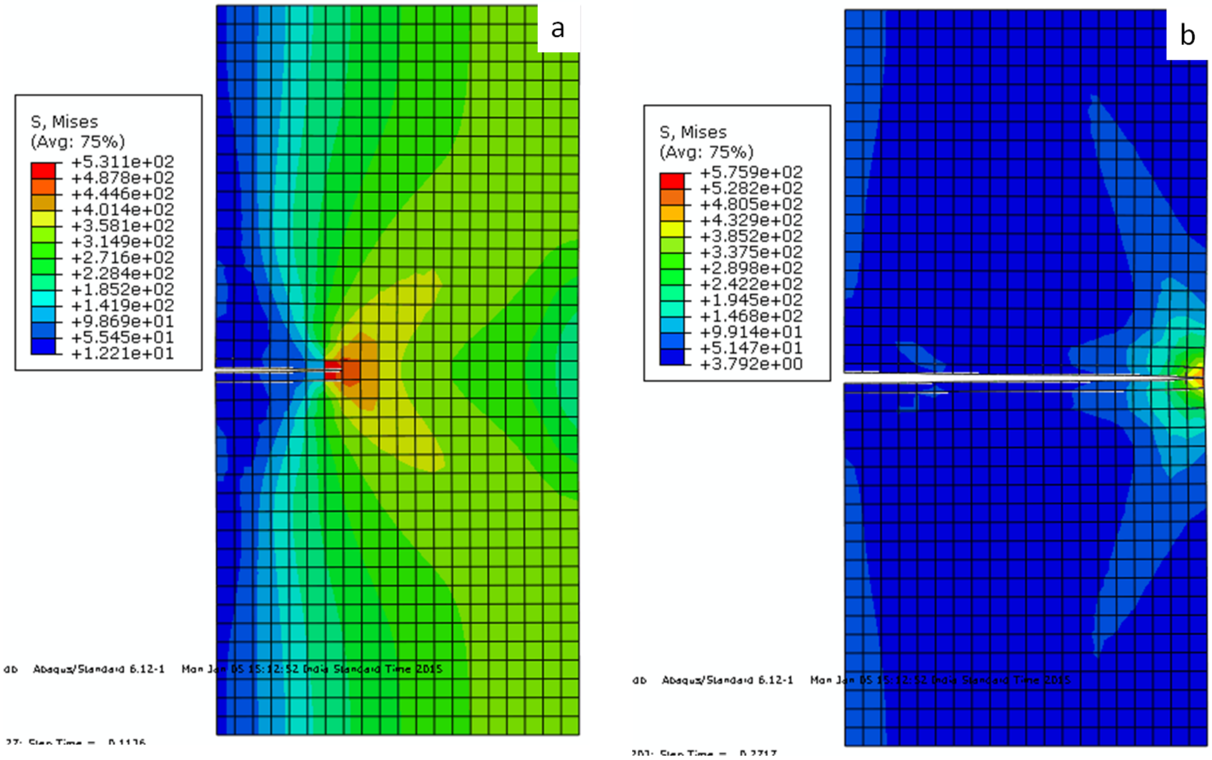

Figure 5.29 von-Mises Stress distribution **(a)** Crack Initiation **(b)** Final Rupture of Edge Crack Specimen for MQ Zircaloy-2

5.2.4.5 Center Crack with Mode I Loading

The simulation of 40 x 20 mm rectangular plate having a center crack of 5 mm with 1 mm thickness is performed by XFEM. A displacement control load with a strain of 10^{-6} is applied on the specimen. CPS4R elements are used for the meshing of the center cracked plate. One side of the plate is fixed while displacement is applied on the other side. Load vs. displacement curves are obtained from XFEM. The von-Mises stress distribution, crack growth and final rupture plots are shown in **Figure 5.30(a), Figure 5.30(b)** and **Figure 5.30(c)** respectively. The fracture toughness

(K_{IC}) obtained through XFEM simulation is presented in **Table 5.3, Table 5.4, Table 5.5** and **Table 5.6** for 25%, 50%, 75% and 85% rolled zircalloy-2 samples respectively. It can be found that the fracture toughness of as received and MQ samples show a good agreement between experimental and simulation results.

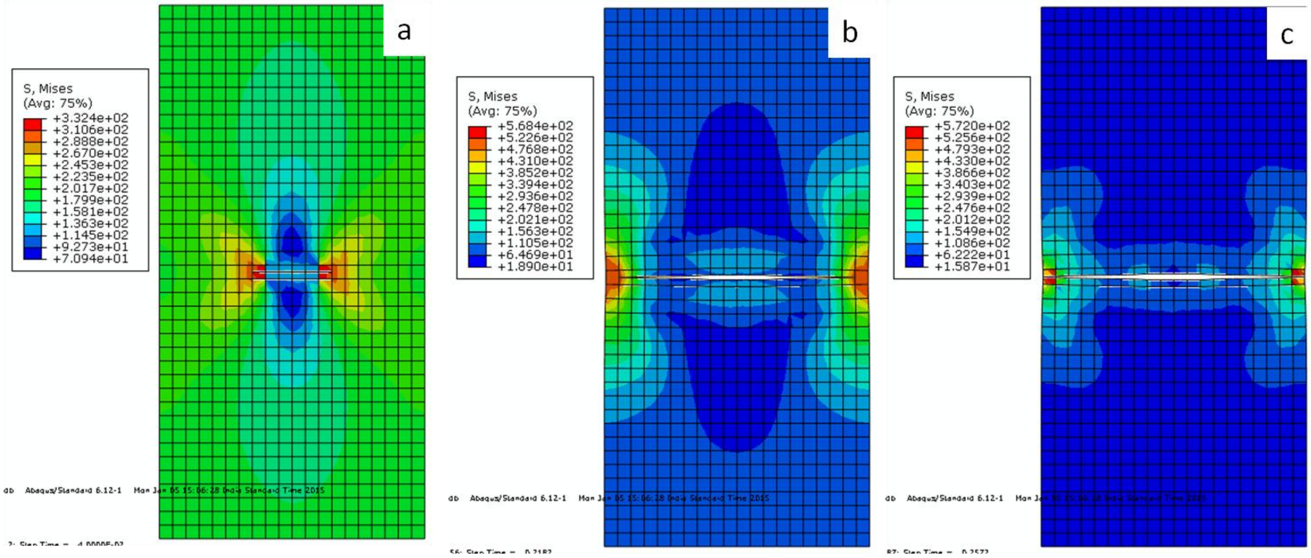

Figure 5.31: von-Mises Stress distribution **(a)** Crack Initiation, **(b)** Growth and **(c)** Final Rupture of Center Crack Specimen for MQ Zircaloy-2

5.2.4.6 Three-Point Bend Specimen

A three point bend specimen with an initial crack length of 16 mm is modeled and simulated by XFEM. A displacement control load with a strain rate of 10^{-6} is applied as shown in **Figure 5.31(a)**. CPS4R elements are used for meshing of the domain. A von-Mises stress distribution of the deformed structure obtained through XFEM simulation is shown in **Figure 5.31(b)**. Load vs displacement curves are obtained for MQ, CR, RTR, CCR and RTCR. The fracture toughness (K_{IC}) evaluated through simulation is presented in **Table 5.3, Table 5.4, Table 5.5 and Table 5.6** for 25%, 50%, 75% and 85% rolled zircalloy-2 samples respectively. From **Table 5.3,** it can be seen that as received and MQ experimental results show a good match with the simulation results while the results of deformed samples are not in good agreement.

Table 5.3 Critical Stress Intensity Factor of 25% Rolled Zircaloy-2 obtained after XFEM Simulation

	Compact Tension b = 3.2 mm (MPa $m^{1/2}$)	Edge Cracked b = 1 mm (MPa $m^{1/2}$)	Center Cracked b = 1 mm (MPa $m^{1/2}$)	Three Point Bend b = 1 mm (MPa $m^{1/2}$)
As received	36.15	22.32	36.24	32.33
MQ	28.55	16.67	28.15	26.27
25% CR	35.26	20	31.05	29.59
25% CR annealed	33.2	18.56	30.71	28.9
25% RTR	28.9	17.79	29.2	24.18
25% RTR annealed	27.02	16.79	28.64	23.8
25% RTCR	37.2	21.12	34.51	35.98
25% RTCR annealed	34.08	20.01	31.36	32.67
25% CCR	39.04	22.91	36.86	37.93
25% CCR annealed	37	20.47	3.01	33.2

Table 5.4 Critical Stress Intensity Factor of 50% Rolled Zircaloy-2 obtained after XFEM Simulation

	Compact Tension b = 3.2 mm (MPa $m^{1/2}$)	Edge Cracked b = 1 mm (MPa $m^{1/2}$)	Center Cracked b = 1 mm (MPa $m^{1/2}$)	Three Point Bend b = 1 mm (MPa $m^{1/2}$)
50% CR	38.6	22.25	36.72	33.58
50% CR annealed	36.09	20.46	33.65	31.14
50% RTR	29.73	17.93	30.03	27.57
50% RTR annealed	28.44	17	29.9	26.73
50% RTCR	39.6	22.86	38.49	38.27
50% RTCR annealed	38.29	22.2	38.1	35.54
50% CCR	43.22	23.99	39.69	39.26
50% CCR annealed	41.23	21.09	35.99	36.59

Table 5.5 Critical Stress Intensity Factor of 75% Rolled Zircaloy-2 obtained after XFEM Simulation

	Compact Tension b = 3.2 mm (MPa $m^{1/2}$)	Edge Cracked b = 1 mm (MPa $m^{1/2}$)	Center Cracked b = 1 mm (MPa $m^{1/2}$)	Three Point Bend b = 1 mm (MPa $m^{1/2}$)
75% CR	41.9	24.87	39.5	36.78
75% CR annealed	39.25	22.9	36.89	34.48
75% RTR	31.7	18.15	30.17	29.92
75% RTR annealed	31.6	17.76	30.1	29.8
75% RTCR	43.8	25.26	40.92	42.28
75% RTCR annealed	42.5	22.89	39.86	38.62

Table 5.6 Critical Stress Intensity Factor of 85% Rolled Zircaloy-2 obtained after XFEM Simulation

	Compact Tension b = 3.2 mm (MPa $m^{1/2}$)	Edge Cracked b = 1 mm (MPa $m^{1/2}$)	Center Cracked b = 1 mm (MPa $m^{1/2}$)	Three Point Bend b = 1 mm (MPa $m^{1/2}$)
85% CR	45.38	27.16	44.61	40.79
85% CR annealed	44.12	26.21	42.84	39.08
85% RTR	36.63	20.47	32.94	33.79
85% RTR annealed	35.65	19.58	32.05	32.95
85% RTCR	52.9	29.85	48.12	44.46
85% RTCR annealed	45.11	24.99	43.8	40.34

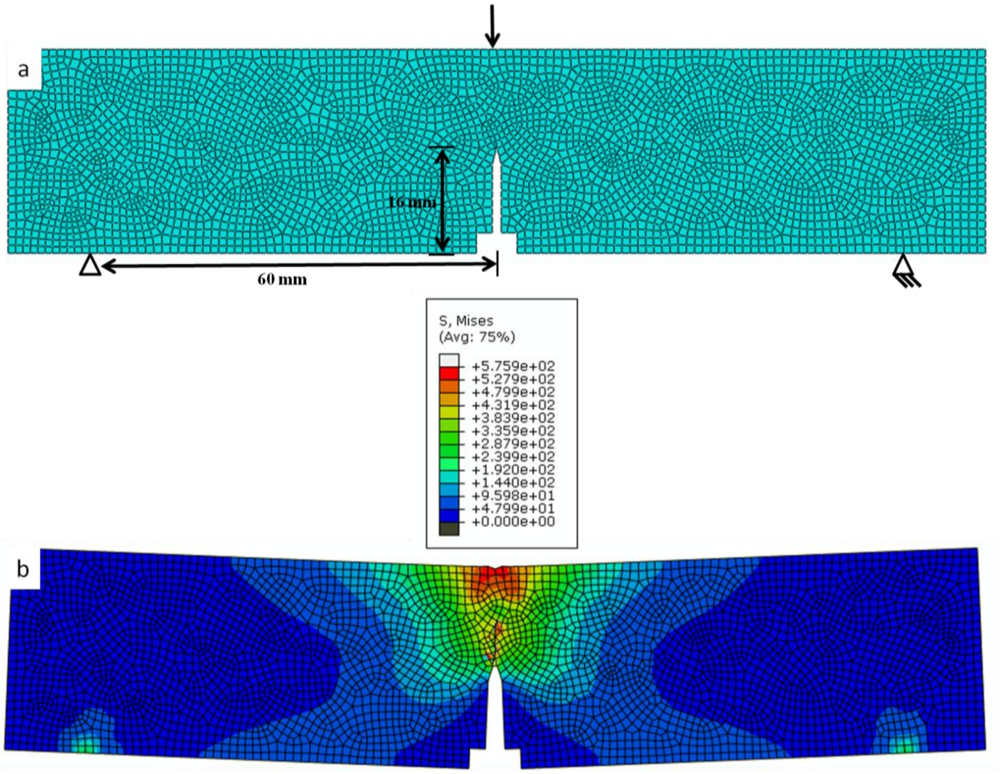

Figure 5.31(a) Geometry, Meshing and Boundary Conditions **(b)** von-Mises Stress distribution in case of Three Point Bend Specimen for MQ Zircaloy-2

5.2.5 Summary

- The rolled sample shows better crack arrest capabilities due to larger back stress produced during loading. High dislocation density results in high fracture toughness.
- The fracture surface shows the reduction in dimple sizes with the increase in dislocation density which is due to the formation of micro-voids as a results of severe strain induced during rolling.
- CT simulation results show a good match for undeformed samples (MQ), while for severely deformed samples, the values are found less as dislocations are not modeled in the simulation.
- Except edge crack, center crack and three point bend simulations show a good match with the experimental values for as received and mercury quenched samples.

CHAPTER 6

CONCLUSIONS AND SUGGESTIONS FOR FUTURE WORK

This chapter presents the summary of major findings of the research work and directions for future work. The present work provides fundamental understanding of the influence of rolling temperature (cryorolling, room temperature rolling and cross rolling) and various thickness reductions (strains), post process annealing treatments, on evolution of microstructure and mechanical properties (hardness, tensile and fracture toughness). In addition, the finite element simulations (FEM) to estimate the fracture toughness of zircaloy-2 under different deformation processing conditions are made.

6.1 Conclusions

- Cryorolling produced ultrafine grained zircaloy-2 with high strength and good ductility. The yield strength (835 MPa) after cryorolling was close to the tensile strength(891 MPa), which is desirable for structural applications.
- Fragmentation of grains with high dislocation density inside the grains structure is obtained after cryorolling. Dislocation cells and dislocation tangles are formed inside the grains after cryorolling due to the suppression of dynamic recovery during rolling at cryo temperature.
- CR has shown significant effect on increasing tensile strength, but the ductility has reduced. The hardness and tensile strength of 85% CR is found to be 282 HV and 891 MPa, respectively, and for the annealed alloy, it is observed to be 282 and 841 MPa in rolling direction and 931 MPa in transverse direction. Post CR annealing at 400 °C for 30 minutes has resulted in UFG structure (150 nm), which is due to combined effect of static recovery and recrystallization.
- After RTR, microstructure reveals the average grain size of 60 nm in the as deformed condition , while 110 nm in 400^{o} C annealed condition. The orientation of IDBs in the macroscopic planes in the direction of macroscopic plastic flow causes formation of nanograins in the materials.
- The difference observed in mechanical properties in rolling and transverse direction of the sample is due to preferential inclination of ‘c’ axis of grain is 20^{o} to 5^{0} towards transverse in CR, while 10^{o} to 30^{o} towards transverse direction in RTR. If ‘c’ axis of the crystal is

perpendicular to the loading direction, $\{10\bar{1}0\}<11\bar{2}0>$ (prism slip) having CRSS of 6.4 N/mm^2 under compression is active and if the ‘c’ axis is parallel to the loading direction, $\{10\bar{1}2\}$ tensile twining having 9.6 N/mm^2 CRSS and $\{11\bar{2}1\}$ twinning is active with twice the strength as compared to the perpendicular case.

- RTCR produced large amount of stored energy in the deformed alloy. Annealing at 400^o C for 30 minutes facilitates the large number of nucleation sites, which in turn enables formation of the ultrafine grains (average grain size of 156 nm) in the alloy. After 85% reduction in thickness, a tensile strength of 991 MPa with 7.5% ductility is observed. Annealing at 400^o C for 30 minutes results in annihilation of dislocations, thus improving ductility of cross-rolled alloy up to 11%. 25% CCR samples are deformed due to $\{11\bar{2}2\}$ active compressive twinning with some traces of $\{11\bar{2}1\}$ tensile twinning. However, in 25% and 50% RTCR, deformation takes place by activation of basal <a> slip, prismatic slip and pyramidal <c+a> slip.

- 25% CCR and 25%, 50% RTCR shows low average Taylor factor while high Schmid factor values for basal slip. Mercury quenched and 50% CCR show low Taylor factor as well as low Schmid factor for basal slip. Texture, Taylor factor and Schmid factor analysis confirms the high propensity of activation of Basal<a> slip.

- Initial grain size after water quenching is 20 µm, which is larger than mercury quenched sample due to higher cooling effect of mercury as compared to water. After RTR, the grain size has reduced to the range from 50nm to 5µm with areas where ultrafine grain exhibits average grain size of 167 nm. Annealing at 400^{o}C for 30 minutes increases the average grains size to 220 nm and 320 nm after annealing at 450^o C. The grains size increases to 800 nm after annealing at 500^o C for 30 minutes.

- In 85% cryorolled zircaloy-2, large value of *J*-integral and internal energy has been found in different crack problems for both plane stress and plane strain conditions. With the decrease in thickness, the plastic zone size at the crack tip is reduced due to strain hardening. Fatigue simulations showed that 85% cryorolled zircaloy-2 exhibits maximum fatigue life.

- The rolled sample shows better crack arresting capabilities due to larger back stress produced during loading. The fracture toughness has improved due to the presence of large dislocation density in the alloy. The fracture surface shows the reduction in dimple sizes with the increase in dislocation density, as micro voids are formed due to severe strain induced in the alloy during rolling.

- CT results obtained after XFEM simulation show a good match for undeformed samples (MQ), while for severely deformed samples, the Fracture toughness values obtained is less because dislocations are not modeled in the simulation.

6.2 Suggestions for Future Work

The present work has provided a fundamental knowledge about the processing of zircaloy-2 at low temperature, after cryo rolling, room temperature rolling and cross rolling on the microstructural evolution and mechanical behavior. The effect of the above processed conditions on the fatigue, corrosion resistance and creep behaviour of the alloy should be studied. Hence, the following suggestions are proposed for the future work as an extension of current work:

- The effect of low temperature and deformation strain, during rolling, on the slip and twinning activity as well as texture evolution ought to be studied using HRTEM and EBSD, respectively.
- Low cycle and high cycle fatigue behavior and fracture toughness of zircaloy-2 subjected to different thermomechanical processing ought to be studied.
- Corrosion and creep behaviour of the Zircaloy-2 processed by cryorolling requires detailed investigation to substantiate the influence of grain size effect and defect densities in the alloy.
- Constitutive model accounting the grain size effect can be formulated for the FEM simulation of tensile and fatigue behaviour of the Zircaloy-2.

LIST OF PUBLICATIONS

1) **Sunkulp Goel,** Nachiket Keskar, R. Jayaganthan, I.V. Singh, D. Srivastava, G.K. Dey, N. Saibaba, (2014), Mechanical behaviour and microstructural characterizations of ultrafine grained Zircaloy-2 processed by cryorolling, Materials Science and Engineering: A, 603, pp. 23-29.
2) **Sunkulp Goel**, R. Jayaganthan, I.V. Singh, D. Srivastava, G.K. Dey, N. Saibabad, (2014), Mechanical and microstructural characterizations of ultrafine grained Zircaloy-2 produced by room temperature rolling, Materials & Design, 55, pp.612–618.
3) **Sunkulp Goel**, Nachiket Keskar, R. Jayaganthan, I.V. Singh, D. Srivastava, G.K. Dey, and N. Saibaba, (2014), Development of Ultrafine Grained Zircaloy-2 by Room Temperature Cross Rolling, Journal of material engineering and performance, DOI: 10.1007/s11665-014-1287-y.
4) **Sunkulp Goel**, Nachiket Keskar, R. Jayaganthan, I. V. Singh, D. Srivastava, G. K. Dey, S. K. Jha, N. Saibaba, (2014), Texture and Mechanical Behavior of Zircaloy-2 Rolled at Different Temperatures, Journal of material engineering and performance, DOI: 10.1007/s11665-014-1315-y
5) **Sunkulp Goel**, Kumar Gaurav, R. Jayaganthan, I.V. Singh, D. Srivastava, G.K. Dey, N. Saibaba, (2014), Experimental evaluation of mechanical properties and fracture-fatigue simulation of cryo– and room–temperature–rolled zircaloy–2, International Journal of Microstructure and Materials Properties, 9 pp. 120-135.
6) **Sunkulp Goel**, R. Jayaganthan, I.V.Singh, D.Srivastava, G.K.Dey and N.Saibaba, (2014), Texture Evolution and Ultrafine Grain Formation in Cross Cryo Rolled Zircaloy-2, Acta Metallurgica Sinica, 2015 (Accepted).

REFERENCES

1. **Abriata, I. P.**, Bolcich, I. C., "Zr-Nb (Zirconium-Niobium) System Bull", Alloy Phase Diagrams. 3:1710-1712, 1982.
2. **Abriata, J.P.**, Garces, J., Versaci, R., "The O-Zr (Oxygen-Zirconium) System", Bull. Alloy Phase Diagrams 7:116-124, 1986.
3. **Akhtar, A.** and Teghtsoonian E., "Plastic deformation of zirconium single crystals," Acta Metallurgica 19: 655-663, 1971.
4. **Akhtar, A.**, "Basal slip in zirconium", Acta Metallurgica 21: 1-11, 1973b.
5. **Akhtar, A.**, "Compression of zirconium single crystals parallel to the c-axis", Journal of nuclear materials, 47:79-86, 1973a.
6. **Akhtar, A.,** "Prismatic slip in zirconium single crystals at elevated temperatures", Metallurgical Transactions A, 6 ,1975
7. **Alexander, D. J.**, "New methods for severe plastic deformation processing", Journal of Material Engineering Performance 16: 360-374, 2007.
8. **Alhamidi, A.**, Edalati, K., Horita, Z., Hirosawa, S., Matsuda, K., Terada, D., "Softening by severe plastic deformation and hardening by annealing of aluminum–zinc alloy: Significance of elemental and spinodal decompositions", Materials Science and Engineering: A, 610:17-27, 2014
9. **Arias, D.**, Abriata, I. P., "The Zr-Fe (zirconium-iron) System", Bull. Alloy Phase Diagrams 9: 597-604, 1988.
10. **Arias, D.**, Abriata, I. P., "Zr-Cr (Zirconium-Chromium) System", Bull. Alloy Phase Diagrams 7: 237-243, 1986.
11. **Averbach, B. L.**, Bever, M. B., Comerford, M. F., Leach, J. S., "X-ray and calorimetric investigations of cold working and annealing of a gold-silver alloy", Acta Metallurgica. 4 :477–484, 1956.
12. **Avettand-Fènoël,** M. N., Simar, A., Shabadi, R., Taillard, R., de Meester, B., "Characterization of Oxide Dispersion Strengthened Copper Based Materials Developed by Friction Stir Processing", Materials & Design, 60: 343–357, 2014.
13. **Azushima, A.**, Aoki, K., "Properties of ultrafine-grained steel by repeated shear deformation of side extrusion process", Material Science and Engineering A 337: 45-49, 2002.

14. **Ballinger R. G.** and Pelloux R. M., "The Effect of Anisotropy on the Mechanical Behavior of Zircaluy-2", Journal of Nuclear Materials 97: 231-253, 1981.
15. **Ballinger, R. G.**, Lucas, G. E. and Pelloux R.M., "The effect of plastic strain on the evolution of crystallographic texture in Zircaloy-2", Journal of Nuclear Materials 126: 53-69, 1984.
16. **Barrett, C. S.**, Massalski, T. B., "Structure of Metals", McGraw-Hill Book Company, NY, 1966.
17. **Becker, W. T.**, Lampman, S., "Fracture Appearance and Mechanisms of Deformation and Fracture", Materials Park, OH: ASM International 2002.
18. **Belytschko, T.** and Black, T., "Elastic crack growth in finite elements with minimal remeshing", International Journal of Fracture Mechanics 45: 601–620, 1999.
19. **Beyerlein, I. J.**, and Tome, C. N., "A dislocation based constitutive model for pure Zr including temperature effects", International Journal of Plasticity 24:867– 95, 2008.
20. **Bhanumurthy, K.**, Kale, G. B., Khera, S. K., "Reaction diffusion in the zirconium-iron system", Journal of Nuclear Materials 185: 208-213, 1991.
21. **Bhowmik, A.**, Biswas, S., Suwas, S., Ray, R. K., Bhattacharjee, D., "Evolution of grain-boundary microstructure and texture in interstitial-free steel processed by equal-channel angular extrusion", Metallurgical and Materials Transactions A, 40:2729-2742, 2009.
22. **Bind, A. K.**, Singh, R. N., Sunil, S., Khandelwal, H. K., "Comparison of J-parameters of cold worked and stress relieved Zr–2.5Nb pressure tube alloy determined using load normalization and direct current potential drop technique", Engineering Fracture Mechanics105: 200–210, 2013.
23. **Bochniak W.**, Marszowski, K., Korbel, A., "Theoretical and practical aspects of the production of thin-walled tubes by the KOBO method", Journal of Material Processing Technology, 169: 44-53, 2005.
24. **Borbely A.,** and Groma, I., "Variance method for the evaluation of particle size and dislocation density from x-ray Bragg peaks", Applied Physics Letters 1972-1974, 2001.
25. **Bouaziz O.**, Estrin, Y. S., Kim, H. S., "Severe plastic deformation by the cone-cone method: Potential for producing ultrafine grained sheet material", La Revue de etallurgie CIT, Revue de Metallurgie, France 104:318-322, 2007.
26. **Bradbrook, J. S.**, Lorimer, G. W., Ridley, N., "The precipitation of zirconium hydride in zirconium and zircaloy-2", Journal of Nuclear Materials 42: 142-160, 1972.

27. **Bridgman, P. W.**, "Effects of High Shearing Stress Combined with High Hydrostatic Pressure", physical review, 48:825-847, 1935a.
28. **Bridgman, P. W., "**Effects of high shearing stress combined with high hydrostatic pressure", Physical Review, 48: 825-847, 1935b.
29. **Bridgman, P. W.**, "On Torsion Combined with Compression", Jounal of Applied Physics 14:273-283, 1943.
30. **Bridgman, P.W.**, "Flow Phenomena in Heavily Stressed Metals" Journal of Applied Physics 8:328-336, 1937.
31. **Bunge, H. J.**, "Some applications of the Taylor theory of polycrystal plasticity", - Kristall und Technik 5:145-175, 1970.
32. **Byskov, E.**, "Calculation of Stress Intensity Factors Using the Finite Element Method with Cracked Elements", International Journal of Fracture Mechanics 6:159-167,1970.
33. **Cáceresa, C. H.**, P. Lukáč, "Strain hardening behaviour and the Taylor factor of pure magnesium", Philosophical Magazine, 88:977–989, 2008.
34. **Chan, S. K.**, Tuba, I. S. and Wilson W. K., "On the Finite Element Method in Linear Fracture Mechanics", Engineering Fracture Mechanics 2:1-17, 1970.
35. **Charquet, D.**, Alheritiere, E., "Proc. Workshop: Second Phase Particles in Zircaloys", Erlangen, F.R.G. Kerntechnische Gesellschaft, 5-11, 1985.
36. **Charquet, D.**, Hahn, R., Ortlieb, E., Gros, I. P., Wadier, I. F., 8th Int. Conf. Zr Nucl. Ind., June 19-23, 1988, San Diego, CA: ASTM-STP 1023. Philadelphia, PA: American Society Testing Materials, pp. 405-422, 1989.
37. **Chemelle, P.**, Knorr, D. B., Van Der Sande, J. B., and Pelloux, R. M., "Morphology and Composition of Second Phase Particles in Zircaloy-2" Journal of Nuclear Materials 58-64, 1983.
38. **Choubey, A.**, Sehgal, D. K. and Tandon, N., "Finite element analysis of vessels to study changes in natural frequencies due to cracks", International Journal of Pressure Vessels and Piping 83:181–187, 2006.
39. **Choy, K.,** "Chemical vapour deposition of coatings", Progress in Material Science, 48: 57-70, 2003.
40. **Chun, Y. B.**, Yu, S. H., Semiatin, S. L., Hwang, S. K., "Effect of deformation twinning on microstructure and texture evolution during cold rolling of CP-titanium", Materials Science and Engineering A 398: 209–219, 2005.

41. **Chung, K.**, Barlat, F., Yoon, J. W., Richmond, O., Brem J. C., Lege, D. J., "Yield and strain rate potentials for aluminum alloy sheet forming design", Metal and Materials, 4: 931–938, 1998.
42. **Corchia, M.,** Righini, F., "Kinetic Aspects of the Phase, Transformations in Zircaloy-2", Journal of Nuclear Materials, 97:137-148, 1981.
43. **Cox, H. L.**, Sopwith, D. G., "The effect of orientation on stresses in single crystals and of random orientation on strength of polycrystalline aggregates", Proc. Phys. Soc. 49: 134-151, 1937.
44. **Cullity, B. D.**, "Elements of X-Ray Diffraction", 2nd ed., Addinson-Wesley, (1978).
45. **Das, P.**, Jayaganthan, R., Singh, I. V., "Tensile and impact-toughness behaviour of cryorolled Al 7075 alloy", Materials & Design 32:1298-1305, 2011.
46. **Dawson, C. W.**, Sass, S. L., "The as-quenched form of the omega phase in Zr-Nb alloys", Metallurgical Transactions. 1: 2225-2233, 1970.
47. **Degueldre, C.**, Raabe, J., Kuri, G., Abolhassani, S., "Zircaloy-2 secondary phase precipitate analysis by X-ray microspectroscopy", Talanta 402–406, 2008.
48. **Derep, J. L.**, Ibrahim, S., Rouby, R., Fantozzi, G., "Deformation behaviour of zircaloy-4 between 77 and 900K", Acta Metallurgica 28:607-619, 1980.
49. **Dickson, J. I.,** and Craig, G. B., "Room-temperature basal slip in zirconium", Journal of Nuclear Materials 40: 345-348, 1971.
50. **Dolbow, J. E.**, "An extended finite element method with discontinuous enrichment for applied mechanics" PhD dissertation, Theoretical and Applied Mechanics, Northwestern University, USA, 1999.
51. **Duarte, C. A.,** and Oden, J. T., "An H-p adaptive method using clouds", Computer Methods in Applied Mechanics and Engineering 139:237–262, 1996.
52. **Dumstorff, P.,** and Meschke, G., "Finite element modelling of cracks based on the partition of unity method", Proceedings of Applied Mathematics and Mechanics (PAMM), 2: 226–227, 2003.
53. **Dybiec, H.,** "Plastic consolidation of metallic powders", Archieves of Metallury and Materials, 52, 61-170, 2007.
54. **Edalati, K.**, Horita Z., Yagi S., Matsubara, E., "Allotropic phase transformation of pure zirconium by high-pressure torsion", Materials Science and Engineering A 523: 277–281, 2009.

55. **Edalati, K.**, Horita, Z., "Continuous high-pressure torsion", Journal of Materials Science 45:4578-4582, 2010.
56. **Eduardo, R.** De Arantes, Oliveira, E., “Theoretical Foundations of the Finite Element Method”, International Journal Solids Structures, 4:929-952, 1968.
57. **Erb, U.,** “Electrodeposited nanocrystals: Synthesis, properties and industrial applications”, Nanostructured Materials, 6:533-538, 1995.
58. **Estrin, Y.**, Ferkel, H., Hellmig, R. J., Lamark, T., Popov, M. V., German patent DE102005049369, Germany, 2008.
59. **Estrin, Y.**, Vinogradov, A., “Extreme grain refinement by severe plastic deformation: A wealth of challenging science”, Acta Materialia, 61:782–817, 2013.
60. **Etherington, C.**, “A New Concept for the Continuous Extrusion Forming of Metals”, J Eng Ind, 96, 863-900, 1974.
61. **Etou, M.**, Fukushima, S., Sasaki, T., Haraguchi, Y., Miyata, K., Wakita, M., Tomida, T., Imai, N., Yoshida, M., Okada, Y., “Super short interval multi-pass rolling process for ultrafine grained hot strip”, ISIJ International, 48:1142-1147, 2008.
62. **Every, R. L.,** Hartherly, M., “Oriented Nucleation in low carbon steel”, Texture, 1:183–194, 1974.
63. **Farshidi, M. H.**, Kazeminezhad, M., “Deformation Behavior of 6061 Aluminum Alloy Through Tube Channel Pressing: Severe Plastic Deformation”, Journal of Material Engineering and Performance, 21: 2099-2105, 2012.
64. **Fatemi, A.,** and Vangt, L., “Cumulative fatigue damage and life prediction theories: a survey of the state of the art for homogeneous materials”, International Journal of Fatigue, 20:9-34, 1998.
65. **Fischer, E. S.**, Renken, C. J., “Single-Crystal Elastic Moduli and the hcp → bcc Transformation in Ti, Zr, and Hf”, Physical Review A. 135:482-494, 1964.
66. **Frank, F. C.**, “Report on the Symposium on the Plastic Deformation of Crystalline Solids”, Carnegie Institute of Technology 150–154, 1950.
67. **Fujioka, T.**, Horita Z., “Development of high-pressure sliding process for microstructural refinement of rectangular metallic sheets”, Material Transactions, 50:930-933, 2009.
68. **Garrison, Jr W. M.**, Moody, N. R., “Ductile fracture”, Journal of Physics and Chemistry of Solids, 48:1035–1074, 1987.

69. **Geist, D.**, Rentenberger, C., Karnthaler, H. P., “Extreme structural inhomogeneities in high-pressure torsion samples along the axial direction”, Acta Materiala, 59:4578-4586, 2011.
70. **Gleiter, H.,** "Materials with ultrafine grain size. In:N.Hansen, editor, deformation of polycrystals: mechanism and microstructures”, Riso National Laboratory, Roskilde, 15, 1981.
71. **Gleiter, H.,** "Nanocrystalline materials", Progress in Material Science", 33:223-315, 1989.
72. **Godfrey, A.,** Cao, W. Q., Liu, Q., Hansen, N., “Stored energy, microstructure, and flow stress of deformed metals”, Metallurgical and Materials Transactions A, 36: 2371-2378, 2005.
73. **Gopala Krishna, K.**, Singh, N., Venkateswarlu, K., Hari Kumar, K. C., “Tensile behavior of ultrafine-grained Al-4Zn-2Mg alloy produced by cryorolling”. Journal of Material Engineering Performance, 20:1569-1574, 2011.
74. **Groma, I.**, “X-Ray Line Broadening Due to an Inhomogeneous Dislocation Distribution” Physical Review B 7535-7542, 1998.
75. **Groves, G.W.**, Kelly A., “Independent slip systems in crystals”, Philosophical Magazine, 89: 877−887, 1963.
76. **Guo D.**, Li M., Shi, Y., Zhang, Z., Ma, T., Zhang, H. and Zhang, X., “Simultaneously enhancing the ductility and strength of cryorolled Zr via tailoring dislocation configurations”, Materials Science & Engineering A, 558:611–615, 2012a.
77. **Guo, D.**, Li M., Shi, Y., Zhang, Z., Zhang, H., Liu, X. and Zhang, X., “Effect of strain rate on microstructure evolutions and mechanical properties of cryorolled Zr upon annealing”, Materials Letters 66: 305–307, 2012b.
78. **Guo, D.**, Li, M., Shi, Y., Zhang, Z., Zhang, H., Liu, X., Wei, B., and Zhang, X., “High strength and ductility in multimodal-structured Zr”, Materials and Design 34:275–278, 2012c.
79. **Guo, D.**, Zhang, Z., Zhang, G., Li, M., Shi, Y., Ma, T., Zhang, X., “An extraordinary enhancement of strain hardening in fine-grained zirconium”, Materials Science & Engineering A 591:167–172, 2014.
80. **Gurao, N. P.**, Sethuraman, S., Suwas, S., “Evolution of Texture and Microstructure in Commercially Pure Titanium with Change in Strain Path during Rolling”, Metallurgical and Materials Transactions A 44:1497-1507, 2013.

81. **Gurao, N. P.,** Suwas, S., “Deformation mechanisms during large strain deformation of nanocrystalline nickel”, Applied Physics Letter 94:191902, 2009.
82. **Gusakov-Stanyukovich, I. V.**, Poluektov, P. P., and Radchenko, M. V., “Properties of Recycled Zirconium”, Atomic Energy, 108:319–320, 2010.
83. **Habibi, M. K.**, Gupta, M., Joshi, S. P., "Size-effects in textural strengthening of hierarchical magnesium nano-composites", Materials Science and Engineering A, 556:855-863, 2012.
84. **Hall, E.O.,** “The Deformation and Ageing of Mild Steel: III Discussion of Results”, Proceedings of Physical Society 64:747-753, 1951.
85. **Hansen, N.**, “New Discoveries in Deformed Metals”, Metallurgical and Materials Transactions A 2917-2935, 2001.
86. **Horita, Z.,** Smith, D. J., Furukawa, M., Nemoto, M., Valiev, R. Z., Langdon, T. G., “An investigation of grain boundaries in submicrometer-grained Al-Mg solid solution alloys using high-resolution electron microscopy”, Journal of Materials Research 11:1880-1890, 1996.
87. **Huang, J. Y.**, Zhu, Y. T., Alexander, D. J., Liao, X. Z., Lowe, T. C., Asaro, R. J., “Development of repetitive corrugation and straightening”, Material Science and Engineering A 371:35-39, 2004.
88. **Huang, J.**, Zhu, Y. T., Alexander, D. J., Liao, X., Lowe, T. C., Asaro, R. J., "Development of repetitive corrugation and straightening", Materials Science and Engineering A 371: 35–39, 2004.
89. **Huang, L.**, Zhang, Z., Zhao, Y., Yao, W., Mukherjee, A. K., Schoenung, J. M., "Scratch-induced deformation in fine- and ultrafine-grained bulk alumina", Scripta Materialia, 63: 528–531, 2010.
90. **Huang, Y.**, Prangnell, P. B., “Continuous frictional angular extrusion and its application in the production of ultrafine-grained sheet metals”, Scripta Materiala 56:333-336, 2007.
91. **Hughes, D. A.**, Hansen, N., Bammann, D. J., “Geometrically necessary boundaries, incidental dislocation boundaries and geometrically necessary dislocations”, Scripta Materialia 147–153, 2003.
92. **Humphreys, F. J.,** and Hatherly, M., “Recrystallization and Related Annealing Phenomena”, 2004.
93. **Hurst**, “Canada Enters the Nuclear Age”, Atomic Energy of Canada Limited, 1997.
94. **Hutchinson, J. W.**, “Fundamentals of the phenomenological theory of nonlinear fracture mechanics”, Journal of Applied Mechanics 50:1042-1051, 1983.

95. **Hutchinson, W. B.**, “Development and control of annealing textures in low-carbon steels”, International Metals Review 29: 25–42, 1984.

96. **Ibrahim, E. F.**, "In-Reactor Creep of Zirconium-Alloy Tubes and Its Correlation with Uniaxial Data," Applications-Related Phenomena for Zirconium and Its Alloys, ASTM STP 458, American Society for Testing and Materials 18-36, 1969.

97. **Iwahashi, Y.,** Horita, Z., Nemoto, M., Langdon, T. G., “The process of grain refinement in equal channel angular pressing”, Acta Materialia 46:3317-3331, 1998.

98. **Jaeger, R. C.,** "Film Deposition: Introduction to Microelectronic Fabrication”, Upper Saddle River: Prentice Hall, ed. 2nd, ISBN 0-201-44494-1, 2002.

99. **Jayakumar, T.,** Palanichamy, P., and Raj, B. “Detection of hard intermetallics in β-quenched and thermally aged Zircaloy-2 using ultrasonic measurements” Journal of Nuclear Materials 255:243–249, 1998.

100. **Jiang, J.**, Britton, T. B. and Wilkinson, A. J., “Accumulation of geometrically necessary dislocations near grain boundaries in deformed copper”, Philosophical Magazine Letters, 580–588, 2012.

101. **Jiang, L.**, Pe´rez-Prado, M. T., Gruber, P. A., Arzt, E., Ruano, O. A., Kassner, M. E., “Texture, microstructure and mechanical properties of equiaxed ultrafine-grained Zr fabricated by accumulative roll bonding”, Acta Materialia 56:1228–1242, 2008.

102. **Jiang, L.**, Ruano, O. A., Kassner, M. E., and Pérez-Prado, M. T., “The Fabrication of Bulk Ultrafine-Grained Zirconium by Accumulative Roll Bonding”, Journal of Materials 42-45, 2007.

103. **Jin, Y. G.**, Baek, H. M., Im, Y.T., and Jeon, B. C., “Continuous ECAP process design for manufacturing a microstructure-refined bolt,” Materials Science and Engineering A, 530: 462–468, 2007.

104. **Jirásek, M.,** and Zimmermann, T., “Embedded crack model. Part I: Basic formulation” International Journal for Numerical Methods in Engineering 50: 1269–1290, 2001a.

105. **Jirásek, M.,** and Zimmermann, T., “Embedded crack model. Part II: Combination with smeared cracks”, International Journal for Numerical Methods in Engineering 50:1291-1305, 2001b.

106. **Judge Colin, D.**, “Lattice Strain and Texture of Plastically Deformed Zircaloy-2 at 77K”, Thesis Queen’s University Kingston, 2009.

107. **Kad, B. K.**, Gebert, J. M., Perez-Prado, M. T., Kassner, M. E., Meyers, M. A., “Ultrafine-grain-sized zirconium by dynamic deformation”, Acta Materialia 54: 4111–4127, 2006.

108. **Kaibyshev, O. A.**, “Grain Refinement in Commercial Alloys Due to High Plastic Deformations”, Journal of Material Processing and Technology 117:300-306, 2001.

109. **Kalland, J. S.,** Huang, Y. C., Metal Sci. 18:381–385, 1984.

110. **Kamalanath, P. A. R.** and Sarkar, A., “Tensile Behavior of Cryorolled Zircaloy-2”, Global Journal of Researches in Engineering Mechanical and Mechanics Engineering, 12. 2012.

111. **Kawasaki, M.**, Figueiredo, R. B., Langdon, T. G., “Twenty-five years of severe plastic deformation: recent developments in evaluating the degree of homogeneity through the thickness of disks processed by high-pressure torsion”, Journal Material Science 47:7719–7725, 2012.

112. **Kearns, J. J.**, Woods, C. R., “Effect of texture, grain size, and cold work on the precipitation of oriented hydrides in Zircaloy tubing and plate”, Journal of Nuclear Materials 20:241-261, 1966.

113. **Kim, Y. S.**, Perlovich, Y., Isaenkova, M., Kim, S. S., Cheong, Y. M., “Precipitation of reoriented hydrides and textural change of α-zirconium grains during delayed hydride cracking of Zr–2.5%Nb pressure tube”, Journal of Nuclear Materials 297, 2001.

114. **Knezevic, M.**, Beyerlein, I. R., Nizolek, T., Mara, N. A., Pollock, T. S., “Anomalous Basal Slip Activity in Zirconium under High strain Deformation”, Material Research Letter 1:133–14, 2013.

115. **Knorr, D. B.**, Pelloux, R. M., and Van Swam, L. F. P., “Effects of material condition on the iodine SCC susceptibility of zircaloy-2 cladding”, Journal of Nuclear Materials 110, 1982.

116. **Kobayashi, Oh.,** Altan., “Metal Forming and the Finite Element Method”, Oxford University Press, New York 41-44, 1989.

117. **Koch, C. G.,** “Synthesis of nanostructured materials by mechanical milling: problems and opportunities", Nanostructured materials 9:13-22, 1997.

118. **Kolobov, Y. R.**, “Nanotechnologies for the formation of medical implants based on titanium alloys with bioactive coatings”, Nanotechnology Russia 4:758-775, 2009.

119. **Krishnan., R.**, Asundi, M. K., “Zirconium alloys in Nuclear technology” In: S. Ranganathan et al., (Ed.), Alloy Design, Indian Academy of Sciences 1981.

120. **Kurzydlowski, K. J.**, Mater Sci Forum 341: 503–504, 2006.

121. **Lapovok, R.**, Timokhina, I., McKenzie, P. W. J., Donnell, R. O, "Processing and properties of ultrafine-grain aluminium alloy 6111 sheet", Journal of Material Processing and Technology 200: 441-450, 2008.

122. **Lapovok, R.**, Toth, L. S., Winkler, M., Semiatin, S. L., "A comparison of continuous SPD processes for improving the mechanical properties of aluminum alloy 6111", Journal of Material Research 24: 459-469, 2009.

123. **Lee, B. S.**, Kim, M. H., Hwang, S. K., Kwun, S. I., Chae, S. W., "Grain refinement of commercially pure zirconium by ECAP and subsequent intermediate heat treatment", Materials Science and Engineering A 449–451:1087–1089, 2007.

124. **Lee, D.**, "Role of plastic anisotropy in the fatigue behavior of zircaloy", metallurgical transactions 3, 1972.

125. **Lee, J. W.**, Park, J. J., "Numerical and experimental investigations of constrained groove pressing and rolling for grain refinement", Journal of Material Processing and Technology 208:130–131, 2002.

126. **Lee, S. H.**, Sakai, T., Saito, Y., Utsunomiya, H., Tsuji, N., "Strengthening of Sheath-Rolled Aluminum Based MMC by the ARB Process", Material Transaction JIM 40:1422-1428, 1999.

127. **Lee, T. R.**, Chang, C. P., Kao, P. W., "The tensile behavior and deformation microstructure of cryo-rolled and annealed pure nickel", Materials Science and Engineering A, 408:131–135, 2005.

128. **Lemaignan, C.**, Motta, A. T., "Zirconium alloys in nuclear applications", Materials Science and Technology, Wiley Online Library, 1984.

129. **Li, L.**, Unga, T., Wang, Y. D., Fan, G. J., Yang, Y. L., Jia, N., Ren, Y., Tichy, G., Lendvai, J., Chooa, H., and Liawa, P. K., "Simultaneous reductions of dislocation and twin densities with grain growth during cold rolling in a nanocrystalline Ni–Fe alloy", Scripta Materialia 60:317–320, 2009.

130. **Li, M.**, Guo, D., Ma, T., Zhang, G., Shi, Y., Zhang, X., "High fracture toughness in a hierarchical nanostructured zirconium", Materials Science & Engineering A 606: 330–333, 2014.

131. **Liu, P.,** Yu, T., Bui, T. Q., Zhang, C., Xu, Y., Lim, C. W., "Transient thermal shock fracture analysis of functionally graded piezoelectric materials by the extended finite element method." International Journal of Solids and Structures 51: 2167–2182, 2014.

132. **Liu**, Q., Hansen, N., "Geometrically Necessary Boundaries and Incidental Dislocation Boundaries Formed During Cold Deformation" Scripta Metallurgica et Materilia 1289-1295, 1995.

133. **Liu, Q.**, Jensen, D. J., Hansen, N., "Effect of Grain Orientation on Deformation Structure in Cold-Rolled Polycrystalline Aluminium", Acta Materialia 46: 5819–5838, 1998.

134. **Liu, X. D.,** Wang, J. T., Ding B. Z., "Preparation and properties of nanocrystalline $(Fe_{0.99}Mo_{0.01})_{78}Si_9B_{13}$ alloy." Scripta Metallurgica Materialia 28:59-64.1993.

135. **Lu, L.,** Shwaiger, R., Shan, Z. W., Dao, M., Lu, K., Suresh, S., "Nano-sized twins induce high rate sensitivity of flow stress in pure copper." Acta Materialia 53:2169-2179, 2005.

136. **Luan, B. F.**, Ye, Q., Chen, J. W., Yu, H. B., Zhou, D. L., Xin, Y. C., "Deformation twinning and textural evolution of pure zirconium during rolling at low temperature." Transaction of Nonferrous Metallurgical Society of China 23:2890−2895, 2013.

137. **Macewen, S. R.,** Faber, J. Jr. and Turner, A. P. L. "The Use Of Time-Of-Flight Neutron Diffraction to Study Grain Interaction Stresses." Acta Materilia 31 (5):657-676, 1983.

138. **Maiti, S. K.,** and Patil, D. P., "Detection of multiple cracks using frequency measurements." Engineering Fracture Mechanics 70:1553–157, 2003.

139. **Manna R**. , Mukhopadhyay, N. K. , Sastry, G. V. S, "Strengthening behavior of bulk ultra-fine grained aluminum alloys", Materials Science Forum, 710:241-246, 2011.

140. **Massih, A. R.**, Andersson, T., Witt, P., Dahlback, M., Limback, M., "Effect of quenching rate on the β-to-α phase transformation structure in zirconium alloy." Journal of Nuclear Materials 322:138–151, 2003.

141. **Massih, A. R.,** Dahlback, M., Limback, M., Andersson, T., Lehtinen, B., "Effect of beta-to-alpha phase transition rate on corrosion behaviour of Zircaloy." Corrosion Science 48:1154–1181, 2006.

142. **Matsuo, M.,** Hayami, S., and Nagashima, S., Adv. X-ray Anal. 14:214–230, 1971.

143. **McCabe, R. J.**, Cerreta, E. K., Misra, A., Kaschner, G. C., Tome, C. N., "Effects of texture, temperature and strain on the deformation modes of zirconium." Philosophical Magazine 86:3595-3611, 2006.

144. **McCabe, R. J.**, Proust, G., Cerreta, E. K., Misra, A., "Quantitative analysis of deformation twinning in zirconium." International Journal of Plasticity 25:454–472, 2009.

145. **Mehan, R. L.,** Wiesinger, F. W., "Mechanical properties of Zircaloy-2." AEC Research and development report, 1961.

146. **Melenk, J. M.** and Babuska, I., “The partition of unity finite element method: basic theory and applications”, Seminar fur Angewandte Mathematik, Eidgenossische Technische Hochschule, Research Report No. 96-01, CH-8092 Zurich, Switzerland, 1996.

147. **Meng, X.,** and Northwood, D. O., “Second phase particles in Zircaloy-2”, Journal of Nuclear Materials 168:125-136, 1989.

148. **Meyers, M. A.**, Mishra, A., Benson, D. J., “Mechanical properties of nanocrystalline materials.” Progress in Materials Science 51:427–556, 2006.

149. **Miquet, A.**, Charquet, D., Michaut, C, Allibert, C. H., “Effect of Cr, Sn and O contents on the solid state phase boundary temperatures of Zircaloy-4.” Journal of Nuclear Materials 105:142-148, 1982.

150. **Mises, R. V.,** “Mechanik der plastischen Formänderung von Kristallen”, Zeitschrift angewandte Mathematik Mechanik 8:161-185, 1928.

151. **Mishra, R. S.**, Ma, Z.Y., “Friction stir welding and processing.” Material Science and Engineering Rep 50:1-78, 2005.

152. **Mizunuma, S.,** “Large straining behavior and microstructure refinement of several metals by torsion extrusion process.” Material Science Forum 503–506:185-190, 2006.

153. **Moës, N.**, Dolbow, J., and Belytschko, T., “A finite element method for crack growth without remeshing.” International Journal for Numerical Methods in Engineering 46:131–150, 1999.

154. **Monnet, G.,** Devincre, B., Kubin, L. P., “Dislocation study of prismatic slip systems and their interactions in hexagonal close packed metals: application to zirconium.” Acta Materialia 52:4317–4328, 2004.

155. **Moran, B.,** Shih, C. F., “A general treatment of crack tip contour integrals.” International Journal of Fracture 35:295-310, 1987.

156. **Mughrabi, H.**, Höppel, H. W., “Cyclic deformation and fatigue properties of very fine-grained metals and alloys.” International Journal of Fatigue 32:1413–1427, 2010.

157. **Mukherjee, P.**, Sarkar, A., Barat, P., Bandyopadhyay, S. K., Sen, P., Chattopadhyay, S.K., Chatterjee, P., Chatterjee, S. K. and Mitra, M. K., “Deformation characteristics of rolled zirconium alloys: a study by X-ray diffraction line profile analysis.” Acta Materialia 52: 5687–5696, 2004.

158. **Murthy, K. L.**, Charit, I., “Texture development and anisotropic deformation of zircaloys.” Progress in Nuclear Energy 48:325-359, 2006.

159. **Nakamura, K.**, Neishi, K., Kaneko, K., Nakagaki, M., Horita, Z., "Continuous grain refinement using severe torsion straining process." Material Science Forum 503–504:385-390, 2006.

160. **Nash, P.**, Jayanth, C. S., "Zr-Ni (Zirconium-Nickel) System." Bull. Alloy Phase Diagrams 5:1111 -1779, 1984.

161. **Nguyen-Vinh, H.,** Bakar, I., Msekh, M. A., Song, J. H., Muthu, J., Zi, G., Le, P., Bordas, S., Simpson, R., Natararajan, S., Lahmer, T., Rabczuk, T., "Extended finite element method for dynamic fracture of piezo-electric materials." Engineering Fracture Mechanics 92:19–31, 2012.

162. **Nieh, T. G.**, Zhang, M., Zinkle, S. J., McGreevy, T. E., Hoelzer, D. T., and Speakman, S. A., "Effect of texture on the high temperature mechanical properties of Nb–1%Zr alloy." Scripta Materialia 55, 2006.

163. **Nishida, Y.**, Arima, H., Kim, J.-C., Ando, T., "Rotary-die equal-channel angular pressing of an Al–7 mass% Si–0.35 mass% Mg alloy." Scripta Mater 45:261-266, 2001.

164. **Nurse, A. D.** and Patterson, E. A., "A photoelastic technique to predict the direction of edge crack extension using blunt cracks." International Journal of Mechanical Sciences 32: 253–264, 1990.

165. **Nye.,** "Physical Properties of crystals." 1957.

166. **Orlov, D.**, Beygelzimer, Y., Synkov, S., Varyukhin, V., Tsuji, N., Horita, Z., "Plastic flow, structure and mechanical properties in pure Al deformed by twist extrusion." Material Science and Engineering A 519:105-111, 2009.

167. **Orlov, D.**, Raab, G., Lamark, T. T., Popov, M., Estrin, Y., "Improvement of mechanical properties of magnesium alloy ZK60 by integrated extrusion and equal channel angular pressing." Acta Materiala 59:375-385, 2011.

168. **Ostberg, G.,** "Crack Propagation in Hydrided Zircaloy-2." The International Journal of Fracture Mechanics 4, 1968.

169. **Panigrahi, S. K.,** and Jayaganthan, R., "Development of ultrafine-grained Al 6063 alloy by cryorolling with the optimized initial heat treatment conditions." Materials and Design 32:2172–2180, 2011.

170. **Pardis, N.**, Ebrahimi, R., "Different processing routes for deformation via simple shear extrusion (SSE)." Material Science and Engineering A 527:6153-6156, 2010.

171. **Pardis, N.**, Talebanpour, B., Ebrahimi, R., Zomorodian, S., “Cyclic expansion-extrusion (CEE): A modified counterpart of cyclic extrusion-compression (CEC).” Material Science and Engineering A 528:7537-7540, 2011.

172. **Pathak, H.**, Singh, A., “Fatigue crack growth simulations of 3-D Problems using XFEM”, International Journal of Mechanical Science, 76:112-131, 2013.

173. **Patzak, B.,** and Jirásek, M., “Process zone resolution by extended finite elements.” Engineering Fracture Mechanics 70:957–977, 2003.

174. **Perlovich, Y.**, Isaenkova, M., Fesenko, V., Grekhov, M., Yu, S. H., Hwang, S. K., Shin, D. H., “Features of Texture and Structure Development in Zirconium under Equal Channel Angular Pressing.” Material science forum 503-504:859-864, 2006.

175. **Petch, N. J.,** “The cleavage strength of polycrystals”, Journal of the Iron and Steel Institute 174:25, 1953.

176. **Picklesimer, M. L.,** “Deformation creep and fracture in alpha zirconium alloys.” Electrochemiacal Technology 4:289-300, 1966.

177. **Proust, G.,** Tome, C. N., and Kaschner, G. C., “Modeling texture, twinning and hardening evolution during deformation of hexagonal materials.” Acta Materialia 55:2137–2148, 2007.

178. **Raab, G. J.**, Valiev, R. Z., Lowe, T. C., Zhu, Y. T., “Continuous processing of ultrafine grained Al by ECAP.” Material Science and Engineering A 382:30, 2004.

179. **Rangaraju, N.**, Raghuram, T., Vamsi, K. B., Prasad, K. R., Venugopal, P., “Effect of cryo-rolling and annealing on microstructure and properties of commercially pure aluminium.” Materials Science and Engineering A 398:246–251, 2005.

180. **Rapperport, E .J.,** Trans. TMS AIME 218:869- 876**,** 1960.

181. **Rapperport, E. J.,** “Room temperature deformation processes in zirconium.”, Acta Metallurgica. 7:254-260, 1959.

182. **Reed-Hill, R. E.**, Hartt, W. H. and Slippy, W. A., "Transaction Metallurgical Society AIME 242: 2211-2215, 1968.

183. **Rice, J. R.,** “A path independent integral and the approximate analysis of strain concentration by notches and cracks.” Journal of Applied Mechanics 35:379-386, 1968.

184. **Rickover, H. G.,** “History of development of zirconium alloys for use in nuclear power reactors.” US ERDA, NR&D, 1975.

185. **Rittenhouse, P. L.,** “Determination of the Anisotropy of Yielding and Flow in Zircaloy-2 from a Single Test.” Journal of Nuclear Materials 23:183-191, 1967.

186. **Rogerson, A.**, Murgatroyd, R. A., “Irradiation-growth in annealed Zr-2.5 wt% Nb at 353 K.” Journal of Nuclear Materials 80:260-266, 1979.

187. **Sahoo, S. K.,** Hiwarkar, V. D., Samajdar, I., Dey, G. K., Srivastav, D., Tiwari, R., and Banerjee, S., “Heterogeneous deformation in single-phase Zircaloy 2.” Scripta Materialia 56:963–966, 2007.

188. **Sahoo, S. K.,** Hiwarkar,V. D., Mani Krishna, K. V., Samajdar, I., Pant, P., Pujari, P. K., Dey, G. K., Srivastav, D., Tiwari, R., Banerjee, S., “Grain fragmentation and twinning in deformed Zircaloy 2: Response to positron lifetime measurements.” Materials Science and Engineering A 527:1427–1435, 2010.

189. **Saito, Y.**, Utsunomiya, H., Suzuki, H., Sakai, T., “Improvement in the r-value of aluminum strip by a continuous shear deformation process.” Scripta Materiala 42:1139. 2000.

190. **Sarkar, A.,** Mukherjee, P., and Barat, P., “X-ray diffraction studies on asymmetrically broadened peaks of heavily deformed zirconium-based alloys.” Materials Science and Engineering: A 485:176–181, 2008.

191. **Sarkar, A.**, Murty, K. L., “Microstructure–mechanical property correlation of cryo rolled Zircaloy-4.” Journal of Nuclear Materials 456:287–291, 2015.

192. **Sauvage, X.**, Wilde, G., Divinsky, S., Horita, Z., Valiev, R. Z., “Grain boundaries in ultrafine grained materials processed by severe plastic deformation and related phenomena.” Material Science and Engineering A 540:1-12, 2012.

193. **Schemel, J. H.,** “ASTM manual on zirconium and hafnium.” 1977.

194. **Segal, V. M.** “Materials processing by simple shear.” Material Science and Engineering A 197:157–164, 1995

195. **Segal, V. M.**, Reznikov, V. I., Kopylov, V. I., Pavlik, D. A., Malyshev, V. F., “Processy Plasticheskogo Structyroob razovania Metallov.” Minsk: Sci Eng. 1994.

196. **Sell, H. J.,** Ortlieb, E., Moan, G. D., and Rudling, P., “Effects of Alpha-Beta Transformation on High Temperature (LOCA) Creep Behavior of Zr-Alloys." Zirconium in the Nuclear Industry: Thirteenth International Symposium, ASTM STP 1423: 658-672, 2002.

197. **Shahbaz, M.**, Pardis, N., Ebrahimi, R., Talebanpour, B., “A novel single pass severe plastic deformation technique: Vortex extrusion.” Material Science and Engineering A 530:469-472, 2011.

198. **Shaltiel, D.**, Jacob, I., Davidov, D., “Hydrogen absorption and desorption properties of AB2 laves-phase pseudobinary compounds.” Journal of Less Common Metals 53:117-131, 1976.

199. **Sharma, K.,** Bui, T. Q., Zhang, Ch., Bhargava, R. R., “Analysis of a subinterface crack in piezoelectric bimaterials with the extended finite element method.” Engineering Fracture Mechanics 104:114–139, 2013.

200. **Shen, J. H.,** Li, Y. L., Wei, Q., “Statistic derivation of Taylor factors for polycrystalline metals with application to pure magnesium, Materials Science and Engineering: A 582:270–275, 2013.

201. **Shi, Y. D.**, Guo, D. F., Li, M., Zhang, Z. B., Ma, T. Y., and Zhang, X. Y., “Formation processes of dislocation cells in cryorolled Zr upon annealing.”, Materials Science and Technology 29:921-924, 2013a.

202. **Shi, Y.**, Li, M., Guo, D., Ma, T., Zhang, Z., Zhangm, G., Zhang, X., “Tailoring grain size distribution for optimizing strength and ductility of multi-modal Zr.”, Materials Letters 108:228–230, 2013b.

203. **Shimokawa, T.**, Tanaka, M., Kinoshita, K., Higashida, K., "Roles of grain boundaries in improving fracture toughness of ultrafine-grained metals", Physiacal Review B 83: 214113, 2011.

204. **Shivamurthy, B.**, Udaya Bhat, K., Anandhan, S., “Mechanical and sliding wear properties of multi-layered laminates from glass fabric/graphite/ epoxy composites”, Materials and Design, 44: 136-143, 2013

205. **Singh, S. P.,** Bhattacharya, S., Sehgal, D. K., “Evaluation of high temperature mechanical strength of Cr–Mo grade steel through small punch test technique, Engineering Failure Analysis 39:207–220, 2014.

206. **Sukumar, N.**, Srolovitz, D. J., Baker, T. J., and Prevost, J. H., “Brittle fracture in polycrystalline microstructures with the extended finite element method.” International Journal for Numerical Methods in Engineering 56:2015–2037, 2003.

207. **Tabachnikova, E. D.**, Podolskiy, A. V., Bonarski, B., Mangler, C., Bengus, V. Z., Smirnov, S.N., Velikodny, A. N., Tikhonovsky, M. A., and Zehetbauer, M. J., “Mechanical properties and microstructure evolution during deformation of ultrafine grained zirconium at low temperatures.” Rev.Adv.Mater.Sci. 25:168-175, 2010.

208. **Taheri, M.,** Weiland, H., Rollett, A., “A Method of Measuring Stored Energy Macroscopically Using Statistically Stored Dislocations in Commercial Purity Aluminum.” Metallurgical and Materials Transactions A 37:19-25, 2006.

209. **Takayama, Y.,** Szpunar, J. A., “Stored Energy and Taylor Factor Relation in an Al-Mg-Mn Alloy Sheet Worked by Continuous Cyclic Bending”, Materials Transactions, 45:2316-2325, 2004.

210. **Talebi, H.,** Silani, M., Bordas, S. P. A., Kerfriden, P., Rabczuk, T., “Molecular dynamics/XFEM coupling by a three-dimensional extended bridging domain with applications to dynamic brittle fracture.” International Journal for Multiscale Computational Engineering 11:527–541, 2013.

211. **Tenckhoff, E.,** “Deformation Mechanisms, Texture, and Anisotropy In Zirconium And Zircaloy.” American Society for Testing and Materials, 1988.

212. **Tenckhoff, E.,** “Zirconium in Nuclear Applications” ASTM STP 551:180-198, 1974.

213. **Tome, C. N.**, Maudlin, P. J., Lebensohn, R. A., Kaschner, G. C., “Mechanical Response of Zirconium—I. Derivation of a Polycrystal Constitutive Law and Finite Element Analysis.” Acta Mater. 49:3085–3096, 2001.

214. **Tong, H. Y.,** Wang, J. T., Ding, B. Z., Jiang, H. G., Lu, K. J., “The structure and properties of nanocrystalline $Fe_{78}B_{13}Si_9$ alloy.” Journal of Non-Crystalline Solids 150:444-447, 1992.

215. **Tong, P.,** Pian, T. H. H., “The Convergence of Finite Element Method in Solving Linear Elastic Problems.” International Journal of Solid Structures 3:865-879, 1967.

216. **Tóth, L. S.**, Arzaghi, M., Fundenberger, J. J., Beausir, B., Bouaziz, O., Arruffat-Massion, R., “Severe plastic deformation of metals by high-pressure tube twisting.” Scripta Materialia 60:175-177, 2009a.

217. **Toth, L. S.**, Lapovok, R., Hasani, A., Gu, C. F., “Non-equal channel angular pressing of aluminum alloy.” Scripta Materialia 61:1121-1124, 2009b.

218. **Um, H. Y.**, Yoon, E. Y., Lee, D. J., Lee, C. S., Park, L. J., Lee, S., Kim, H. S., “Hollow cone high-pressure torsion: Microstructure and tensile strength by unique severe plastic deformation”, Scripta Materialia, 71:41-44, 2014.

219. **Unga, T.,** Castelnau, O., Ribarik,, G., Drakopoulos, M., Bechade, J. L., Chauveau, T., Snigirev, A., Snigireva, I., Schroer, C., Bacroix, B., “Grain to grain slip activity in plastically deformed Zr determined by X-ray micro-diffraction line profile analysis.” Acta Materialia 55:1117–1127, 2007.

220. **Vadiraj, A.,** and Kamaraj, M., “Damage characterization of unmodified and surface modified medical grade titanium alloys under fretting fatigue condition.” Material Science and Engineering A 416:253–260, 2006a.

221. **Vadiraj, A.,** Kamaraj, M., “Characterization of fretting fatigue damage of PVD TiN coated biomedical titanium alloys.” Surface and Coatings Technology 200:4538–4542, 2006b.

222. **Valiev, R. Z.**, Estrin, Y., Horita, Z., Langdon, T. G., Zechetbauer, M. J., Zhu, Y. T., “Producing bulk ultrafine-grained materials by severe plastic deformation.” 58:33-39, 2006.

223. **Valiev, R. Z.,** Islamgaliev, R. K., Alexandrov, I. V., “Bulk nanostructured materials from severe plastic deformation.” Progress in Material Science 45:103-189, 2000.

224. **Valiev, R. Z.**, Korznikov, A. V., and Mulyukov, R. R., “Structure and properties of ultrafine-grained materials produced by severe plastic deformation.” Materials Science and Engineering, A 168:141-148, 1993.

225. **Valiev, R. Z.,** Krasilnikov, N. A., Tsenev, N. K., “Plastic deformation of alloys with submicron-grained structure.” Material Science Engineering A, 137:35-40, 1991.

226. **Vanitha, C.**, Kiran, M. K., Dey, G. K., Srivastava, D., Tewari, R., and Banerjee S., “Recrystallization texture development in single-phase Zircaloy 2.” Materials Science and Engineering A 519:51–60, 2009.

227. **Vedani, M.,** Bassani, P., Tuissi, A., Angella, G., “Ultrafine grained alloys produced by severe plastic deformation: issues on microstructural control and mechanical behavior.” Metallurgical Science and Technology 21-30, 2004.

228. **Ventura, G.**, Moran, B., and Belytschko, T., “Dislocations by partition of unity.” International Journal for Numerical Methods in Engineering 62:1463–1487, 2005.

229. **Veubeke, B.,** Fraeijs, de, Zienkiewicz, O. C., Holister, G. S., “Displacement and equilibrium models in the Finite element method.” International Journal of Numerical Methods in Engineering 52:287–342, 2001.

230. **Wang, Y. N.,** Huang, J. C., “Review: Texture analysis in hexagonal materials.” Materials Chemistry and Physics 81:11–26, 2003.

231. **Wang, Y.**, Chen, M., Zhou, F., Ma, E., “High tensile ductility in a nanostructured metal.” Nature 419:912-914, 2002.

232. **Watwood, V. B. Jr.,** “Finite Element Method for Prediction of Crack Behavior.” Nuclear Engineering and Design 11:323-332, 1969.

233. **Weatherly, G. C.,** “The precipitation of γ-hydride plates in zirconium.” Acta Metallurgica 29:501-512, 1981.

234. **Westlake, D. G.,** “Cross-Glide and twinning in crystals of quenched zirconium-hydrogen alloys.” Journal of Nuclear Materials 13:113-115, 1964.

235. **Whitmarsh, C. L.,** "Review of zircaloy-2 and zircaloy-4 properties relevant to n.s. savannah reactor design" Oak Ridge National Laboratory Oak Ridge, Tennessee Operated "By Union Carbide Corporation for The U. S. Atomic Energy Commission 1962.

236. **Williams, C. D.**, Gilbert, R. W., "Tempered structures of a Zr-2.5 wt % Nb alloy", Journal of Nuclear Materials 18:161-166, 1966.

237. **Wilsdorf, D. K.**, Hansen, N., "Geometrically Necessary, Incidental and Subgrain Boundaries" Scripta Metallurgica 1557-1562, 1991.

238. **Xu, F.**, Holt, R. A., Daymond, M. R., "Evidence for basal <a>-slip in Zircaloy-2 at room temperature from polycrystalline modeling", Journal of Nuclear Materials 373:217-225, 2008a.

239. **Xu, F.**, Holt, R. A., Daymond, M. R., "Modeling lattice strain evolution during uniaxial deformation of textured Zircaloy-2". Acta Materialia 56: 3672–3687, 2008b.

240. **Yoon, J. W.**, Barlat, F., Dick, R. E., "Plane stress yield fnction for aluminum alloy sheet-Part II: FE formulation and its implementation", International Journal of Plasticity, 20: 495–522, 2004.

241. **Yu, Q.**, Sun, J., Morris, J. W. Jr., and Minor, A. M., "Source mechanism of non-basal <c + a> slip in Ti alloy", Scripta Materialia 69:57–60, 2013.

242. **Zamal, M.**, "On the Finite Element Method", Numerische Mathematik, 12: 394-409, 1968.

243. **Zhao, Y. H.**, Liao, X. Z., Cheng, S., Ma, E., and Zhu, Y. T., "Simultaneously Increasing the Ductility and Strength of Nanostructured Alloys", Advance Materials 18:2280–2283, 2006.

244. **Zherebtsov, S. V.**, Dyakonov, G. S. , Sokolenko, A. A. S., Salishchev, G. A., Semiatin, S. L., "Formation of nanostructures in commercial-purity titanium via Cryorolling", Acta Materialia, 61, 1167–1178, 2013.

245. **Zhong, S.,** and Oyadiji, S. O., "Crack detection in simply supported beams without baseline modal parameters by stationary wavelet transform", Mechanical Systems and Signal Processing, 21:1853–1884, 2007.

246. **Zhu, L.**, Lu, Z., "Modelling the plastic deformation of nanostructured metals with bimodal grain size distribution", International Journal of Plasticity 30–31:166–184, 2012.

247. **Zhu, Y. T.,** Langdon, T. G., "Influence of Grain Size on Deformation Mechanisms: an extension to nanocrystalline materials", Material Science and Engineering A 409: 234-242, 2005.

248. **Zhu, Y.**, Jiang, H., Huang, J., Lowe, T., "A new route to bulk nanostructured metals", Metall Mater Trans A, 32:1559-1562, 2001.

249. **Zuzek, E.**, Abriata, J. P., Martin, A. S., Manchester, F. D., "Zr-H (Zirconium-hydrogen) system", Bull Alloy Phase Diagrams 11: 385-395, 1990.